THE UNIVERSITY OF MANCHESTER

Improving the Thermal Performance of Parabolic Trough Collectors using Modelling and Simulations

A thesis submitted to The University of Manchester for the degree of

Doctor of Philosophy (PhD)

in the Faculty of Science and Engineering

2021

Nabeel Khaleel Abed

School of Mechanical, Aerospace and Civil Engineering

Table of Contents

List of Tables

List of Figures

List of publications

1- Abed, Nabeel and Afgan, Imran. 2019. "Enhancement Techniques of Parabolic Trough Collectors: A Review of Past and Recent Technologies". Advancements in Civil Engineering & Technology. 3 (3). **No. of citation: 8.**

2- Abed, Nabeel, and Imran Afgan. "An extensive review of various technologies for enhancing the thermal and optical performances of parabolic trough collectors". International Journal of Energy Research, 2020, 44 (7): 5117-5164. **Q1, I.F.: 3.741, No. of citation: 27**.

3- Abed, Nabeel, Imran Afgan, Andrea Cioncolini, Hector Iacovides, and Adel Nasser. "Assessment and Evaluation of the Thermal Performance of Various Working Fluids in Parabolic Trough Collectors of Solar Thermal Power Plants under Non-Uniform Heat Flux Distribution Conditions". Energies, 2020, 13 (15): 3776. **Q2, I.F.: 3.004, No. of citation: 11.**

4- Abed, N., Afgan, I., Nasser, A., Iacovides, H., Cioncolini, A. and Meakhail, T. Numerical investigations of parabolic trough collectors using different nanofluids. Proceedings of 5th International Conference on Energy Engineering, December 24–26, 2019, Aswan-Egypt. **No. of citation: 8.**

5- Abed, N.; Afgan, I.; Cioncolini, A.; Iacovides, H.; Nasser, A.; Mekhail, T. "Thermal performance evaluation of various nanofluids with non-uniform heating for parabolic trough collectors". Case Stud. Ther. Eng. 2020, 22, 100769. **Q1, I.F.: 4.01, No. of citation: 10.**

6- Abed, N., Afgan, I., Iacovides, H., Cioncolini, A., Khurshid, I. and Nasser, A. "Thermal-Hydraulic Analysis of Parabolic Trough Collectors Using Straight Conical Strip Inserts with Nanofluids". Nanomaterials, 2021, 11 (4): 853. **Q1, I.F.: 5.076, No. of citation: 4.**

7- Abed, N., Afgan, I., Iacovides, H., Cioncolini, A., and Nasser, A. "Effect of various multiple strip inserts and nanofluids on the thermal-hydraulic performances of parabolic trough collectors". The revised version has been submitted to the journal of applied thermal engineering. **Q1, I.F.: 4.725.**

Abstract

A wide range of engineering industrial applications requires both the thermal and optical efficiencies of the system to be maximized with a reasonable low penalty for the friction factor and subsequently low losses in pressure. Amongst the family of concentrated solar power systems, parabolic trough collectors (PTC) which have recently received significant attention, face similar challenges. To effectively enhance the thermal performance of the PTC system four enhancement techniques were numerically investigated and addressed in this thesis; changing heat transfer fluids, replacing the working fluids with nanofluids that have better thermal-physical properties than those of base fluids, inserting different turbulators with various design configurations and finally combining the advantages of nanofluids and swirl generators in the same application. All simulations were assumed to be in steady-state and three dimensions with a range of Reynold's number ($Re=10^4$-10^5). For the simulation the Monte Carlo Ray Tracing (MCRT) model was used to represent the non-uniform heat flux around the absorber tube of the PTC. Two low-Reynold's turbulence models were used; Launder and Sharma (LS) k-epsilon and Shear Stress Transport (SST) k-omega models. In order to assess the performance of each enhancement technique, a number of parameters were analyzed including average Nusselt (Nu) number, specific pressure drop distributions, thermal losses, overall collector efficiency and exergy efficiency of the PTC system. Three categorized-types of pure fluids were used firstly. Secondly, numerical simulations were performed for a solar collector to test the effectiveness of six non-metallic nanoparticles dispersed individually in three different base working fluids with three different volume fractions. The third step was to study the effect of the variation of geometrical properties of a single canonical insert to find the optimized shape then increase the number of strips to two, three and four around the central rod. The final step was to assess the effect of various straight strip shapes with and without nanofluids. Four different strip arrangements were considered; large conical-shape strips, small conical-shape strips, rectangular-shape strips and elliptical-shape strips.

Results showed that, the largest enhancements in the overall collector efficiency and thermal exergy efficiency were achieved by the hybrid system of combining both large conical-shape strips and 6% of SiO_2 dispersed in therminol VP-1 which are 15.41% and 15.32% respectively compared to a typical system.

Declaration

I declare that no portion of this work referred to in the thesis has been submitted in support of an application for another degree or qualification of this or any other university or other institute of learning.

Nabeel Khaleel Abed
Date: September 14, 2021

Copyright Statement

Acknowledgements

I would like to thank my supervisors: Dr. Imran Afgan, Prof. Hector Iacovides and Dr Andrea Cioncolini for their continued help and assistance without which this work could not have been completed. They have been exceedingly patient and helpful every time I have come across obstacles, and have been understanding of my ambitions to work in field of Thermofluids modelling.

I am also grateful to the University of Manchester for providing me the PhD scholarship.

I am extremely grateful for my wife and my lovely daughters (Jannat and Sarah) for their significant support and help during the turbulent period of my PhD research. Many thanks are sent to my parents, my brothers and sisters and all the family-members of my father-in-law.

Special thanks to both (Higher Committee for the Development of Education and the Ministry of higher education and scientific research in Iraq) for supporting me and granting me a permission to complete the PhD study.

Finally, I am grateful to all my friends at the University of Manchester, Abdulmajid, Firas, Khalil, Ehimen, Diego, Maxim, Ansab, Mobin and Constantinosa who have witnessed my PhD struggles on the frontline and have supported me to overcome them.

Nomenclature

Latin symbols

A_a	Collector aperture area.
$C_{p,nf}$	Nanofluid specific heat capacity.
$C_{p,f}$	Fluid specific heat capacity.
$C_{p,s}$	Solid specific heat capacity.
D_i	Absorber tube inner diameter.
D_o	Absorber tube outer diameter.
D_{oe}	Outer surface diameter of the glass envelope.
E	Extra sours term
E_m	Modulus of elasticity.
E_s	Available solar exergy.
E_u	Useful output exergy.
F	Body force.
$F_1$and F_2	Blending functions.
f	Flow friction factor.
f_o	Friction factor of pure fluid.
f_L	The focal line.
f_2 and f_μ	Damping functions
G_b	Solar beam radiation.
H	Strip height.
h_{out}	Ambient heat transfer coefficient.
k	Turbulent kinetic energy.
k_f	Fluid thermal conductivity.
k_{nf}	Nanofluid thermal conductivity.
k_s	Solid thermal conductivity.
L	Solar tube length.
$\dot{m}$	Mass flow rate.
$m_f^{\cdot}$	Face mass flow rate.
$\underline{n}$	Unit vector.
Nu	Nusselt number.
Nu_o	Nusselt number of the pure fluid.
P	Horizontal pitch distance.
P_k	Energy production.
Pr	Prandtl number.
Q_{loss}	Thermal losses.
Q_s	Available solar energy.
Q_u	Useful thermal energy.
R_t	Turbulent Reynold's number
Re	Reynold's number.
S	Volumetric heat source.
S_i	Surface area.
S_{ij}	Strain tensor rate.
t	Strip thickness.
T_{am}	Ambient temperature.
T_{ave}	Average fluid temperatures.
T_f	Mean fluid temperature.
T_{in}	Inlet fluid temperature.
T_o	Outer surface temperature of the solar receiver.
T_{oe}	Outer surface temperature of the glass envelope.

T_{out}	Outlet fluid temperature.
T_{sky}	Sky temperature.
T_{sun}	Sun temperature.
T_w	Inner wall temperature.
U	Bulk fluid velocity.
U_i	Flow instantaneous velocity of the ith vector component.
$u_i u_j$	Reynold's stress tensor.
$\overline{u_i \mathrm{t}}$	Turbulent heat flux.
$\dot{V}$	Volumetric flow rate.
V_f	Base fluid volume.
V_s	Solid particle volume.
V_w	Wind speed.
w_a	Aperture width.
W_p	Pumping power.
y	Distance from the solid wall to the first cell.
y^+	Mean non-dimensional distance.

Greek symbols

α	The particle radius.
β	Thermal expansion coefficient.
ε_o	Solar receiver emissivity
ε	Dissipation rate
ε_{oe}	Glass envelope emissivity
$\tilde{\varepsilon}$	Quasi-homogeneous dissipation rate.
η_{el}	Power-block electrical efficiency
η_{ex}	Exergy efficiency.
$\eta_{overall}$	Overall collector efficiency
μ_f	Fluid dynamic viscosity.
μ_{nf}	Nanofluid dynamic viscosity.
ν	Nanofluid kinematic viscosity.
υ_P	Poisson's ratio.
$\mathcal{V}_t$	Eddy viscosity.
ρ_{nf}	Nanofluid density.
ℓ	Length scale.
ζ	Time scale
ρ_f	Fluid density.
ρ_s	Solid density.
σ	Stefan-Boltzmann constant.
σ_θ	The circumferential stress.
φ	Volume fraction.
φ_r	Rim angle.
τ_w	Wall shear stress.
ΔP	Flow pressure drop.
θ	Strip angle.
Ψ	The shape factor.
δ_{ij}	The Kronecker delta.
ω	Specific dissipation rate.
Ω	vorticity (mean strain-rate tensor)
ϕ	Scalar parameter.
ϒ	Flux limiter function.

Abbreviations

CD	Central differencing
CFD	Computational Fluid Dynamics
CNT	Carbon nano-tubes
CSP	Concentrated solar power
DNS	Direct numerical simulation
DNI	Direct normal irradiance.
EES	Engineering Equation Solver
FEM	Finite Element Method.
FVM	Finite volume method
GCR	Geometrical concentration ratio
HCE	Heat collection element
HTF	Heat Transfer Fluid
LES	Large eddy simulation
LS	Launder and Sharma
LCR	Local concentration ratio
MS	Molten salt
MCRT	Monte Carlo Ray Tracing
NP	Nanoparticle
Open FOAM	Open Field Operation and Manipulation
PEC	Performance evaluation criterion
PTC	Parabolic Trough Collectors
RANS	Reynolds-Averaged Navier-Stokes
SST	Shear Stress Transport
STPP	Solar thermal power plants
SWCNT	Single wall carbon nano-tubes
TKE	Turbulent kinetic energy
TO	Therminol VP-1
TVD	Total Variation Diminishing
UD	Upwind differencing
VF	Volume fraction
W	Water

Chapter 1: Introduction

1.1. Concentrated solar power (CSP) technology

It is widely known that global warming has become a defining issue of our time, with consequences that include shifting weather patterns, rising sea levels, and compromised food production. To address global warming, clean, renewable and sustainable sources of energy should be identified to reduce the amount of CO_2 emissions. Solar thermal energy is one of the viable solutions to reduce reliance on fossil fuels, decrease the level of greenhouse-gas emissions, and meet the requirements of human societies with electrical power, water heating systems and other industrial processes.

Concentrating solar power (CSP) plants, in particular, rely on the direct normal irradiance which can be described as the amount of solar energy received per unit area on the surface held normal to the rays of the sun. The CSP plant technology can be categorised into four main families depending on the method used to collect the solar radiant energy: 1) parabolic trough collectors (PTC), 2) linear Fresnel reflectors, 3) parabolic dishes, and 4) solar towers. The operating principle of each technology is shown in Figure 1.1 (Blanco and Miller (2017), Abed and Afgan (2019)), whilst their main properties are listed in Table 1-1 (Philibert and Frankl (2010)).

Presently, the most cost-effective and commercially developed technology among CSPs is the PTC system, particularly for medium-temperature applications, thus this system is the subject of the present study.

(Parabolic trough collector) (Linear Fresnel reflector)

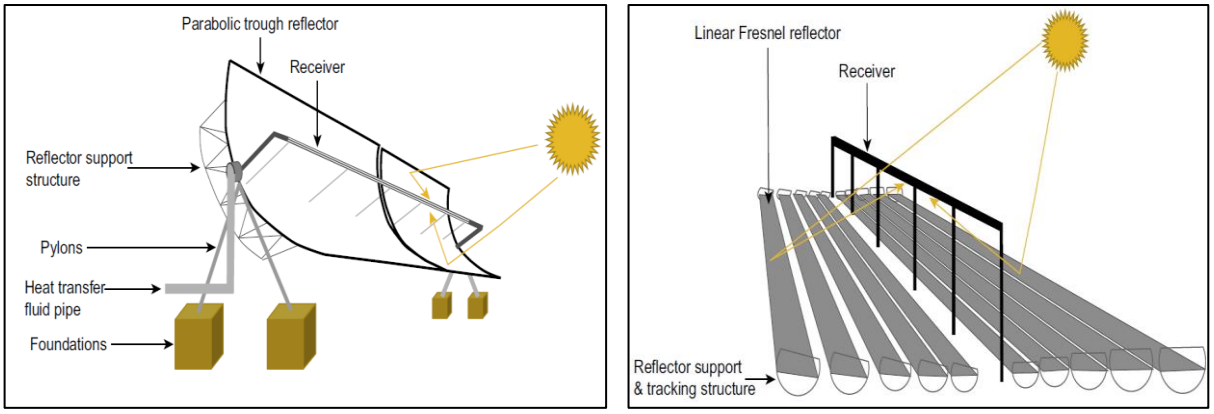

(Parabolic dish reflector) (Solar tower)

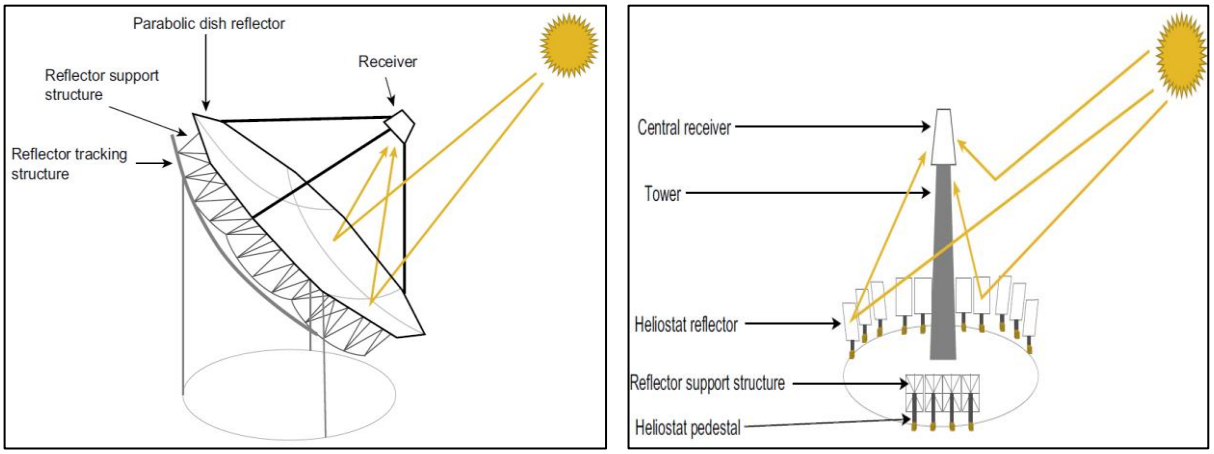

Figure 1.1: Current CSP technologies, Blanco and Miller (2017).

Table 1-1: The main properties of the four CSP technologies, Philibert and Frankl (2010)...

Focus Category / Absorber Category		**Line Focus** The sun is tracked along a single axis by collectors with focusing the irradiance only on a linear absorber making the tracking sun simpler.	**Point Focus** The sun is tracked along two axes by collectors with focusing the irradiance only on a single point absorber allowing for larger temperature.
Fixed	The absorber is a stationary tool and it is independent of the focusing apparatus. However, the transfer of the collected thermal energy to the power section is easier.	**Linear Fresnel Reflectors**	**Central Receiver**
Mobile	The mobile absorber moves together with the concentrating apparatus. However, more energy can be collected by both mechanisms (Point focus and line focus).	**Parabolic Trough Collectors**	**Parabolic Dishes**

1.2. Fundamentals of Parabolic Trough Collector (PTC)

As shown in Figure 1.2, PTC systems can be basically regarded as large heat exchangers, with the major components being the solar absorber, the glass envelope, the positioning system, the support structure, and the reflector surface; some of the main components of PTC systems are described below.

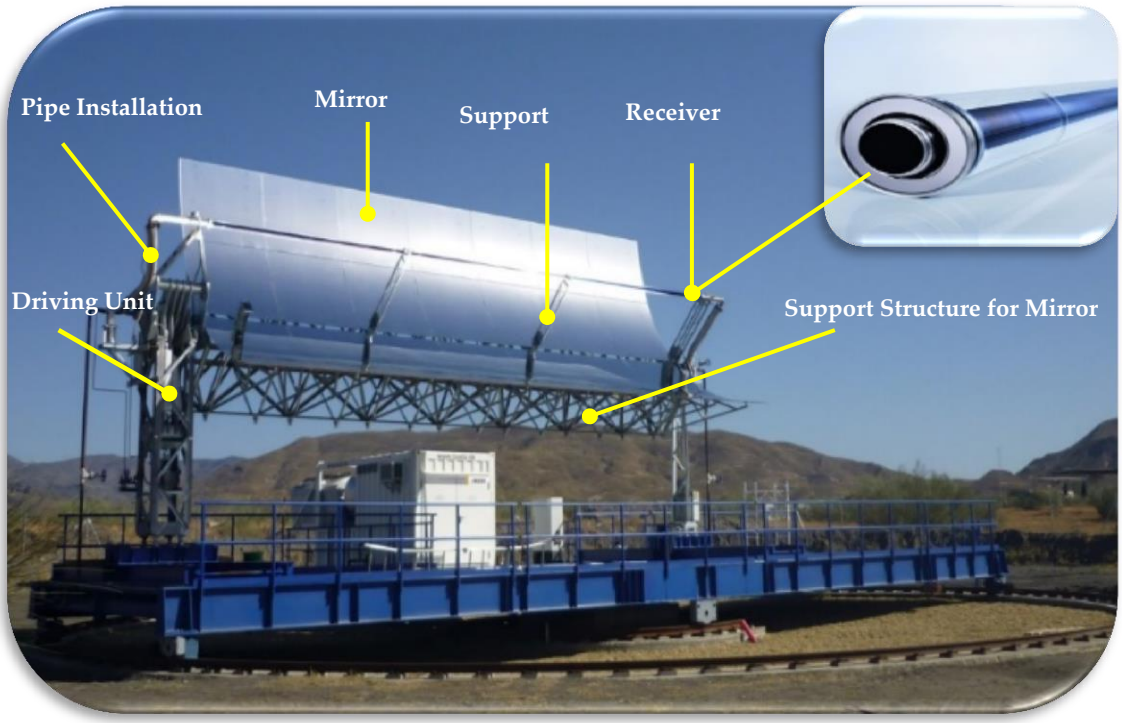

Figure 1.2: The structure and elements of parabolic trough collector, from (www. dlr.de.com)[(1)].

1.2.1. Reflectors

This element consists of high specular reflectance (more than 88 %) mirrors and structural components used to reflect the solar energy onto the receiver. Mirrors are normally made from low-iron float glass (approximately 4 mm thickness) of large solar transmittance, silvered from the back and coated with selective coatings to maximize their solar reflectance (SR = 0.93) and durability. The installation, as well as the mounting of the structures, has a large effect on the overall performance of the plant (Kreith and Goswami (2007)).

(1) Adapted from (https://www.dlr.de/dlr/en/desktopdefault.aspx/tabid-10202/334_read-1557/year-2011/#/gallery/3281), accessed 12.10.2018.

1.2.2. Absorber tube

The solar receiver converts the absorbed incident solar radiation into the thermal energy which is carried through the absorber via the heat transfer fluid. This component (also called a heat collection element (HCE) or receiver) is the most important element in the PTC system, and is made typically from a steel tube that is coated with a multilayer cermet coating to provide good optical properties, low thermal emissivity and large solar absorptivity. Its length is generally 4 m between the two support braces and might be extended to 150 m. The inner and outer diameters of the absorber tube are typically of about 66 mm and 70 mm, respectively, whereas the inner and outer diameters of the glass envelope are of about 115 mm and 120 mm (Price et al. (2002a) and Abed and Afgan (2020)). The annular space between the absorber tube and the glass envelope is generally kept at vacuum conditions (air pressure in the gap typically maintained at 0.013 Pa) to further reduce the heat losses (Hachicha et al. (2013)).

1.2.3. Heat Transfer Fluid (HTF)

The function of the HTF is to collect the thermal energy absorbed by the receiver and to transport it to the storage system or directly to the power block in the case of solar thermal power plant application. Selecting the appropriate HTF is application-specific and depends on the operating conditions and design peculiarities of each installation. Ideally, HTFs should have good thermal stability, should be able to operate safely throughout the range of temperatures of interest, should have good chemical compatibility with the tubing wall materials, and finally should be low cost and environmentally friendly (Abed et al. (2020a). Additionally, fluids with a high thermal conductivity, high heat capacity, and large heat transfer coefficient are normally desired to maximize the heat transfer effectiveness, together with a low viscosity and a small thermal expansion coefficient to reduce pumping power and thermal expansion concern (Nahhas et al. (2017)).

1.3. The PTC applications

The practical significance of PTC systems is rather broad: to date, PTC systems have been successfully used in a range of applications, including power generation, water treatment (desalination and/or pasteurization), air conditioning and refrigeration, and hot water production, as summarized in Table 1-2 where selected key reference studies are also included.

Table 1-2: Main engineering and industrial applications of PTCs utilized in the preceding studies.

No.	Main application type	Reference
1	Electrical power generation	Hachicha et al. (2013)
2	Water desalination process	Raja and Vijay (2019)
3	Water pasteurization process	Bigoni et al. (2014)
4	Air-conditioning and solar refrigeration	Fadar et al. (2009)
5	Hot water production	Hewett et al. (1991)
6	Pumping irrigation water	Larson (1987)
7	Solar cooker	Noman et al. (2019)
8	Industrial processes	Kizilkan et al. (2016)

1.4. Aim and Methodology of the study

The main aim of this study is to improve the thermal performance represented by the thermal energy gain, thermal loss reduction and thermal efficiency as well as the thermodynamic performance represented by the thermal exergy efficiency of the parabolic trough collector using numerical simulations. In order to achieve this aim, the following objectives have been considered:

1. Modelling the flow characteristics and conjugated heat transfer inside a solar receiver using RANS models (Launder and Sharma (LS) k-ε and k-ω SST) in three dimensions and steady-state conditions using three different working fluids (water, therminol VP-1 and molten salt) over a wide range of inlet temperatures and Reynolds (Re) numbers.

2. Investigating the influence of different types of nanoparticles with different base heat transfer fluids (water, therminol VP-1 and molten salt) on the thermal performance using actual non-uniform heat flux distribution over a range of Re number of (10^4-10^5) and various volume fractions.

3. Studying the effects of optimized straight conical strip inserts attached to the central rod under a non-uniform heat flux profile around the absorber tube. After obtaining the optimum strip height and angle, the number of strips was increased stepwise from one to four over a wide range Re numbers.

4. Examining the effect of Four different strip arrangements: 1) large conical-shape strips, 2) small conical-shape strips, 3) rectangular-shape strips, and 4) elliptical-shape strips; and every arrangement was examined for a range of application-representative Re number values from 10^4 to 10^5 using Therminol® VP-1 base fluid at an inlet temperature of 400 K and non-uniform heat flux distribution.

5. Assessing the effect of best candidate of nanofluids combined with the optimized four-strip arrangements for a range of application-representative Re number values from 10^4 to 10^5 using Therminol® VP-1 base fluid at an inlet temperature of 400 K and non-uniform heat flux distribution.

1.5. Outline of the thesis

The structure of the present study is organized as follows: the background and literature review of the PTC are presented in chapter two. The third chapter shows the numerical methodology used in the current work explaining the discretization numerical approach (Finite volume method) in details. The turbulence modelling is also presented in chapter three with explaining the turbulence models used in the present work. However, the effect of changing heat transfer fluids on the thermal performance using conjugated heat transfer model is illustrated in chapter four. Whereas the effect of numerous types of nanofluids on the thermal performance is clarified in chapter five using conjugated heat transfer model. Optimizing the straight strip and its effect on the thermal performance of PTCs with and without nanofluid is presented in chapter six. However, chapter seven illustrates the effect of multiple strip shapes with and without nanofluid technology. Finally, the conclusion and planning of the future work are summarized in chapter eight.

Chapter 2: Literature review and background

2.1. Introduction

The current chapter presents a review of the PTC systems comparing recent and past technologies which are widely being used to improve and enhance the thermal and optical efficiencies. Some technologies are comprehensively addressed to effectively enhance the thermal performance of the PTC's; changing working heat transfer fluids, replacing the working fluids by nanofluids (single and hybrid) that have higher thermal-physical properties than those of base working fluids, inserting different turbulators with various design configurations.

2.2. Mathematical Formulations of PTCs.

A parabolic trough collector (PTC) is made up of long, linear parabolic-shaped concentrating system of mirrors and a receiver tube that is placed along the focal axis of the parabola. A schematic diagram of the parabolic trough and its receiver is illustrated in Figure 2.1. It can be observed from the Figure 2.1 that the PTC arrangement consists of a parabolic trough, which is made from mirror shaped like a parabola. The metallic solar receiver is usually externally coated by a special material. Depending upon the configuration it may or may not be encapsulated by a glass envelope. The internal space of the solar receiver is filled with an appropriate heat transfer working fluid. The thermal process in a PTC system depends on the thermal balance between this HTF and its surrounding. The parabolic trough receives solar energy from the sun and reflects it onto the solar receiver. Inside the solar receiver, the absorber tube absorbs part of the reflected energy and raises the temperature of the HTF.

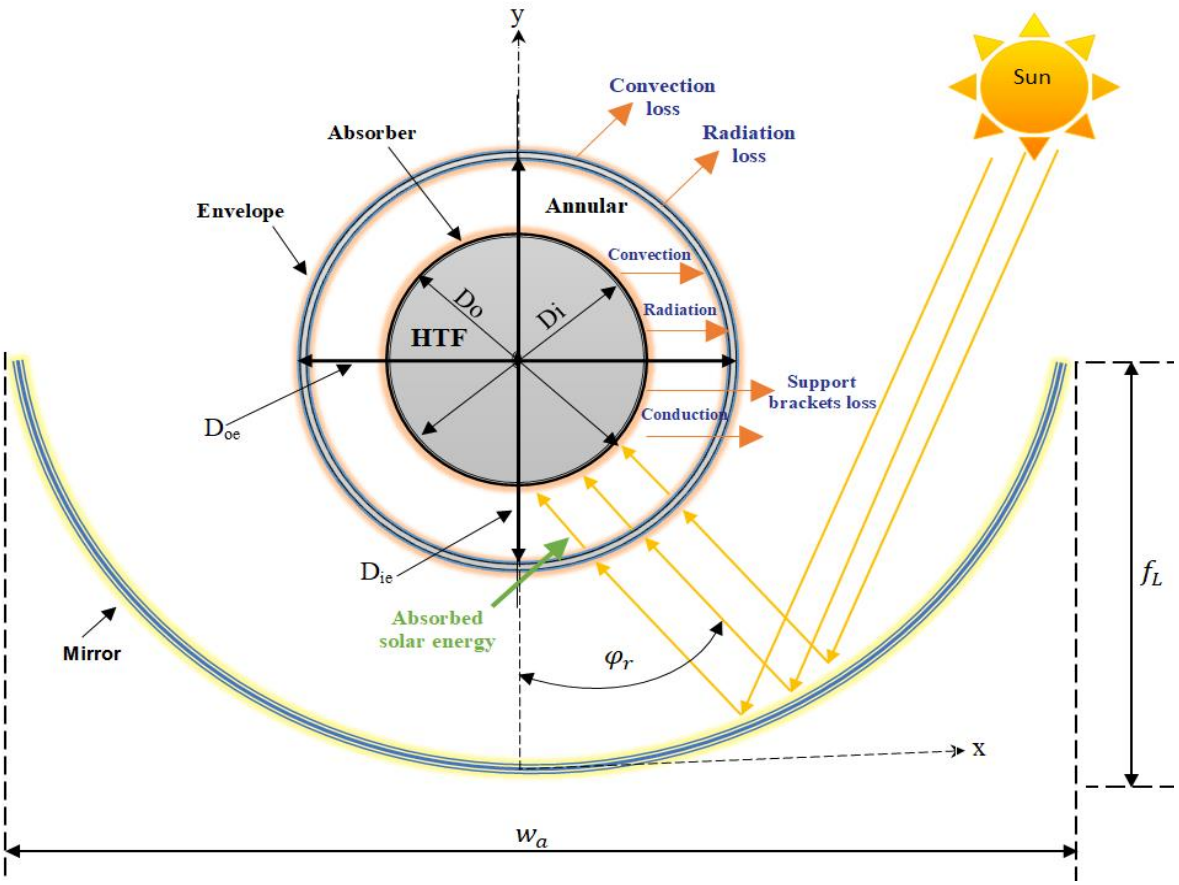

Figure 2.1: Schematic diagram of the parabolic trough and its receiver.

The remaining energy is sent back to the outer surface of the HCE via conduction, which in turn sends the energy to the internal surface of the glass envelope via convection and radiation. The energy continues transferring from the internal surface of the glass envelope to the external surface of the glass envelope via conduction and then from the external surface to the ambient via convection and to the surrounding via radiation as losses, as shown in the thermal resistance model presented in Figure 2.2. The convection heat transfer is assumed to occur from the solar receiver to the inner wall of the glass envelope in the circumferential direction.

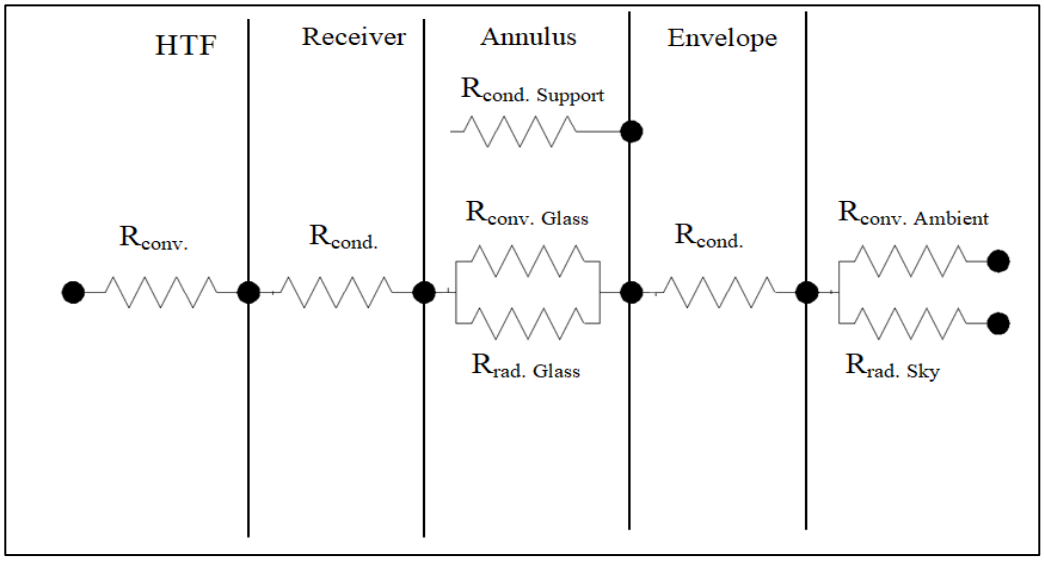

Figure 2.2: The parabolic trough collector (PTC) thermal resistance model.

2.2.1. Mathematical Analysis of the Geometrical Design

The geometrical profile of the typical PTC can be described by the following expression (Duffie and Beckman (2013)):

$$x^2 = 4yf_L. \tag{2.1}$$

The parameter f_L is the focal line which represents the position of the solar receiver. This parameter is determined by the following formula:

$$f_L = \frac{w_a}{4\tan(\frac{\varphi_r}{2})}. \tag{2.2}$$

In the equation above, w_a is the width of the collector's aperture and φ_r represents the rim angle. This angle can be calculated by the following expression:

$$\varphi_r = tan^{-1}\left[\frac{8(\frac{f_L}{w_a})}{16(\frac{f_L}{w_a})^2 - 1}\right] = sin^{-1}\left(\frac{w_a}{2r_r}\right). \tag{2.3}$$

The variable r_r is the rim radius which can be obtained from the following formula:

$$r_r = \frac{2f_L}{1 + cos\varphi_r}. \tag{2.4}$$

Other important parameters related to the collector's geometry are the total collector aperture area A_a and the outer surface area of the solar absorber A_o which can be calculated as follows:

$$A_a = w_a L. \tag{2.5}$$

$$A_o = \pi D_o L. \quad (2.6)$$

The parameter L is the length of the collector aperture. From the above equations, the geometrical concentration ratio GCR represents the collector's aperture area to the outer surface area of the absorber as following:

$$GCR = \frac{A_a}{A_o}. \quad (2.7)$$

2.2.2. Thermal analysis of PTC's system

In this section, the main parameters related to the thermal performance of the PTC are presented. These include the thermal efficiency, the thermal exergy, the solar available radiation, the useful exergy and useful energy, the heat transfer behaviour, the friction factor and the corresponding pressure drop. The useful thermal energy Q_u carried by the heat transfer fluid is determined by using the thermal energy balance on its control volume which is given in the following equation based on the mass flow rate $\dot{m}$, specific heat capacity C_p and fluid temperatures (T_{out} and T_{in}) (Duffie and Beckman (2013)):

$$Q_u = \dot{m} C_p (T_{out} - T_{in}). \quad (2.8)$$

The solar energy Q_s that is received by the solar collector can be determined as the solar beam radiation G_b multiplied by the reflector aperture area A_a as reported in the equation below:

$$Q_s = A_a \, G_b. \quad (2.9)$$

Then, the thermal efficiency is the ratio of the useful thermal energy to the absorbed solar energy which can be given in the following expression:

$$\eta_{th} = \frac{Q_u}{Q_s}. \quad (2.10)$$

However, the overall collector efficiency is the ratio of the useful thermal energy to the absorbed solar energy taking the effect of pumping power into consideration, as suggested by Wirz et al. (2014) as follows:

$$\eta_{overall} = \frac{Q_u - W_p/\eta_{el}}{Q_s}, \quad (2.11)$$

where η_{el} is the electrical efficiency of the power block which was taken as 32.7%. However, W_p is pumping power and can be calculated by the following equations:

$$W_p = \Delta P V^{\cdot}, \tag{2.12}$$

where $V^{\cdot}$ is volumetric flow rate and ΔP is the pressure drop which can be calculated by using the Darcy–Weisbach equation as follows:

$$\Delta P = f \frac{L}{D_i} \frac{\rho\, U^2}{2}. \tag{2.13}$$

$$f = \frac{8\tau}{\rho U^2}, \tag{2.14}$$

where f is friction factor, U is the fluid velocity, L is the absorber length, D_i is the inner absorber diameter, ρ is the fluid density and τ is the wall shear stress. The useful thermal exergy E_u output from the solar collector can be calculated from the following equation (Yazdanpanahi et al. (2015)):

$$E_u = Q_u - m^{\cdot} C_p\, T_{am} \ln\left(\frac{T_{out}}{T_{in}}\right) - m^{\cdot} T_{am} \frac{\Delta P}{\rho T_f}. \tag{2.15}$$

Here T_f represents the average fluid temperature and T_{am} is the ambient temperature. The last term of pressure drop is typically very small in practical applications, especially with liquids working fluids, and can therefore be neglected.

The available solar exergy E_s can be calculated from the following equation suggested by Petela (2003):

$$E_s = Q_s \left[1 - \frac{4}{3}\left(\frac{T_{am}}{T_{sun}}\right) + \frac{1}{3}\left(\frac{T_{am}}{T_{sun}}\right)^4\right]. \tag{2.16}$$

The sun temperature in the above equation is (5800 K) which is the real temperature in its outer layer. The exergetic efficiency then can be calculated as the ratio of the useful exergy to the input exergy, as follows:

$$\eta_{ex} = \frac{E_u}{E_s}. \tag{2.17}$$

It is very important to take the exergetic efficiency into account because it is related to the maximum possible produced work. For the thermal losses from the glass envelope to the environment, the following energy balance given by Bhowmik and Mullick (1985) can be used

$$Q_{loss} = L\pi D_{oe} h_{out}(T_{oe} - T_{am}) + L\pi D_{oe}\, \sigma \varepsilon_{oe}\left(T_{oe}^4 - T_{sky}^4\right). \tag{2.18}$$

In the above formulation the subscript oe represents the outer surface of the glass envelope and o refers to the external wall of the solar receiver. The parameter T_{am} represents the ambient temperature, ε_{oe} the emissivity of the glass envelope and σ the Stefan-Boltzmann constant (5.67 x 10^{-8} W/m^2 K^4). Here the ambient convection heat transfer coefficient (h_{out}) is obtained by Bhowmik and Mullick (1985) as

$$h_{out} = 4V_w^{0.58} D_{oe}^{-0.42}. \tag{2.19}$$

The variables D_{oe} and V_w are the outer diameter of the glass envelope and the wind speed respectively. Finally, the parameter T_{sky} represents the sky temperature which can be calculated using the correlation suggested by Swinbank (1963) as

$$T_{sky} = 0.0552\, T_{am}^{1.5}. \tag{2.20}$$

It is worth noting that in the case of analyzing only the bare receiver (such as the present study without the glass envelope), the thermal losses take place directly from the solar receiver to the sky by radiation and to the ambient by convection. Thus, equation (2.18) can be rewritten as

$$Q_{loss} = L\pi\, D_o h_{out}(T_o - T_{am}) + L\,\pi\, D_o \sigma\, \varepsilon_o \left(T_o^4 - T_{sky}^4\right). \tag{2.21}$$

The external surface emissivity of the solar receiver depends on the selected coating and mean external surface temperature T_o in degree Celsius of the solar receiver given by Dudley et al. (1994) as

$$\varepsilon_o = 0.062 + 2 \times 10^{-7} \times T_O^2. \tag{2.22}$$

For the bare receiver, the ambient convective heat transfer coefficient reads as

$$h_{out} = 4V_w^{0.58} D_o^{-0.42}. \tag{2.23}$$

In addition to the previous equations of the useful thermal energy, the thermal energy transferred from the absorber wall to heat transfer fluid is the main parameter of heat transfer analysis which strongly depends on the convection heat transfer coefficient. Therefore, the useful thermal energy can also be given in the form below (Duffie and Beckman (2013)):

$$Q_u = h\,A_i\left(T_i - T_f\right). \tag{2.24}$$

The parameter A_i is the inner surface area of the absorber tube. However, the convection heat transfer coefficient is determined from the Nu number, which depends on the absorber geometry and flow conditions. Besides, two important non-dimensional numbers are involved in the calculation of Nu number: the Re number and Prandtl number Pr. For the case of solar absorber, these numbers (Nu, Re and Pr) are given in the equations below, (Incropera et al. (2006)):

$$Nu = \frac{hD_i}{k}. \tag{2.25}$$

$$Re = \frac{\rho\,U\,D_i}{\mu}. \tag{2.26}$$

$$Pr = \frac{\mu\,C_p}{k}. \tag{2.27}$$

The variables k, ρ, U, μ and C_p are fluid thermal conductivity, fluid density, fluid velocity, fluid dynamic viscosity and fluid specific heat capacity respectively, whereas the tube diameter is taken as the hydraulic diameter in the presence of central rod cases, which can be calculated as $(D \equiv D_i - D_r)$ and taken as the internal absorber diameter in the typical system.

In solar receiver geometries when $Re \geq 4000$, the flow is fully turbulent and the corresponding average Nu number can be predicted using the empirical correlations proposed by Petukhov (1970) or Gnielinski (1976) as

$$Nu = \frac{\left(\frac{f}{8}\right) Re\,Pr}{1.07 + 12.7\left(\frac{f}{8}\right)^{0.5}\left(Pr^{\frac{2}{3}} - 1\right)} \quad for \begin{Bmatrix} 0.5 \leq Pr \leq 2000 \\ 10^4 < Re < 5 \times 10^6 \end{Bmatrix} \tag{2.28}$$

$$Nu = \frac{\left(\frac{f}{8}\right)(Re - 1000)\,Pr}{1 + 12.7\left(\frac{f}{8}\right)^{0.5}\left(Pr^{\frac{2}{3}} - 1\right)}. \quad for \begin{Bmatrix} 0.5 \leq Pr \leq 2000 \\ 3 \times 10^3 < Re < 5 \times 10^6 \end{Bmatrix} \tag{2.29}$$

This equation has been used to validate the numerical simulations performed in the current study. However, it must be noted here that the friction parameter f is strongly dependent upon the chosen Re number. For the comparison of the friction factor of the numerical simulations, the empirical correlation proposed by Petukhov (1970) as shown below is used.

$$f = (0.75\,ln\,Re^{-1.64})^{-2}. \quad for\,\{3000 < Re < 5 \times 10^6\} \tag{2.30}$$

2.3. Literature review of PTCs.

2.3.1. Experimental studies

This section discusses only the most important experimental studies showing the experimental set up, main findings, design parameters and operational conditions under different climates such as US, UK, France, India, China, Iran, Algeria, Morocco, Greece, etc.. Dudley et al. (1994) studied experimentally the effect of thermal losses on the solar collector efficiency through the parabolic solar collector of Solar Electric Generating System (SEGS) plants using different coating materials for the collectors and Syltherm 800 oil as HTF. They proposed experimental correlations of the collector thermal efficiency for all types of annular cases and selective coatings under considerations as summarized in Table 2-1. Where (ΔT) is the average fluid temperature above the ambient temperature (°C) and (I) is the solar irradiation (W/m^2).

Table 2-1: Experimental correlations of the collector thermal efficiency proposed by Dudley et al. (1994).

Annular	Coating	Thermal efficiency Correlations
Vacuum	Cermet	$\eta = 73.3 - 0.007276(\Delta T) - 0.496\left(\frac{\Delta T}{I}\right) - 0.0691(\frac{\Delta T^2}{I})$
Air	Cermet	$\eta = 73.4 - 0.00803(\Delta T) - 9.68\left(\frac{\Delta T}{I}\right) - 0.0669(\frac{\Delta T^2}{I})$
Vacuum	Black chrome	$\eta = 73.6 - 0.004206(\Delta T) + 7.44\left(\frac{\Delta T}{I}\right) - 0.0958(\frac{\Delta T^2}{I})$
Air	Black chrome	$\eta = 73.8 - 0.00646(\Delta T) - 12.16\left(\frac{\Delta T}{I}\right) - 0.0641(\frac{\Delta T^2}{I})$

To estimate the maximum efficiency under dynamic conditions, Xu et al. (2012) tested an outdoor rig and compared the results with a simple multiple linear regression solver. The reported maximum efficiency for the outdoor rig was around 42%. To further understand the receiver heat losses in the PTC system, Lei et al. (2013) performed measurements for a new design solar receiver using energy balance for steady and quasi-steady-state equilibrium conditions. Results revealed that the thermal emittance and the receiver temperature, which are very important parameters in the calculation of thermal losses, were both affected by non-uniform heat flux. Moreover, experimental correlations have been proposed of total thermal losses per meter of absorber length for any collector with a glass envelope and restricted to some limitations as clarified in Table 2-2.

Table 2-2: Experimental correlations of the total heat losses proposed by Lei et al. (2013).

Variable	Limitations	Experimental Correlations
$T_{absorber}$	T_{amb}: 10-30(°C), wind: 0-2(m/s) and T_{abs}: 200-410(°C)	$Q_{loss} = 0.1479T_{abs} + 8.1786 \times 10^{-9}T_{abs}^4$
$\Delta T = (T_{glass}-T_{ambient})$	Negligible wind velocity	$Q_{loss} = 5.2057\Delta T + 2.0916 \times 10^{-5}\Delta T^4$

Researchers mentioned in the preceding studies considered the typical type of solar absorber material (i.e., steel) whereas Geete et al. (2016) examined the thermal performance of the fabricated PTC using four arrangements: copper-engine oil (a pipe is made from copper and engine oil is the working fluid), copper-water, mild steel-engine oil and mild steel-water combinations. According to their results, the highest temperature difference was 59°C using mild steel-engine oil arrangement operated at 12:30 PM with a mass flow rate of 0.0024 kg/s.

To study the performance of the solar field as a whole, Kumaresan et al. (2012) and Sivaram et al. (2016) investigated experimentally the performance of a PTC with a storage system during the charge process. They measured the solar irradiation intensity using a pyrheliometer at every 15 minutes and temperatures of HTF (water) at inlet and outlet using thermocouples connected with a data acquisition system. Moreover, they measured errors related to the fundamental data, i.e. mass flow rate, temperature and solar insolation using the root sum square approach in order to determine the collector efficiency. It was pointed out that the instantaneous collector efficiency is highly dependent on two important factors: useful heat gain and incident beam irradiation; the experimental set up Kumaresan et al. (2012) is presented in Figure 2.3.

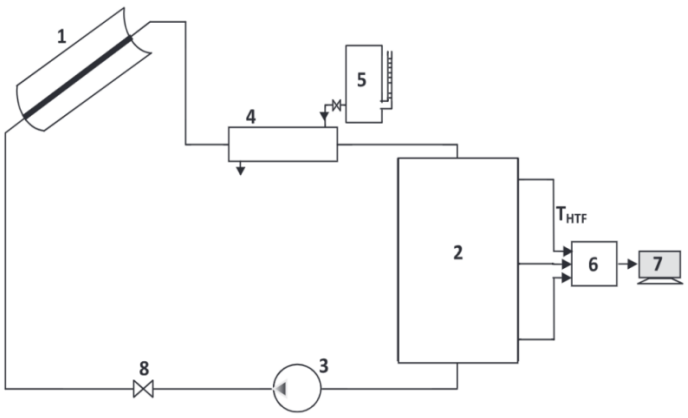

(1) PTC.
(2) Storage tank.
(3) Pump
(4) Heat exchanger
(5) Water tank
(6) Data acquisition unit
(7) Computer
(8) Valve and temperature sensors

Figure 2.3: Experimental set up of Kumaresan et al. (2012).

To gain more understanding about the PTC mechanisms, Kumar and Kumar in (2016) used two different modes: tracking and south facing under the Indian climate with and without a glass envelope. As a consequence, the maximum outlet temperature was observed at the minimum mass flow rate (T= 54.7°C at $\dot{m}$ = 0.001 kg/s of the south facing orientation and T= 45.6°C in the mode of tracking). Furthermore, by increasing the mass flow rate for all the south facing cases (0.024 kg/s), the thermal efficiency was increased to 53.33% with glazing and to 46.17% without glazing. The interesting observation noticed from this research is that there is no significant change in the thermal efficiency by further increasing the mass flow rate beyond 0.024 kg/s. Tajik et al. (2017) investigated experimentally the thermal efficiency of the solar PTC using porous medium instead of classical working fluids. Three different fill cases have been examined; free absorber, partly filled with copper foam and fully filled copper foam, see Figure 2.4 for more details. Results revealed that the overall thermal loss coefficient with fully filled copper foam case has reduced to 45% and thus the thermal efficiency increased accordingly.

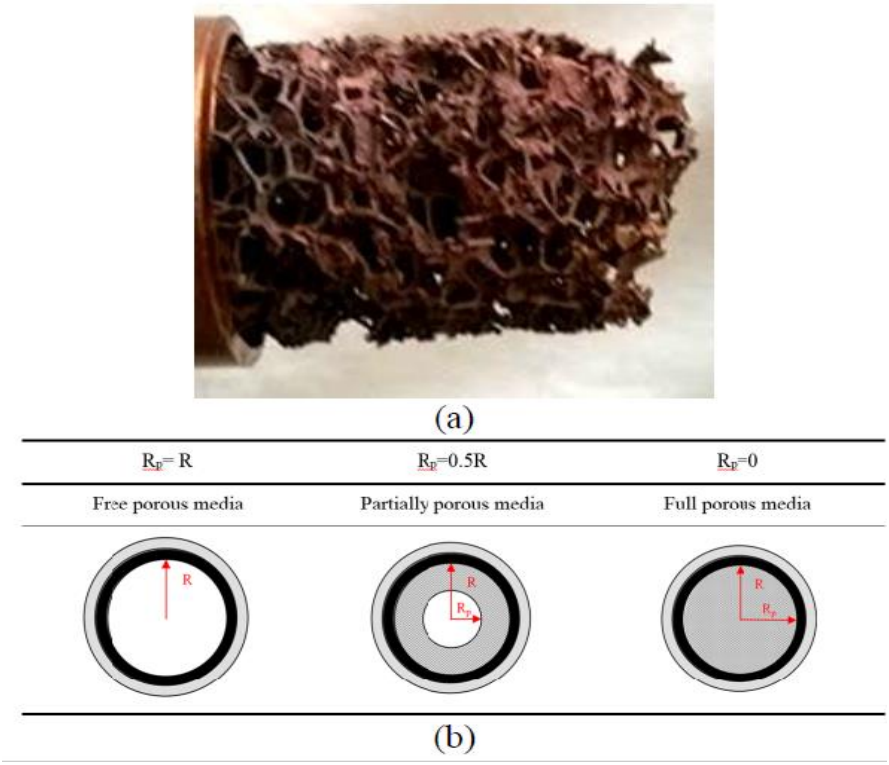

Figure 2.4: (a) copper foam, and (b) configurations of absorber, Tajik et al. (2017).

Agagna et al. (2018) experimentally investigated the optical and thermal performances of a small-scale parabolic trough power plant called (MicroSol-R) with a single storage tank system, the system diagram is presented in Figure 2.5. Three PTCs are installed in this platform in different directions: one of them is oriented in North-South direction whereas others are oriented in East-West directions. The optical efficiency range obtained was between 40% on December (13:00) and 77% on June (8:00 to 16:00).

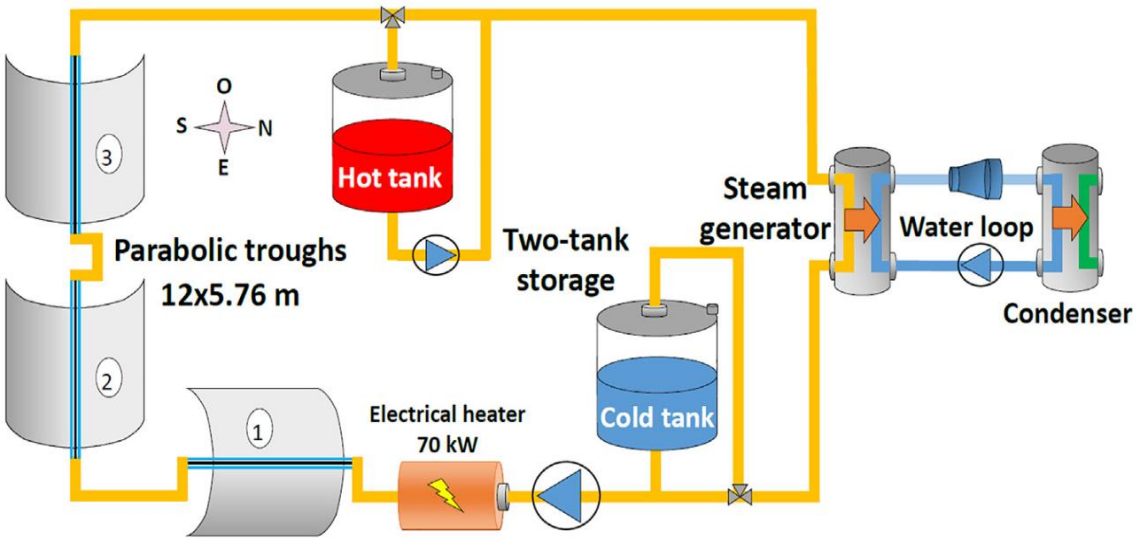

Figure 2.5: Diagram of MicroSol-R PTC power plant, Agagna et al. (2018).

Mouaky et al. (2019) studied the thermal performance of the 186 kWth PTC under a semi-arid climate in Morocco concerning the effect of soiling on the energy production of the system. Results revealed that the proposed design can produce 388 Tons of steam at 500 kPa. Regarding the exergy performance in PTCs, the huge amount of exergy destruction results from the concentration of sun rays on the absorber coatings. One possible solution has been provided recently by Wang et al. (2018) by comparing experimentally the exergy destruction considering the rotatable axis performance and a fixed axis oriented in North-South direction under the Chinese climate. The proposed idea of rotatable axis has reduced the exergy destruction and thus the exergy efficiency of the PTC could be enhanced by 3 % annually. This is because the angle of the PTC can be easily perpendicular to the sun location with rotatable axis compared to the fixed one; the diagrams of both configurations are illustrated in Figure 2.6. However, Bakos (2006) studied experimentally the effect of performing tow-axes tracking system compared with a fixed-axis system oriented in the South direction under the Greece climate. The solar energy collected has enhanced up to 46.46% with the proposed system.

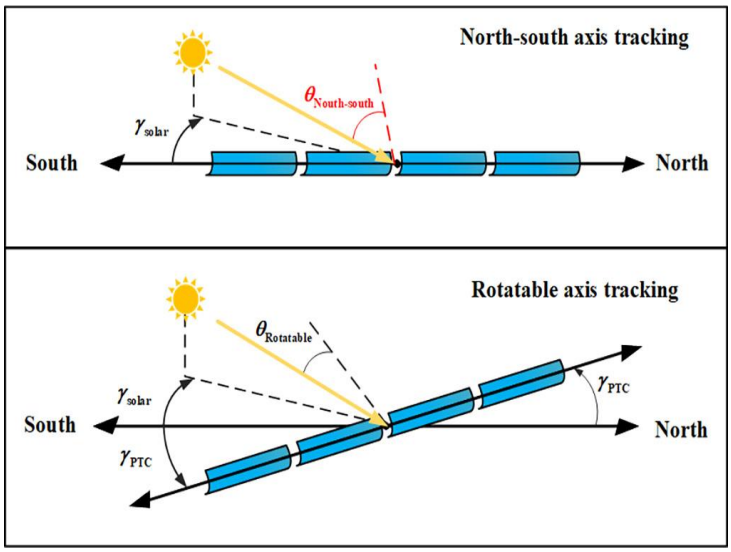

Figure 2.6: Diagrams of fixed axis and rotatable one of the PTC, Wang et al. (2018).

2.3.2. Analytical and Numerical Investigations

The mathematical models in the early time of PTC technologies were simplified and therefore not adequate for predicting the effective thermal performance, for informing design procedure analysis, or for controlling the accuracy of numerical predictions. Therefore, the numerical computation of the collector thermal performance and the assessment of the optical efficiency were really difficult to accurately obtained (Jeter (1979)).

Researchers paid attention after that and significantly improved the mathematical models and combined both optical and thermal features besides all components of the PTC system in order to effectively assess their behaviour (Price et al. (2002)). Advances in the modelling and simulation of engineering applications have led to tremendous growth in modelling capability of PTC systems, where extensive elaborate information can now be achieved computationally. Experimental investigations, on the other hand, are considerably more expensive and time consuming than numerical simulations and not all parameters of interest can be easily measured. In this section, different works are presented showing the main modelling approach and their achievements. Within a PTC system, there still remain a number of issues that needs addressing, one of them being the performance of the solar collector tube receiver. Due to the inherent design of the solar collector tube (one side always exposed to the direct sunlight and the other to reflect light through mirrors), the heat flux around the periphery is never uniform. This non-uniform heating within the pipe leads to local stratification and other heat flux mixing problems, eventually reducing the operational efficiency of the whole plant. Various methodologies currently exist to

mathematically address this problem of non-uniform heat flux distribution around a solar receiver. Jeter (1986) studied this problem with an analytical model where he derived a semi-finite formulation from the first integral of the concentrated flux density differential equations for the types of trough collectors. Thomas and Guven (1994) also studied the effect of the heat flux distribution around the receiver of a PTC system for several optical configurations. It was deduced that the heat flux around the collector receiver is non-uniform in the circumferential direction for the horizontal tubes but symmetrical for the vertical receivers.

2.3.3. Ray-Tracing Method

To really understand the non-uniform heat flux distribution around the absorber tube numerically and how to apply the non-uniform heat flux distribution in CFD solvers, the Ray-tracing technique is very common tool used to analyse and design the optical optimization and performance of the PTC. This technology provides detailed information about the optical features of the PTC with many surface options of imaging equations (Gaussian, Newtonian, etc.). In the literature, several tools use the ray-tracing technology, including SimulTrough, Opticad, SolTrace, TracePro and ASAP; a visualization example found in literature is presented in Figure 2.7. However, for the analysis of the optical characteristics of the PTC system, researchers in the numerical field have used extensively the MCRT model by either writing their own codes or utilizing the previous tools.

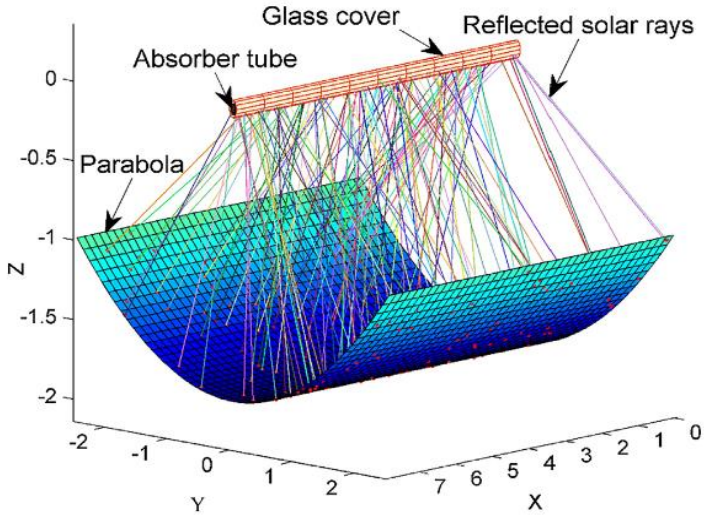

Figure 2.7: Visualization of the PTC under non-uniform solar energy using ray-tracing model, Agagna et al. (2018).

Grena (2009) reported optical simulation of the PTC with and without glass envelope under realistic solar irradiation using a ray-tracing approach in three dimensions. The

optical properties were considered as wavelength-dependent and the light-ray was taken as the basic element of simulations. More aspects have been also modelled realistically such as investigating the effect of tracking error and studying the intensity absorbed by the solar receiver. Yang et al. (2010) performed their own MCRT code considering different parameters: geometrical concentration ratio, rim angle, and tracking errors, whereas the solar rays were assumed to be non-parallel. The obtained result is the local concentration ratio (LCR) profile of an ideal PTC which was compared with the analytical results of Jeter (1986). The resulting curve showed the same trend as Jeter's.

He et al. (2011) produced an optical model based on combining the MCRT model with finite volume method (FVM) to solve the conjugated heat transfer models in the PTC considering the effect of various geometric concentration ratios and different ring angles on the optical performance. Their results have been compared with the analytical results of Jeter (1986), finding less than 2% average errors.

Cheng et al. (2012a) performed a CFD simulation on the receiver tube in three dimensions using the k-ε turbulence model. The MCRT model was combined with CFD solver in order to apply the non-uniform heat flux distribution as shown in Figure 2.8. The authors compared results with the measurements of Dudley et al. (1994) and reported a difference of roughly 2% and good agreement with the profile presented by Jeter (1986).

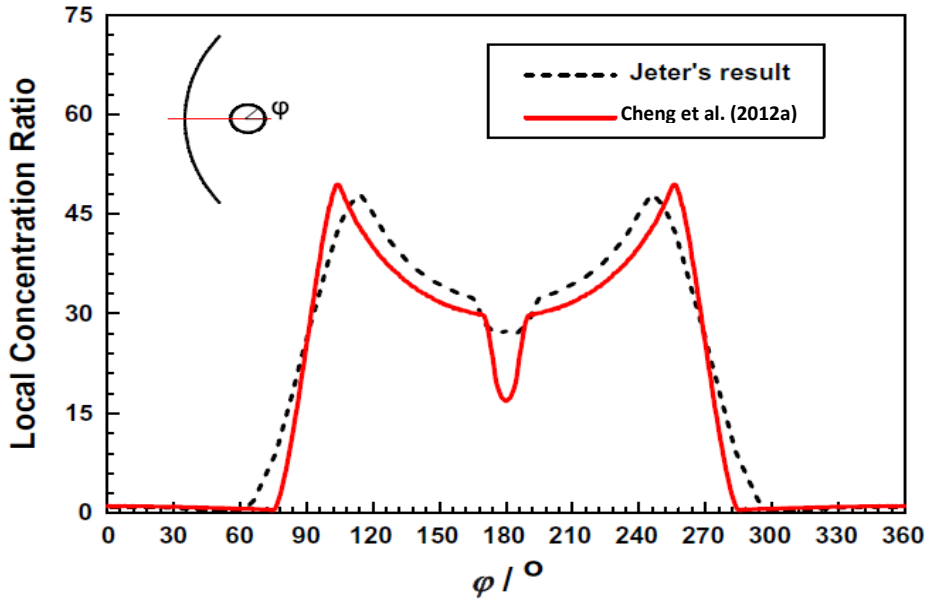

Figure 2.8: The LCR distribution adapted from in Cheng et al. (2012a).

Later, Zhao et al. (2015) developed their own MCRT simulation code to optimize and calculate the heat/density flux distributions on the solar receiver, considering in their simulations rim angles, geometrical concentration ratios, glass envelope transmittance,

receiver absorption, envelope reflectivity, mirror reflectivity and non-parallelism of the sun rays (using cone optics). Their results yielded good agreement with Jeter (1986). Moreover, Kaloudis et al. (2016) represented the approximated local concentration ratio by producing 7-curve fitting equations compared with the MCRT model suggested by Cheng et al. (2012a). The curves generated are 3rd degree polynomial functions in a form of: ($LCR = b_3\emptyset^3 + b_2\emptyset^2 + b_1\emptyset + b_0$), where $\emptyset$ is an absorber angle and b_3, b_2, b_1, b_0 are constants have different values depending on the range of the absorber angle, given in Table 2-3. The obtained LCR profile is presented in Figure 2.9.

Table 2-3: Coefficients of the LCR curves, Kaloudis et al. (2016).

Part	**$\emptyset$ range (Deg.)**	b_3	b_2	b_1	b_0
1	0-75	0.0	-1.071170E-4	-8.100954E-4	1.112046
2	75-104	-2.544403E-3	6.878607E-1	-5.974390E1	1.685403E3
3	104-171.2	-6.602394E-5	3.196692E-2	-5.280388	3.275329E2
4	171.2-188.8	0.0	1.524597E-1	-5.488588E1	4.957224E3
5	188.8-256	5.961826E-5	-3.504845E-2	6.979938	-4.403785E2
6	256-285	2.493475E-3	-2.019052	5.427366E2	-4.840387E4
7	285-360	0.0	-7.511141E-5	2.688045E-2	-9.606886

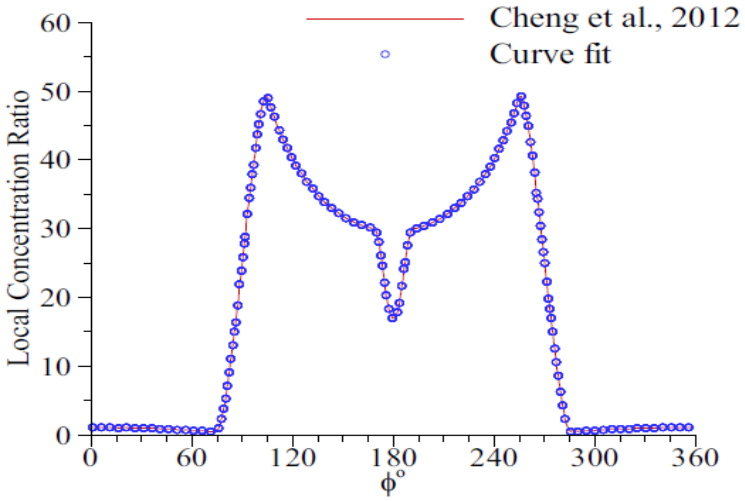

Figure 2.9: The LCR distribution curve-fitting equations presented in Kaloudis et al. (2016).

Agagna et al. (2018) introduced three different models of variable degree of sophistication for PTCs using the MCRT: model 1 is a simple one-dimensional model and simpler, model 2 is a two-dimensional model that can be used to predict the thermal characteristics of the PTC system, while model 3 is the most accurate and can provide detailed information about the realistic non-uniform heat flux distribution on the solar receiver. Hoseinzadeh et

al. (2018) also introduced their own code based on MCRT method to produce optical and thermal models in MATLAB with optimizing three different design parameters: the collector aperture, the solar absorber diameter, and the rim angle.

From the scenario explained previously, the main objective of all researchers is to produce the distribution of the local concentration ratio (LCR) which represents the heat flux distribution around the solar receiver after multiplying it by the direct normal irradiation. Once that is applied properly, there is no need to take the parabolic structure into account.

2.3.4. Design Parametric Investigations of PTCs

Forristall (2003) developed a comprehensive study of heat transfer model using Engineering Equation Solver (EES) by utilizing both one- and two-dimensional heat transfer models. It was concluded that the predicted performance of heat collector was in good agreement with the experimental data of AZTRAK (Dudley et al. (1994)). It was also determined that the best material for the absorber tube was type 321H stainless steel due to its strength and reduction in the bending problem. Furthermore, the coating type (its emittance is 0.07@ 400^{o}C proposed coating) increased the efficiency by 8.5% whereas the vacuum annulus type led to the best performance. Tao and He (2010) studied the heat transfer and fluid flow behaviour inside the solar collector and inside the annular gap as well for different Rayleigh numbers and tube diameter ratios (inner absorber diameter/inner envelope diameter). They found that with increasing the tube diameter ratio, the Nusselt number in the annular gap dropped gradually while increasing in the inner tube diameter. They also highlighted that the natural convection process in the annular gap must be considered when the Rayleigh number is higher than 10^5.

Lu et al. (2013) investigated analytically the effect of both uniform and non-uniform heat transfer distributions on the thermal performance under on-sun and off-sun conditions. They reported that the receiver heat transfer was non-uniform with a larger heat loss and surface temperature under on-sun conditions, while the receiver heat transfer was more or less uniform with only slight differences in surface temperature and heat loss coefficient under off-sun conditions. Another numerical approach proposed by Cheng et al. (2014) was aimed at combining the MCRT model with the FVM in a parametric study on the heat flux density and temperature distribution.

Wu et al. (2014) examined the heat loss from a PTC with annular gap in conjugated heat transfer configuration using the FVM coupled with the MCRT model and the standard k-ε turbulence model. It was concluded that the thermal loss resulted from bellows is about 7% of the total thermal loss. Moreover, it was found that an inverse relation exists between the HTF velocity and the temperature gradient of the absorber metal. However, an alternative numerical approach to represent the non-uniform heat flux was presented by Okafor et al. (2017) using the sine equation expression in terms of concentrated base-level heat flux under laminar flow regime. Different Re numbers, different receiver diameters and different fluid inlet temperatures have been considered to study their effect.

Ray et al. (2018) preformed numerical 3D simulations considering the glass envelope as semi-transparent and modelling the selective coating on the outer surface of the solar absorber with a range of DNI (750-1000 W/m^2) and different mass flow rates of the working fluid (1.7-17.6 kg/s). Results showed that the temperature difference in the circumferential direction decreased by 71.95% with increasing the mass flow rate from (1.7-17.6 kg/s) and the thermal efficiency has been affected slightly with increasing the DNI as well as mass flow rate.

Tripathy et al. (2018) examined the effect of different absorber materials on the thermal and mechanical performances using steel, copper, Bimetallic and Tetra-layered laminate with different flow rates. According to their results, the effect of changing the absorber material on the transferred energy to HTF is quite small and can be neglected. However, it has a considerable influence on the bending owing to the thermal expansion and self-weight. They found that steel causes poor temperature distribution in the circumferential direction due to its lower thermal conductivity, whereas copper behaves better, but has heavier self-weight. Finally, the Tetra-layered laminate provided the best temperature distribution and reduced the maximum deflection by 45-49% as compared to steel.

Xu et al. (2019) introduced a mathematical model to study the unsteady thermal performance of the PTC under different fluid inlet temperatures and DNIs. It was concluded that the working fluid motion has no strong effect on the receiver temperatures. García et al. (2019) studied the temperature distribution on the solar receiver and thermal efficiency of the PTC by developing a reduced-order mathematical model based on the steady-state heat transfer behaviour. After comparing results with previous references, less than 10% relative error was recorded. Khandelwal et al. (2019) studied the PTC thermal performance under different geometrical and operational parameters, various aperture diameters, different mass flow rates, and various working fluids. A considerable drop in

the temperature gradient has been noticed when using liquid sodium compared with other fluids and the temperature profile on the circumferential direction became more uniform. Moreover, the PTC with larger aperture performed better than this with smaller in terms of absorbing more energy and reducing the thermal gradient.

Norouzi et al. (2020) studied numerically the effect of different parameters on the collector's performance including absorber materials, Re numbers, nanofluids and rotational speed of the absorber in 2D and 3D unsteady models. It was concluded the collector's efficiency using Aluminium absorber material is 25% larger than any other materials with rotational speed of 0.25 (rad/s) and volume fraction of 3%. It was also suggested that, because the thermal efficiency could either increase or decrease as the rotational speed is changed due to the fluctuating performance of the thermal efficiency, the rotational speed should be chosen properly.

2.3.5. Thermal losses

The most important issue in PTC systems is how to maximize the gain thermal energy and minimize the overall heat losses which would act to greatly improve the thermal performance of PTCs which in turn leads to gradually enhance the overall collector efficiency. On the other hand, the absorber heat loss has negative effect on decreasing the HTF temperature delivered by the solar field. For this reason, the heat collection element should be effectively designed to minimize heat losses to the free air. The process of covering the receiver tube with a glass envelope acts to reduce the radiative and convective heat losses to the environment. Furthermore, coating the absorber tube with a selective coating (having large absorption rates, more than 0.95) helps also in reduction of radiative heat losses. To seek a further reduction in the thermal losses, the gap between the receiver and glass envelope can be operated under vacuum conditions with very small air pressure (0.013 Pa), which helps to significantly reduce the natural convection heat loss. Another possible approach is designing the absorber tube to be long ($L \geq 4m$) and choosing the absorber diameter to be small relative to the collecting aperture, which leads to minimization of conduction heat losses at the absorber ends (Burkholder and Kutscher (2009)). A summary of various techniques to improve the thermal performance of the PTC system is provided in Table 2-4.

Table 2-4: Some solutions proposed in the previous studies might affect the heat losses.

Reference	Study Type	Used Techniques	Achievements
Odeh et al. (1998)	Numerical	Using water instead of Syltherm 800 oil as HTF	Reduction in thermal losses when using water as working fluid.
Forristall (2003)	Numerical	Testing the effect of different working fluids on the thermal performance.	Selected (Xceltherm 600 and Syltherm 800) as the best candidates which led to noticeable increase in the thermal efficiency and reduction in the heat losses.
Gong et al. (2010)	Experimental	The ends of absorber were covered by heat insulator.	46.18 % reduction in heat losses.
Roesle et al.(2011)	Numerical	Keeping low pressure in the gap between the receiver and the glass jacket using a vacuum pump.	If the operating temperature increases to more than 400°C, the absorber tube would suffer from extreme heat losses.
Lei et al. (2013)	Experimental	Using a new solar receiver with a high vacuum system and a vacuum gauge.	The new design provided better thermal performance since the heat losses drastically reduced.
Yaghoubi et al. (2013)	Experimental & Numerical	Three types of covers used in PTC; vacuum, lost vacuum and broken glass tube.	Heat losses in cases of lost vacuum and broken glass tube were 46% and 58.5% respectively larger than that of vacuum tube leading to a drop of 3-5% and 19% respectively in the overall system performance.
Zhang et al. (2013)	Experimental	A new structure of the solar absorber in U-type shape with a double-glazing vacuum.	Thermal efficiency increased from 79.1% to 79.2% on a calm day and 47.2% to 66.3% on a windy day where the heat losses increased from 0.183 to 0.255 kW.
Wu et al. (2015)	Experimental	Using molten salt to achieve the heat loss of the solar collector as the temperature of HTF changed.	The thermal losses at the joints increase from 5% to 18% with removing the thermal insulation.
Sanchez and Rosengarten (2015)	Numerical	Reducing the absorber diameter	Thermal losses reduced gradually with increasing the pressure drop and accordingly pumping power.
Khandelwal et al. (2019)	Numerical	Using liquid sodium as HTF instead of Molten salt, Therminol oil VP1 and NaK78	Significant reduction in thermal losses from 11 times to three times.
Osorio and Rivera-Alvarez (2019)	Numerical	Using double glass envelops outside the absorber tube	Both optical and thermal efficiencies enhanced especially under partially cloudy climate. More reduction in thermal losses compared with typical PTC.

2.3.6. Effect of changing working fluids on thermal and hydraulic performances

The working fluid is one of the most important elements in determining the thermal performance of PTC systems. Recent estimates until 2016 reported that there are about sixty-three fully operational solar thermal power plants (STPP) with PTC systems around the world. Sixty-one of these plants use thermal oils as the working heat transfer fluid with the maximum working temperature of 398 °C. The main reasons for the use of thermal oils are: low vapour pressure, affordable price, long life, and thermal stability. However, this does not in any way mean that thermal oils are the best candidates for the working fluid as they also have some key drawbacks, including the limitation of temperature (around 400 °C), and environmental toxicity and flammability (Blanco and Miller (2017)). There are currently three alternative heat transfer fluids that have been examined in the literature: liquid-water/steam (referred to direct steam generation), pressurized gases, and molten salts. Each of these working fluids has its own advantages and disadvantages when compared to thermal oils. A brief comparison between different working fluids is presented in Table 2-5. It can be clearly observed from this table that none of the considered fluids is a perfect solution as they all have some constraints or technical issues that need to be resolved.

Table 2-5: Advantages and limitations of alternative HTFs compared to thermal oils, Blanco and Miller (2017).

HTF	T (°C)	Advantages	Drawbacks
Direct Steam Generation	250	1- Simpler plant configuration. 2-The steam temperature is larger. 3-No pollution and no fire hazard.	1-No thermal storage system. 2-The solar field control is more complex. 3-Pressure in the solar field is larger.
Compressed Gases	More than 500	1-The steam temperature is larger. 2-Thermal storage is cheaper. 3-No pollution and no fire hazard.	1-Heat transfer coefficient is smaller. 2-The solar field control is complex. 3-Higher pressure in the solar field. 4-Pumping power required is larger.
Molten salts	230– 600	1-Plant configuration is simpler. 2-The steam temperature is larger. 3-Thermal storage is cheaper. 4-No pollution and no fire hazard.	1-Electricity self-consumption larger 2-Freezing hazard. 3-Design of solar field is complicated.

A further review of the different heat transfer fluids used in the PTC systems is summarized in Table 2-6.

Table 2-6: Summery of the heat transfer fluid studies presented in the available literature.

Reference	Working Fluid	Details of Findings
Odeh et al. (1998)	Syltherm 800 oil and water	Water shows a lower thermal loss coefficient than Syltherm 800 oil
Forristall (2003)	Therminol VP1, Xceltherm 600, Syltherm 800, 60-40 Salt, and Hitec XL Salt	Effect of working fluid smaller than other parameters. The maximum thermal efficiency was observed when using Xceltherm 600 and Syltherm 800, however, these fluids are relatively expensive.
Ouagued and Khellaf (2012)	Syltherm 800, Syltherm XLT, Santotherm 59, Marlotherm X, and Therminol D12.	The Syltherm 800 can be operated at a temperature higher than 700 K, while the working fluids marlotherm X and syltherm XLT can only be operated at temperatures less than 700K; other working fluids tested could be operated between 650 K and 750 K.
Ouagued et al. (2013)	Syltherm 800, Santotherm 59, Marlotherm X, Therminol D12, Syltherm XLT, Santotherm LT, and Marlotherm SH.	The maximum range was recorded for Syltherm 800 (700-800) K, which was deemed as the most appropriate choice from the thermal capacity point of view. The highest cost was with the Santotherm LT which was 129 US $/kW h/day.
Biencinto et al. (2014)	Pressurized nitrogen and synthetic oil	Slight differences observed in the net electrical power between fluids, only (less than 0.91%), while the gross electrical production per year was found to be the same.
Good et al. (2014)	Air	The operating temperature has exceeded 600°C.
Wang et al. (2014a)	Molten salt and Thermal oil	Using molten salt provided higher pressure drop and lower thermal efficiency.
Selvakumar et al. (2014)	Therminol D-12 and hot water	Therminol D-12 performed better and stable for more than 100 cycles of operation.
Wu et al. (2015)	Molten-salt compared with the results of PTR70	The heat losses resulted from the fluid of PTR70 are smaller than those resulted from molten-salt.
Qiu et al. (2017)	Supercritical CO_2 (S-CO_2) under two different cases; Rankine and Brayton cycles	The collector efficiency in two cycles has been achieved in the range of 81.93%-84.7% (Rankine) and 18.78%-84.17% (Brayton).
Tahtah et al. (2017)	Thermal oil and water	A rapid increase was noticed in the temperature evaluation using the thermal oil compared to water. Thus, water was found to be good candidate in terms of heat storage medium.
Bellos et al. (2017a)	Pressurized water, Therminol VP-1, nitrate molten salt, sodium liquid, air, carbon dioxide and helium.	The performance of liquid fluids is generally higher than this of gas fluids.
Aguilar et al. (2019)	Synthetic oil, sub-critical carbon dioxide and super-critical carbon dioxide.	Larger solar irradiation has been absorbed when using super-critical carbon dioxide.

2.3.7. Thermal performance improvement by adding nanoparticles.

One of the most useful techniques used to improve the thermal performance in PTCs is to add metallic or non-metallic nanoparticles to the base working fluid which leads to the creation of a so-called nanofluid. The added nanoparticles having different thermal properties than those of the base working fluid make the working fluid mixture more efficient and effective; in particular, the higher thermal conductivity which leads to enhance the overall thermal performance of the absorber tube through enhancing the convection heat transfer and reducing the thermal losses. Furthermore, the presence of nanoparticles in the base fluid helps also in a notable decrease in effective thermal stresses on the absorber tube. However, a further increase in nanoparticle volume fractions can lead to the agglomeration and clustering of the nanoparticles inside the solar receiver thereby resulting in increasing the requirement of pumping power. For this reason, the nanoparticle volume fraction has to be optimized for an efficient heat transfer augmentation and reasonable friction factor and accordingly pressure drop. The nanoparticles utilized currently in the PTC applications can be metallic (like Al, Ag, Au, Cu, Fe etc.), non-metallic (such as Al_2O_3, CuO, Fe_2O_3, SiO_2, TiO_2, NiO, ZnO etc.) or carbon nanotubes such as (CNT, SWCNT and MWCNT).

2.3.8. Proposed correlations of Thermo-physical properties

From a numerical modelling perspective, a nanofluid can be simulated using either as a single-phase or a two-phase model. Both of these approaches have been used in literature with the two-phase model approach being the more accurate one. However, the selection of the thermo-physical properties is critical, when it comes to ensuring acceptable predictions via modelling nanofluids. For this reason, various models and correlations from the literature are presented below.

2.3.8.1. *Density of nanofluid, ρ_{nf}, (kg/m3)*

The mixture of base fluid and nanoparticles is considered to be a heterogeneous mixture which can be composed of different parts and can easily be distinguished either by the naked eyes or by a microscope see Figure 2.10.

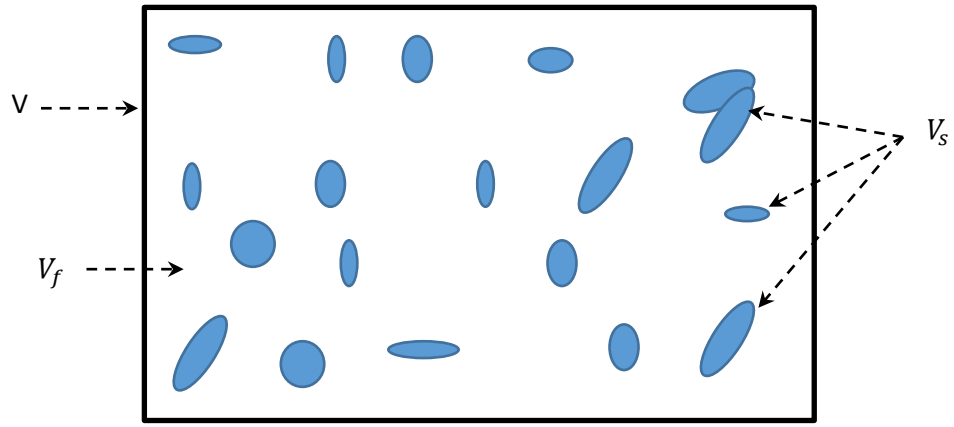

Figure 2.10: Heterogeneous mixture of fluid and nanoparticles.

The total mass of both solid and fluid materials can be introduced in the heterogeneous mixture in terms of densities as expressed below (Pak and Cho (1998)):

$$\rho_{nf} = \frac{m}{V} = \rho_s \varphi + \rho_f (1 - \varphi). \tag{2.31}$$

2.3.8.2. *Specific heat capacity of nanofluid, $C_{p,nf}$, (J/kg.K)*

This property can be derived based on the energy balance for incompressible substances which is expressed in the following way (Xuan and Wilfried (2000)), which is used very commonly in the literature:

$$C_{p,nf} = \frac{1}{\rho_{nf}} \left[\rho_s C_{p,c} \varphi + C_{p,f} \rho_f (1 - \varphi)\right]. \tag{2.32}$$

Another correlation was proposed by Pak and Cho (1998) based on the volume fraction of two substances is given by the following formulation:

$$C_{p,nf} = C_{p,s} \varphi + C_{p,f} (1 - \varphi). \tag{2.33}$$

It should be noted that the correlation proposed by Xuan and Wilfried (2000) (equation 2.31) is widely applicable and more accurate than the one given by Pak and Cho (1998) (equation 2.32) as the latter correlation is based on a universally representing property, i.e. the nanofluid density. Further evidence is provided by O'Hanley et al. (2012), which compare the results from both the correlations with the experimental data of different nanofluids. O'Hanley et al. (2012), reported that the results predicted by the Xuan and Wilfried (2000) correlation were much closer to the experimental data than those predicted through the Pak and Cho (1998) correlation for all nanofluids.

2.3.8.3. *Dynamic viscosity of nanofluid, μ_{nf}, (kg/m.s)*

The dynamic viscosity of solid-fluid suspension was first proposed analytically by Einstein (1906) and Einstein (1911) based on the molecular model which considered the solid particles as non-interacting spheres as follows:

$$\mu_{nf} = \mu_f(1 + 2.5\varphi). \tag{2.34}$$

This model is only applicable to nanofluids with low volume fraction ≤ 2%. After that, Brinkman (1952) developed the previous analytical model by adding the effect of the velocity modification resulted from the presence of sphere particles and giving the following formulation for uniform mixture:

$$\mu_{nf} = \mu_f \frac{1}{(1-\varphi)^{2.5}}. \tag{2.35}$$

This model is assumed to be applicable for high concentration ratio, φ ≤ 4%. However, this model has been extended further by Batchelor (1977) to take the Brownian motion effect into account in addition to the hydrodynamic interactions of the sphere particles with a volume fraction less than 10%:

$$\mu_{nf} = \mu_f(1 + 2.5\varphi + 6.2\varphi^2). \tag{2.36}$$

For a typical volume fraction, the last three models would produce almost identical results. For example, at 1% (0.01) volume fraction, the effective viscosity (μ_{nf}/μ_f) of the last three models are 1.025, 1.0254 and 1.0256 respectively. Another analytical attempt was performed by Happel (1957) considering the tangential stress resulted from the presence of solid particles under creeping flow conditions:

$$\mu_{nf} = \mu_f(1 + 5.5\varphi). \tag{2.37}$$

However, this expression produces very high nanofluid viscosity compared to the preceding models. On the other hand, experimental studies have also contributed different expressions of dynamic viscosity of nanofluid, one being performed by Buongiorno (2006) where the author used the experimental data of Pak and Cho (1998) and correlated the dynamic viscosity for both γ-Al_2O_3-water and TiO_2-water and presented in the following expressions respectively:

$$\mu_{nf} = \mu_f(1 + 39.11\varphi + 534\varphi^2). \tag{2.38}$$

$$\mu_{nf} = \mu_f(1 + 5.45\varphi + 108\varphi^2). \tag{2.39}$$

Khanafer and Vafai (2011) considered the same experimental data of Pak and Cho (1998) and derived the following formulations of the dynamic viscosity for both nanofluids (γ-Al_2O_3-water and TiO_2-water) respectively:

$$\mu_{nf} = \mu_f(1 + 23.1\varphi + 1525\varphi^2). \quad (2.40)$$

$$\mu_{nf} = \mu_f(1 + 3.54\varphi + 169\varphi^2). \quad (2.41)$$

Although all four previous viscosity models are based on the same experimental data, the factors in the corresponding expressions are apparently different. However, the resulted viscosity values for the same nanofluid are comparable. Another experimental study was performed by Wang et al. (1999) where they measured the viscosity of Al_2O_3-water which was higher than that measured by the Pak and Cho (1998) by 2.5 times. That could be due to the effect of particle size and shape or might be due to the effect of non-Newtonian flow behaviour which has a vital role in nanofluid measurements. However, Maiga et al. (2005) used the same data of Wang et al. (1999) and derived the following expression:

$$\mu_{nf} = \mu_f(1 + 7.3\varphi + 123\varphi^2). \quad (2.42)$$

It is noticeable that factors of this model are considerably smaller than those of Pak and Cho (1998) but clearly larger than those of analytical correlation proposed by Batchelor (1977). This model is very common and widely used in the available literature and it can be recommended for more accurate results. Chen et al. (2007) measured experimentally the effective viscosity of another nanofluid (TiO_2-ethyl glycol) and derived the following correlation:

$$\mu_{nf} = \mu_f(1 + 10.6\varphi + 112\varphi^2). \quad (2.43)$$

This correlation is valid for a volume fraction up to about 10%. It is noticeable from the correlations presented previously that the viscosity equation is currently modelled with a polynomial expression of degree two. However, some authors, including Mooney (1951) followed by Tseng and Chen (2003) and Tseng and Lin (2003), proposed a viscosity equation in the exponential form as below:

$$\mu_{nf} = A\mu_f exp^{(B\varphi)}. \quad (2.44)$$

Where A and B are empirically determined factors which are considerably different in all studies.

On the other hand, Nguyen et al. (2007) derived and supplied two correlations in two different functions (exponential and polynomial) for the same nanofluid (Al_2O_3-water) in the following expressions respectively:

$$\mu_{nf} = \mu_f(1 + 2.5\varphi + 150\varphi^2). \quad (2.45)$$

$$\mu_{nf} = 0.904\,\mu_f exp^{(14.8\varphi)}. \quad (2.46)$$

It is worth noting that the coefficient value of the second term of the polynomial model of Nguyen et al. (2007) is equal to the results of analytical expressions for spherical particles (2.35). Moreover, this model proposes non-Newtonian behaviour of the resulted nanofluids. Whereas the exponential correlation proposed by Tseng and Lin (2003) was given by:

$$\mu_{nf} = 13.47\,\mu_f exp^{(35.98\varphi)}. \quad (2.47)$$

To conclude, the exponential expression for the nanofluid viscosity is not recommended due to higher values predicted as compared with the polynomial expressions. Moreover, a small error in volume fraction calculation would lead to significant error in the viscosity value when using the exponential function. Therefore, it is currently recommended to utilize the polynomial function with degree two based on the temperature-dependent base fluid viscosity (Michaelides (2016)).

2.3.8.4. *Thermal conductivity of nanofluid, k_{nf} , (W/m.K.)*

The first model for calculating the electrical conductivity of a heterogeneous solid-fluid mixture of spherical particles was proposed by Maxwell (1881) in the following expression:

$$k_{nf} = k_f \left[1 + \frac{3(k_s - k_f)\varphi}{(k_s + 2k_f) - (k_s - k_f)\varphi}\right]. \quad (2.48)$$

This model is only applicable for a volume fraction less than 1%. The same analytical investigation had been proposed by Bruggeman (1935) to derive an expression of thermal conductivity of nanofluid with different regular shapes. The resulted correlation is given by:

$$k_{nf} = k_f \left[1 + \frac{n(k_s - k_f)\varphi}{k_s + (n-1)k_f - (k_s - k_f)\varphi}\right]. \quad (2.49)$$

The coefficient (n) represents the particle shape. It is 3 when the particle is sphere and 6 for cylinders. For irregular shape, Hamilton and Crosser (1962) proposed a generic model to include different shapes of irregular particles and derived the following correlation:

$$k_{nf} = k_f \left[1 + \frac{3\left(k_s - k_f\right)\varphi/\Psi}{k_s + k_f\left(\frac{3}{\Psi} - 1\right) - (k_s - k_f)\varphi}\right]. \quad (2.50)$$

The parameter (Ψ) represents the shape factor. For a sphere particle shape, ($\Psi = 1$) and the above expression will be reduced to the Maxwell's expression whereas ($\Psi = 5$) for cylindrical particle shapes. However, Bruggeman (1935) proposed another model based on homogenous spherical solid-fluid mixture with no limitations to the volume fraction. This model supplies prediction slightly better than those discussed previously and can be presented in the following correlation:

$$k_{nf} = k_s(3\varphi - 1) + [3(1 - \varphi) - 1]k_f + \sqrt{\Delta}, \quad (2.51)$$

where:

$$\Delta = (3\varphi - 1)^2 {k_s}^2 + [3(1 - \varphi) - 1]^2 {k_f}^2 + 2[2 + 9\varphi(1 - \varphi)]k_s k_f.$$

Another model was derived by Nan et al. (2003) based on very long aspect ratios of particle sizes and assumption of ($k_s \gg k_f$) which is appropriate for very high thermal conductivity particles such as CNT, SWCNT etc. This model is represented by the following expression:

$$k_{nf} = k_f \left[1 + \frac{k_s \varphi}{3k_f}\right]. \quad (2.52)$$

This expression cannot be applied for general nanofluids since it is only derived for high-thermal conductivity nanoparticles.

Khanafer and Vafai (2011) developed a model from experimental data of Al_2O_3 and CuO particles mixed with water base fluid. The derived expression is a statistical expression of thermal conductivity of nanofluid at ambient conditions which is given by:

$$k_{nf} = k_f \left[1 + 1.0112\varphi + 2.4375\varphi \frac{23.5}{\alpha} + 0.0248 \frac{k_s \varphi}{k_f}\right]. \quad (2.53)$$

The parameter α in the above equation represents the particle radius (in nm). This formula introduces adversely relation between the thermal conductivity of nanoparticles and base fluids and also there is no explanation about how to define the particle size for non-spherical particles. Others models are presented in more details in Michaelides (2016). The previous discussion clarifies that the thermal conductivity of nanofluids depends strongly on different parameters: both conductivities of fluid and solid particles, mixture temperature, a volume fraction value and size dimensions of particles.

2.3.9. History of investigations using nanofluids in PTCs.

There are a few experimental studies which used nanoparticles in PTCs analysis, and the majority of them used water as the base working fluid. Chaudhari et al. (2015), Subramani

et al. (2018a) and Bretado et al. (2018) used Al_2O_3 with water in a PTC system. According to their results, the maximum thermal efficiency was enhanced up to 24%. While Coccia et al. (2016) examined (Fe_2O_3, SiO_2, TiO_2, ZnO, Al_2O_3 and Au) immersed in water for different volume fractions. As per their findings, there was no marked enhancement in the thermal efficiency compared to the base fluid.

The usage of Al_2O_3 and Fe_2O_3 nanoparticles in water with different concentrations (0.20%, 0.25% and 0.30%) was studied by Rehan et al. (2018). The authors reported an increase in the thermal efficiency by 13% with Al_2O_3 and 11% with Fe_2O_3 mixed with water. Moreover, Subramani et al. (2018b) tested the usage of TiO_2/water nanofluid in the PTC using different volume fractions (0.05%, 0.10%, and 0.20%). The authors reported an 8.66% increase in the thermal efficiency for the highest concentration (0.20%).

Natividade et al. (2019) studied a promising new type of nanoparticles called multilayer graphene (MLG) suspended in water as a base fluid, with different flow rates and two-volume fractions (0.00045% and 0.00068%). It was noticed that a significant improvement in thermal efficiency was obtained with increasing the volume fraction where it was 31% with volume fraction of 0.00045% whereas it reached up to 76% with the largest volume fraction compared to the base fluid.

On the other hand, the experimental investigation using Ethylene glycol (EG) as a base fluid was conducted by Kasaeian et al. (2017) using MWCNT and nanosilica nanoparticles with volume fractions of 0.1%, 0.2% and 0.3%. The preparation of nanofluids was done by dispersing the nanoparticles inside the based fluid using a magnetic stirrer for 5 h at 900 rpm in order to avoid the effect of particle agglomeration. The authors found that the thermal efficiency at 0.3% concentration was 17% higher than that obtained by the base working fluid. The summarized review of previous investigations illustrating the use of nanofluids in PTCs of numerical studies and main findings are listed in Table 2-7.

Table 2-7: Effects of nanoparticles (NP) used in literatures and their outcomes.

Reference	Limitations	NP type	Base fluid	VF (φ) (%)	Achievements
Sokhansefat et al. (2014)	Single-phase model and three inlet temperatures.	Al_2O_3	Synthetic oil	1, 3, 5	Considerable increase in heat transfer coefficient with increasing nanoparticle volume fraction.
Paul et al. (2015)	One inlet temperature, laminar and turbulent flow.	Al_2O_3	Ionic Liquids	0.18, 0.36, 0.9	0.9% of φ enhanced the thermal conductivity by about 11% and heat capacity by 49%.
Zadeh et al. (2015)	Using single-phase and two-phase models.	Al_2O_3	Synthetic oil	0, 1, 2, 3, 4, 5	11.5% and 36% increase in the heat transfer coefficient using 5% of φ for models 1 and 2 respectively.
Mwesigye et al. (2015a)	Single-phase model, different Re numbers and different inlet temperatures.	Al_2O_3	Synthetic oil	0-4, 0-6, 0–8	The heat transfer performance increased by 35%, 54% & 76% with increasing φ respectively. The maximum efficiency enhancement was 7.6% recorded at the smallest temperature and minimum Re number.
Mwesigye et al. (2015b)	Single-phase model, different Re numbers and different inlet temperatures.	CuO	Syltherm800	1-6	38% improvement in the heat transfer performance and 15% increase in the thermal efficiency.
Basbous et al. (2015)	Single-phase model and different inlet temperatures.	Al_2O_3	Syltherm800	1, 3, 5	18% enhancement in convective heat transfer coefficient and 10% reduction in thermal loss at the largest volume fraction.
Abu-Hamdeh and Almitani (2016)	Single-phase model.	Al_2O_3, Fe_3O_4, ZnO	Water	1-4	5.5-9.01%, 6.2-12.3% and 7.2-14.4% improvements in convection heat transfer coefficient with ZnO-water, Fe_3O_4-water and Al_2O_3-water respectively.
Basbous et al. (2016)	Single-phase model, different Re numbers and different inlet temperatures.	Cu, CuO, Ag, Al_2O_3	Syltherm800	5	36% enhancement in convective heat transfer coefficient and 21% reduction in overall thermal loss coefficient using Ag-Syltherm 800 nanofluid.
Bellos et al. (2016)	Single-phase model and different inlet temperatures.	Al_2O_3	Thermal oil	2	4.25% improvement in the thermal efficiency.

Table 2-7: Effects of nanoparticles (NP) used in literatures and their outcomes (continued).

Reference	Limitations	NP type	Base fluid	VF (φ) (%)	Achievements
Kaloudis et al. (2016)	Single- and two-phase models, the receiver was subjected under constant wall temperature.	Al_2O_3	Syltherm800	0 - 4	10% enhancement obtained in the collector efficiency at φ of 4%. Better results obtained by the two-phase model.
Toghyani et al. (2016)	Single-phase model, different flow rates, different DNI and different inlet temperatures.	CuO, SiO_2, TiO_2, Al_2O_3	Therminol-55	2-5.5	The increase in overall exergy efficiency was 3%, 6%, 9% and 11% when using CuO, TiO_2, SiO_2 and Al_2O_3 respectively.
Ghasemi and Ranjbar (2016)	Single-phase model, uniform heat flux and different Re numbers.	CuO, Al_2O_3	Water	0.5, 1.5, 3	The heat transfer coefficient increased up to 35% for CuO and 28% for Al_2O_3 at volume fraction of 3%. However, the friction factor of $Al_2O_3$was smaller than that of CuO.
Ferraro et al. (2016)	Single-phase model, different flow rates, different DNI and different inlet temperatures.	Al_2O_3	Synthetic oil	5	A slight improvement in thermal efficiency and higher pumping power.
Wang et al. (2016)	Single-phase model, different DNIs, different inlet velocities and inlet temperatures.	Al_2O_3	Synthetic oil	0, 0.01, 0.03, 0.05	The absorber deformation decreases moderately from 2.11 mm to 0.54 mm by increasing the φ from 0% to 0.05%.
Mwesigye et al. (2016a)	Single-phase model, different flow rates and different inlet temperatures.	Cu	TherminolVP-1	0, 1, 2, 4, 6	Heat transfer enhanced by 8%, 18% and 32% at φ of 2%, 4% and 6% respectively. Moreover, the system thermal efficiency increased by 12.5% as the φ increased from 0 to 6% and the entropy generation rate decreased from 20-30%.
Khakrah et al. (2017)	Single-phase model, different flow rates, wind velocities and different orientations	Al_2O_3	Synthetic oil	1, 3, 5	The thermal efficiency when using φ of 5% enhanced by 12.4% and 14.3% for rotated and horizontal reflector's orientations respectively.
Alashkar and Gadalla (2017)	Single-phase model, different flow rates, different DNI and different inlet temperatures.	Al_2O_3, Cu, SWCNT	Syltherm800	1-5	The candidate 5% Cu led to increase the annual energy from 163 to 167GW.
Abid et al. (2017)	Single-phase model, different flow rates, different DNI, various ambient temperatures and different inlet temperatures.	Al_2O_3, Fe_2O_3	Water	Wt.: 2-2.5	0.65% enhancement in thermal efficiency using Al_2O_3-water and 0.59% when using Fe_2O_3-water.
Mwesigye and Meyer (2017)	Single-phase model, different flow rates, and different inlet temperatures.	Al_2O_3, Ag, Cu	TherminolVP-1	0, 1, 2, 4, 6	The maximum enhancement in the thermal efficiency was 13.9% recorded by silver-Therminol while Al_2O_3-Therminol provided the smallest enhancement 7.2% at the maximum solar concentration ratio of 113.

Table 2-7: Effects of nanoparticles (NP) used in literatures and their outcomes (continued).

Reference	Limitations	NP type	Base fluid	VF(φ) (%)	Achievements
Bellos and Tzivanidis (2017)	Single-phase model, different flow rates and different inlet temperatures.	Al_2O_3, CuO	Syltherm800	4	The thermal efficiency increased by 1.26% using CuO-Syltherm800 and 1.13% using Al_2O_3-Syltherm800.
Kasaeian et al. (2017)	Using glass-glass absorber tube.	MWCNT, nanosilica	Ethylene glycol (EG)	0.1, 0.2, 0.3	Compared to the base fluid, the thermal efficiency increased by 30.4% with an increase of 15.7K in the outlet temperature using MWCNT/EG. For nanosilica/EG the efficiency increase was 14% with an increase of 7.7 K at the outlet temperature.
Paul et al. (2017)	Measuring the thermal properties at different temperatures.	Al_2O_3	Ionic Liquids	0.5, 1.0, 2.5	Using 2.5% of nanoparticles led to an enhancement of thermal conductivity by about 11% for [C4mim][NTf2], while the heat capacity enhancement reached up to 62% for [C4mpyrr][NTf2].
Allouhi et al. (2018)	Single-phase model, different DNIs and different wind velocities.	Al_2O_3, CuO, TiO_2	Syltherm800	3, 5	The thermal energy enhances by 1.46, 1.25, and 1.40 using Al_2O_3, CuO, and TiO_2 respectively. The maximum exergy efficiency was about 9.05% by using 3% of CuO.
Kasaiean et al. (2018)	Different DNIs, different Incident angles and different inlet temperatures.	MWCNT, CuO	Ethylene glycol (EG)	0.3, 6	15% increase in convection heat transfer coefficient using 6% MWCNT-EG.
Alashkar and Gadalla (2018)	With/without storage system.	Cu, Ag	TherminolVP-1 Syltherm800	1-5	The better performance was obtained when using 4% Ag-TherminolVP-1 nanofluid.
Bellos et al. (2018a)	Single model, different inlet temperatures and single flow rate.	CuO	Syltherm800, Molten salt	6	40% Nu number improvement using CuO- Syltherm800 and up to 13% when using CuO-Molten salt.
Mwesigye et al. (2018)	Single-phase model, different flow rates and different inlet temperatures.	SWCNT	TherminolVP-1	0.25, 0.5, 1, 2, 2.5	234% enhancement in the heat transfer performance and 4.4 increase in thermal efficiency at 2.5% volume fraction.
Khakrah et al. (2018)	Single-phase model, different inlet temperatures and different wind speeds.	Al_2O_3	Synthetic oil	0-5	19% increase in the relative exergy efficiency at 5% φ.

Table 2-7: Effects of nanoparticles (NP) used in literatures and their outcomes (continued).

Reference	Limitations	NP type	Base fluid type	VF (φ) (%)	Achievements
Ebrahimi-Moghadam et al. (2018)	Different inlet temperatures, Re numbers and particle diameters.	Al_2O_3	Ethylene glycol (EG)	0.01-0.1	Using nanofluids caused a reduction in the thermal entropy generation and rising the pressuredrop.
Razmmand et al. (2019)	Two-phase model.	Ag, Al, Au, Ni, TiO_2	Water	0.1, 0.3, 0.5, 1, 2	Heat flux at the critical length when using Al-H_2O and Au-H_2O was increased by 2.3 and 2.7 times respectively compared with base fluid.
Korres et al. (2019)	Single-phase model and different inlet temperatures in laminar flow.	CuO	Syltherm800	5	2.76% enhancement in the thermal efficiency and 2.6% improvement in the exergy efficiency.
Peng et al. (2019)	Experimental and two-phase model numerical studies using different Re numbers.	Cu, CNT	Gallium (Ga)	2, 5, 8, 10	Forced heat transfer coefficient enhanced by 34.5% and 45.2% when using Cu-Ga and CNT-Ga respectively.
Abed et al. (2019)	Single-phase model, different Re numbers, and uniform heat flux distribution.	TiO_2, Cu Al_2O_3,CuO	Water	2, 4, 6	Using 6% volume fraction led to enhance the performance evaluation criteria (PEC) by 1.214, 1.2, 1.18, and 1.155 when using TiO_2, Al_2O_3, CuO, and Cu, respectively.
Bozorg et al. (2020)	Single-phase model and porous in annular space, different Re number and different inlet temperatures.	Al_2O_3	Synthetic oil	1.5, 3	By using 3% nanofluid and porous in annular, the heat transfer coefficient increased by 7% and 20%, whereas the thermal efficiency has raised by 5% and 14%, while the pressure drop increased by 42.5% and 42% respectively.

2.3.10. The Effect of Inserting Swirl Generators on the Thermal Performance

The use of swirl generators inside the receiver tube is a passive technique can be used to enhance the convection heat transfer rate. These devices could be shaped as twisted tapes, fins, coils, wires and spiral grooved tubes etc. The flow across such devices has important features, such as an intense mixing between flow in the near-wall region and main-stream, a reduction in the thickness of the thermal boundary layer, and an increment in the tangential velocity component. Such techniques improve the thermal efficiency of PTC, reduce the thermal losses of the absorber tube and improve the overall system reliability subsequently.

A wide range of insert types have been studied in the past. Kasperski and Nemś (2013) investigated the effect of multiple-fin arrays inside the solar receiver on the thermo-hydraulic efficiency of the PTC compared with the smooth receiver. Up to 14% efficiency enhancement resulted in the case of half-pipe finned arrangement. Song et al. (2014) studied numerically the effect of helical screw-tape with a core rod inside the receiver of the PTC on the thermal performance. Results proved that the usage of the helical screw-tape decreased the surface temperature and heat losses by a small amount (less than those predicted by the tubular tube by six times at 0.11 kg/s and inlet temperature of 373K). On the other hand, the pressure drop increased with increasing the mass flow rate by four times in the typical receiver while the pressure drops increase by 23 times in the case of using the helical screw tape insert.

Mwesigye et al. (2016b) studied numerically a new type of insert called a twisted type with wall-detached inside the solar receiver. Results revealed that the temperature gradient of the absorber tube in the circumferential direction was reduced by 68% and the thermal efficiency was increased by 5-10% at a twist ratio of greater than 1 due to the presence of twisted tapes. Furthermore, the largest reduction in the entropy generation was about 58.8%. Chang et al. (2018) investigated numerically a new type of inserts in which they used concentric and eccentric rod turbulator in different positions with molten salt as a base fluid. The normalized Nusselt number resulted from the simulations increased from 1.1 to 7.42 times with respect to the typical solar receiver. Bellos and Tzivanidis (2018) used a star-design as a turbulator inside the solar receiver with different dimensions of star configurations. According to results obtained based on the optimum star configuration, up to 60 % enhancement in the heat transfer coefficient and 14 % reduction in thermal losses whereas up to 900 % increase in the pressure drop.

Liu et al. (2019a) studied numerically inclined conical strip inserts in the PTC system considering the effect of the geometrical parameters additional to different flow conditions. Results clarified that using this type of inserts led to an increase in the Nusselt number by 45-203 % with a large reduction in both thermal losses and entropy generation reached to 82.1% and 74.2 % respectively. Moreover, the overall enhancement in thermal efficiency and exergetic efficiency increased by 0.02-5.04% and 5.7% respectively.

A large number of papers in the literature presented different types of inserts, some of them are shown in Figure 2.11. Besides, many types of swirl generators are individually investigated in previous studies taking into account the effect of geometrical arrangements of inserts, various rotating positions of inserts, different flow conditions, various ambient conditions and a wide range of solar irradiations. Table 2-9 summarizes these works and main achievements where the abbreviations that are used in Table 2-9 are listed in Table 2-8.

Table 2-8: The abbreviations used in Table 2-9.

W.R.	Width ratio	C.W.	Coiled wire	Q/d	Fin distance / inner receiver diameter
Th. Pe.	Thermal performance	Lpm	Litter per minute	λ	tip-to-base ratio of fin
T.R.	Twisted ratio	ΔP	Pressure drop	H.T.E	Heat transfer enhancement
Exe. Per	exergetic performance	H.L.	Heat losses	H.T.C	Heat transfer coefficient
F.F.	Friction factor	T_{in}	Inlet temperature	Th.E.F	Thermal efficiency factor
T.T	Twisted tape	F.th.	Fin thickness	H	Height of metal foam in tube
H.T	Heat transfer	F.L.	Fin length	F_0	Friction factor of the smooth tube
I.T.	Insert type	E.G.	Entropy generation	d/D	Ring diameter/inner receiver diameter
Pr.	Prantle number	A.R.	Aspect ratio	C.R.	Clearance ratio
I.A.	Incidence angle	Th. L.	Thermal losses	Th.E. I.	Thermal enhancement index
V	velocity	Th.E.	Thermal efficiency	δ	Distance between two fins

Table 2-9: The effect of insert types relative to the tubular tube in recent investigations.

Reference	Examined parameters	Typical output	Augmentations obtained by inserting swirl generators compared with the typical receiver							
			Increase	Technique 1	Increase	Technique 2	Increase	Technique 3	Increase	Technique 4
Reddy and Satyanarayana (2008)	Re: (3-25.1)10^4 λ: 0-0.75 0.8-6.8 kg/s	H.T.C. & ΔP (pa)	490-2200 Up to 1850	Trapezoidal fins	500-2300 Up to 2400	Circular fins	490-2200 Up to 1600	Triangular fins	-	-
Reddy et al. (2008)	Re: (3-25.1)10^4 A.R.: 0-2.2 Pr: 8.11	Nu: 229-1286	Nu: 302-1412	Porous fins	Nu: 263-1357	Solid fins	-	-	-	-
Kumar and Reddy (2009)	Re: 31845–254765 Pr: 8.11, I.A.: 30°-60°	Nu number	Nu : 64.3%	Top porous discs	-	-	-	-	-	-
Sundar and Sharma (2010)	Re: (10-22)10^3 TR: 0-83	H.T. & F.F	H.T. (%) 22.76-30.30	0.5% Al_2O_3	H.T. & F.F 33.51-42.17% 1.01-1.26	T.T. of 5 T.R.	-	-	-	-
Cheng et al. (2012b)	Re: (3.8-38) 10^4 DNI: 100-1000 W/m^2	Nu & F.F. & Th. L. (%) & (PEC)	160 & 276.4 & 13.39 % & 1.18	Milt-longitudinal vortexes	-	-	-	-	-	-
Kasperski and Nemś (2013)	(0.002-0.1) m^3/s	Heat gain (W): 58.5	135.5, 148	Long. Fins, Diff. height fins	179.6, 236.5, 255.5	Ring shape, wood-grain, wavy fins	423	Fully finned	434	Half-pipe finned
Wang et al. (2013)	H: 0-1 (m) V: 0-27 (m/s)	Nu (times) & F.F. (times) & (PEC)	10-12, 400-700, 1.1-1.5	Metal foam (H=0.75 top)	5–10, 10-20, 1.4-3.2	Metal foam (H=0.25 bottom)	-	-	-	-
Soo and Benito (2013)	HTF: Air, Helium, CO_2), IT: helical coil, TT, dimple, porous foam.	Th.E (%), power (W), ΔP. (kPa)	80.4%, 16.5, 5.26	Dimple & helium	-	-	-	-	-	-
Ghadirijafarbeigloo et al. (2014)	Re: (5-30)x10^3 TR: 2.67-5.33	Nu (%) F.F. (%)	Nu: 37%	T.T.	Nu & F.F. 150% & 210%	Louvered T.T.	-	-	-	-

..Table 2-9: The effect of insert types relative to the tubular tube in recent investigations (continued).

Reference	Examined parameters	Typical output	Augmentations obtained by inserting swirl generators compared with the typical receiver							
			Increase	Technique 1	Increase	Technique 2	Increase	Technique 3	Increase	Technique 4
Waghole et al. (2014)	Re: 500-6000 TR: 0.577-1.732	H.T. (times) F.F.(times) Th. E. (%)	1.25-2.1, 1-1.75, 135- 205%	T.T. and 0.1% of silver.	-	-	-	-	-	-
Xiao et al. (2014)	Re: 117.6- 480.3.	H.L. (W)	26.6	V-cavity receiver	16.3	V-cavity with fins	-	-	-	-
Jafar and Sivaraman (2014)	Re: 710-2130	Nu (%)	16 %	T.T.& 0.3% of Al_2O_3	20 %	Nail.T.T.& 0.3% of Al_2O_3	-	-	-	-
Mwesigye et al. (2014)	Re: 10200-738000 T_{in}: 400-650 K	Nu & F.F & Th.E.F. & E.G	133.5, 1.05, 95, -52.7	Perforated plate	-	-	-	-	-	-
Huang et al. (2015)	Re: 10^4 - $2x10^4$	PEC	1.23-1.37	Dimples	1.125-1.225	Helical fins	1.13-1.41	Protrusions	-	-
Reddy et al. (2015)	(100-1000)L/h	Th. E.(%): 57.21- 66.96	58.98-67.59%	Bottom insert	59.41-67.78%	U-shaped	60.5-67.43%	Inclined insert	61.18-69.03%	Alternative insert
Chang et al. (2015)	T.R.: 2.5-41.7 C.R.: 0 – 1 Re: 7485-30553	Nu(times) & F.F. (times)	2.9 & 1.24	T.T.	-	-	-	-	-	-
Şahin et al. (2015)	Re: (3-17)x 10^3	H.T.E (times)	1.95	C.W. Pitch = 45 mm	2.07	Pitch = 30mm	2.28	Pitch = 15mm	-	-
Jaramillo et al. (2016)	T.R.: 1-5 (1 – 6) Lpm	Th. E. (%) & F.F.(times)	Up to 9% & 26	T.T.	-	-	-	-	-	-
Mwesigye et al. (2016b)	Re: $10x10^3$-$14x10^5$ T.R.: 0.5-2.0 W.R.: 0.53-0.91	H.T.E., F.F. Th. E. (%)& E.G.	1.05-2.69, 1.6 -14.5, 5-10% & -58.8%	T.T with wall-detached	-	-	-	-	-	-

Table 2-9: The effect of insert types relative to the tubular tube in recent investigations (continued).

Reference	Examined parameters	Typical output	Augmentations obtained by inserting swirl generators compared with the typical receiver							
			Increase	Technique 1	Increase	Technique 2	Increase	Technique3	Increase	Technique 4
Xiangtao et al. (2017)	N: 1,3,5,9 Re: (2-11.25)10^3 δ/L: 0.1-0.025	Nu (%) & Th. Pe. (%)	9 % & 12%	Arrays of pin fins	-	-	-	-	-	-
Amina et al. (2016)	Re: (25.7-257) 10^3	Nu (times) & F.F. (times)	1.3-1.8 & 1.66	Triangular fins	1.3-1.8 & 1.57	Rectangular fins	Nu: 150%	Fins & 0.01 of nanofluid	-	-
Ghasemi and Ranjbar (2017)	Re:(3-25.1)10^4	Nu: 229-1286	374.63-1766	Porous rings	-	-	-	-	-	-
Zhu et al. (2017)	Re: (7.2-21.6)10^4	Nu (%), F.F (%), H.L (%), E.G.(%)	(261-310), (382-405), -(17.5-33.1), -(30.2-81.8)	Wavy-tape	-	-	-	-	-	-
Zheng et al. (2017)	Re: 10^3 -10x10^3	H.T.C. (%) & E.G. (%)	25.53% & -29.1%	Dimpled T.T.	58.96% in H.T.C.& 5.05% in F.F	Dimpled T.T. & Al_2O_3	-	-	-	-
Bellos et al. (2017b)	50-250 Lpm F.th. : 2,4,6 mm F.L.: 5-20 mm	Th.E. I. & Nu (times)	1.483 & 2.65	Fins	-	-	-	-	-	-
Bellos et al. (2017c)	Fin L: 0-15 mm	Exe. Per. (%) & Th. E. (%)	42.7% & 70.82%	Longitudinal fins with helium	40.76% & 70.54%	Longitudinal fins with air	41.97% & 69.93%	Longitudinal fins with Co2	-	-
Bellos et al. (2018b)	Re: (1-14)10^4 T_{in}: 300-650K	Th.E (%) 68.24	68.62%	6% CuO-Oil	68.8%	Thermal oil -Finned tube	69.02%	Nanofluid-Finned tube	-	-
Bellos et al. (2018c)	Different fin positions	Th.E.(%): 68.24	68.40%, 68.50%	One fin, two fins	68.59%, 68.63%	Three fins, four fins	68.71%, 68.74%	Five fins, six fins	68.78%, 68.80%	Seven fins, eight fins

Table 2-9: The effect of insert types relative to the tubular tube in recent investigations (continued).

Reference	Examined parameters	Typical output	Augmentations obtained by inserting swirl generators compared with the typical receiver							
			Increase	Technique 1	Increase	Technique 2	Increase	Technique3	Increase	Technique 4
Okonkwo et al. (2018b)	(40-200) Lpm, T_{in}: 350-650K	Exergy enhancement 16.39(%)	16.41%	Al_2O_3-Oil	16.42%	Al_2O_3-Oil in Finned tube	16.41%	Al_2O_3-Oil + T.T.	16.51%	Al_2O_3-Oil in Con.Div. Tube
Bellos et al. (2018d)	Different cylindrical insert positions	Th.E.(%): 67.7	0.119%	One cylindrical rod	+0.387%	Two cylindrical rods	+0.589%	Three cylindrical rods	+0.656%	Four cylindrical rods
Bilal et al (2018)	T_{in}: 29-38℃ (2.5-20) LPM DNI: 600-950W/m^2	Nu (%)	(56-75)%	C.R. (0.6%) of Fe_3O_4	(59-73)%	T.T.	(63-87)%	T.T. and C.R. (0.6%) of Fe_3O_4	-	-
Kurşun (2019)	Re: 2x10^4-8x10^4 T_{in}: 300-600K	Nu (%)	25%	Flat fins	75%	Sinusoidal fins	-	-	-	-
Malekan et al. (2019)	Re: 3x10^4-25x10^4 Particle size:10, 20	Th.E.F (%)	1.35%	CuO-Oil	4%	CuO-Oil+Fins	-	-	-	-
Suresh et al. (2020)	Re: (7-12) x10^3	Nu (%)	(5-40)%	T.T.	(11-101)%	Rings attached T.T.	(7-77)%	Modified rings attached T.T.	-	-
Liu et al. (2019b)	Different ribs insert positions	Nu (%)	(1.41-2.98)%	Ribs in (SADIR)	(1.58-3.21)%	Ribs in (SCSIR)	-	-	-	-
Valizade et al. (2020)	(20-100) Lph Re: 500-1800	Th.E. (%)	28.84%	Free-porous	49.42%	Semi-porous	60.23%	Full-porous	-	-

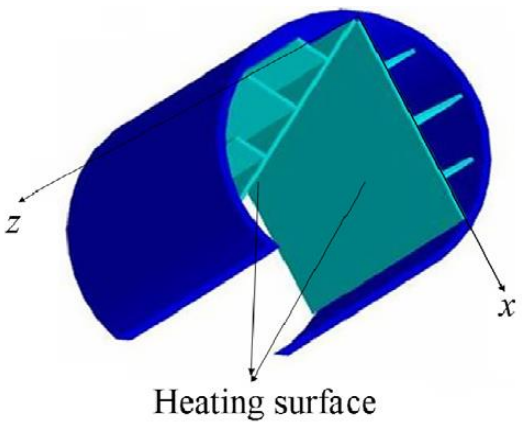

V-cavity receiver of Xiao et al. (2014).

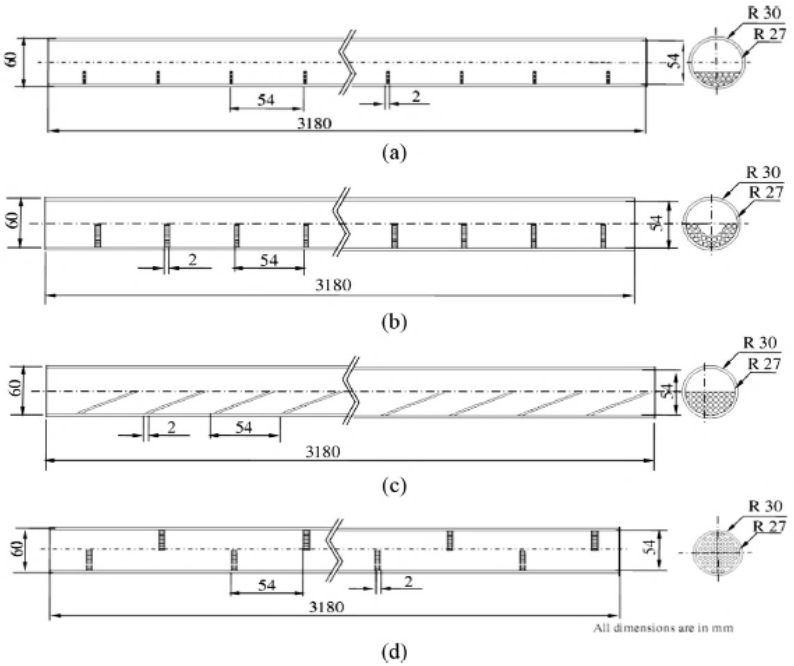

Porous disc, Reddy et al. (2015).

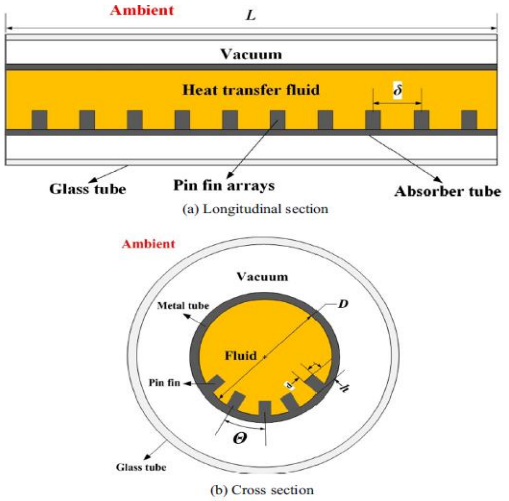

Pin fin arrays, Xiangtao et al. (2017).

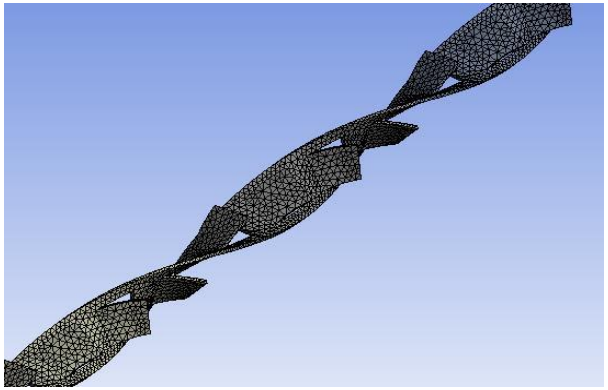

Louvered twisted tape, Ghadirijafarbeigloo et al. (2014)

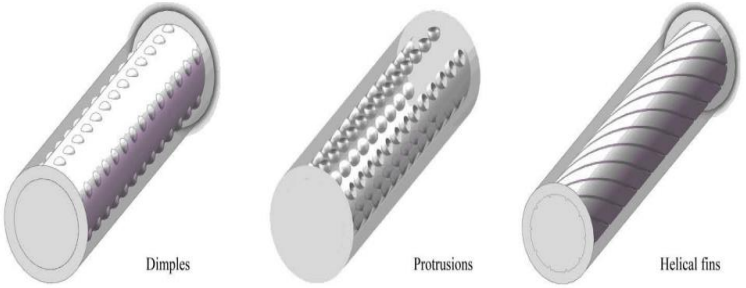

Huang et al. (2015)

Nail twisted tape, Jafar and Sivaraman (2014).

Figure 2.11: Parabolic trough receiver with different inserting types.

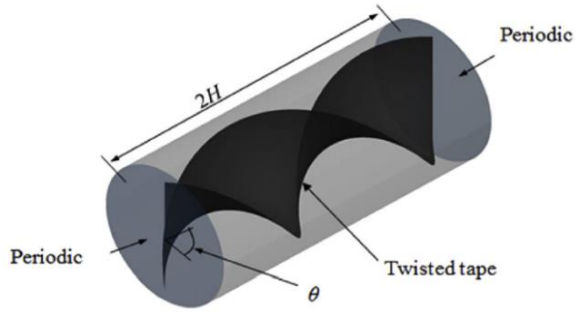

Twisted type, Mwesigye et al. (2016b).

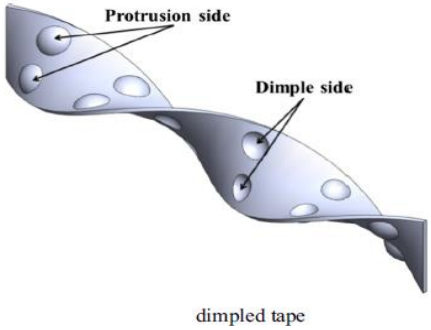

Zheng et al. (2017)

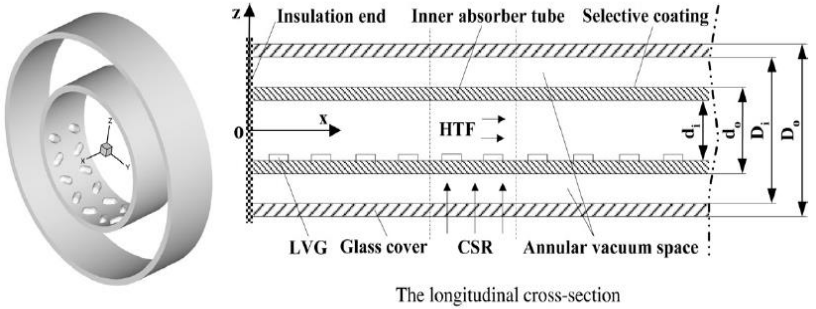

Unilateral longitudinal vortex generators, Cheng et al. (2012b).

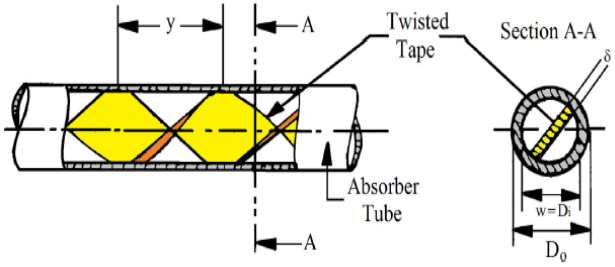

Twisted tape, Jaramillo et al. (2016).

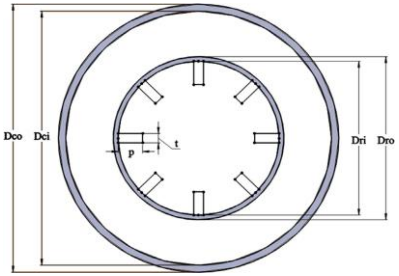

Fins, Bellos et al. (2017b).

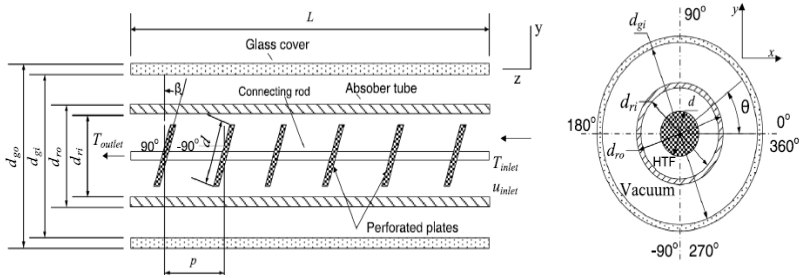

Perforated plate inserts, Mwesigye et al. (2014)

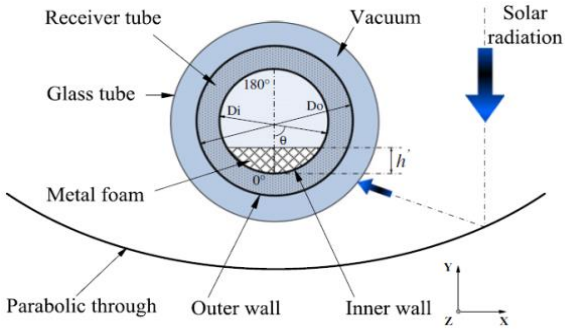

Metal foams, Wang et al. (2013).

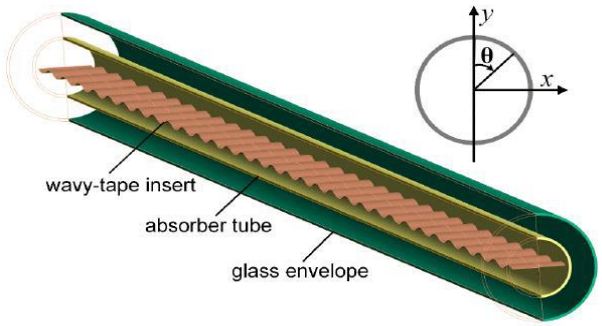

Wavy-tape inserts, Zhu et al. (2017).

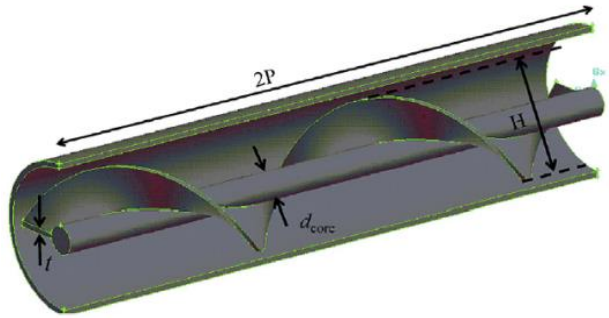

Helical screw-tape with core rod, Song et al. (2014).

Figure 2.11: Parabolic trough receiver with different inserting types (continued).

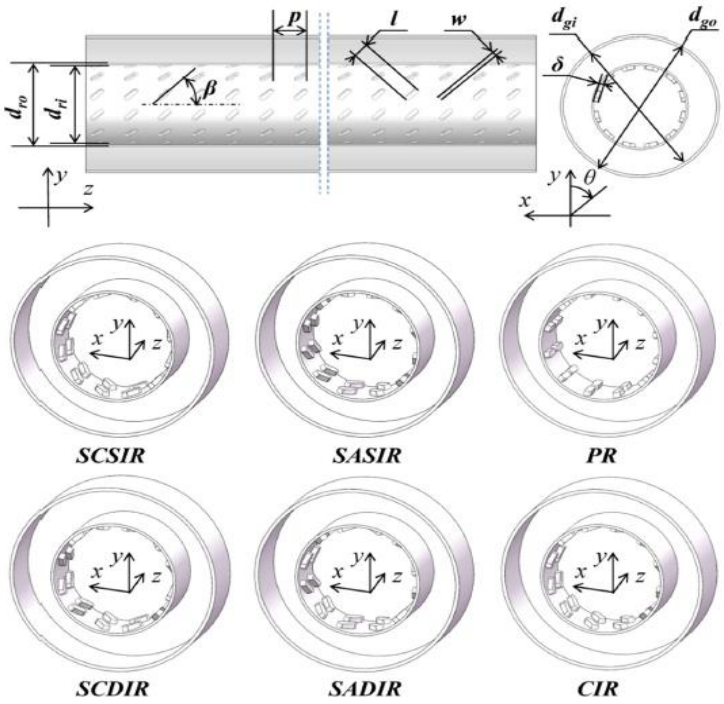

Rib arrangements, Liu et al. (2019b).

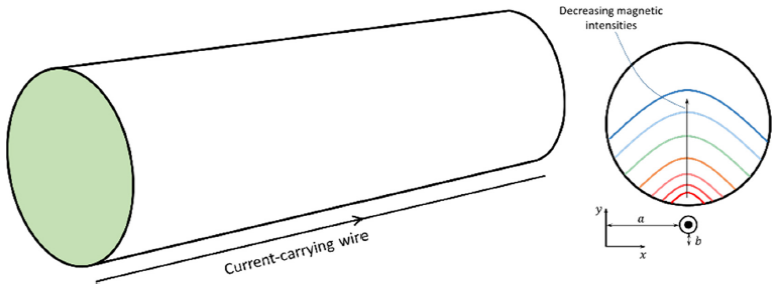

Electrical wire and magnetic field, Malekan et al. (2019).

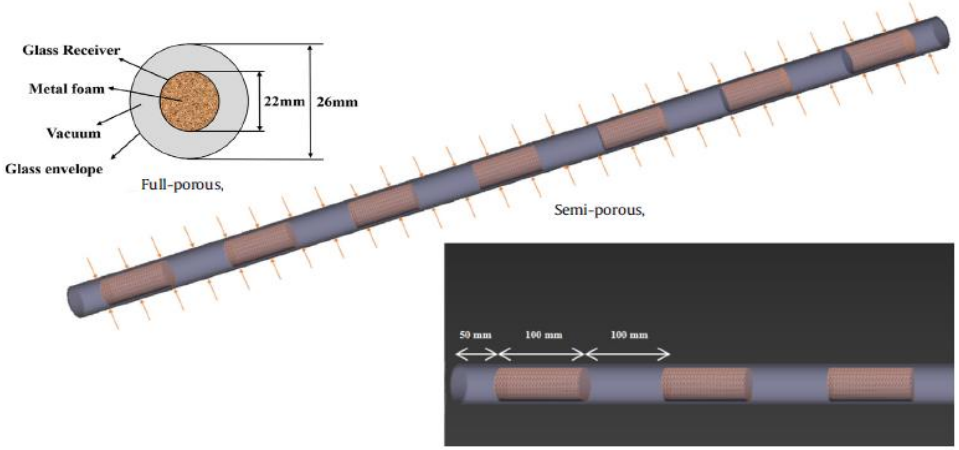

Copper metal foam, Valizade et al. (2020).

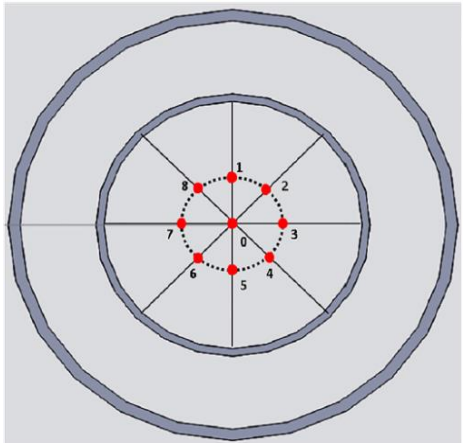

Cylindrical rods, Bellos et al. (2018d).

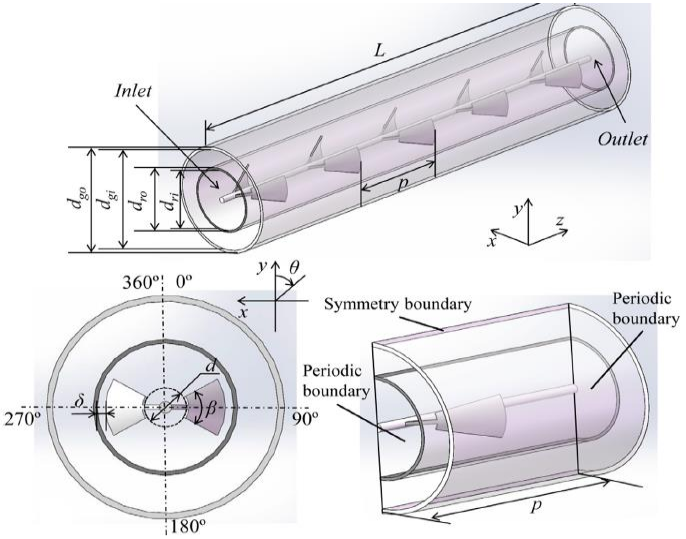

Conical strip inserts, Liu et al. (2019a).

Figure 2.11: Parabolic trough receiver with different inserting types (continued).

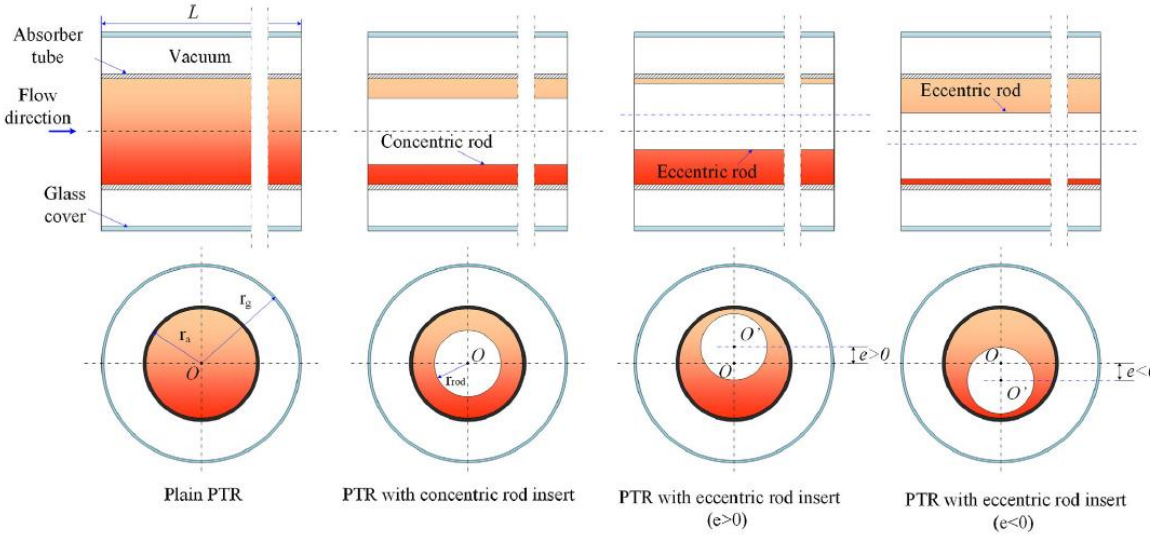

Concentric and eccentric rods, Chang et al. (2018).

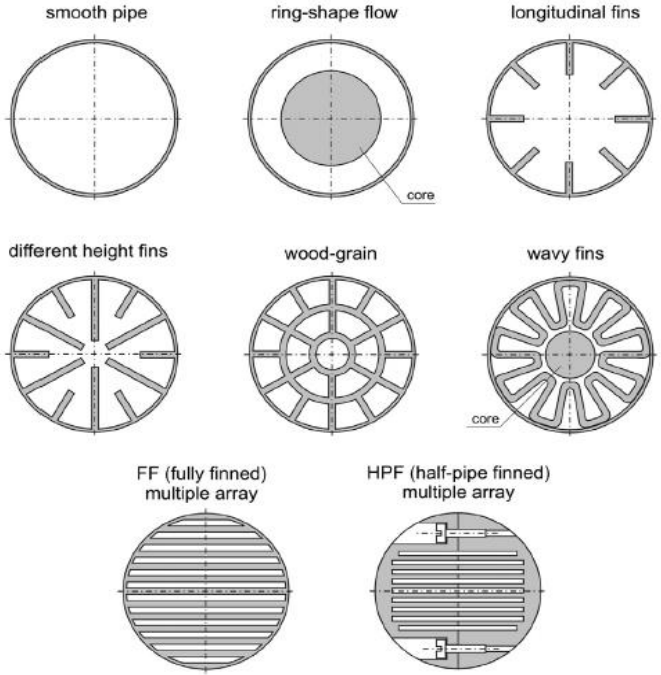

Multiple-fin arrays, Kasperski and Nemś (2013).

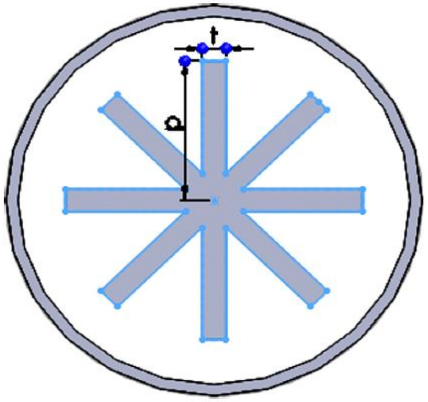

Flow star insert, Bellos and Tzivanidis (2018).

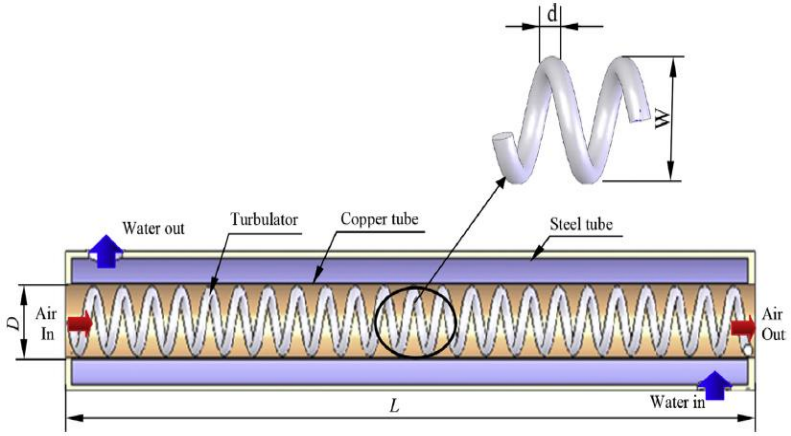

Coiled wire turbulators, Şahin et al. (2015)

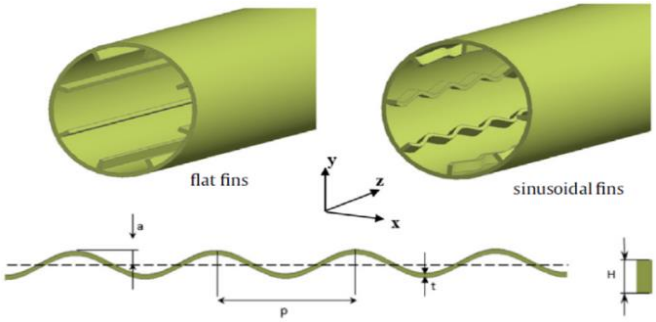

Flat fins and sinusoidal fins, Kurşun (2019).

Figure 2.11: Parabolic trough receiver with different inserting types (continued).

2.4. Conclusions

PTC systems play a key role in solar thermal energy. Numerous technologies and different techniques have been investigated to improve the overall performance of the PTC optically, thermally and hydraulically, using experiments, simulations, or analytical approaches. As previously discussed, PTC systems performance-enhancement approaches can be basically categorized into two main families: technologies used to improve the thermal performance, and technologies used to enhance the optical characteristics. The investigations focused on enhancing the thermal performance are currently more numerous than those addressing the optical performance; probably due to the fact that the tools needed to investigate the thermal characteristics are more extensively available.

In this chapter, research investigations performed experimentally and numerically to improve the thermal and the optical performances of PTC systems have been reviewed. It is clear that experimental studies are less numerous in a comparison with numerical investigations, because of the cost associated with experiments, particularly when carried out at representative scale.

Based on the available literature, it can be concluded that the utilisation of nanofluids for improving thermal properties is promising but still an emerging field. The knowledge gap in the literature is still considerable in terms of testing different types of nanoparticles with different volume fractions and different base fluids for conjugated heat transfer problems. Even though a lot of data is available in literature related to the improvement of thermal performance using swirl generators (or other flow-modifying devices) and nanoparticles, there is yet a rather large void when it comes to the use of both nanoparticles and swirl generators together. Studies related to the testing of the combined effect of these are much needed and should be the focus of further research. Thus, in this research, the gap of knowledge is addressed according to several steps; examining three different base fluids with different operating conditions, then examining six different nanoparticles with these base fluids. Then, examining the effect of different shapes of swirl generators and finally, testing the effect of combining both technologies of nanofluids and swirl generators.

Chapter 3: Computational Fluid Dynamics (CFD)

3.1. Introduction

In the current work, open-source CFD software named the Open Field Operation and Manipulation (OpenFOAM) has been used. This software is written in C++ language with a choice of different solvers depending on the case problem and corresponding physics. This software was selected for the current research as it is highly versatile and fully open source. Thus, it allows modifications to all its solvers, thermo-physical properties, schemes, boundary conditions and discretization methods. Furthermore, it is highly parallelizable and free to use. Among the solvers available in the OpenFOAM library, a solver named conjugated heat transfer multi region simple foam (chtMultiRegionSimpleFoam) was used for all cases in the present research. This solver can be used for simulating the flow characteristics and heat transfer in conjugated solid-fluid problem cases with no limitations for solid or fluid regions.

3.2. Turbulence modelling

Fluid flows can be divided into three main types based on the flow properties: laminar flows, transitional flows, and turbulent flows. More often than not, fluid flows of relevance in industrial and engineering applications are turbulent. For example, the flow around flight vehicles is turbulent, the majority of combustion processes involves high turbulent motion, the natural gas and oil flow inside pipes are turbulent, the wake flow of ships and submarines are turbulent, the flow of water current below the ocean surfaces is turbulent, the smoke flow from a chimney is turbulent, the gulf stream flow is believed to be a turbulent wall-jet flow, etc. It is clearly obvious that turbulence is an interdisciplinary phenomenon that covers a wide range of applications in fluid dynamics, whereas laminar flows are of more restricted and/or academic interest. Transport phenomena are enhanced by turbulence, and this explains the relevance of turbulent flows in practical applications; Tennekes and Lumley (1994), Mathieu and Scott (2000) and Pope (2019).

3.2.1. Turbulence characteristics

Turbulence is a feature that does not belong to the fluid rather its flow. Turbulent flows have neither a precise definition in the fluid dynamics nor any general theory due to challenges of the turbulence nature, Schiestel (2010). Thus, several following observable features can characterize the turbulent flow and distinguish it from the laminar flow.

- The flow variables in turbulent flow conditions vary in random, chaotic and irregular way in both time and space. The turbulent flow structure consists of various eddy scales in which the largest eddies have size on the order of the flow geometry whereas the smallest eddies are dissipated into internal energy and are therefore controlled by viscosity, Schiestel (2010).

- The flow diffusivity in turbulent flows increases gradually with increasing the turbulent level. Increasing the flow diffusivity acts also at increasing the wall friction (resistance) in internal flows such as pipes and channels, Davidson (2018).

- The turbulent kinetic energy in the small-scale eddies is dissipated into internal energy. This means that the turbulent flow is characterized as dissipative during a cascade process since the smallest eddies receive the kinetic energy from larger eddies, and the larger eddies receive the kinetic energy from even larger eddies and so on until the largest eddies extract the kinetic energy from the mean flow, Tennekes and Lumley (1994).

- The transition from laminar to turbulent flow depends on the value of the Re number. For instance, the transition to turbulent flows in external boundary layers occurs when the Re number exceeds about 100,000, whereas a Re number greater than about 2300 marks the transition to turbulent flow in circular pipes, Davidson (2018).

- Turbulence is distinguished as continuum phenomenon as it is always three dimensional and unsteady. Such flows are characterized by large fluctuating contributions.

The flow regime can be characterized based on a non-dimensional number called the Reynold's number which can be described as a ratio of inertial force to viscous force expressed as:

$$Re = \frac{U\,\ell}{\nu}. \tag{3.1}$$

The variable U is an average velocity scale (m/s), ℓ is a length scale (m) which is taken as a pipe diameter and ν is a kinematic viscosity of fluid (m^2/s). In a case of circular pipe flows, Re number is demonstrated as laminar flow when $Re \leq 2300$, while the flow became turbulent when the $Re \geq 4000$ and in between, the flow is transition.

3.2.2. Governing equations of fluid flow and heat transfer

Fluid flows are governed by a set of equations that enforce the conservation of mass, momentum, energy and species. The mass (continuity) conservation equation is derived from the mass balance applied on the infinitesimal control volume. The continuity equation can be written for incompressible flow (with constant density) as follows:

$$\frac{\partial U_i}{\partial x_i} = 0 \tag{3.2}$$

The variable U_i represents a flow instantaneous velocity of the ith vector component. The momentum conservation equation is derived by applying the second law of Newton to an infinitesimal control volume. The momentum equation for incompressible flow is formulated as:

$$\frac{\partial U_i}{\partial t} + U_j \frac{\partial U_i}{\partial x_j} = -\frac{1}{\rho}\frac{\partial P}{\partial x_i} + \frac{\partial}{\partial x_j}\left(\frac{\mu}{\rho}(2S_{ij})\right) + F. \tag{3.3}$$

The parameter F represents the body force, ρ is the fluid's density and the S_{ij} represents the strain tensor rate which is defined as:

$$S_{ij} = \frac{1}{2}\left(\frac{\partial U_i}{\partial x_j} + \frac{\partial U_j}{\partial x_i}\right). \tag{3.4}$$

The energy transport equation for incompressible flow is derived from the first law of thermodynamics applied on the control volume as follows:

$$\frac{\partial T}{\partial t} + U_i \frac{\partial T}{\partial x_i} = \frac{\partial}{\partial x_j}\left(\frac{k}{\rho c}\frac{\partial T}{\partial \mathrm{x}_j}\right) + \frac{S}{\rho c}. \tag{3.5}$$

The parameter S represents the volumetric heat source. Other variables c, k, ρ and μ represent the thermal properties of fluid (specific heat capacity, thermal conductivity, density and viscosity respectively). The above continuity and momentum equations formulate a set of partial differential equations called the Navier-Stokes equations.

For turbulent flows, numerical solution techniques are used to solve for the flow quantities. There are three main approaches to solve for such turbulent flows; direct numerical simulation (DNS), in which the Navier-Stokes equations are solved directly without any modelling, large eddy simulation (LES) in which the Navier-Stokes equations are solved only for the large-scale eddies with small scale motion being modelled, the third approach is to model all scales of motion, Reynolds-Averaged Navier-Stokes (RANS).

In the DNS, a proper simulation requires a highly refined mesh resolving all scales of motion that is ensuring that the mesh spacing is smaller than the smallest flow length scale as well as corresponding time step. This ensures that all flow eddies starting from the largest eddies down to the smallest Kolmogorov scales are solved and all detailed information of turbulence eddies are produced. The corresponding computational cost is significantly huge and it is usable only for relatively low Re number flows and simple flow geometries, Hanjalic and Launder (2011).

For simulating moderate to larger Re number flows, RANS and/or LES are more appropriate, where some/all flow variables are modelled, respectively. The LES numerical technique is an intermediate approach in which the small turbulence eddies are modelled using a sub-grid-scale model whereas the large turbulence scales are resolved.

In this technique, since most of the energy spectrum is resolved, the mathematical model requirement is not that complex compared to RANS modelling. On the other hand, all turbulent scales are modelled in the RANS approach. The main advantage of the RANS technique is the lower computational time/resources compared to DNS and LES. However, this comes at the cost of reduced accuracy especially if the flow is statistically unsteady. The RANS approach is used in the current study.

3.2.3. Reynolds-Averaged Navier-Stokes (RANS) equations

In turbulent flow, the variables in the continuity and momentum equations are all instantaneous quantities. However, Reynolds (1895) proposed the ensemble averaging concept in which the instantaneous quantities for the flow are decomposed into mean and fluctuating parts as shown below:

$$U_i = \overline{U}_i + u_i. \tag{3.6}$$

$$P = \bar{P} + p. \tag{3.7}$$

The same approach is taken with other field parameters. The definition of the time-average variable (take velocity as an example) is expressed by:

$$\overline{U} = \lim_{T\to\infty} \frac{1}{T} \int_t^{t+T} U(x_i)dt. \tag{3.8}$$

The variables $\overline{U}_i and\ \bar{P}$ are the time-averaged flow velocity and pressure whereas u_i and p are the fluctuating variables of corresponding instantaneous flow variables.

Therefore, the continuity, momentum and energy equations in the time-averaging operation for incompressible flow are respectively written as:

$$\frac{\partial \bar{U}_i}{\partial x_i} = 0. \tag{3.9}$$

$$\frac{\partial \bar{U}_i}{\partial t} + \bar{U}_i \frac{\partial \bar{U}_i}{\partial x_j} = -\frac{1}{\rho}\frac{\partial \bar{P}}{\partial x_i} + \frac{\partial}{\partial x_j}\left(\frac{\mu}{\rho}\left(\frac{\partial \bar{U}_i}{\partial x_j}\right) - \overline{u_i u_j}\right). \tag{3.10}$$

$$\frac{\partial \bar{T}}{\partial t} + \bar{U}_i \frac{\partial \bar{T}}{\partial x_i} = \frac{\partial}{\partial x_j}\left(\frac{k}{\rho c}\frac{\partial \bar{T}}{\partial x_j} - \overline{u_i t}\right) + \frac{\bar{S}}{\rho c}. \tag{3.11}$$

Here, the term $\overline{u_i u_j}$ is known as Reynold's stress tensor which has to be modelled for the RANS equations. This tensor is symmetric (i.e. $u_i u_j = u_j u_i$) and its trace is equivalent to twice the turbulence kinetic energy.

Two strategies have been proposed to model the Reynold's stress. One strategy is to solve the transport equations for six Reynolds stresses this in turn leads to extra computational cost. In (1877) Boussinesq proposed another approach, called the Boussinesq approximation, through linking the Reynold's stresses to the mean strain rate (mean velocity gradient) by algebraic relationship via a turbulent viscosity. This approach, strictly speaking, is only applicable for homogeneous isentropic flows. Models based on this approach are called the linear eddy viscosity models. In the time-average energy transport equation, the term $\overline{u_i t}$ is called a turbulent heat flux which can be modeled through linking the mean flow and thermal fields.

Based on the Boussinesq's hypothesis, the turbulent stress is linearly linked to the average strain rate via the proportionality constant which is turbulent eddy viscosity which represents the turbulence property. The mathematical formulation of the Boussinesq's hypothesis is expressed as, (Tabatabaian 2015):

$$\overline{u_i u_j} = -\mathcal{V}_t\left(\frac{\partial U_i}{\partial x_j} + \frac{\partial U_j}{\partial x_i}\right) + \frac{2}{3}k\delta_{ij}, \tag{3.12}$$

where (δ_{ij}) is the Kronecker delta, which then equal 1 only if $i = j$. The variable k is the mean turbulent kinetic energy per unit mass which is expressed as a function of normal stresses (with $i = j$) as:

$$k = \frac{1}{2}\overline{u_i u_i}. \tag{3.13}$$

In the linear eddy viscosity models, it is assumed that the turbulence shear stress $\overline{u_\iota u_j}$ (with $i \neq j$) are linked to the mean flow velocity gradients via the turbulent viscosity property. Similarly, the turbulent heat flux $\overline{u_\iota \mathrm{t}}$ can be modelled by using the gradient diffusion hypothesis which assumes that the turbulent heat flux is proportional to the mean temperature gradient which is expressed as:

$$\overline{u_\iota \mathrm{t}} = -\frac{\nu_t}{Pr_t}\frac{\partial \bar{T}}{\partial \mathrm{x}_j}. \tag{3.14}$$

The parameter Pr_t is a turbulent Prandtl number which is usually taken as constant value in most engineering applications (usually taken as 0.9 in the internal flows, as in the current study, whereas 0.7 is chosen for the external flows).

Based on how many transport equations are required to achieve the turbulent eddy viscosity, the linear eddy viscosity models are basically classified into three main families:

- Zero-equation models. The turbulent viscosity is assumed to be constant and calculated from algebraic relation(s) but there are no partial differential equations involved. Therefore, the equation system consists only average velocity components and pressure such as Cebeci-Smith model and Baldwin-Lomax model.

- One-equation models. In these models, a partial differential equation is implemented to generate either eddy viscosity or turbulent kinetic energy such as Prandtl's one-equation model and Spalart-Allmaras model. However, in spite of the fact that the one-equation models can present benchmarked enhancement in the flow prediction when compared to the zero-equation models, there is still a challenge in most turbulent problems in terms of prescribing an appropriate turbulent length scale.

- Two-equation models. Two additional transport equations of turbulent quantities are derived to provide a complete modeling framework through describing transport of two turbulent scales such as k-epsilon models and k-omega models, Davidson (2018).

3.2.4. Turbulence models used in the present work

In the present work, two turbulence models which belong to the two-equation category are used: Launder and Sharma $k-\varepsilon$ model and shear stress transport (SST) $k-\omega$ model. These models are briefly explained in the following sections.

3.2.4.1. *Launder and Sharma $k-\varepsilon$ model*

The standard k-ε model was developed by Jones and Launder (1972) to solve two transport equations, one for the turbulent kinetic energy *k* and another one for its dissipation rate ε to obtain the length scale ℓ and time scale ζ as follows respectively:

$$\ell = \frac{k^{3/2}}{\varepsilon}. \tag{3.15}$$

$$\zeta = \frac{k}{\varepsilon}. \tag{3.16}$$

This model was able to predict the correct flow physics only away from the solid-wall regions. Thus, several attempts have been proposed to improve its performance in the near wall region. Among them, Launder and Sharma (LS) in (1974) developed the another model, improving the prediction capability not only from the main core flow region but also from the solid wall region with a fine mesh near the wall, i.e. y^+ about one.

The LS version of this model is a two-equation model as well, one equation for the turbulent kinetic energy, *k* and the second equation for the quasi-homogeneous dissipation rate, $\tilde{\varepsilon}$. As per LS (1974), the turbulent viscosity is expressed as:

$$\mathcal{V}_t = c_\mu f_\mu \frac{k^2}{\tilde{\varepsilon}}. \tag{3.17}$$

Authors formulated the transport equations for the turbulent kinetic energy, *k*, and its dissipation rate, $\tilde{\varepsilon}$, of this model as follows respectively:

$$\frac{Dk}{Dt} = P_k - \underbrace{\left(\tilde{\varepsilon} + 2\mathcal{V}\left(\frac{\partial k^{\frac{1}{2}}}{\partial x_j}\right)^2\right)}_{\varepsilon} + \frac{\partial}{\partial x_j}\left((\mathcal{V} + \mathcal{V}_t)\frac{\partial k}{\partial x_j}\right). \tag{3.18}$$

$$\frac{D\tilde{\varepsilon}}{Dt} = c_{\varepsilon 1}\tilde{\varepsilon}\frac{P_k}{k} - c_{\varepsilon 2} f_2 \frac{\tilde{\varepsilon}^2}{k} + E + \frac{\partial}{\partial x_j}\left(\left(\mathcal{V} + \frac{\mathcal{V}_t}{\sigma_\varepsilon}\right)\frac{\partial \tilde{\varepsilon}}{\partial x_j}\right). \tag{3.19}$$

The parameters P_k and $\tilde{\varepsilon}$ represent the energy production and quasi-homogeneous dissipation rate of turbulent kinetic energy respectively which are defined as:

$$P_k = -\overline{u_\iota u_\jmath}\frac{\partial U_i}{\partial x_j}. \tag{3.20}$$

$$\tilde{\varepsilon} = \varepsilon - 2\mathcal{V}\left(\frac{\partial k^{\frac{1}{2}}}{\partial x_j}\right)^2. \tag{3.21}$$

The LS $k-\varepsilon$ model was proposed to predict the flow physics in all flow regions, however, it still requires a correction to the turbulence behavior near the solid-wall regions. This is

achieved by the use of damping functions which are f_2 and f_μ. These functions can be defined based on the turbulent Reynolds number, R_t, as:

$$f_2 = 1 - 0.3\exp\left(-{R_t}^2\right). \tag{3.22}$$

$$f_\mu = exp\left(\frac{-3.4}{\left(1+\frac{R_t}{50}\right)^2}\right). \tag{3.23}$$

$$R_t = \frac{k^2}{\mathcal{V}\varepsilon}. \tag{3.24}$$

The term E in the equation (3.19) represents an extra sours term which works only close to the solid-wall region which makes it possible to obtain both turbulent kinetic energy and its dissipation down to the viscous sub-layer. This term is given by the following formula:

$$E = 2\,\mathcal{V}.\mathcal{V}_t.\left(\frac{\partial^2 U_i}{\partial x_j \partial x_k}\right)^2. \tag{3.25}$$

The remaining model parameters are constant and their values are given in Table 3-1.

Table 3-1: The values of constants and damping function of the LS k-ε model.

c_μ	$c_{\varepsilon 1}$	$c_{\varepsilon 2}$	σ_k	σ_ε	f_1
0.09	1.44	1.92	1.0	1.3	1.0

As this model predicts the flow turbulence in regions down to the solid walls, this model is called a Low-Reynolds-number model. On the other hand, High-Reynolds number models cannot capture turbulence effect in the viscous wall region. The wall function concept can be used with high-Reynolds number models to deal with the effect of near-wall regions. The wall functions can be defined as empirical correlations which can be used to link the near-wall region between the core-flow region and near-wall region in which the first cell center has to be positioned in the log-law region.

3.2.4.2. *The $k-\omega$ Shear Stress Transport model*

This model proposed by Menter (1993) which is also an eddy-viscosity model solves two additional transport equations; one for turbulent kinetic energy and one for the specific dissipation rate, ω. The model switches from a low Re treatment $k-\omega$ model near the wall to a k-ε model away from walls based on a blending function. The model has the same k-equation that appears in the standard $k-\omega$ model with a small change in the production term whereas ε is calculated as product of k and ω. Changing the turbulence model from near-wall regions to the free-stream locations is performed by a blending function which is

used to switch the model from ω transport equation to an equivalent ε transport equation. The $k-\omega$ SST model does not require a wall function to improve the turbulence characteristics closes to the wall. The transport equations for turbulent kinetic energy k and its specific energy dissipation rate ω are defined as:

$$\frac{Dk}{Dt} = \frac{\tau_{ij}}{\rho}\frac{\partial U_i}{\partial x_j} + \frac{\partial}{\partial x_j}\left((\mathcal{V} + \sigma_k \mathcal{V}_t)\frac{\partial k}{\partial x_j}\right) - \beta^* k\omega. \tag{3.26}$$

$$\frac{D\omega}{Dt} = \frac{\gamma}{\mathcal{V}_t}\frac{\tau_{ij}}{\rho}\frac{\partial U_i}{\partial x_j} - \omega^2\beta + \frac{\partial}{\partial x_j}\left((\mathcal{V} + \sigma_\omega \mathcal{V}_t)\frac{\partial \omega}{\partial x_j}\right) + 2(1-F_1)\sigma_{\omega 2}\frac{1}{\omega}\frac{\partial k}{\partial x_j}\frac{\partial \omega}{\partial x_j}. \tag{3.27}$$

The last term of the ω-equation uses the blending function F_1 to interpolate the model constants as follows:

$$\begin{aligned} \beta &= F_1\beta_1 + (1-F_1)\beta_2. \\ \gamma &= F_1\gamma_1 + (1-F_1)\gamma_2. \\ \sigma_k &= F_1\sigma_{k1} + (1-F_1)\sigma_{k2}. \\ \sigma_\omega &= F_1\sigma_{\omega 1} + (1-F_1)\sigma_{\omega 2}. \end{aligned} \tag{3.28}$$

All model constants are listed in Table 3-2. Whereas, the blending function F_1 is expressed based on the distance from the flow field point to the closest solid wall y and the positive portion of the cross-diffusion term $CD_{k\omega}$ as follows:

$$F_1 = \tanh\left[min\left\{max\left(\frac{\sqrt{k}}{\beta^*\omega y}, \frac{500\nu}{d^2\omega}\right), \frac{4\rho\sigma_{\omega 2}k}{CD_{k\omega}y^2}\right\}\right]^4. \tag{3.29}$$

$$CD_{k\omega} = max\left(2\rho\sigma_{\omega 2}\frac{1}{\omega}\frac{\partial \omega}{\partial x_j}, 10^{-20}\right). \tag{3.30}$$

This function is unity away from the solid wall towards the free-stream and asymptotes to zero at the solid wall. In other words, it can be defined as:

$$F_1 = \begin{cases} \to 0, & reaching\ the\ wall, \quad behaves\ like\ k-\omega\ model \\ \to 1, & away\ from\ the\ wall, \quad behaves\ like\ k-\varepsilon\ model \end{cases} \tag{3.31}$$

The eddy viscosity is defined in this model based on an assumption that the Reynolds shear stress is related proportionally to the turbulent kinetic energy as follows:

$$\mathcal{V}_t = \frac{a_1 k}{\max(a_1\omega, \Omega F_2)}. \tag{3.32}$$

This assumption limits the turbulent viscosity by preventing the production term to exceed the dissipation. The parameters F_2 and Ω represent the blending function and the

magnitude of the absolute value of the vorticity (mean strain-rate tensor) which are defined as:

$$F_2 = \tanh\left[max\left(\frac{2\sqrt{k}}{\beta^*\omega y}, \frac{500\nu}{d^2\omega}\right)\right]^2. \tag{3.33}$$

$$\Omega = \sqrt{2S_{ij}S_{ij,}} \tag{3.34}$$

where

$$S_{ij} = \frac{1}{2}\left(\frac{\partial U_i}{\partial x_j} + \frac{\partial U_j}{\partial x_i}\right). \tag{3.35}$$

The blending function F_2 is zero for free share layers and asymptotes to unity for boundary-layer flows. Here, the expression of production term of ω reads as follows:

$$P_\omega = \gamma \frac{\omega}{k}\tau_{ij}\frac{\partial U_i}{\partial x_j}, \tag{3.36}$$

where

$$\tau_{ij} = \mu_t\left(\frac{\partial U_i}{\partial x_j} + \frac{\partial U_j}{\partial x_i} - \frac{2}{3}\frac{\partial U_k}{\partial x_k}\delta_{ij}\right) - \frac{2}{3}\rho k\delta_{ij}. \tag{3.37}$$

..

Table 3-2: The constants of the SST k-ω model.

a_1	$\sigma_{\omega 1}$	$\sigma_{\omega 2}$	β^*	β_1	β_2	σ_{k1}	σ_{k2}	γ_1	γ_2
0.31	0.5	0.856	0.09	0.075	0.0828	0.85	1.0	5/9	0.44

3.3. Numerical Treatment and Solvers

The flow governing Navier-Stokes equations defined in the previous sections cannot be solved analytically for turbulent flows. However, one can use the numerical techniques to solve these equations iteratively to a desired accuracy. The three most common discretization approaches used in CFD solvers are: the Finite Volume Method (FVM) (with a share of about $\approx 80\%$), the Finite Element Method (FEM) (with a share of about $\approx 15\%$) and the Finite Difference Method (FDM) (with a share of about $\approx 2\%$). The remaining 3% of the available CFD codes rely on different approaches such as the boundary element method, the spectral method, the Lattice Boltzmann method and Vorticity method, Petrova (2012).

The approximated partial differential equations in the FDM are based on the Taylor series expansion, and the accuracy of this method depends on the grid size and grid properties such as skewness ratio, stretch ratio, aspect ratio etc. Indeed, increasing the mesh points

leads to better prediction accuracy; however, major difficulties are experienced in the solution procedure owing to the matrix inversion at the algebraic equations. On the other hand, the partial differential equations in the FVM are transformed into discrete algebraic equations over small non-overlapping volumes of the flow domain. Then, the approximated algebraic equations are solved within each control volume to compute the values of the dependent variables. In comparison to the FVM, the FEM is commonly used in the computational solid-mechanic problems as compared to the computational fluid-mechanic problems. However, the FDM is the oldest traditional method whereas the FVM is relatively more recent method applied in the CFD since it was proposed as a better alternative technique for solving the partial differential equations for complicated-geometry fluid problems. Among different characteristics which are associated to make the FVM quite appropriate for numerical simulations of a wide range of fluid flow and heat transfer applications, the mass and momentum are strictly conserved in the FVM since the flux entering a certain control volume and leaving the adjacent one is identical, Moukalled et al. (2016).

The detailed discretization of the FVM as employed in the software OpenFOAM is described in appendix A.

Boundary conditions

The boundary conditions used in numerical methods are listed below:

- **Dirichlet boundary conditions**: a value on the domain boundary is specified.
- **Neumann boundary conditions**: a variable gradient perpendicular to the boundary of the domain is specified.
- **Robin boundary conditions**: a combination of the value of a variable and its derivative is required on the domain boundary.

Details of the implemented boundary conditions in the current work are given below:

- At the inlet boundary, uniform temperature and fixed velocity values are applied, along with the turbulence flow properties such as turbulent kinetic energy and specific dissipation rate based on the Re number and thermo-physical properties of heat transfer fluid. However, the pressure is applied as a zero gradient boundary condition.

- At the outlet boundary, the flow is assumed to be fully developed. Thus, the velocity and temperature are applied as zero gradients, as well as all turbulence characteristics (specific dissipation rate and turbulent kinetic energy). The pressure is applied at fixed values with a zero-boundary condition.

- At solid walls, the condition of no-slip is applied for velocity and a zero fixed value for turbulent kinetic energy, whereas a very large fixed value for the specific turbulence dissipation rate ω is used, as recommended by Menter (1994). According to the following expression based on the distance between the first cell and solid wall y_1, the density and dynamic viscosity of the heat transfer fluid, the specific turbulence dissipation rate ω is given by:

$$\omega = \frac{60\mu}{0.075\rho y^{+2}}. \tag{3.38}$$

- The boundary condition on the external wall of the absorber tube is non-uniform heat flux as clearly shown in Figure 3.1. This profile is achieved using the curve fitting equations proposed by Kaloudis et al. (2016) which is a result of the MCRT method. These equations are presented in Table 2-3.

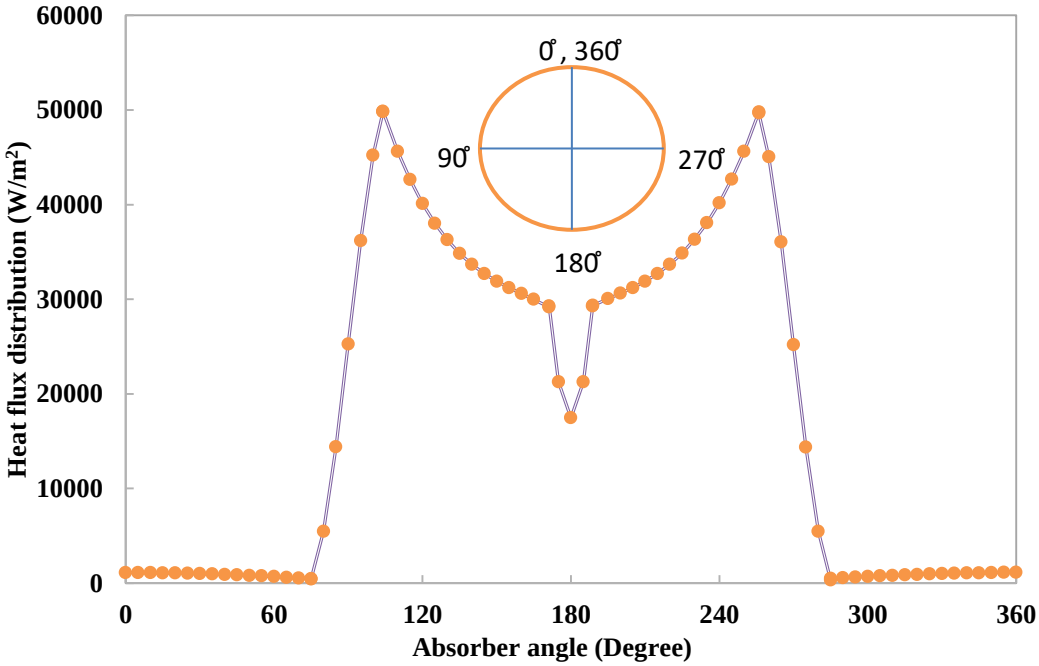

Figure 3.1: Heat flux distribution over the external surface of the absorber tube.

Since the coding software (OpenFOAM) is used in the current study, then the most appropriate approach to specify this boundary condition is to use (codedMixed) boundary condition. This boundary condition represents the Neumann boundary condition and

depending on the conduction heat transfer, the temperature gradient can be expressed as independent variable as

$$q = -k_s \frac{dT}{dz} \ \ or \ \frac{dT}{dz} = -\left(\frac{G_b}{k_s}\right).LCR, \tag{3.39}$$

where the parameters G_b, k_s and LCR are the solar beam radiation, the thermal conductivity of the absorber solid material and local concentration ratio, respectively. The local concentration ratio represents the heat flux distributions around the absorber tube. This boundary condition is written in C++. The final form of this boundary condition is expressed below with some comments as follows:

```
EXTERNALWALL // The name of the boundary.
{
    type          codedMixed; // The type of boundary condition.
    refValue      uniform $wlrefTemp; //default value of temperature if needed.
    refGradient   uniform $constGrad;// the solar beam radiation (Gb).
    valueFraction uniform 0;
    redirectType  nonuniformHeatFlux; // The name of boundary condition.
        code
    #{
        scalar R = 0.035;  // Outer radius of the absorber tube (m).
        scalar wlrefTemp = 0;
        scalar constGrad = 1000; // The solar beam radiation (Gb) (W/m2).
        scalar ksolid = 17.3; // The thermal conductivity of the absorber (W/mK).
        const vectorField& Cf = patch().Cf(); // Get centre coordinate;
        scalarField& rvf = this-> refValue();
        scalarField& rgf = this-> refGrad();
        scalarField& vf = this-> valueFraction();
        forAll(Cf, faceI)
        {
            scalar theta = Cf[faceI].z() * 180.0/R; // R: outer absorber radius (m).
```

```
    if (theta >= 0 and theta <= 75)

    {

rvf[faceI] = max(wlrefTemp, 0.0);

rgf[faceI] = max(−1 ∗ constGrad ∗ (0 ∗ theta ∗ theta ∗ theta − 1.07117e − 4
             ∗ theta ∗ theta − 8.100954e − 4 ∗ theta + 1.112046)/ksolid, 0.0);

vf [faceI] = 0.0;

     }

     else if (theta > 75 and theta <= 104)

    {

  rvf[faceI] = max(0,0.0);

  rgf[faceI] = max(−1 ∗ constGrad ∗ (−2.544403e − 3 ∗ theta ∗ theta ∗ theta
               + 6.878607e − 1 ∗ theta ∗ theta − 59.7439 ∗ theta
               + 1685.403) /ksolid, 0.0);


  vf [faceI] = 0.0;

    }

      else if (theta > 104 and theta <= 171.2)

   {

 rvf[faceI] = max(0,0.0);

 rgf[faceI] = max(−1 ∗ constGrad ∗ (−6.602394e − 5 ∗ theta ∗ theta ∗ theta
              + 3.196692e − 2 ∗ theta ∗ theta − 5.280388 ∗ theta
              + 327.5329) /ksolid, 0.0);


 vf [faceI] = 0.0;

    }

      else if (theta > 171.2 and theta <= 188.8)

    {

 rvf[faceI] = max(0,0.0);

 rgf[faceI] = max(−1 ∗ constGrad ∗ (0.0 ∗ theta ∗ theta ∗ theta + 1.524597e − 1
              ∗ theta ∗ theta − 54.88588 ∗ theta + 4957.224)/ksolid, 0.0);

 vf [faceI] = 0.0;

    }
```

```
      else if (theta > 188.8 and theta <= 256)

    {

rvf[faceI] = max(0,0.0);

rgf[faceI] = max(−1 ∗ constGrad ∗ (5.961826e − 5 ∗ theta ∗ theta ∗ theta
             − 3.504845e − 2 ∗ theta ∗ theta +      6.979938 ∗ theta
             − 440.3785) /ksolid, 0.0);


vf [faceI] = 0.0;

    }

      else if (theta > 256 and theta <= 285)

   {

rvf[faceI] = max(0,0.0);

rgf[faceI] = max(−1 ∗ constGrad ∗ (2.493475e − 3 ∗ theta ∗ theta ∗ theta
             − 2.019052 ∗ theta ∗ theta + 542.7366 ∗ theta
             − 48403.87) /ksolid, 0.0);


vf [faceI] = 0.0;

     }

      else

     {

rvf[faceI] = max(0,0.0);

rgf[faceI] = max(−1 ∗ constGrad ∗ (0.0 ∗ theta ∗ theta ∗ theta − 7.511141e − 5
             ∗ theta ∗ theta + 5.688045e − 2 ∗ theta − 9.606886) /ksolid, 0.0);


vf [faceI] = 0.0;

      }

     }

    };
```

Chapter 4: Assessment and evaluation of the thermal performance of various working fluids of PTCs

4.1 Introduction

Changing the heat transfer fluid is a viable approach to study the corresponding effect on the thermal and hydraulic performances of PTCs. Three categorized-types of pure fluids are used in this study; water, Therminol® VP-1 and molten salt. The parametric comparison between pure fluids is also studied considering the effect of various inlet fluid temperatures and different Re numbers on the thermal performance. However, selecting the appropriate HTF is a difficult choice. Apart from being environmentally friendly, the HTF should have a high thermal stability, a wide liquid temperature range of operation, low vapor pressure, large heat transfer coefficient and should not react to the containment wall material (Nahhas (2007)). For these reasons alone, investigation of an appropriate HTF in a PTC system is very important and has thus become the subject of many research studies. Furthermore, the use of an appropriate HTF can also reduce the solar receiver operational cost, thereby making the whole power cycle more efficient and lucrative.

Odeh et al. (1998) showed numerically that the thermal loss coefficient recorded by Syltherm® 800 oil in the PTC was higher than that recorded by water. Forristall (2003) examined different working fluids namely; Therminol® VP1, Xceltherm® 600, Syltherm® 800, 60-40 Salt, and Hitec® XL Salt under uniform heat flux. As per his results, the effect of a change in the working fluid was very small compared to other parameters with selecting Xceltherm® 600 and Syltherm® 800. Ouagued and Khellaf (2012) examined the thermal oils category only. They used Syltherm® 800, Syltherm® XLT, Santotherm® 59, Marlotherm® X, and Therminol® D12 under different inlet temperatures as the working fluid. Their results showed that Marlotherm® X and Syltherm® XLT can only be operated at temperatures less than 700 K whereas Syltherm® 800 can be operated at a temperature higher than 700 K. Other fluids seemed to operate better between 650 K and 750 K. Biencinto et al. (2014) numerically studied the effect of two different fluid types (pressurized nitrogen and synthetic oil) on the net electrical power. However, they reported a difference of only 0.91% in the net electrical power between the two fluid cases. The performance of gas as the working fluid has also been tested by various researchers; Muñoz-Anton et al. (2014) showed that the highest temperature that can be reached by tested gas was only 673 K. However, Good et al. (2014) experimentally operated at a temperature of more than 873 K using air as the heat transfer fluid.

Wang et al. (2014) numerically compared the thermal performance of molten salt and thermal oil with the latter showing higher thermal efficiency. Selvakumar et al. (2014) measured the effect of Therminol® D-12 and hot water on the thermal performance of PTC systems. They reported that Therminol® D-12 was the better option as it was stable for more than 100 cycles of operation. On the other hand, Tahtah et al. (2017) concluded that water can be considered as better than thermal oils as far as heat storage medium is concerned. Bellos et al. (2016) also reported that the pressurized water performs better than thermal oils over a wide range of inlet fluid temperatures due to better thermal properties such as dynamic viscosity and thermal conductivity. Islam et al. (2015) performed a parametric study of concentration ratio, receiver diameters and mass flow rates for three different heat transfer fluids: carbon dioxide, ammonia and nitrogen. They reported that carbon dioxide showed the maximum thermal efficiency followed by nitrogen and ammonia. Another important study was carried out by Bellos et al. (2017a) where they compared the thermal performance of various liquids and gases. They reported that the performance of liquid is generally higher than that of gases. Aguilar et al. (2019) examined novel fluids such as Synthetic oil, sub-critical carbon dioxide and super-critical carbon dioxide. Their results showed that the super-critical carbon dioxide was able to absorb more solar irradiation than the other tested fluids. Vutukuru et al. (2019) compared the suitability of various working fluids for high-temperature solar thermal applications. They examined both liquid and gaseous working fluids namely Therminol® VP-1, Dowtherm® Q, Hitec® XL and helium. As per their findings, better thermal performance was achieved using thermal oils and molten salt for a medium temperature range (150–550) °C whereas at higher temperatures (more than 550 °C) gas fluid (helium) was a better alternative. Arslan and Günerhan (2019) studied the effect of various working fluids including Dowtherm® A, air and molten salt on the energetic and exergetic performances. They reported that the maximum exergy efficiency (of 41.19%) was obtained by molten salt at 422 °C, followed by Dowtherm® A (40.82% at 400 °C) and air (40.33% at 402 °C).

It is evident from the literature studies summarized above that changing the working fluid is a viable approach to optimize the thermal and hydraulic performance of the PTC systems. However, there are still some gaps in the literature especially when it comes to comparative studies among various heat transfer fluids in terms of thermal performance, hydraulic behavior and thermal stresses over a wide range of operating temperatures under realistic thermal environment.

The present chapter abridges this gap by presenting comparisons of various working fluids from different categories which are examined by means of numerical simulations taking into consideration the heat transfer performance, pumping power, thermal losses, thermal stresses and overall thermal efficiency under realistic non-uniform heat flux distribution using the MCRT model. Furthermore, the current study also outlines a parametric study where various fluid behaviors are analyzed under different operating conditions of inlet fluid temperature and Re numbers. For example, water has been used with a temperature range of 320–500 K, Therminol® VP-1 with a temperature range of 320–600 K, and molten salt with a temperature range of 575–800 K; in all these cases the range of Re number values explored was $Re = 10^4 – 10^5$. The main objectives of this study are to examine the flow behavior through a parametric comparison of the heat transfer characteristics, and find the optimum operational conditions for different heat transfer fluids.

4.1. Fluid and Material Properties

4.1.1. Parabolic Trough Collector Design

The optical and geometrical characteristics used in the current study in addition to environmental parameters are listed in Table 4-1. For simplicity, the glass envelope is entirely removed in the current study, duplicating approximately the same model as (LS-2) developed by Dudley et al. (1994), for the bare case.

Table 4-1: The PTC model parameters used in the current work.

Property	**Value**	**Property**	**Value**
Absorber internal diameter, D_i (m)	0.066	Solar irradiation, G_b (W/m^2)	1000
Absorber external diameter, D_o (m)	0.07	Wind speed, V (m/s)	0.5
Aperture width, w_a (m)	8.0	Ambient temperature, T_{am} (K)	300
Solar receiver length, L (m)	4.0		

4.1.2. Thermal Properties of Working Fluids

In order to achieve precise results, it is necessary that the thermal properties of HTF are accurately incorporated in the simulations. In the present work, three different working fluids are used as base fluids; water, Therminol® VP-1 and molten salt (60% sodium nitrate ($NaNO_3$), 40% potassium nitrate (KNO_3)). The thermal properties of water are listed in Table 4-2.

Table 4-2: Thermal properties of water at different inlet temperatures, Incropera et al. (2006). Density, ρ, dynamic viscosity, μ, specific heat capacity, Cp and thermal conductivity, k_f.

Tin (K)	**μ (kg/m·s)**	**ρ (kg/m^3)**	**C_p (J/kg·k)**	**k_f (w/m·k)**	**Pr**
320	0.000577	989.12	4180	0.64	3.77
400	0.000217	937.207	4256	0.688	1.34
500	0.000118	831.2552	4660	0.642	0.86

For the Therminol® VP-1 base fluid, the temperature-dependent thermal properties which are valid for a temperature range of (285.15 K ≤ T ≤ 698.15 K) are given by Mwesigye et al. (2016a) as:

$$\rho = 1.4386 \times 10^3 - 1.8711T + 2.737 \times 10^{-3}T^2 - 2.3793 \times 10^{-6}T^3. \quad (4.1)$$

$(\mathrm{kg.\,m^{-3}})$

$$C_p = 2125 - 11.017T + 0.049862T^2 - 7.7663 \times 10^{-5}T^3 + 4.394 \times 10^{-8}T^4\ . \quad (4.2)$$

$(\mathrm{Jkg^{-1}K^{-1}})$

$$k_f = 0.1464 + 2.035 \times 10^{-5}T - 1.936 \times 10^{-7}T^2 + 1.0614 \times 10^{-11}T^3. \quad (4.3)$$

$(\mathrm{Wm^{-1}K^{-1}})$

$$\mu = 3.661 \times 10^2 - 3.0154T + 8.3409 \times 10^{-3}T^2 - 7.723 \times 10^{-6}T^3.\ (\mathrm{mPa.\,s}) \quad (4.4)$$

For 285.15 K ≤ T ≤ 373.15 K

$$\mu = 23.16 - 0.147T + 3.617 \times 10^{-4}T^2 - 3.984 \times 10^{-7}T^3 + 1.654 \times 10^{-10}T^4. \quad (4.5)$$

$(\mathrm{mPa.\,s})$ For 373.15 K ≤ T ≤ 698.15 K

However, for the molten salt the temperature dependent thermal properties which are valid for a temperature range of (573.15 K ≤ T ≤ 873.15 K) are given by Pacheco et al. (1995) as:

$$\rho = 2090 - 0.636T\ . \qquad (\mathrm{kg \cdot m^{-3}}) \qquad (4.6)$$

$$C_p = 1443 + 0.172T. \qquad (\mathrm{Jkg^{-1}K^{-1}}) \qquad (4.7)$$

$$k_f = 0.443 + 1.9 \times 10^{-4} T. \quad (\mathrm{Wm^{-1}K^{-1}}) \tag{4.8}$$

$$\mu = 22.714 - 0.12T + 2.281 \times 10^{-4} T^2 - 1.474 \times 10^{-7} T^3. \quad (\mathrm{mPa \cdot s}) \tag{4.9}$$

Note that the temperature in the equations of molten salt is in (°C).

4.1.3. Material Properties of Solid Part

As recommended by Forristall (2003), 321H stainless steel is used in the present study for the solid pipe due to its low bending behavior and high strength capability. Properties of 321H stainless steel are given in Table 4-3.

Table 4-3: Mechanical and thermal properties of absorber material.

Property	**Value**	**Property**	**Value**
Thermal conductivity, k_{solid} (W/m K)	17.3	Modulus of elasticity, E_m (GPa)	193
Specific heat capacity, C_{solid} (J/kg K)	512	Poisson's ratio, υ_P	0.28
Thermal expansion coefficient, β (1/°C)	1.89×10^{-5}	Material Density, ρ_{solid} (kg/m^3)	8055

4.2. Numerical Model Validation

4.2.1. Mesh Independence Study

For the considered range of Re number, the non-dimensional variable, Y^+ is less than 1. To obtain this, the distance between the first cell and the wall was adjusted as the Re number varied. By increasing the Re number, the distance from the solid wall has to be decreased as the boundary layer thickness becomes thinner due to an increase in the turbulence level. For the present work the geometry consisted of a 66 mm inner tube diameter, 70 mm outer tube diameter and 4 m tube length. Three different grids were used in order to study the effect of the resolution on the solution; namely coarse mesh with 0.8 million cells, medium mesh with 1.8 million cells and fine mesh with 2.4 million cells, shown in Figure 4.1. All grids were very fine in the near-wall region in order to resolve the viscous sub-layer as the $Y^+ \approx 1$ is considered in the near-wall node.

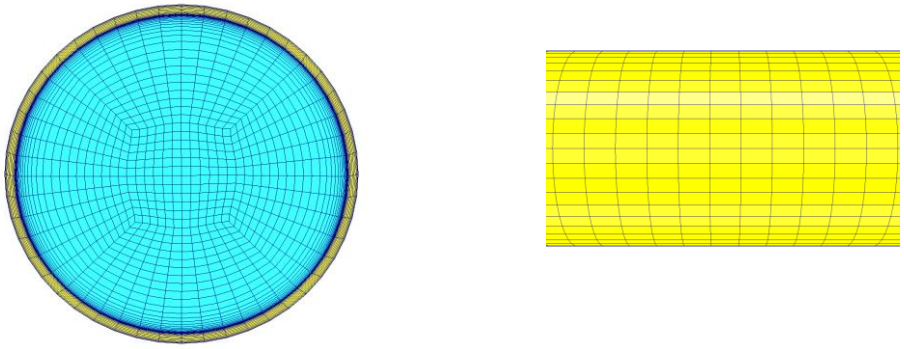

(**a**) Coarse Mesh

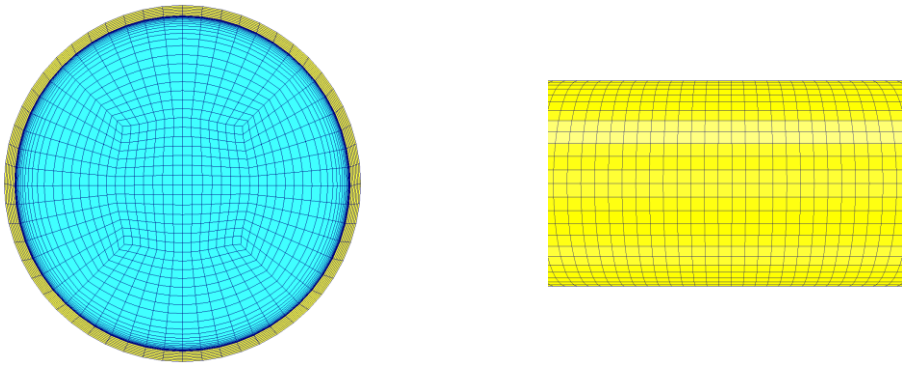

(**b**) Medium Mesh

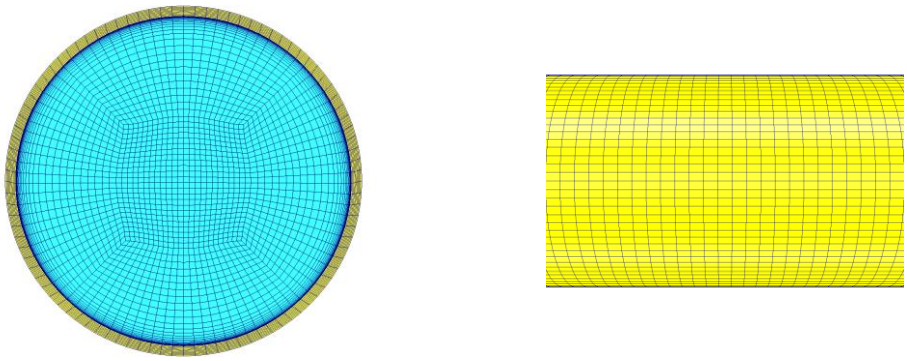

(**c**) Fine Mesh

Figure 4.1: Three dimensional hexahedral meshes used in this study.

The predicted Nu numbers versus Re numbers for all three grids were compared using pure water at inlet temperature of 320 K over a range of Re number (10^4–10^5) as shown in Figure 4.2. As can be seen, the coarse grid failed to predict the Nu number in regimes of the high level of turbulence. After increasing the mesh size in all directions, the new medium mesh was able to capture the thermal physics precisely even in high turbulent-level regions. However, by increasing the mesh size further to Fine level did not change the results. Therefore, the medium grid was found to be the sufficient grid for the present study.

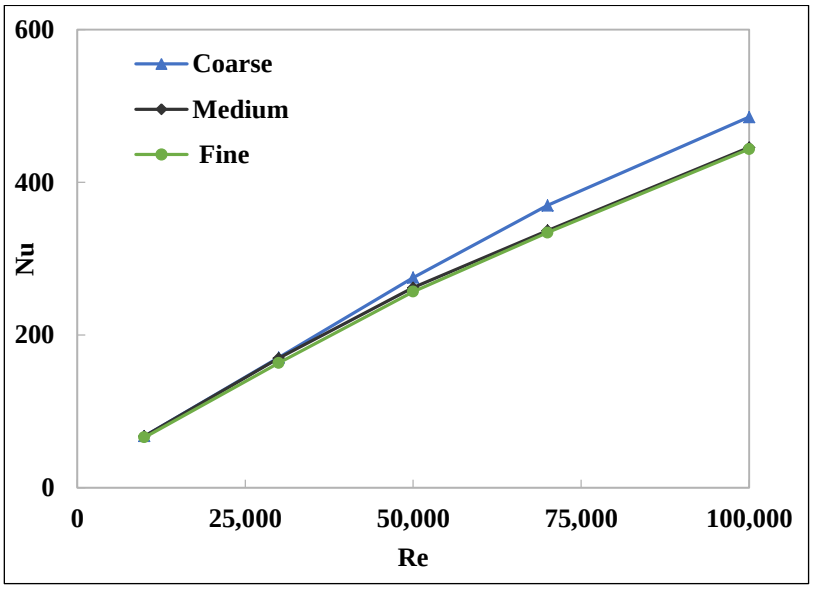

Figure 4.2: Mesh independence study for three different grids used in the present study.

4.2.2. Numerical Model Validation

To obtain an accurate prediction of the solar absorber behavior using the two aforementioned turbulence models, several steps were taken for validation. Firstly, the output temperature of working fluid was validated by using the same geometry and thermal environment conditions as that of Dudley et al. (1994) which preformed experiments of a parabolic trough collector without glass envelope using Syltherm 800 oil as HTF at Sandia national laboratories. Table 4-4 presents the experimental test conditions compared with the numerical results of both turbulence models. It should be noted here that for every single volumetric flow rate, $\dot{V}$ the other test conditions such as wind speed, inlet temperature, T_{in}, ambient temperature, T_{am} and direct normal irradiance, G_b, were varied.

Table 4-4: A comparison between the experimental data and numerical predictions of the output temperature of working fluid.

Dudley et al. (1994)				**k omega SST**		**LS k epsilon**	
$\dot{V}$ **(L/min)**	G_b **(W/m^2)**	T_{in} **(°C)**	T_{out} **(°C)**	T_{out} **(°C)**	**Dev. (%)**	T_{out} **(°C)**	**Dev. (%)**
48.4	801.3	151.7	166.2	168.337	−1.286	171.347	-3.097
49.8	888.6	198.2	215.5	213.294	1.024	215.425	0.035
51.1	920.5	301	314.2	313.809	0.124	314.833	-0.201
55.6	929.4	313.8	324.8	325.340	-0.166	326.375	-0.485
55.8	940.4	384	395	395.446	-0.113	396.435	-0.363
50.9	935.7	252.1	268	266.868	0.422	267.360	0.239
39.8	817.5	101	120.8	127.859	-5.844	136.211	-12.757
50.1	854.5	203.1	219.2	217.292	0.870	219.364	-0.075
50	867.6	203.4	219.6	217.825	0.808	219.210	0.178
48.2	922	100.8	121.1	125.409	-3.558	131.945	-8.955
51.6	927.6	354.4	367.8	366.507	0.352	367.572	0.062
Average Deviations (%):				-0.670		-2.311	

It can be observed from Table 4-4 that the k-ω SST model performed better as it predicted output temperatures, T_{out} closer to the experimental data with an average deviation of only 0.67%. The second parameter selected for the validation was the thermal efficiency of the parabolic trough collector with realistic heat flux boundary condition (non-uniform) on the external wall of the solar absorber. Note that the deviation between predictions and experiments is noisy (positive and negative) and probably due to measurement uncertainty rather than a systematic bias in numerical predictions for which an error of a few percent is generally expected, particularly for heat transfer. The numerical results produced by the considered turbulence models were validated with experimental measurements of the Dudley et al. (1994) as presented in Figure 4.3.

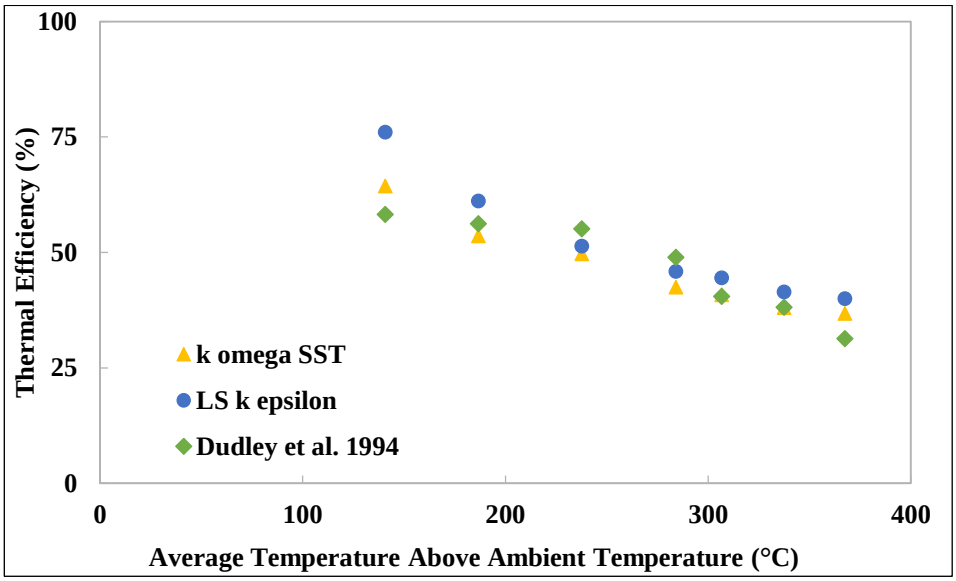

Figure 4.3: Validation of the present study with the thermal efficiency data of Dudley et al. (1994).

It can be seen from the Figure 4.3 that the k-ω SST turbulence model predicted the thermal efficiency better than the LS k-ε model especially for the lower inlet temperature cases. The model was also validated for the Nu number of pure water moving inside the solar receiver with the experimental correlations of Petukhov (1970) and Gnielinski (1976) as shown in Figure 4.4a. Here it can again be observed that the LS k-ε model under predicted the Nu number compared to the k-ω SST model and the correlations. The mean non-dimensional profiles of velocity and temperature close to the outlet wall were also used for the validation with DNS data using both k-ω SST and LS k-ε models as shown in the benchmark results presented in appendix B. The last experimental correlation of Petukhov (1970) for the friction factor was also used to validate the numerical results of the k-ω SST turbulence model only as shown in Figure 4.4b. This correlation is for a fully developed turbulent flow. As shown in the Figure 4.4b that the agreement between numerical results and experimental data is very good in all turbulent regimes. Form all the validation figures presented above, it can be deduced that the k-ω SST model is the better choice and was hence used for all the remaining simulations. It should be noted here that in the case of swirl generators, the selection of some turbulence models has been found to be selected as a common default model in some types of swirl generators such as k-omega SST model which has been selected to predict the flow characteristics in the presence of longitudinal triangular and rectangular fins proposed by Amina et al. (2016), helical screw-tape with core rod proposed by Song et al. (2014) and dimpled twisted tapes investigated by Zheng et al. (2017). However, the Re-Normalization Group (RNG) k-epsilon model has also been selected through investigating different cases of swirl generators such as porous disc configurations proposed by Kumar and Reddy (2009), louvered twisted tapes investigated

by Ghadirijafarbeigloo et al. (2014) and porous rings reported by Ghasemi and Ranjbar (2017). However as explained in many papers or turbulence text-books, e.g. Hanjalic Launder (2011) “linear eddy-viscosity models (EVM) usually perform poorly (in the presence of system rotation or swirl) because the modelled turbulent kinetic energy is “blind” to swirl which causes substantial changes in the stress anisotropy”. On the other hand in Second Moment Closure (full Re stress transport equations), the effects of swirl is represented exactly in the production terms of the full Re stress tensor. For example in the case of swirl downstream of a wing tip vortex Craft et al. (2006) showed that EVMs lead to a dramatic over estimation of turbulence and consequently a severe decay of the swirl whereas a Second Moment Closure simulation is in excellent agreement with measurements.

(a)

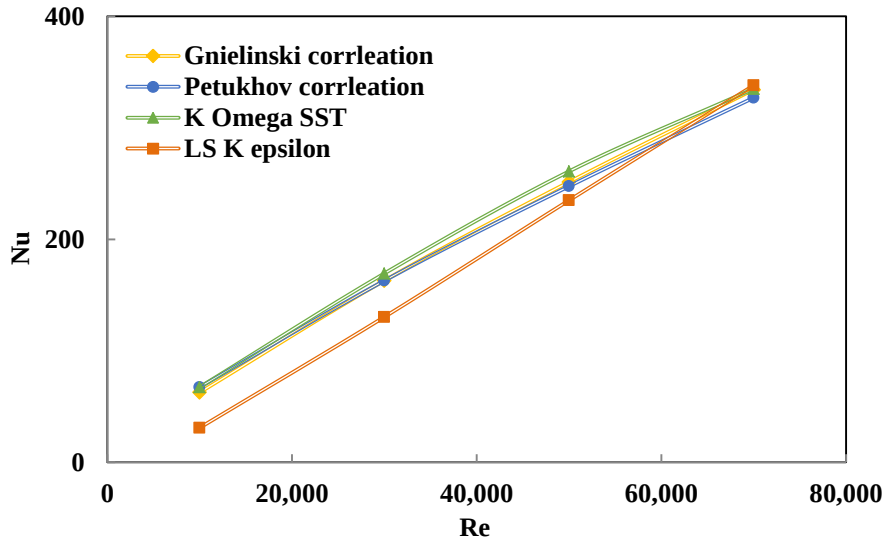

(b)

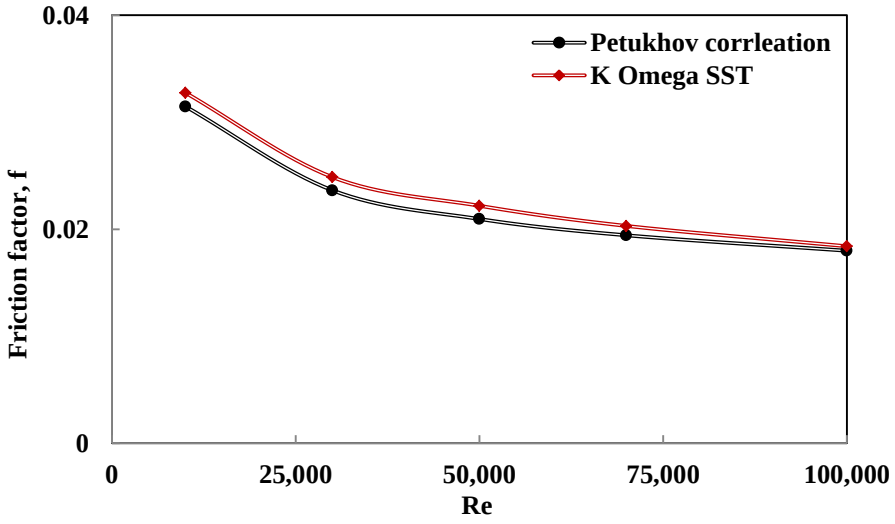

Figure 4.4: Comparisons between the present work with the experimental correlations (a) Average Nusselt number correlations proposed by Petukhov (1970) and Gnielinski (1976) (b) Friction factor, f, correlation proposed by Petukhov (1970).

4.3. Results and Discussions

4.3.1. Heat Transfer Performance

Figure 4.5 (a–c) present the Nu number as a function of the Re number at different inlet temperatures for the three working fluids; water, molten salt and therminol VP-1. It can be seen that the trend is similar for the Nu numbers at the inlet temperatures of all working fluids. The Nu number increases considerably as the Re number increases for all working fluids.

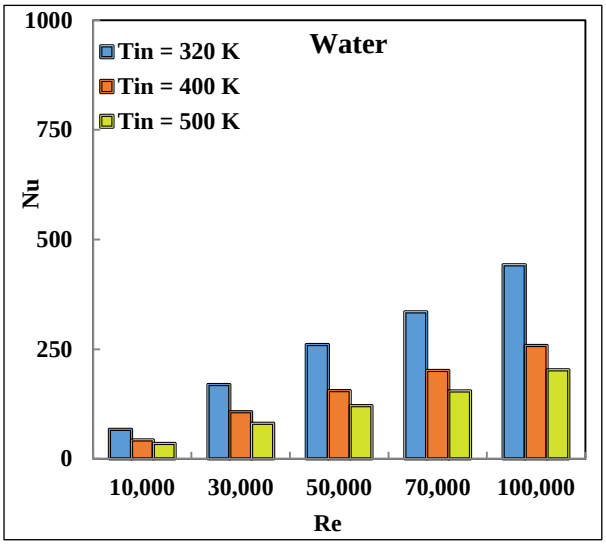

(a) Water

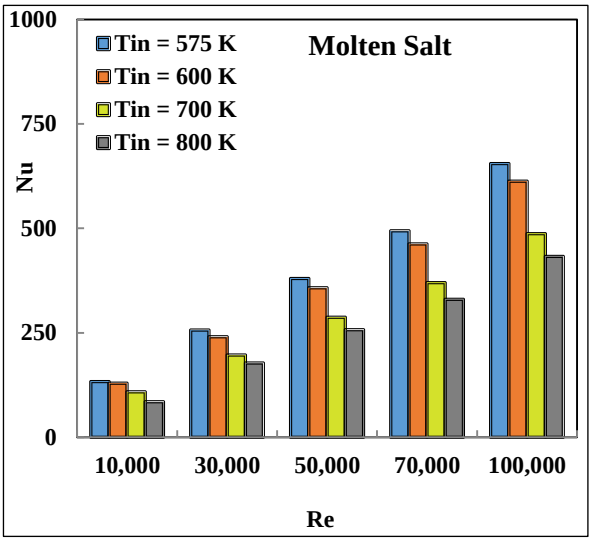

(b) Molten Salt

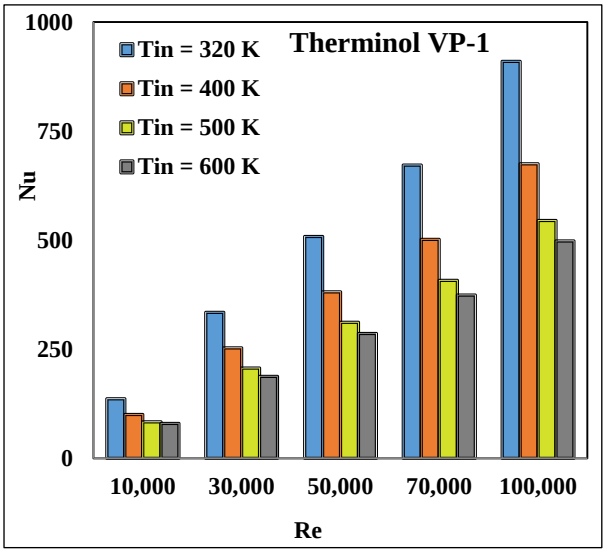

(c) Therminol® VP-1

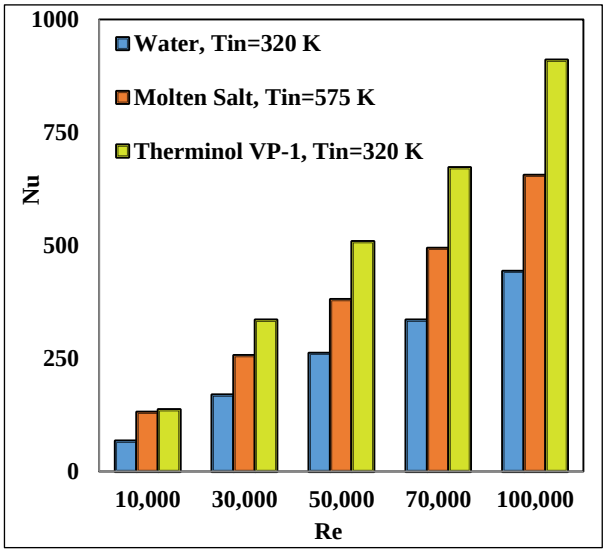

(d) Comparison between all fluids

Figure 4.5: Nusselt number profiles of different fluids used in the present work (a, b and c) and comparison of Nusselt number profiles of different fluids used in the present work (d).

This can be attributed to several reasons; lower inner wall temperature of the solar absorber, thinner thickness of the boundary layer at larger Re number and lower output temperature of the working fluid. Furthermore, by increasing the inlet temperature, the thermal properties of working fluids change consequently, leading to a decrease in the Pr number which results in a lower Nu number prediction. Another important feature that can be noted from this figure is that the working fluid at the smallest inlet temperature provided the largest Nu number for all HTF's due to the larger provided Pr number.

The previous studies such as Mwesigye et al. (2016a) have also reported similar behavior. Figure 4.5(d) shows the Nu profile of all the fluids at the smallest inlet temperature as a function of Re number. It is noticeable that the Nu number of Therminol® VP-1 is the largest for all Re numbers followed by molten salt and water. This is due to the thermal properties of therminol VP-1 which leads to a larger Pr number at all inlet temperatures compared to the other fluids; the Pr number of Therminol® VP-1 is 2.5 times larger than that of molten salt and 6 times greater than that of water. According to the results obtained at the smallest fluid temperature and largest Re number, the Nu number predicted using Therminol® VP-1 is greater than that predicted by water and molten salt by 2.055 and 1.4 times, respectively.

4.3.2. Collector Hydraulic Performance

Figure 4.6 (a–c) present the specific pressure drop behavior (Pa/m) of all base fluids at different inlet temperatures. It can be noticed that the specific pressure drop increases significantly as the Re number increases. This is expected since the mass flow rate increases gradually as Re number increases and the flow becomes highly turbulent; thus, higher pumping power is required to force the flow through the solar absorber. Moreover, the specific pressure drop of all fluids decreases as the temperature of the working fluid increases due to the temperature dependent properties. Similar findings were reported by the previous studies of Arslan et al. (2019) and Mwesigye et al. (2016a).

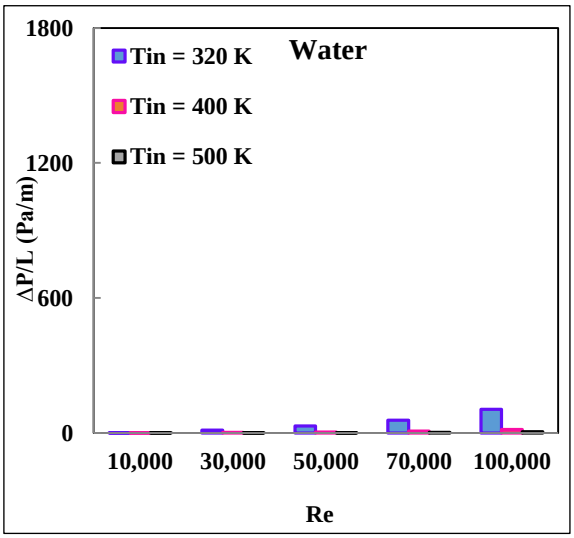

(**a**) Water

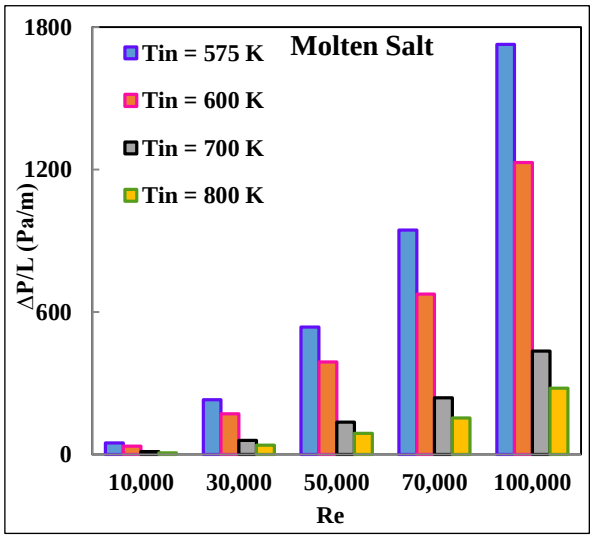

(**b**) Molten Salt

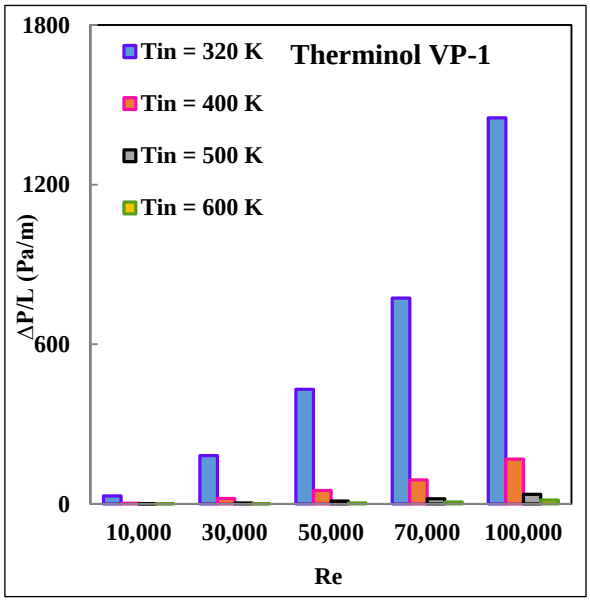

(**c**) Therminol® VP-1

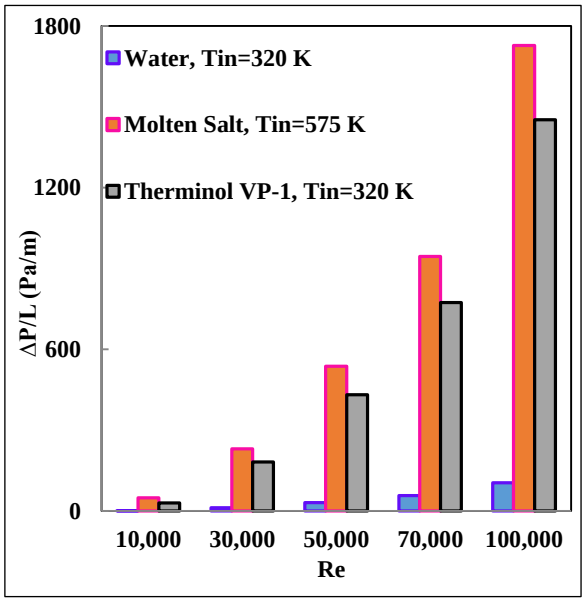

(**d**) Comparison between all fluids

Figure 4.6: The specific pressure drop profiles of all fluids under consideration.

Figure 4.6d presents the specific pressure drop distribution of all fluids at the smallest inlet temperature as a function of the Re number. It is very clear that the specific pressure drop of molten salt is the largest for all Re numbers followed by Therminol® VP-1 and then water. This is because the molten salt fluid flow characteristics (density and viscosity) are relatively higher compared to the other fluids; density approximately 1.8 and 2 times higher and viscosity approximately 2 and 5.7 times higher than that of Therminol® VP-1 and water, respectively. Overall, at the minimum fluid temperature and maximum Re number, the specific pressure drop predicted by molten salt is larger than that predicted by water and therminol VP-1 by 16.5 and 1.2 times, respectively.

4.3.3. Thermal Losses

For the thermal loss analysis of the solar receiver, the main objective is to determine the major factor that affects these thermal losses when the glass envelope is removed. It is observed that the average temperature of the receiver's outer surface is strongly dependent on the inlet fluid temperature. The smaller the inlet fluid temperature the lower the outer surface absorber's temperature, consequently leading to a decrease in thermal losses thereby improving the thermal gain. Among the thermal losses of the solar receiver, the radiation loss is a function of forth-power absolute temperature difference between the outer surface temperature and sky temperature. Since the glass envelope is removed in this study, the outer surface of the solar receiver is greatly radiated. Therefore, the radiation thermal loss is quite sensitive to the absorber's surface temperature rather than the ambient condition. Thus, radiation loss from absorber surface to the sky increases gradually. The second important contribution to thermal losses is the convection heat loss from the outer surface to the ambient air which is approximately from 60 to 70% from the overall thermal losses as shown in Figure 4.7. This is in complete agreement with the findings of Dudley et al. (1994). This behaviour occurs may be due to the fact that the emissivity of the selective coating considered in the present work is in a range of 0.06-0.07. Moreover, the convection heat transfer mechanism is assumed to be forced convection which may act at increasing the convection heat transfer coefficient even higher. These types of losses are a function of two important factors; the outside air heat transfer coefficient and the temperature difference between the receiver outer surface and ambient air.

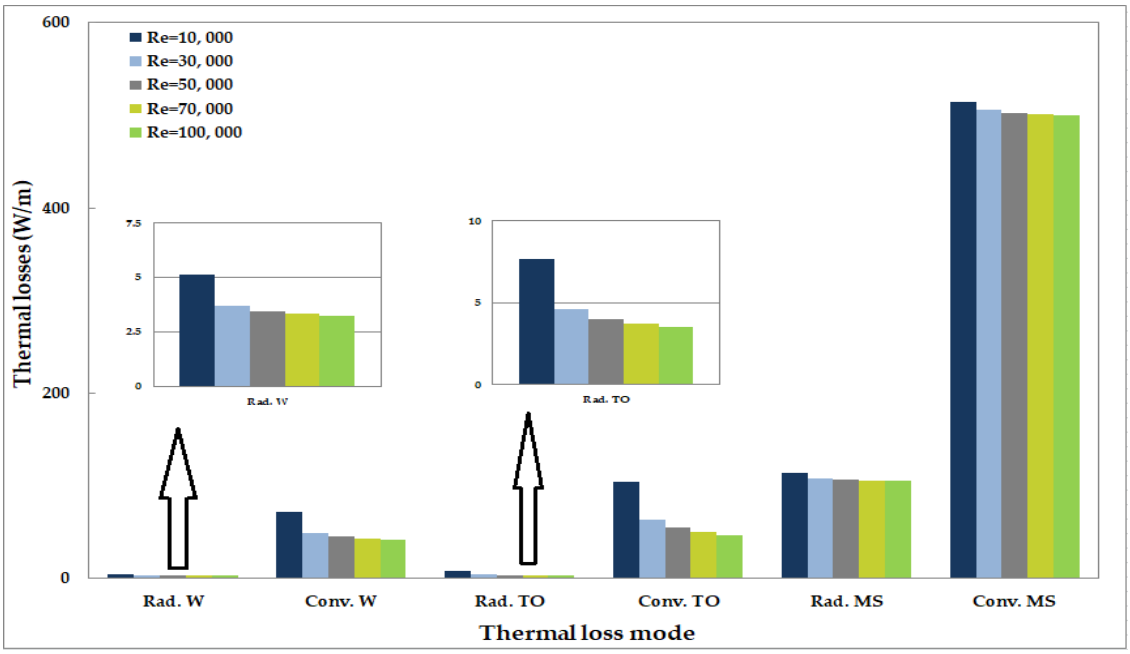

Figure 4.7: Convection (Conv.) and radiation (Rad.) thermal losses at different *Re* numbers at the smallest inlet temperatures of different fluids; W (Water), T (Therminol® VP-1) and MS (Molten Salt).

Figure 4.8 exhibits the results of thermal losses as a function of operating temperature for all the respective fluids at different *Re* numbers. As already mentioned, the outer surface temperature increases considerably with increasing operating temperatures; this significantly enhances the convective heat loss. This behavior is in perfect agreement with Forristall (2003), Bellos et al. (2016) and Dudley et al. (1994). It is observed that the smaller *Re* numbers are associated with the largest thermal losses for all the cases under consideration. This is because the flow with smaller velocity acts to absorb more energy and reflects part of it to the inner surface via convection and from the inner surface to the outer surface via conduction leading to an enhancement of the outer surface's temperature. On the other hand, the solar absorption starts to reduce once the flow velocity increases, leading to energy reduction in the reflected parts. The figure shows that the largest heat losses are obtained when using molten salt due the higher operating temperatures. However, for the fluids with same inlet temperatures (i.e. water and Therminol® VP-1) at 500K, the thermal losses produced by Therminol® VP-1 are larger than those produced by water by 1.2 times. Another important characteristic that can be highlighted here is that the convection heat losses can be highly affected by the wind velocity, especially in the case of no glass envelop. For the no glass envelop case, the ambient air derived by the forced convention is very large and can be decreased by reducing the ambient wind as presented in Figure 4.8 (d). However, in the case of zero air velocity, the convection heat losses should be naturally determined rather than forced convection.

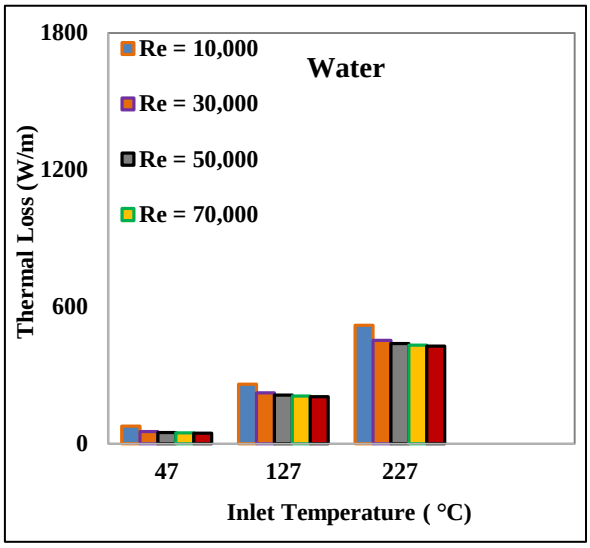

(a) Water

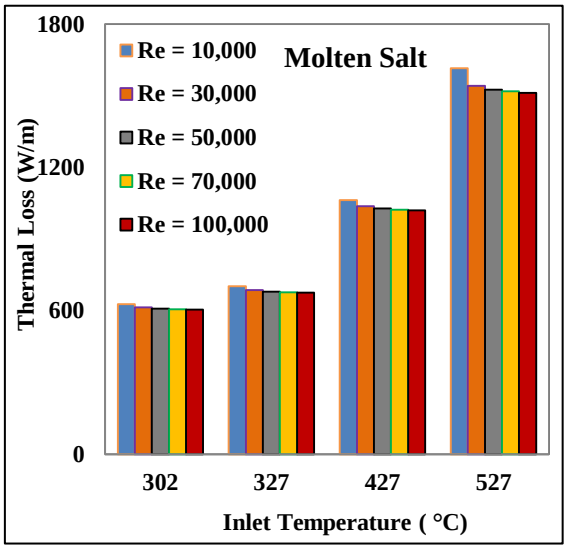

(b) Molten salt

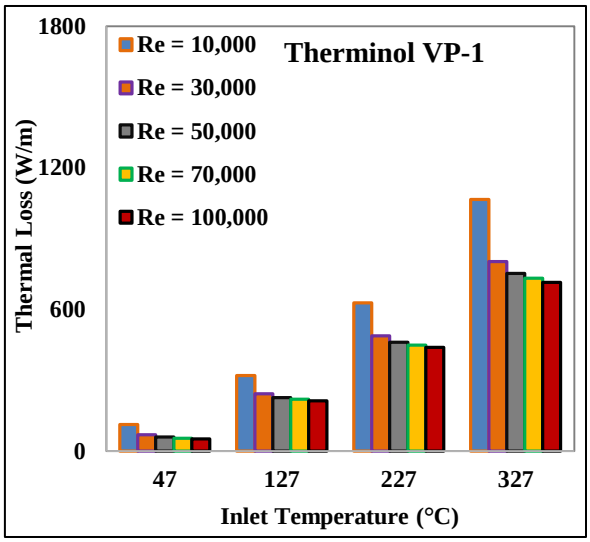

(c) Therminol VP-1

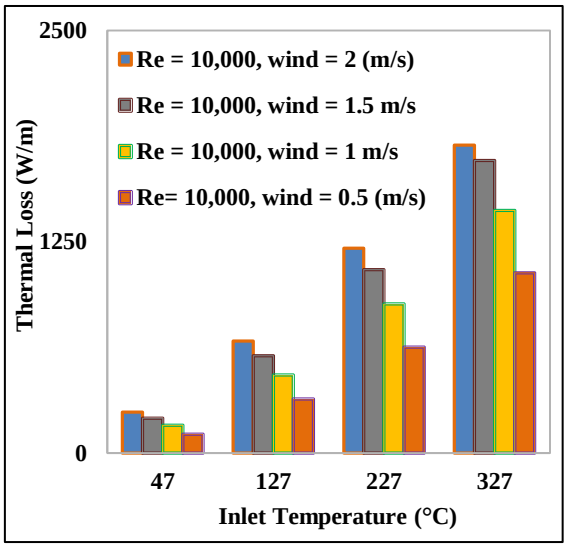

(d) wind effect on the thermal losses

Figure 4.8: Thermal losses behaviour of all pure fluids used in this chapter.

4.3.4. Overall Collector Efficiency

The thermal efficiency of the bare receiver (without glass sleeve) is presented in Figure 4.9 for all fluids over a range of inlet operating temperatutres of (320–800) K and different Re numbers. It can be observed that all the working fluids show similar thermal behaviour in terms of the thermal efficiency which is directly proportional to the inlet operating temperature. In general, the smaller the inlet working temperature, the larger the receiver thermal efficiency. The reason behind is that by increasing the fluid inlet temperature, the outer surface of the solar receiver becomes highly radiated leading to a significant increase in radiation and convection losses. In other words, larger absorber temperature at the outer surface acts to increase thermal losses and consequently reduces the overall thermal efficiency with lower pumping power requirements. However, by increasing the Re number for all cases at a given inlet operating temperature, moderate reduction can be observed in the overall thermal efficiency. This is because to achieve higher Re numbers the flow rate needs to increase which obviously requires larger pumping power, leading to a reduction in the heat gain as can be noted from the efficiency equation. This means that for the same fluid, the thermal efficiency can either be affected by thermal losses (which are dependent upon the inlet fluid temperature) or by the pumping power requirement (which is dependent upon the desired flow rate). This behavior is in agreement with the findings of Forristall (2003), Bellos et al. (2016), Islam et al. (2015) and Dudley et al. (1994).

It is prudent to note here that the Therminol® VP-1 preforms more or less the same as molten salt for the common temperature range whereas the Therminol® VP-1 is the most ideal fluid for the temperature range of 320–500 K.

(**a**) Water

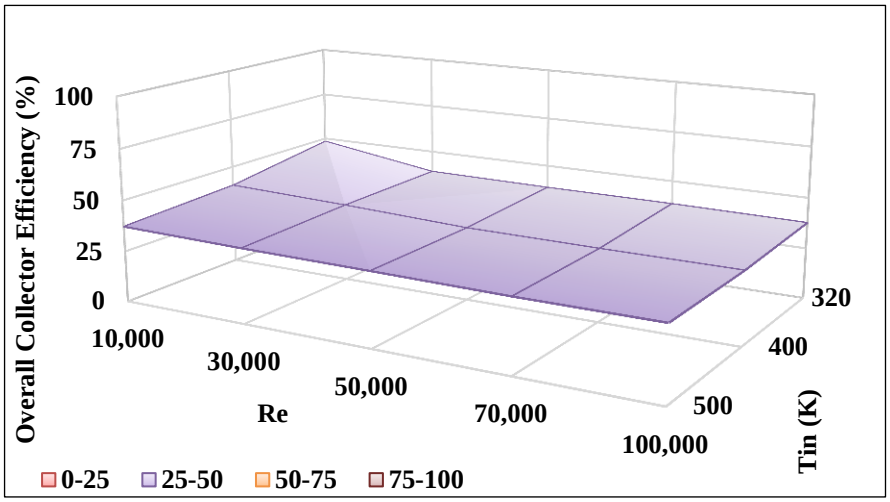

(**b**) Molten Salt

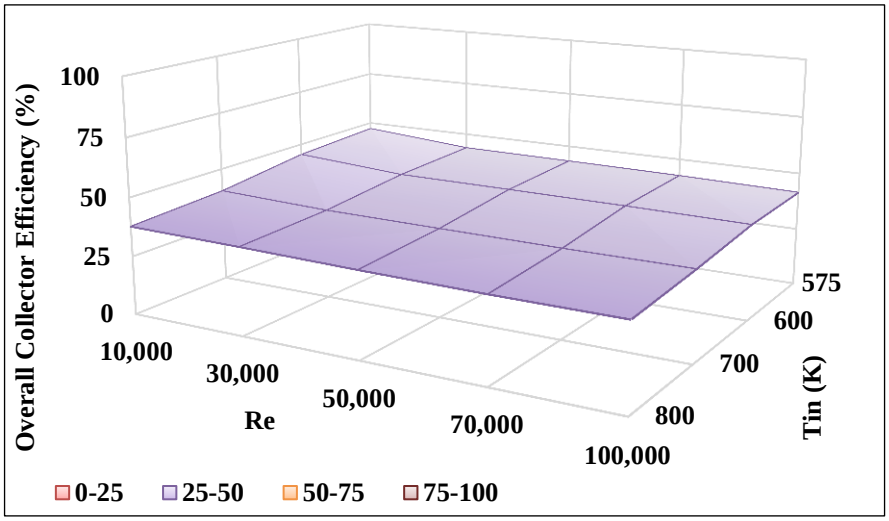

(**c**) Therminol® VP-1

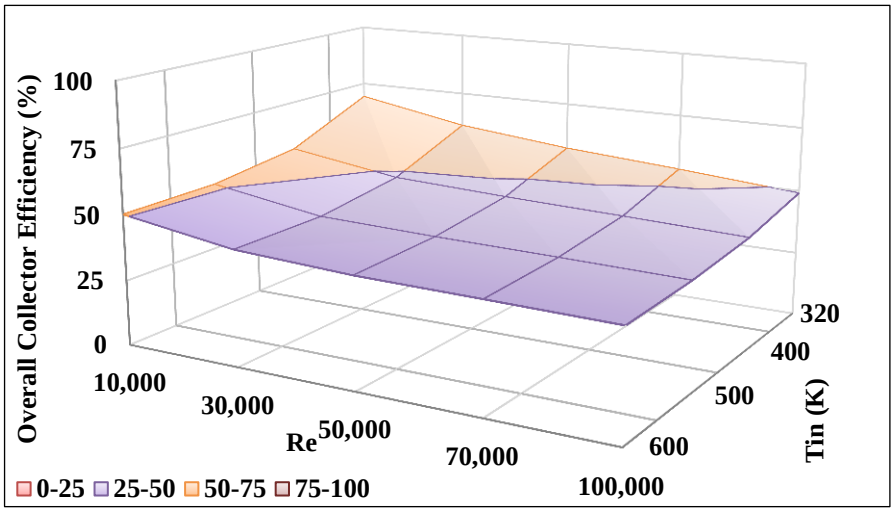

Figure 4.9: Thermal efficiency behaviour of all heat transfer fluids under different parameters.

Furthermore, the thermal properties of fluids play an important role in terms of the absorbed heat gain. For example, the mass flow rates ($\dot{m}$) of water and therminol VP-1 are not the same even at the same Re number and inlet fluid temperature as illustrated in Table 4-5. It is clear that the mass flow rates of therminol VP-1 are larger than those of water by approximately four times at all Re numbers and both inlet temperatures. This enhances the thermal energy gain (Q_u) for Therminol® VP-1 significantly compared to that of water. It is interesting to note here that at higher inlet temperatures (more than 400℃) the Therminol® VP-1 no longer works well which in turn leads to a poor thermal performance, in other words reducing the thermal efficiency of the power plant. It is thus concluded that molten salt is a better candidate at these higher temperatures.

Table 4-5: A comparison between the thermal performances of water and TherminolVP-1.

	Water		**Therminol® VP-1**		**Water**		**Therminol® VP-1**	
Re	$\dot{m}$ (kg/s)	Q_u (W)	$\dot{m}$ (kg/s)	Q_u (W)	$\dot{m}$ (kg/s)	Q_u (W)	$\dot{m}$ (kg/s)	Q_u (W)
	T_{in} = 320 K				T_{in} = 400 K			
10,000	0.29	15,463.05	1.14	22,126.8	0.11	12,850.22	0.38	17,657.12
30,000	0.89	12,451.31	3.44	19,534.1	0.33	12,250.78	1.13	15,558.12
50,000	1.49	12,268.03	5.73	18,038.5	0.56	11,221.59	1.9	14,926.81
70,000	2.09	12,335.38	8.02	17,014	0.78	11,306.02	2.65	14,473.58
100,000	2.9	13,292.31	11.46	15,902.9	1.12	11,511.28	3.8	13,961.22

4.3.5. Thermal Stresses

Another important parameter considered in this work is the thermal stresses in the solid part in the circumferential direction of the absorber tube. The circumferential stress, σ_θ given by Barron and Barron (2013) reads as:

$$\sigma_\theta = -\frac{\beta E_m \Delta T}{2(1-\upsilon_P)}\left[\frac{1+\ln\left(\frac{r}{r_o}\right)}{\ln\left(\frac{r_i}{r_o}\right)}+\frac{\left(\frac{r_o}{r}\right)^2+1}{\left(\frac{r_o}{r_i}\right)^2-1}\right], \tag{4.10}$$

where, β is the thermal expansion of the solid material (1/°C), E_m is the modulus of elasticity (Pa), ΔT is the temperature difference between the outer and inner surfaces (°C), and υ is the Poisson's ratio. Where at $r = r_i$, the circumferential stress in the above equation represents the tensile stress at the inner surface and at $r = r_o$, the stress represents

compression stress at the outer surface. Where r_i and r_o are the receiver inner and outer radiuses respectively.

Structural thermal stresses are a result of the temperature difference between the two sides of the material in the presence of restrictions. These types of stresses, in fact, are mechanical stresses happening due to forces caused by a metal part that tries to contract or expand when it is restricted. Theoretically speaking if there were no restrictions, there would not be any thermal stresses. For the case of parabolic trough collectors, the solar receivers both ends are rigidly fixed and are subjected to a thermal difference between the inner and outer surfaces. Thereby, generating thermal stresses; compressive at the outer surface and tensile stresses at the inner surface. Here two types of restrictions can be addressed; external and internal restrictions. The external restriction caused by the support brackets at the receiver ends which prevents contraction or expansion in the whole system in the presence of temperature difference.

Thermal stresses in the circumferential direction due to the temperature gradient in the solar absorber material are shown in Figure 4.10 for all fluids considered in this study. The positive upper curves represent the tensile stresses whereas the negative lower curves represent the compressive stresses. It is noticed that the circumferential stresses are approximately symmetrical for all flow conditions and all working fluids. For different inlet temperatures both the compressive and tensile stresses increase till a certain Re number and then become constant for all the fluids. This is because an increase in the Re number leads to a decrease in the boundary layer thickness and thus the temperature of the outer surface becomes closer to that of the inner surface. Another important feature that can be noticed from this figure is that the inlet fluid temperature plays a very important role in determining the circumferential stresses; especially, in the low-level turbulence regimes (i.e. low Re numbers). At low Re numbers an increase in the inlet fluid temperature leads to a reduction in the flow Pr number, this in turn leads to an increase in the thickness of the thermal boundary layer. The larger the inlet fluid temperature, the smaller the Pr number leading to smaller tensile circumferential stresses and larger compressive circumferential stresses. The thermal stresses presented by Therminol® VP-1 are smaller than those depicted by other fluids particularly in the low-turbulence regimes for all inlet fluid temperatures. On the other hand, no significant changes were observed when the inlet fluid temperature was increased, particularly from 575 to 700 K.

(**a**) Water

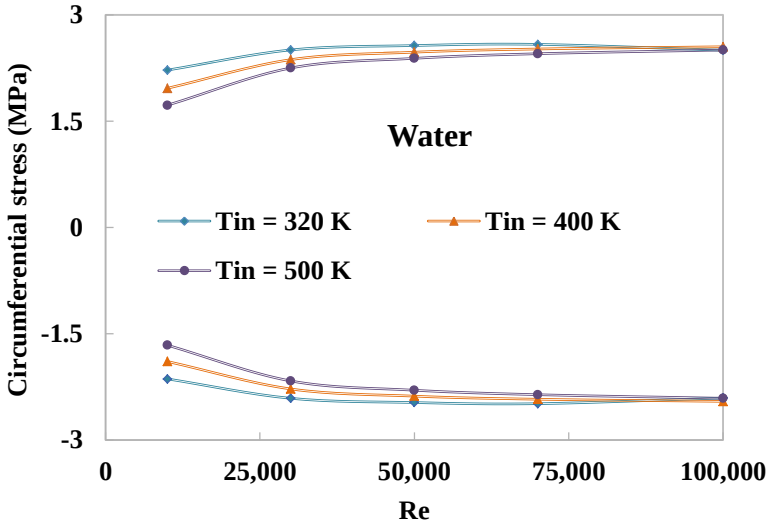

(**b**) Molten salt

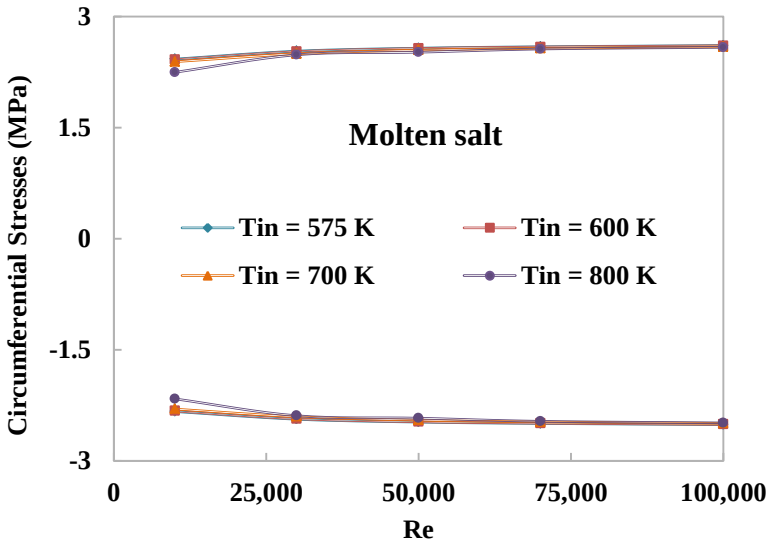

(**c**) Therminol VP-1

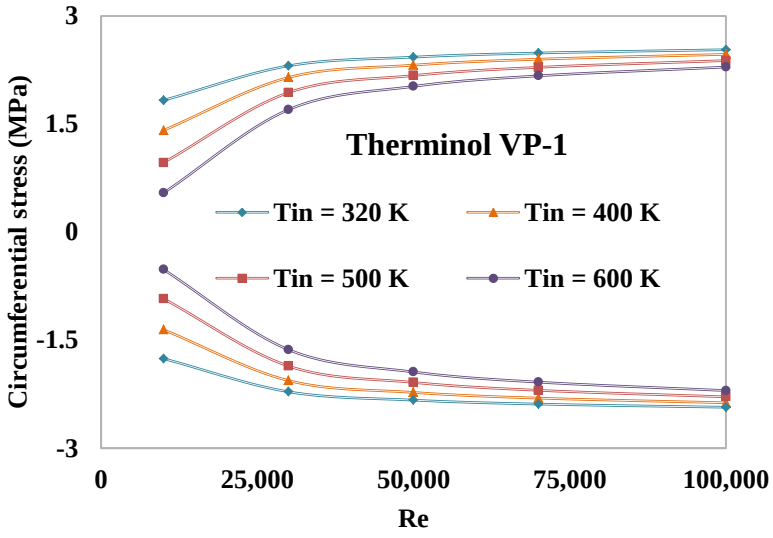

Figure 4.10: Thermal stresses distributions of all working fluids at different inlet fluid temperatures.

4.3.6. Velocity and Temperature Contours

Figure 4.11 depicts the velocity contours of the outlet wall of the solar receiver for all fluids at the smallest inlet temperatures (320 K for water and therminol VP-1 and 575 K for molten salt). The cases presented are for the smallest Re number i.e. 10,000. It is observed from this figure that there is no difference in the flow patterns in terms of velocity contours since all fluids generally behave similar due to the no slip wall boundary condition. However, the magnitude of velocity profiles is different due to a difference in the thermal behavior for each fluid as discussed previously. The non-uniform heat flux distribution on the external wall of the solar receiver is very obvious in the temperature contours of all the fluids as presented in Figure 4.12. It is very clear that the type of fluid could affect the temperature distribution even if they enter the PTC with the same inlet temperature and are subjected to the same heat flux boundary condition by the external walls. For instance, the temperature contour map of water is between 320 K (minimum) and 390 K (maximum) while the temperature contour distribution of Therminol® VP-1 is between 320 K (minimum) and 470 K (maximum). Furthermore, it is evident that the lower solid half of the solar absorber is exposed to larger-temperature variation compared to the upper half due to the non-uniform heat flux around the external wall of the solar receiver. For the fluid part, it is clear that the fluid temperature is very high close to the wall and reduces gradually away from the solid wall reaching minimum values at the top part of the receiver as depicted by the two recirculation regions generated for the water and therminol VP-1 cases.

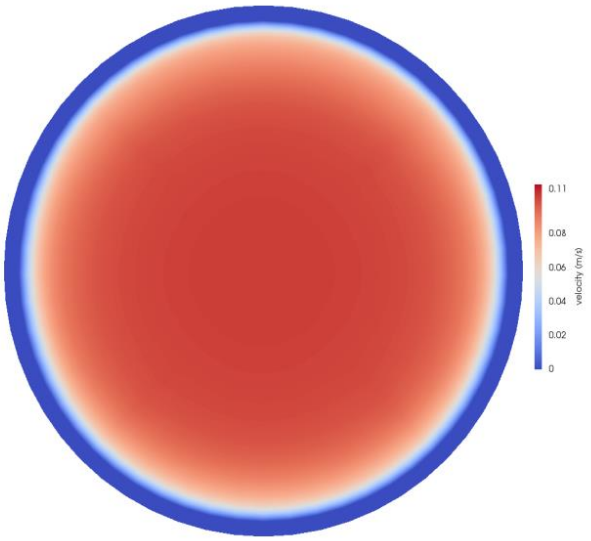

(a) Velocity-Water

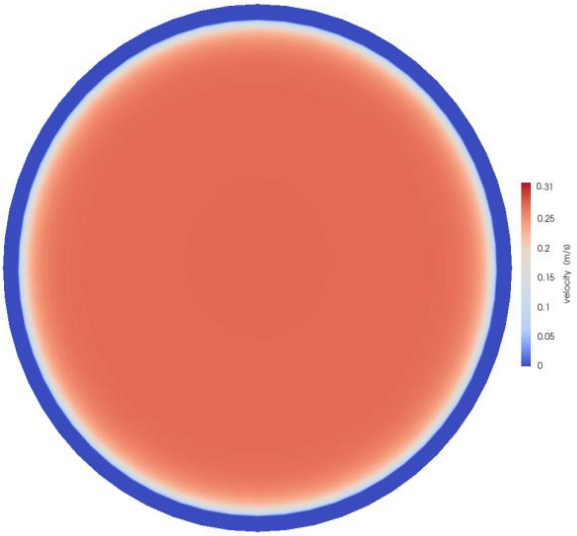

(b) Velocity-Molten salt

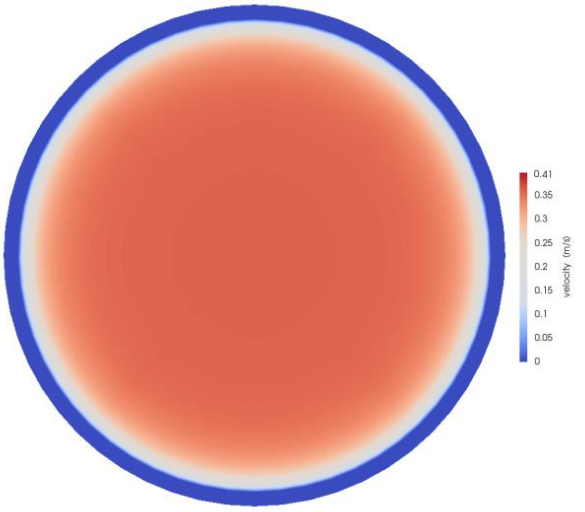

(**c**) Velocity-Therminol® VP-1

Figure 4.11: Velocity contours of all fluids at the smallest inlet temperatures.

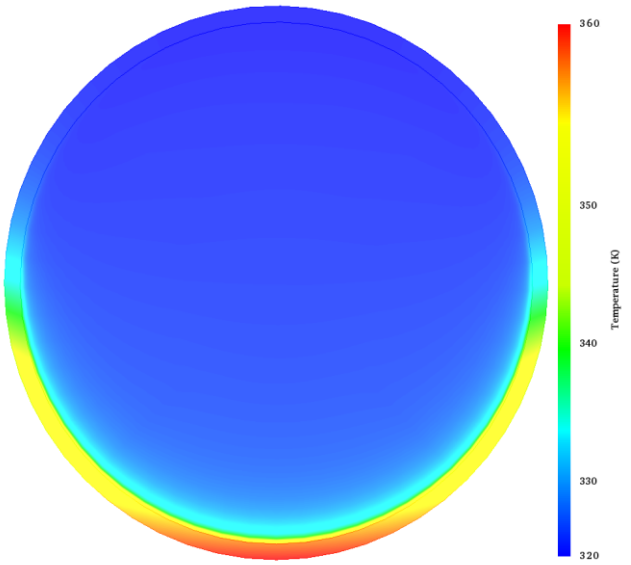

..(a) Temperature-Water

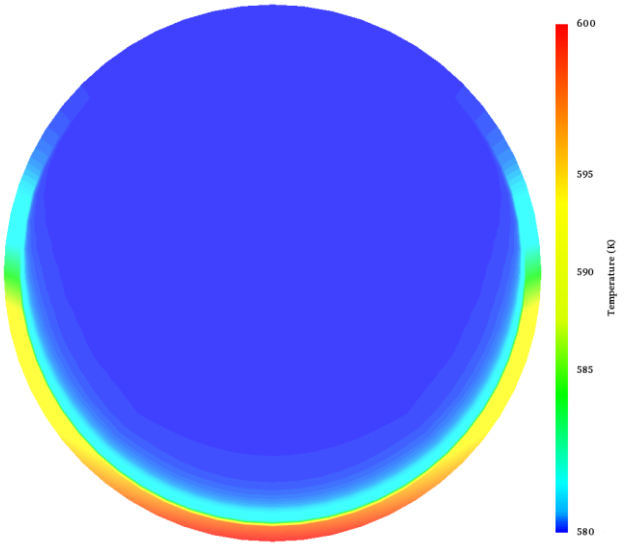

(b) Temperature-Molten salt

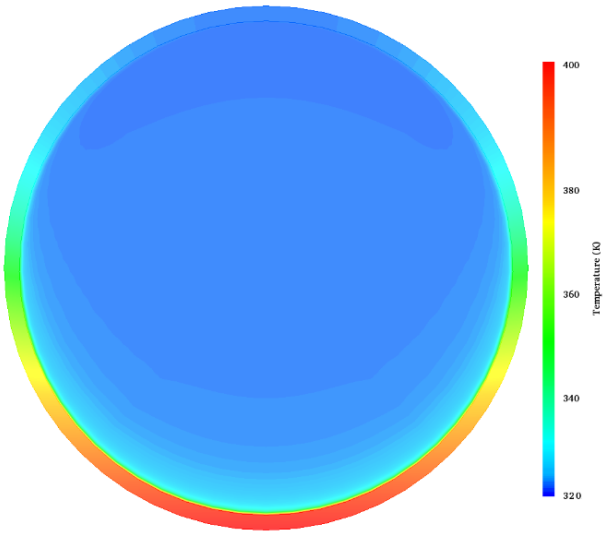

(c) Temperature-Therminol® VP-1

Figure 4.12: Temperature contours of all fluids at the smallest inlet temperatures.

4.3.7. Mean Temperature Profiles

The non-dimensional mean temperature, T^+ of all considered working fluids normalized by the friction temperature, T_τ is another parameter that can be used to study the effect of change in the working fluid on the thermal performance. This parameter can be calculated as, Davidson (2015):

$$T^+ = \frac{\langle T_w \rangle - T}{T_\tau}, \tag{4.11}$$

where, $\langle T_w \rangle$ represents the average internal wall temperature, T is the fluid temperature distribution from the wall to the absorber centre and T_τ represents the friction temperature which can be expressed as

$$T_\tau = \frac{q_w}{\rho C_p U_\tau}. \tag{4.12}$$

Here the variables q_w, ρ and $C_p$are the heat flux, the fluid density and the fluid specific heat capacity, respectively. In Equation (4.12), the parameter, U_τ represents the friction velocity which is a function of the wall shear stress and fluid density calculated as follows:

$$U_\tau = \sqrt{\tau_w / \rho}. \tag{4.13}$$

For the simulations, Y^+ is a function of the first cell height, y, friction velocity and kinematic fluid viscosity, ν and can be calculated from the following expression:

$$Y^+ = \frac{y U_\tau}{\nu}. \tag{4.14}$$

Figure 4.13 shows the mean temperature profiles close to the absorber outlet (at L = 3.8 m) under uniform heat flux for all considered working fluids at specific Re numbers (in this case Re = 10,000). It is observed from these profiles that an increase in the fluid inlet temperature leads to a gradual decrease in the mean temperature profiles inside the logarithmic region, away from the walls. This is accompanied by a gradual decrease in the heat conduction sub-layer close to the wall (at smaller Y^+ values). This is because an increase in the inlet fluid temperature leads to a gradual decrease in the effective Pr number. On the other hand, an increase in the Pr number means that the heat transfer process is favored to take place by the working fluids momentum rather than by its conductive properties. It can be observed from Figure 4.13 that when the inlet fluid temperature increases for Therminol® VP-1 from 320 K to 600 K, the rates of reduction in

the mean temperature profiles in the outer region of boundary layer (tube centre line) is 200%.

However, for the molten salt, this reduction is 84% as the inlet temperature increases from 575 K to 800 K and 170% for water for an inlet temperature increment from 320 K to 500 K. Table 4-6 shows the effective Pr numbers corresponding to each inlet temperature for all heat transfer fluids.

Table 4-6: Effective Pr number of all working fluids examined in the current chapter.

Working fluid	**Water**			
Inlet temperature (K)	320	400	500	-
Pr	3.77	1.34	0.86	-
Working fluid	**Therminol VP-1**			
Inlet temperature (K)	320	400	500	600
Pr	26.88	10.89	6.28	5.06
Working fluid	**Molten salt**			
Inlet temperature (K)	575	600	700	800
Pr	9.62	8.05	4.60	3.53

Keeping the Re number constant for each simulation leads to the representation of the heat transfer performance (Nu number) purely in terms of Pr number as Nu number can be represented in terms of Pr and Re numbers. In fact, the Pr number is effectively a scale of the fluid properties (dynamic viscosity, specific heat capacity and thermal conductivity) which describes the relative importance of the momentum boundary layer to the thermal boundary layer in the thermal energy transfer. Thus a low dynamic viscosity is desirable for a decrease in the friction factor and thereby pumping power. On the other hand, a large thermal conductivity is desirable to improve the heat transfer coefficient, Benoit et al. (2016). As illustrated in Table 4-6 the largest Pr number (26.88) corresponds to therminol VP-1 at the inlet temperature of 320 K. This high Pr number characteristic enhances the heat transfer performance and accordingly the overall thermal efficiency. Therefore, from an engineering point of view, the heat transfer fluid should be carefully selected by looking at the thermal properties especially the Pr number.

(a) Water

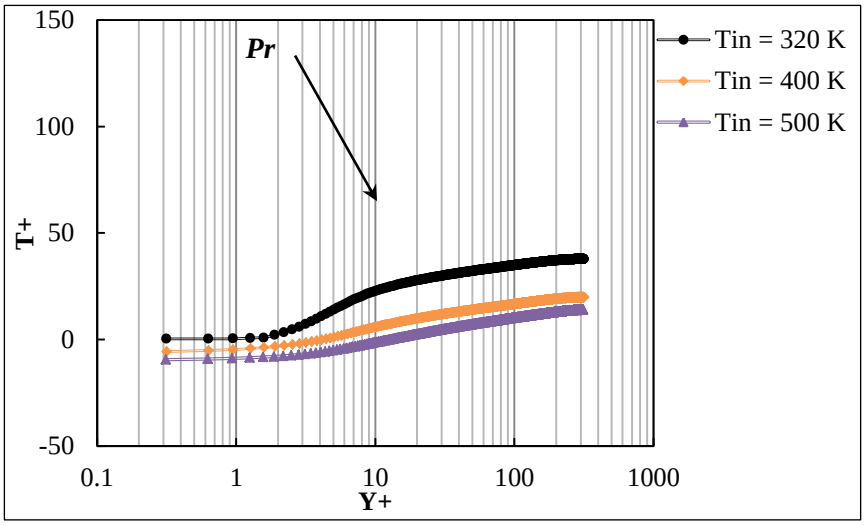

(b) Therminol® VP-1

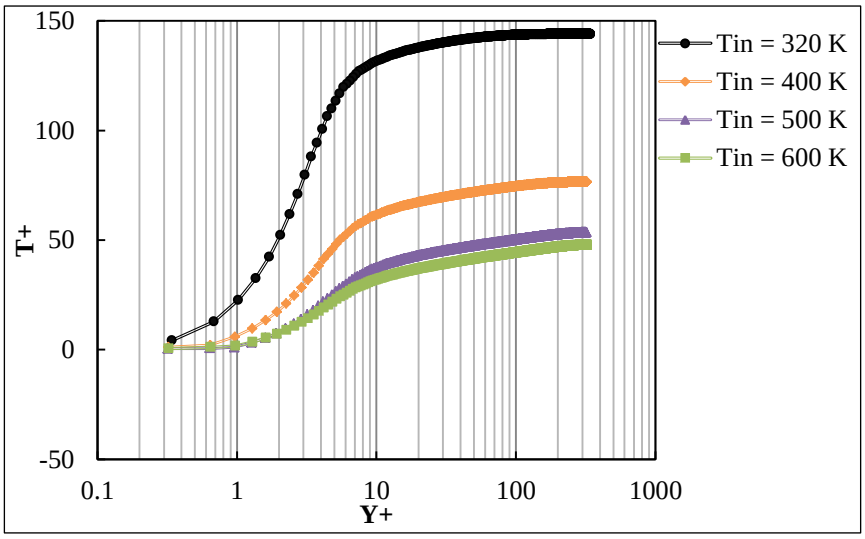

(c) Molten salt

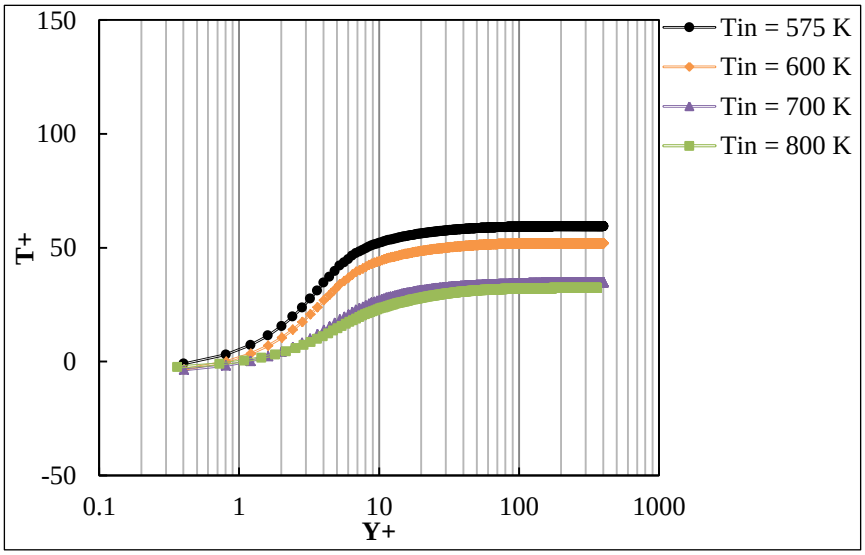

Figure 4.13: Temperature profiles of all working fluids used in the current study.

4.4. Conclusions

Thermal and hydraulic performances of the bare parabolic trough collectors were numerically investigated using three categorized-types of pure fluids; water, Therminol® VP-1 and molten salt. The thermal performance parametric comparison using different pure fluids was also conducted considering the effect of various inlet temperatures and different Re numbers. For the validation of two low-Reynold's turbulence models (Launder and Sharma (LS) k-epsilon and k-omega SST) were used taking into account different parameters; the overall thermal efficiency, the output fluid temperature, average Nu number and average friction factor.

The validations showed that the k-omega SST model performed better when compared to both the experimental data and correlations. In order to assess the performance of each fluid, a number of parameters were investigated such as; average Nu number, specific pressure drop distributions, thermal losses, thermal stresses in the circumferential direction of the absorber tube and overall thermal efficiency of the PTC. Results illustrated that for a temperature-range of (320–500) K, the Therminol® VP-1 performed better than water and provided larger Nu numbers, lower thermal stresses and higher thermal efficiency. However, for the common temperature-range between Therminol® VP-1 and molten salt, both preformed more or less the same with lower thermal stresses in the case of Therminol® VP-1. On the other hand, the molten salt was found to be the best choice for high operating temperatures (up to 873 K) since there was no significant reduction in the overall thermal efficiency at these high temperatures. Finally, the importance of results obtained in the current study illustrate comprehensively that the heat transfer behavior of the working fluid strongly depends upon the Prandtl number.

Chapter 5: Thermal performance evaluation of various nanofluids for PTCs

5.1. Introduction

In the recent past, a number of investigations have assessed the use of different technologies on the thermal performance of the heat transfer fluid (HTF) in PTC systems mainly focusing on water and thermal oils. The main objective so far has been to enhance the heat transfer from the solar receiver to the HTF, whilst at the same time decreasing the inner and outer absorber temperatures. By doing so, the overall thermal losses reduce, thereby increasing the overall collector efficiency. Furthermore, the reduction in the absorber temperature helps in alleviating the receiver deformation problems by decreasing the effective thermal stresses as reported by Fuqiang et al. (2017). Nanofluids are composed of a mixture of very tiny particles possessing thermal properties different to those of the base working fluid. Such a mixture generally acts as a thermally more efficient working fluid with a higher Prandtl number. Nanofluids thus improve the thermal conductivity, increase the dynamic viscosity and lower the specific heat capacity leading to an overall improvement of the resulting fluid performance compared to pure working fluid. There is a considerable scope for further research in nanofluid technology to extend its use in industrial and engineering applications.

The nanofluid technology is also applicable in PTC systems, in which Zadeh et al. (2015) reported that using 5% volume fraction (VF) of Al_2O_3-Synthetic oil enhanced the heat transfer by 11.5% for a single-phase and 36% for two-phase models. Mwesigye et al. (2015a) reported that using 8% VF of Al_2O_3-Syltherm 800 improved the overall collector efficiency by 7.6%. However, using the same nanofluid but with 2% VF, Bellos et al. (2016) observed an increase of only 4.25% thermal efficiency. On the other hand, Kaloudis et al. (2016) observed a 10% improvement in thermal efficiency by using 4% VF of Al_2O_3-Syltherm 800 nanofluid with a two-phase model and a uniform wall temperature over the solar receiver. Thus, nanofluids when added in small VFs help in improving the thermal efficiency but at the cost of greatly increasing the pumping power requirement; Ferraro et al. (2016), showed that by using 5% VF of Al_2O_3-Synthetic oil, the effect of nanofluids was very small compared to the increase in the pumping power requirement. Similarly, Toghyani et al. (2016), showed that by using 5.5% VF of CuO, SiO_2, TiO_2 and Al_2O_3 mixed with Therminol 55 led to improvements in the overall exergy efficiency by 3, 6, 9 and 11% respectively. Mwesigye et al. (2016) showed up to 32% improvement in the heat

transfer coefficient and 20-30% decrease in the entropy generation using 6% VF of Cu-TherminolVP-1. Later, Bellos and Tzivanidis (2017) found that using 4% VF of Al_2O_3 and CuO dispersed in Syltherm 800 resulted in an improvement of thermal efficiency by 1.13 and 1.26% respectively. Another set of nanoparticles called Al_2O_3, Ag and Cu, dispersed in TherminolVP-1, led to the enhancement of the overall thermal efficiency by about 13.9% as reported by Mwesigye and Meyer (2017). However, Alashkar and Gadalla (2018) reported that Ag dispersed in TherminolVP-1 provided better thermal performance than Cu. In the same year using Syltherm 800, Allouhi et al. (2018) recorded an enhancement of the thermal energy by 1.46, 1.25 and 1.4% using 5% VF of Al_2O_3, CuO and TiO_2 respectively. The authors also reported a maximum exergy efficiency increase of 9.05%, for 3% VF of CuO. Bellos et al. (2018a), on the other hand, used only 6% VF CuO with Syltherm800 and Molten salt. They reported a 13% increase in the Nusselt number with CuO-molten salt and 40% with CuO-Syltherm 800. Mwesigye et al. (2018) examined new types of nanoparticles called single-walled carbon nanotubes (SWCNT) dispersed in TherminolVP-1. Their results showed that 2.5% VF of SWCNT improved the thermal efficiency by 4.4%. Kasaiean et al. (2018) also examined a nanoparticle from the same family of carbon nanotubes called multi-walled carbon nanotube (MWCNT) mixed with Ethylene glycol and reported a heat transfer enhancement of 15% using 6% MWCNT. Peng et al. (2020) tested Cu and CNT dispersed in Gallium (Ga) with different VFs of the nanoparticles. Their results showed a 34.5% augmentation in the heat transfer coefficient using Cu-Ga and 45.2% using CNT-Ga. Korres et al. (2019) also reported similar findings that the thermal and exergy efficiencies increased by 2.76 and 2.6% respectively by using 5% VF of CuO-Syltherm 800.

Malekan et al. (2019) reported that 4% VF of Fe_3O_4-Therminol 66 in the presence of a magnetic field enhanced the thermal efficiency by 4%. Using porous materials in annular space and 3% VF of Al_2O_3 with Synthetic oil, Bozorg et al. (2020) observed a 20% enhancement in heat transfer coefficient and 14% in thermal efficiency. This enhancement resulted from a decrease in the absorber wall temperature which consequently led to the reduction of the radiation heat losses. Heyhat et al. (2020) studied the effect of CuO-water nanofluid combined with a metal foam inside the solar receiver. They deduced that by changing the volumetric flow rate from 20 to 100 Lph (liter per hour), the thermal efficiency was increased from 55.65 to 79.29%, when using 0.1% VF of CuO-water and metal foam. Bellos et al. (2020) examined the effect of 4% VF of Cu-Syltherm 800 nanofluid on three different solar collector types; vacuumed-annular tube receiver, air-annular tube receiver and the bare receiver (without glass cover). They concluded that from

a thermal efficiency enhancement perspective the bare tube receiver configuration was the best candidate.

The aforementioned literature clearly shows that most of the numerical studies in the past have focused on utilizing thermal oils, whereas only a few studies exist for water and molten salts as the base working fluid. The literature clearly shows the thermal, hydraulic and thermodynamic performances including thermal efficiency, heat transfer coefficient, pressure drop, entropy generation and performance evaluation criterion compared to the base fluids. Most of these studies, however, have only considered one base working fluid and varied either the nanoparticles or just their concentration to test their effects. The current chapter thus differs from all these previous ones as it investigates the effect of various nanoparticles with different base-fluids (water, thermal oil and molten salts), which is still not fully covered in the literature. In the present chapter six non-metallic nanoparticles namely aluminum oxide (Al_2O_3), cerium oxide (CeO_2), copper oxide (CuO), ferric oxide (Fe_2O_3), titanium oxide (TiO_2) and silicon oxide (SiO_2) are examined by dispersing them individually in three different base fluids; therminol VP-1 (at 400 K), water (at 400 K) and molten salt (at 600 K). The choice of two different working temperatures 400 K (for therminol VP-1 and water) and 600 K for molten salt is based on the broader spectrum of the operating conditions of the wide range of PTC applications. It is typically suggested that the inlet temperature of working fluid in most of the PTC applications is approximately 400 K. However, some PTC applications require higher inlet fluid temperature for the parabolic trough collectors. For such systems the working fluid temperature is generally set at around 600 K.

In this chapter, the nanoparticles concentration ratio was varied from 2 to 6% by VF for each nanofluid. Each configuration was then tested for a range of Re numbers, 10000, 30000, 50000, 70000, and 100000. All cases were assumed to be steady state, fully three-dimensional and incompressible. The main goal here is to produce a parametric comparison between the hydraulic and thermal performances amongst the examined nanofluids, thereby determining the optimum operational conditions for every HTF under realistic heat flux boundary conditions (i.e. non-uniform circumferential heat distribution around the absorber receiver's external surface). Such assessment of the performance of six different nanoparticles dispersed in three different base fluids with the non-uniform heat flux distributions has not been reported anywhere in the literature.

5.2. Thermal properties of the working nanofluids

The first step of the nanofluids investigation is to calculate the thermal properties of the examined nanofluids for the single-phase approach which has been employed in this study. This is achieved by using information from the existing literature and the introduction of some assumptions. The nanofluid density (ρ_{nf}) is calculated depending on the classical form of the heterogeneous mixture proposed by Pak and Cho (1998). Whereas, the specific heat capacity ($C_{p,nf}$) is derived from the thermal equilibrium between the solid particles and its surrounding base fluid as proposed by Xuan and Wilfried (2000). Nevertheless, several models are in use for determining the nanofluid viscosity and thermal conductivity. The model proposed by Maiga et al. (2005) is used for the dynamic viscosity (μ_{nf}) which is based on the experimental data of Wang et al. (1999) where they measured the viscosity of Al_2O_3-water. For the thermal conductivity (k_{nf}) the model proposed by Bruggeman (1935) has been employed in the current study. This model has no limitations on the VF and is based on the homogenous spherical solid-fluid mixture. The aforementioned models are presented below.

$$\rho_{nf} = \rho_s\varphi + \rho_f(1-\varphi). \tag{5.1}$$

$$C_{p,nf} = \frac{1}{\rho_{nf}}\left[\rho_s C_{p,s}\varphi + C_{p,f}\rho_f(1-\varphi)\right]. \tag{5.2}$$

$$\mu_{nf} = \mu_f(1 + 7.3\varphi + 123\varphi^2). \tag{5.3}$$

$$k_{nf} = 0.25[(3\varphi-1)k_s + (2-3\varphi)k_f + \sqrt{\Delta}], \tag{5.4}$$

where: $$\Delta = [(3\varphi-1)k_s + (2-3\varphi)k_f]^2 + 8k_s k_f.$$

Here the volume fraction (φ) represents the ratio of solid particle volume (V_s), divided by the total volume, $V_s + V_f$ as, Michaelides (2016)

$$\varphi = \frac{V_s}{V_s + V_f}. \tag{5.5}$$

In the models above, the subscript, nf represents nanofluids, s refers to the nanoparticle and f refers to the base fluid. Thermal properties of all examined nanoparticles and base fluids are listed in Table 5-1 and Table 5-2 respectively.

Table 5-1: Thermal properties of particles examined in the current chapter.

Type	**ρ (kg/m3)**	**C_p (J/kg.k)**	**k_s (w/m.k)**	**Reference**
Al_2O_3	3970	940	32.4	Mwesigye and Meyer (2017)
CuO	6320	532	77	Turkyilmazoglu et al. (2017)
TiO_2	4230	692	8.4	Allouhi et al. (2018)
Fe_2O_3	5180	670	6.9	Bellos and Tzivanidis (2019)
SiO_2	2200	765	1.4	Abed et al. (2020b)
CeO_2	6757	392.48	5.86	Nelson et al. (2014)

Table 5-2: Thermal properties of base fluids examined in the current chapter.

Fluid	**T** (K)	**μ** (Pa.s)	**ρ** (kg/m^3)	**C_p** (J/kg.k)	**k_f** (w/m.k)	**Pr**	**Reference**
Water	400	0.000217	937.21	4256	0.688	1.34	Incropera et al. (2006)
Therminol VP-1	400	0.000732	975.8	1850.5	0.1243	10.89	Mwesigye et al. (2016a)
Molten salt	600	0.002713	1882.1	1499.2	0.5051	8.05	Pacheco et al. (1995)

5.3. Numerical model validation

In addition to the previous validation steps, the subsequent step was to validate two types of nanofluids with different VFs, both with $k-\omega$ SST model. The experimental data used for the comparisons were taken from Pak and Cho (1998), where the authors examined the effects of nanofluids in a circular duct with a uniform heat flux distribution using water as a base fluid at 300 K inlet temperature. The nanofluid used for the experiments was γ-Al_2O_3-water with VFs of 1.34 and 2.78% (see Figure 5.1a). The friction factor for the numerical simulations was also validated using TiO_2-water nanofluid at 2% VF with experiments of Subramani et al. (2018b), see Figure 5.1b. Based on the findings of all the validation cases, it was concluded that the $k-\omega$ SST model suffices as the turbulence model and that all the adopted numerical procedures are adequate for the modelling requirements of the current cases.

(a)

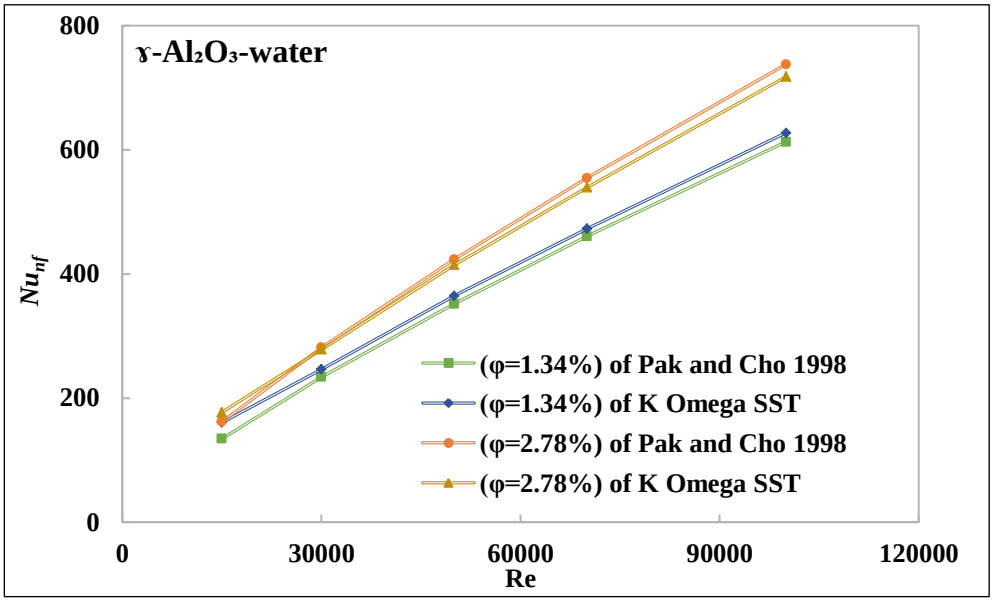

(b)

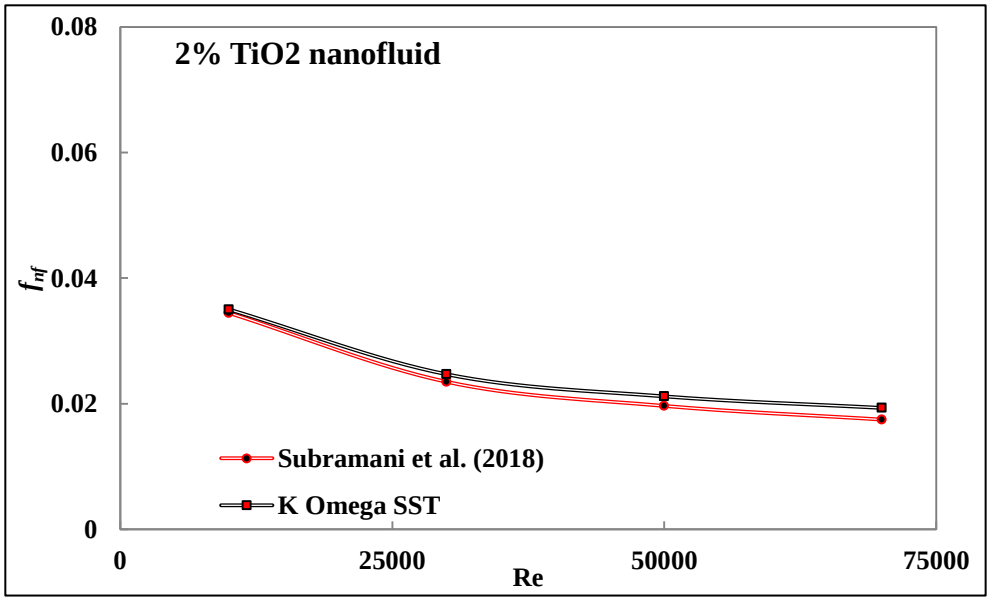

Figure 5.1: Validation the present model with experimental data of nanofluids (a) Nu number of Pak and Cho (1998) and (b) friction factor of Subramani et al. (2018b).

5.4. Results and Discussions

This section presents the thermal performance and flow characteristics of considered nanofluids such as heat transfer performance, pressure drop, performance evaluation criterion, thermal losses, overall collector efficiency and mean temperature profiles respectively.

5.4.1. Heat Transfer Performance

The addition of nanoparticles to a base working fluid changes the thermal properties of the resulting nanofluid, consequently enhancing the convective heat transfer performance. Figure 5.2 illustrates the profiles of the Nu number on the solar receiver as a function of Re number for different nanofluids and their varying VFs. It is clearly seen that by increasing the VF ratio of the nanoparticles, a heat transfer enhancement is achieved; in line with the main findings of previous investigations (Mwesigye et al. (2016) and Subramani et al. (2018b)). The Nu number continues to increase with increasing VFs since more thermal energy is transferred from the solar receiver to the working nanofluid, which leads to an increase in the useful thermal energy. It is further noted from these figures that the introduction of all the working nanofluids results in a similar thermal trend. The highest Nu numbers, however, were achieved with the therminol VP-1 base fluid. It is prudent to mention here that higher Pr numbers were obtained for all the examined nanofluids compared with base fluids as the tested nanoparticles had a lower specific heat capacity, a larger dynamic viscosity and a higher thermal conductivity than the base fluid.

It is observed from Figure 5.2 that even though the use of therminol VP-1 results in the highest Nu numbers, in terms of relative improvement clearly water is the better choice. This is expected as water has a significantly higher thermal conductivity; 1.36 and 5.5 times higher than molten salt and therminol VP-1 respectively. It is also noted here that in terms of the performance CeO_2 nanoparticles were always the least effective whereas SiO_2 nanoparticles produced the strongest thermal enhancement regardless of the choice of the base fluid. The relative effects of the nanoparticles tested were found to be the same for most of the base fluids, the only exception being the therminol VP-1 base fluid, where TiO_2 was found to be less effective than Fe_2O_3 and Al_2O_3 (see Table 5-3 for detailed comparisons). Due to the fact that water has the lowest Pr number, the Nu number for water based nanofluids had the lowest values. Nevertheless, given that Nu≡h.D/k, a lower value for Nu, does not necessarily mean a lower value for the heat flux coefficient h.

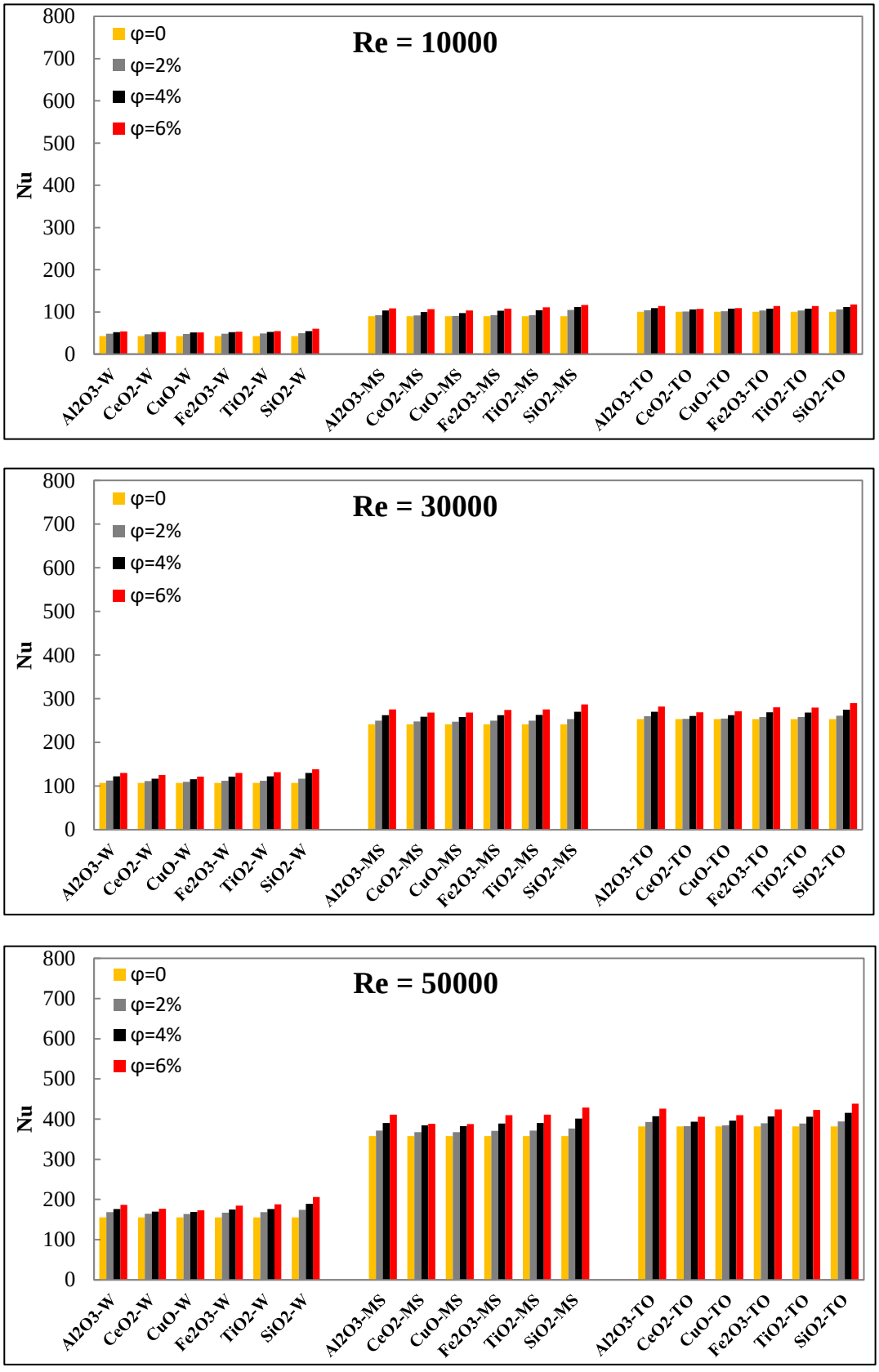

Figure 5.2: Heat transfer performance of all nanoparticles at different *Re* numbers for base fluids of water (W), molten salt (MS) and therminol VP-1 (TO).

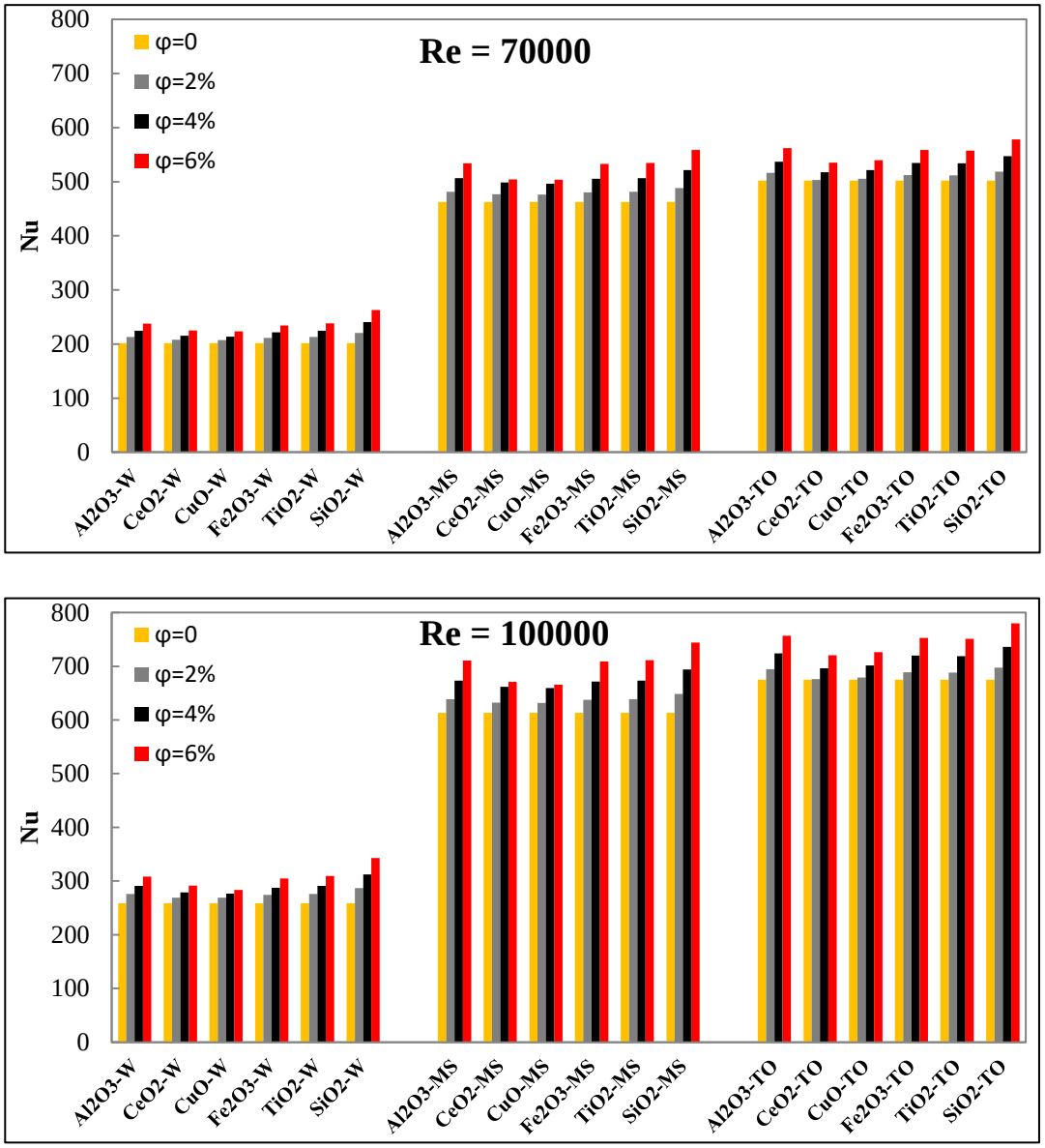

Figure 5.2: Heat transfer performance of all nanoparticles for all base fluids (continued).

Table 5-3: Relative thermal performance improvement (%) with 6% volume fraction and Re =100000.

Nanoparticle / Base fluid	CeO_2	CuO	Fe_2O_3	Al_2O_3	TiO_2	SiO_2
Water	12.72	15.74	17.67	19.15	19.64	32.4
Therminol VP-1	6.75	7.62	11.53	12.2	11.3	15.57
Molten salt	9.4	12.6	15.6	15.93	16.03	21.36

It is prudent to note here that the effective Pr number of resulting nanofluids has a vital role on the thermal performance or Nu number. Since the inclusion of nanoparticles increases the Pr number of the nanofluid, it will also increase the Nu values. For the nanoparticles under consideration, the resulting nanofluids from SiO_2 with all base fluids produces larger Pr numbers at all VFs which in turn enhance the Nu number more than any other nanofluid, see Table 5-4 for more details. It is argued that the SiO_2 nanoparticle has the smallest thermal conductivity but with a moderate specific heat capacity compared to all other tested nanoparticles (as shown in Table 5-1). This result in much larger Pr numbers compared to the other nanoparticles regardless of the choice of the base working fluid. On the other hand, both molten salt and Therminol VP-1 have higher boiling point temperatures than water and hence show larger average values of the Nu number.

Table 5-4: Pr numbers of all nanofluids examined in the current study at 6 % of volume fraction.

Nanoparticle / **Base fluid**	**Al_2O_3**	**CeO_2**	**CuO**	**Fe_2O_3**	**TiO_2**	**SiO_2**
Water	1.753	1.536	1.575	1.71	1.766	2.153
Therminol VP-1	15.14	12.94	13.32	14.27	14.68	16.40
Molten salt	12.00	11.07	11.27	11.915	12.03	13.68

Based on the achieved results of considered nanofluids, three Nu number correlations are proposed in Table 5-5.

Table 5-5: Nu number correlations for all nanofluids examined in the current study.

Base fluid	**nanoparticles**	**Nu correlations**	**Limitations**
Water	Al_2O_3, CeO_2, CuO, Fe_2O_3, TiO_2 and SiO_2	$Nu = 0.0267\ Re^{0.8}\ Pr^{0.42}\ \varphi^{0.02}$	$10^4 \leq Re \leq 10^5$ $1.3 \leq Pr \leq 2.2$ $0.02 \leq \varphi \leq 0.06$
Molten salt	Al_2O_3, CeO_2, CuO, Fe_2O_3, TiO_2 and SiO_2	$Nu = 0.0255\ Re^{0.8}\ Pr^{0.44}\ \varphi^{0.02}$	$10^4 \leq Re \leq 10^5$ $8.0 \leq Pr \leq 14$ $0.02 \leq \varphi \leq 0.06$
Therminol VP-1	Al_2O_3, CeO_2, CuO, Fe_2O_3, TiO_2 and SiO_2	$Nu = 0.0215\ Re^{0.8}\ Pr^{0.49}\ \varphi^{0.02}$	$10^4 \leq Re \leq 10^5$ $11 \leq Pr \leq 17$ $0.02 \leq \varphi \leq 0.06$

5.4.2. Receiver hydraulic performance

Figure 5.3 shows the effect of varying VFs of various nanoparticles on the specific pressure drop (Pa/m) as a function of Re number. The process of adding nanoparticles to the base fluids does not only affect the fluid thermal conductivity but also increases the resulting fluid density and dynamic viscosity. This in turn leads to a reduction of hydraulic performance; due to friction, the pressure drop increases and so does the pumping power requirement with the addition of nanoparticles. Figure 5.3 shows that the specific pressure drop inside the solar receiver increases with increasing VF of the nanoparticles which is in line with the previous literature (Peng et al. (2020) and Bozorg et al. (2020)). However, the hydraulic behavior of nanofluids is relatively different from each other and is also dependent on the density and viscosity of the base working fluid. For example from Table 5-6, we can see that the largest pressure drop is with SiO_2 nanoparticles and the lowest drop is with CeO_2 regardless of the base working fluid. In general, the specific pressure drop is higher when the base working fluid is molten salt regardless of the nanoparticle. Overall, one can conclude that the specific pressure drop is dependent upon both the density and viscosity of the base working fluid and the VF of the nanoparticles.

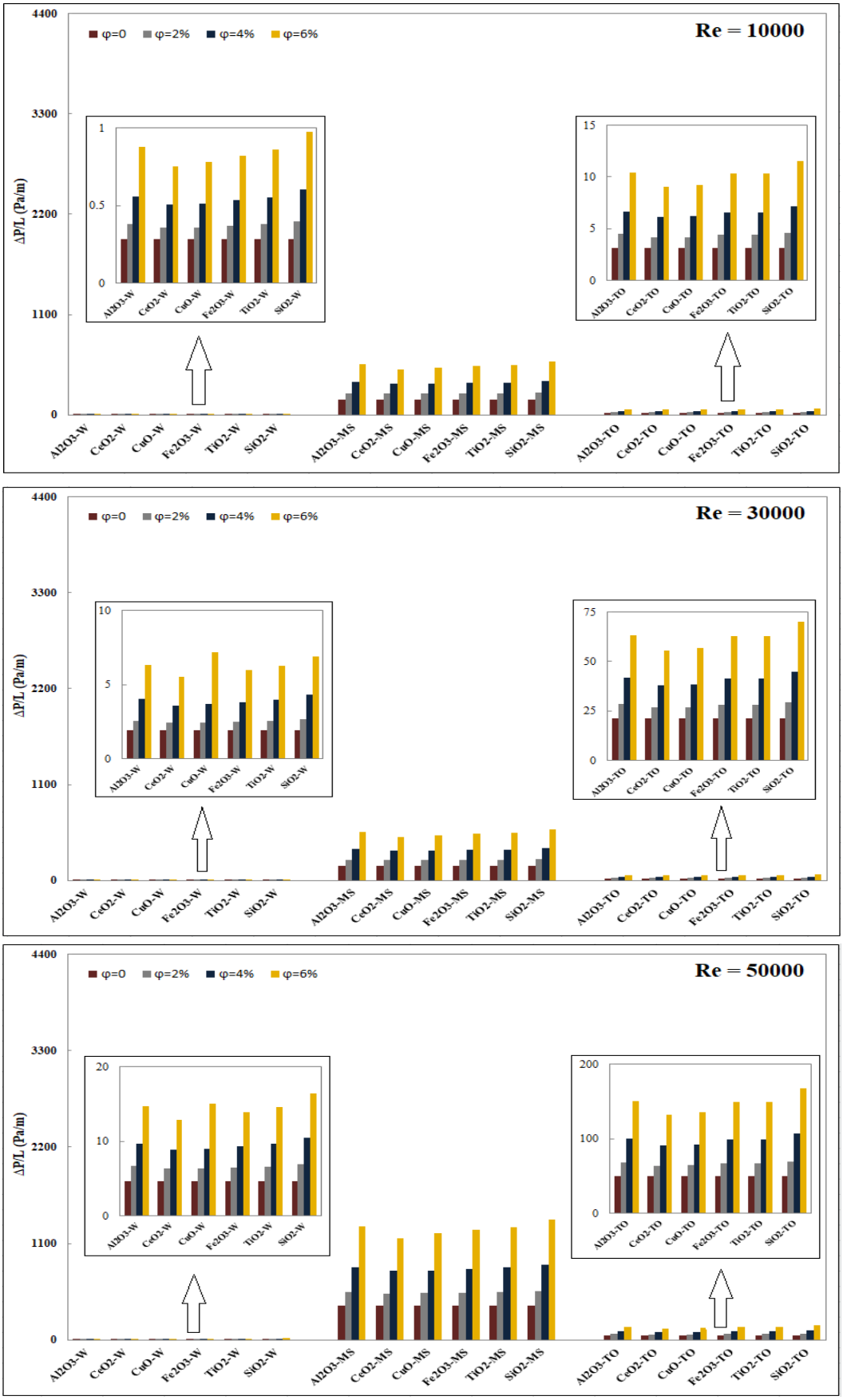

Figure 5.3: Specific pressure drop of all nanofluids at different *Re* numbers for all base fluids.

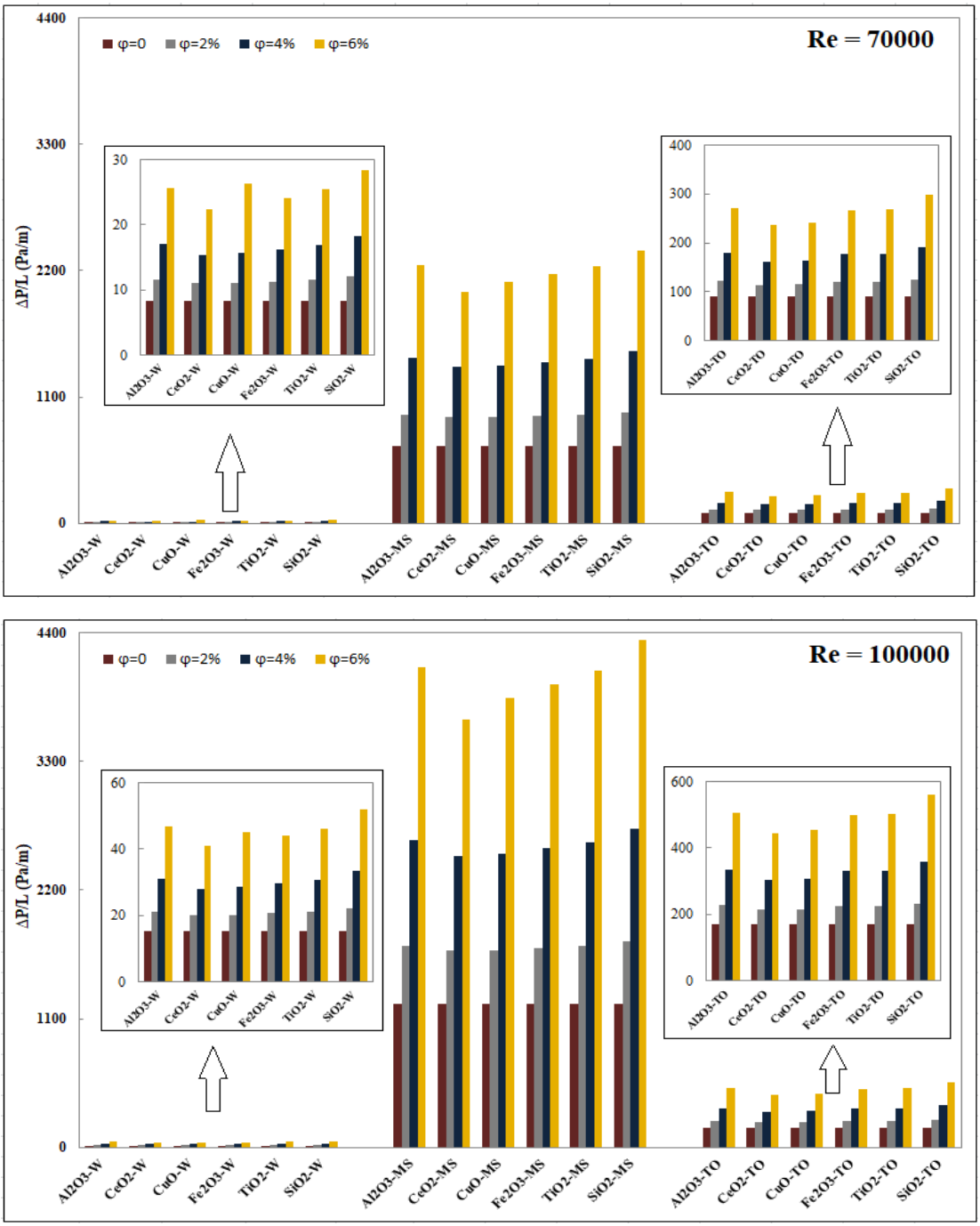

Figure 5.3: Specific pressure drop of all nanofluids at different *Re* numbers for all base fluids (continued).

Table 5-6: Specific Pressure drop increase (%) with 6% volume fraction and Re =100000.

Nanoparticle / Base fluid	CeO_2	CuO	Fe_2O_3	Al_2O_3	TiO_2	SiO_2
Water	163.8	191.2	186	203	199	230
Therminol VP-1	163	168.5	196	200	197	231.18
Molten salt	197	212	222	233.5	231.5	252.7

Furthermore, a high concentration ratio of nanoparticles could lead to particle agglomerating inside the absorber tube resulting in higher friction and greater pumping power requirements. Therefore, the VF should be optimized and selected to provide an effective heat transfer performance with a reasonably acceptable pressure drop.

5.4.3. Performance Evaluation Criterion

Another parameter that can be used to assess the thermal and frictional effects of any active or passive new technology (such as nanofluids, swirl generators etc.) which is the performance evaluation criterion (PEC) given by Ralph (1993). This PEC represents the ratio of heat transfer enhancement and pumping power requirement as a function of the relative friction factors as shown below

$$PEC = \frac{\left(\frac{Nu}{Nu_o}\right)}{\left(\frac{f}{f_o}\right)^{1/3}}. \quad (5.6)$$

Where Nu and f represent the Nusselt number and friction factor of the nanofluids respectively. Whereas Nu_o and f_o represent the Nusselt number and friction factor of the base working fluid without nanoparticles. All Nu, Nu_0, f and f_0 are based on the same Re number. Any value of the PEC over 1 means there are some thermal and hydraulic increase in the flow. Figure 5.4 summarizes the PEC values for all examined nanofluids with 6% VF, at a Re of 100000. It shows a PEC value of over 1 with the highest value of 1.313 being that of SiO_2 mixed with water as the base working fluid. However, the PEC is reduced to 1.21 for therminol VP-1 and finally to 1.155 for using molten salt. Furthermore, the nanoparticles of CeO_2 and CuO, show the lowest PEC values for all the base working fluids.

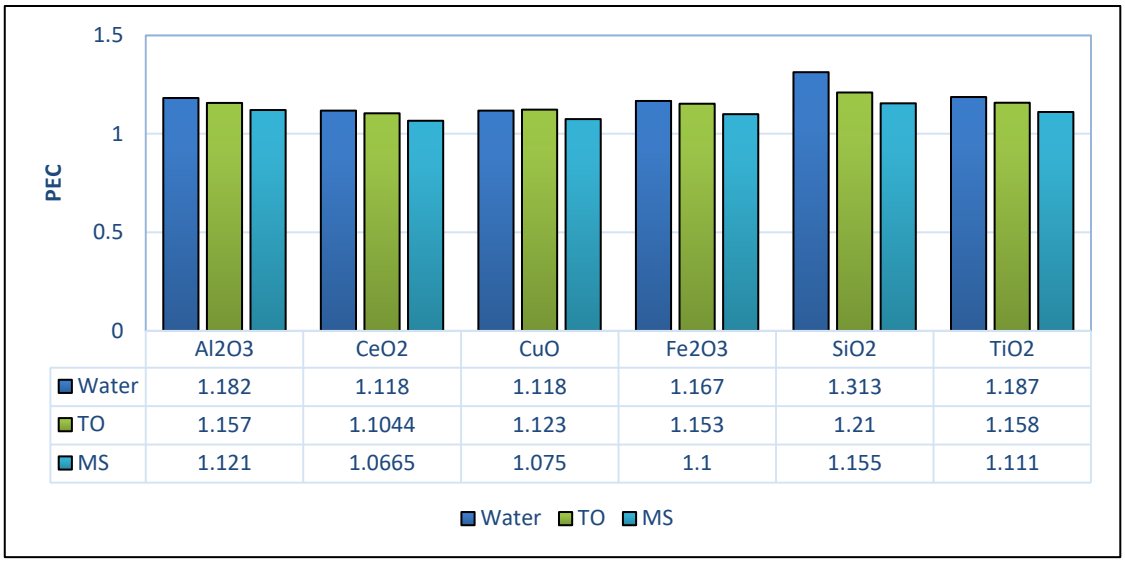

	Al2O3	CeO2	CuO	Fe2O3	SiO2	TiO2
Water	1.182	1.118	1.118	1.167	1.313	1.187
TO	1.157	1.1044	1.123	1.153	1.21	1.158
MS	1.121	1.0665	1.075	1.1	1.155	1.111

Figure 5.4: Performance evaluation criterion of all examined nanofluids, TO: Therminol VP-1 and MS: molten salt.

5.4.4. Thermal losses

One of the most important purposes of using nanofluids is to reduce the external surface temperature of the solar receiver, which greatly minimizes both the modes of thermal losses; convection and radiation. This is because the changes in fluid properties which result from the introduction of nanoparticles, lead to higher values of the extracted convective heat transfer coefficient since more energy was absorbed which in turn lead to effectively increase the Nu numbers as presented in Figure 5.2. Thus, using the nanofluid technology is able to further reduce the receiver temperature and attenuate any circumferential variations. A smaller collector temperature leads to lower thermal losses and higher efficiencies.

The examined non-metallic nanofluids were also compared to assess their effect on thermal losses against Re number for water, therminol VP-1 and molten salts as shown in Figure 5.5. It can be noted from this figure that the nanofluid cases show lower thermal losses compared to their respective base fluid cases. In fact, the greater the concentration of the nanoparticles, the lower the loss. The obvious reason behind this is the outer surface smaller temperature which is achieved via the use of the nanoparticles. Thus, one can conclude that the thermal gradient is the key in reducing the losses.

Indeed, this inference is further substantiated when one observes the behavior of the thermal loss profiles of any of the tested cases; at higher Re numbers, due to higher levels of turbulence, more mixing takes place which leads to higher levels of thermal uniformity and hence reduction of losses. This behavior is evident in the Figure 5.5.

One should also note here, that there are variations in the thermal capability of each type of nanofluids and that the same nanoparticles have also different levels of enhancement when mixed with different base working fluids. It is observed from Figure 5.5 that the maximum reduction in the thermal losses was recorded for therminol VP-1 followed by water and molten salts, respectively.

At the lowest Re number (Re =10000) when the VF was increased from 0 to 6% the reductions in the specific thermal losses were 9.8, 10.7, 11.65, 11.65, 11.9, and 12% for CeO_2-TO, CuO-TO, Fe_2O_3-TO, TiO_2-TO, Al_2O_3-TO, and SiO_2-TO respectively. Moreover, the levels of reduction in thermal losses from the same nanoparticles change when these are used with another base working fluid. For molten salts (MS) with the increasing VF (0 to 6%), the specific thermal loss reductions were 1.125, 1.26, 1.35, 1.46, 1.38, and 1.53% respectively for CeO_2-MS, CuO-MS, Fe_2O_3-MS, Al_2O_3-MS, TiO_2-MS and SiO_2-MS. Finally, similar trends were observed when water was used as the base working fluid.

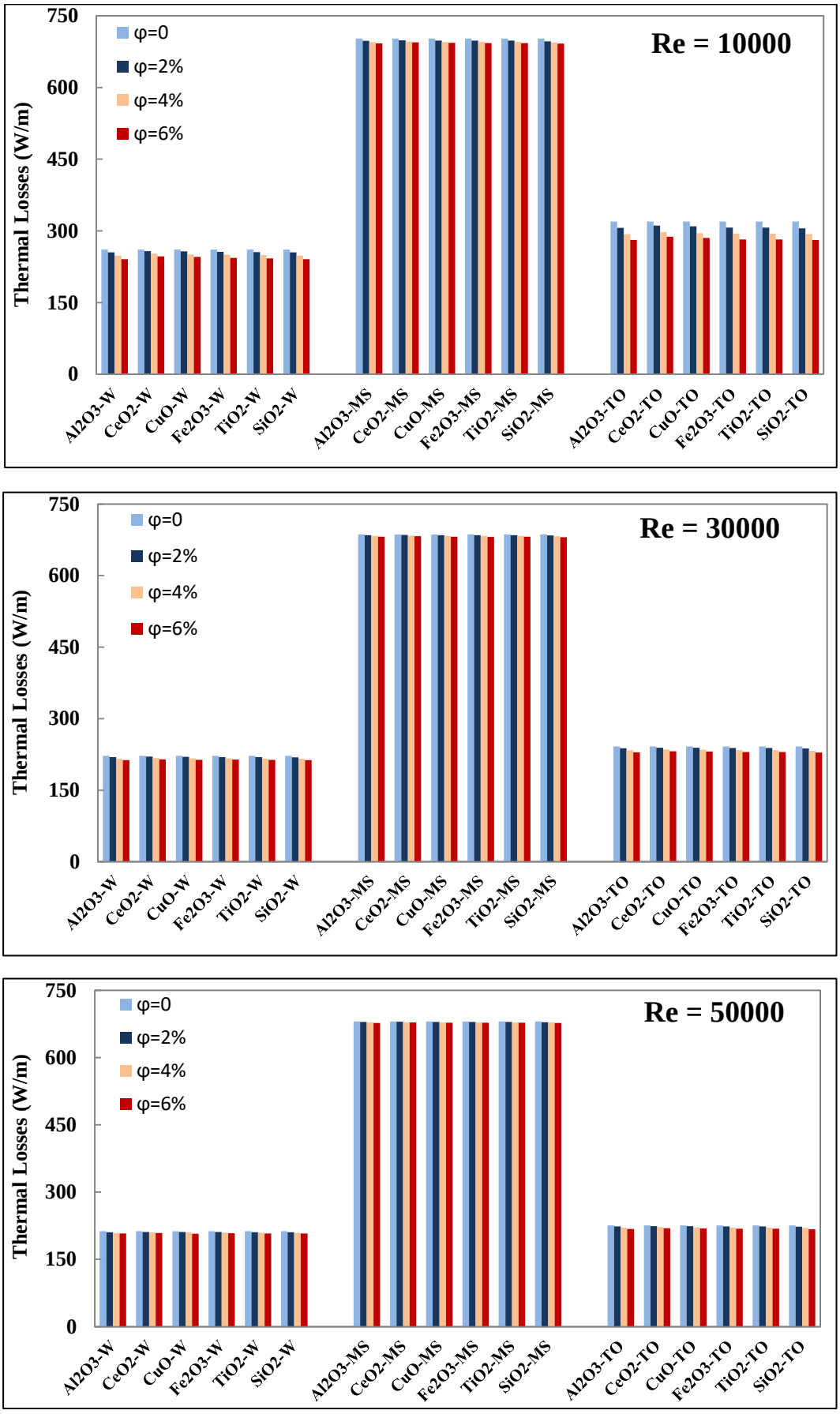

Figure 5.5: Effect of nanofluids on thermal losses with water (W), molten salt (MS) and therminol (TO) base fluids at different Reynolds (Re) numbers.

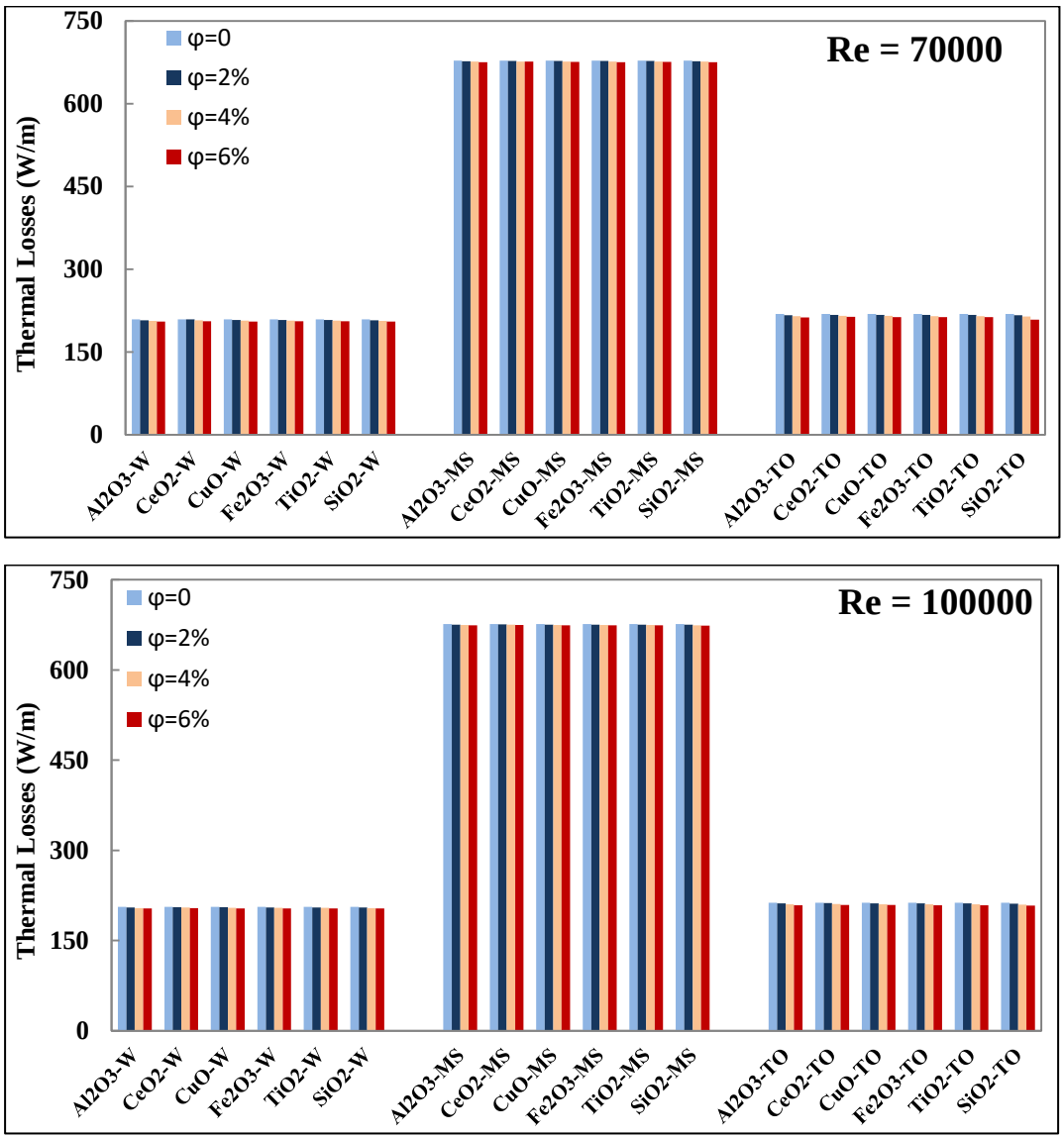

Figure 5.5: Effect of nanofluids on thermal losses for all base fluids (continued).

5.4.5. Overall Collector Efficiency

The overall efficiency of the PTC using all respective nanofluids is assessed by taking the influence of pumping power requirements into account, as indicted in the introduction section. Figure 5.6 and Figure 5.7 present the variation of the overall collector efficiency due to the effect of loading various particle VFs and also different Re numbers for therminol VP-1 (TO) and molten salt (MS). The overall efficiency increases with nanoparticles and the highest efficiency is recorded for SiO_2 nanoparticles for both therminol VP-1 and molten salt. This increase in efficiency is a result of several factors, such as increase in the thermal performance, reduction in thermal losses and enhancement of the useful heat gain. Furthermore, the temperature profiles of the absorber using various nanofluids with therminol VP-1 confirms that the addition of nanofluids lowers the absorber temperature, thereby reducing thermal losses as shown in Figure 5.8.

It can be further noted from Figure 5.6 and Figure 5.7 that gain in efficiency is higher at the lower Re numbers. The reason behind this is that at higher Re numbers, the pumping requirement increases due to an increase in the fluid velocity and turbulence. This is confirmed when one revisits the heat transfer performance shown in Figure 5.2 in conjunction with the pressure drop profiles of Figure 5.3. It can be seen from these figures that by increasing the nanoparticles percentage, the heat transfer performance increases but so does the pressure drop. Thus, raising the power required for pumping the fluid and consequently an overall less gain in the efficiency. In other words, the heat transfer improvement is not enough to compensate for the increase in the power requirements.

The maximum enhancements in the overall collector efficiencies using therminol VP-1 with 6% VF of nanoparticles at Re number of 30000 were 9.11% for SiO_2-TO followed by 7.5% for Al_2O_3-TO and 6.4% for TiO_2-TO. On the other hand, the minimum contribution of 3.29% was obtained by CeO_2-TO. For the same conditions (Re number of 30000 and 6% VF of nanoparticles), for molten salts, the maximum improvement in the collector efficiencies were found to be 9.92% for SiO_2-MS, 7% for TiO_2-MS and 6.8% for Al_2O_3-MS. A complete list of gain in efficiencies with all nanoparticles using water as a base fluid is shown in Table 5-7. It is observed that by adding different VF of various nanoparticles, one obtains an improvement in the overall collector efficiency depending upon their respective thermal properties. A maximum enhancement of 5.11% in the overall collector efficiency was achieved by SiO_2-W whereas the minimum improvement of 2.98% was obtained by CeO_2-W.

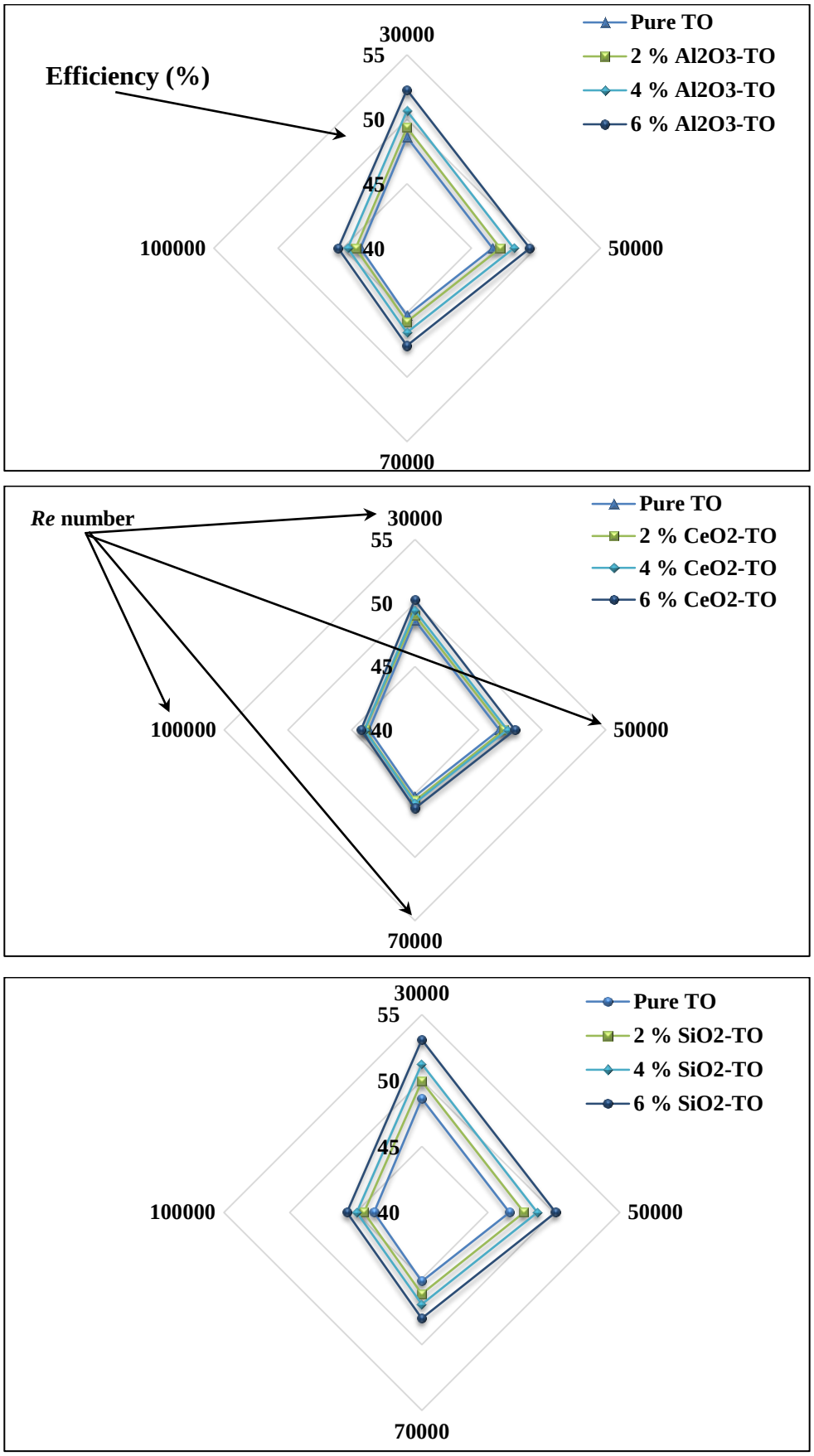

Figure 5.6: Effect of nanofluids on the overall collector efficiency using therminol VP-1 (TO) base fluid.

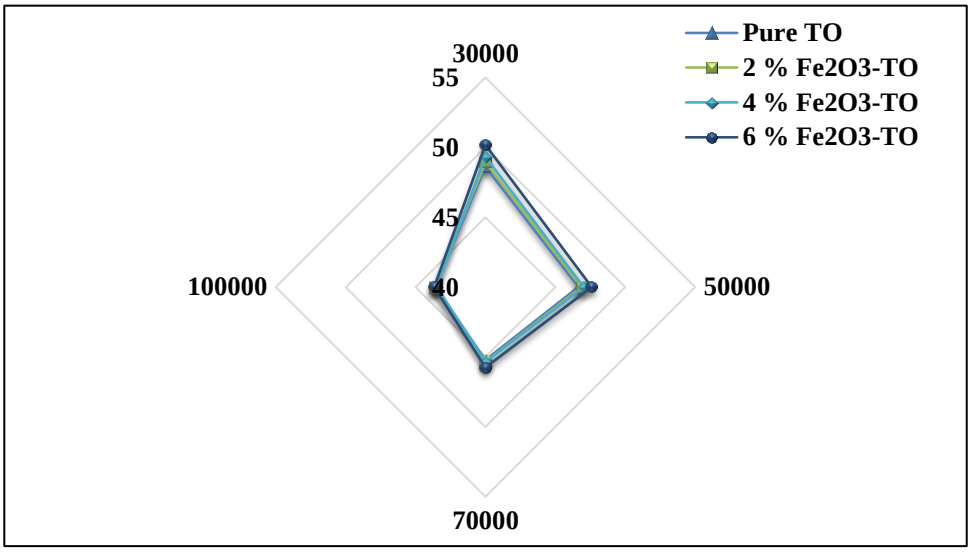

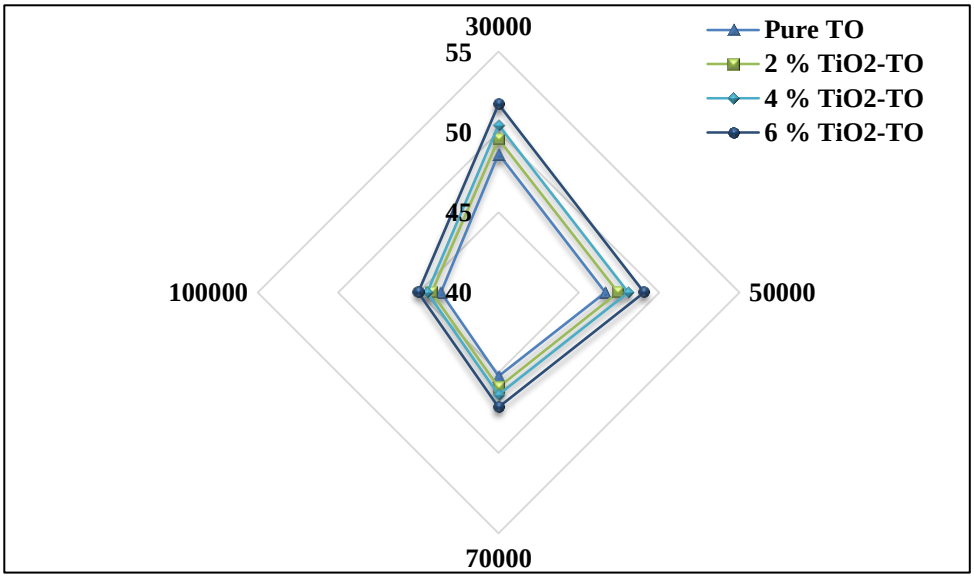

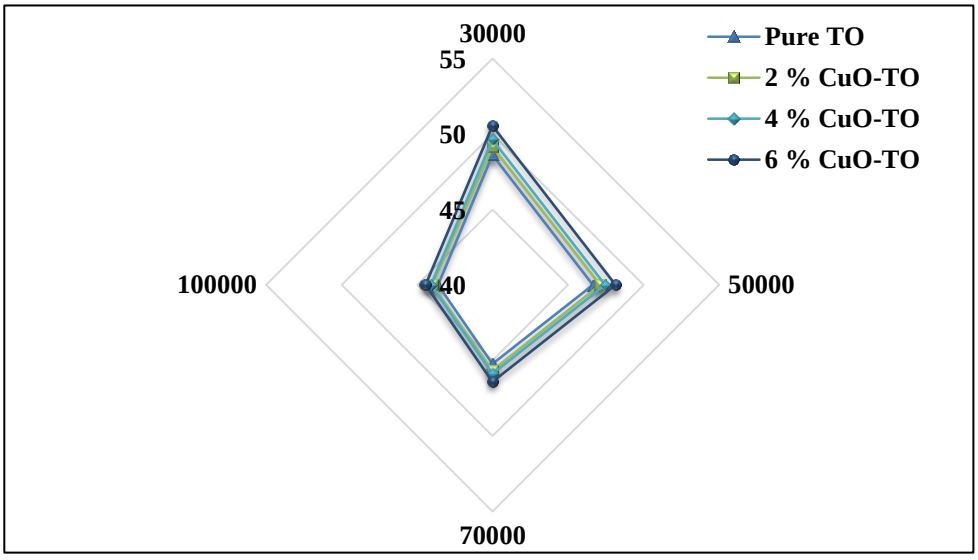

Figure 5.6(continued): Effect of nanofluids on the overall collector efficiency using therminol VP-1 (TO) base fluid.

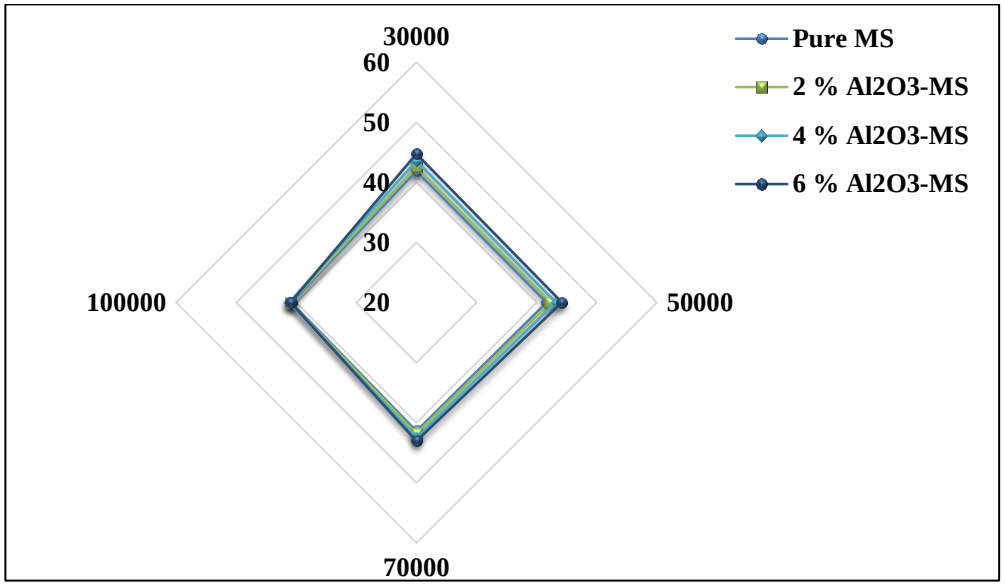

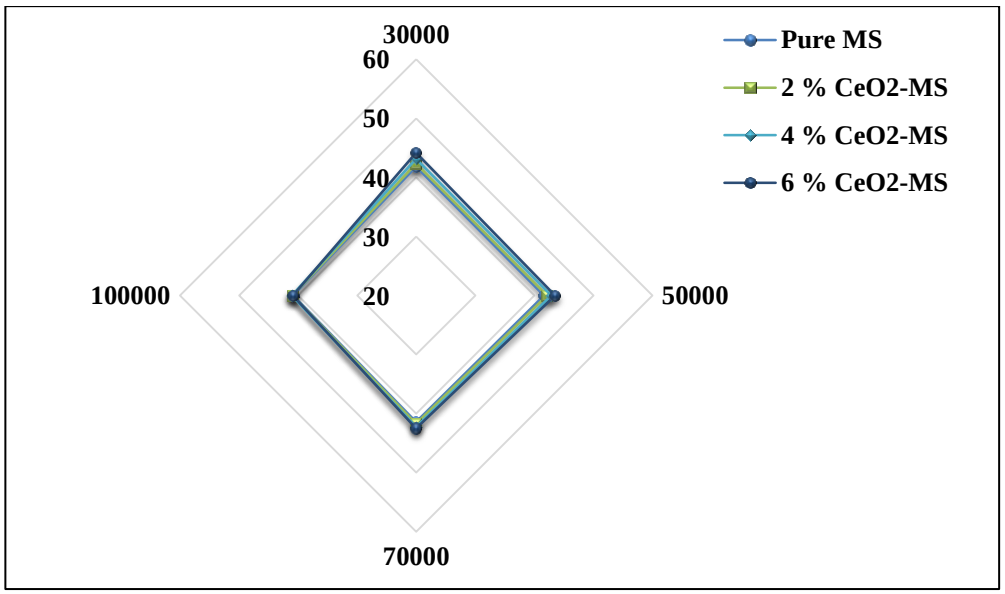

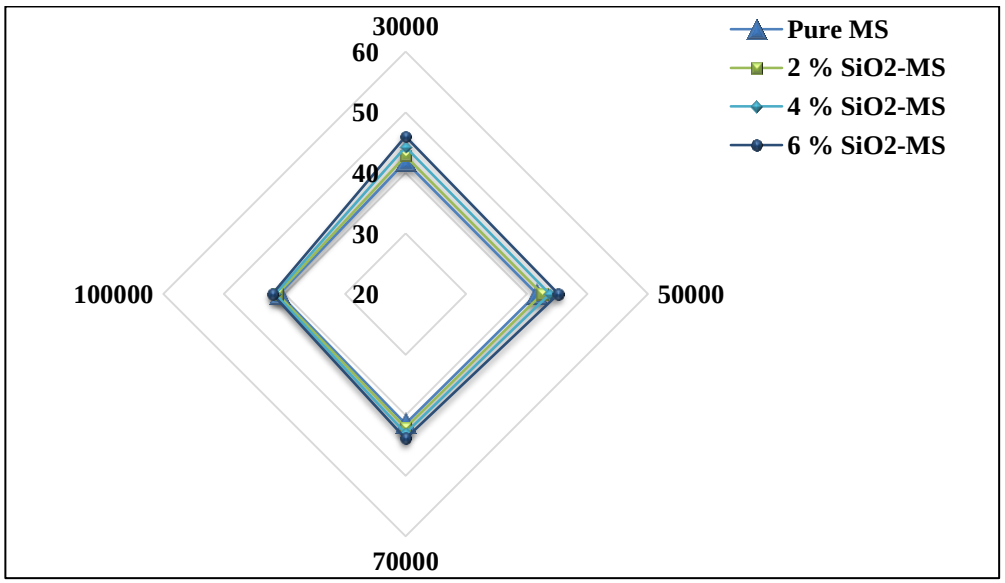

Figure 5.7: Effect of nanofluids on the overall collector efficiency using molten salt (MS) base fluid.

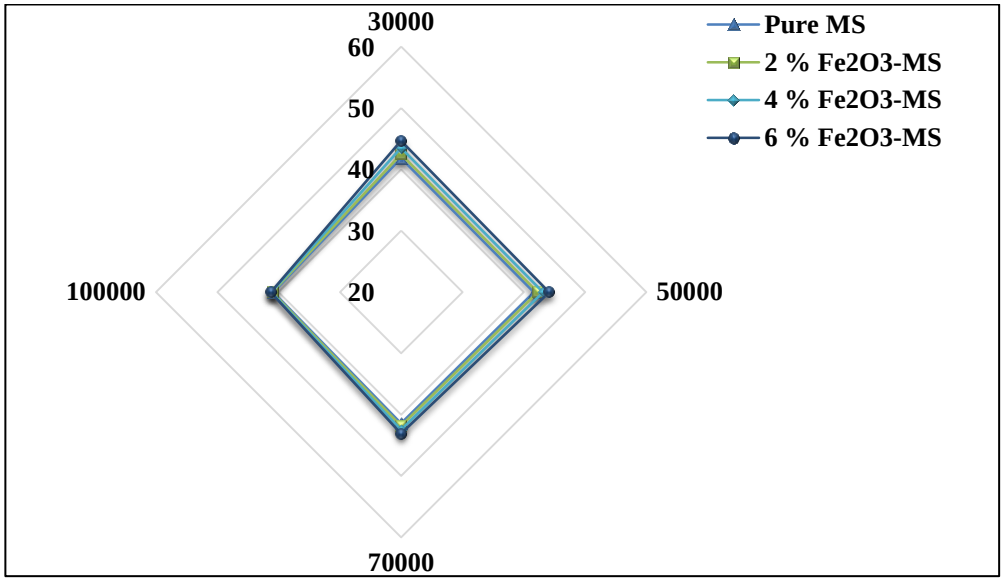

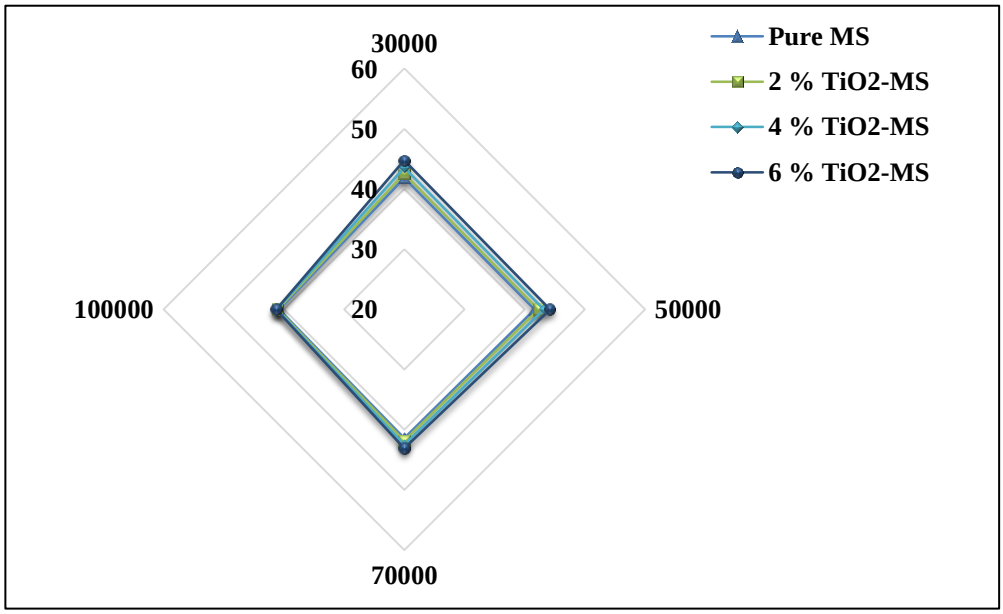

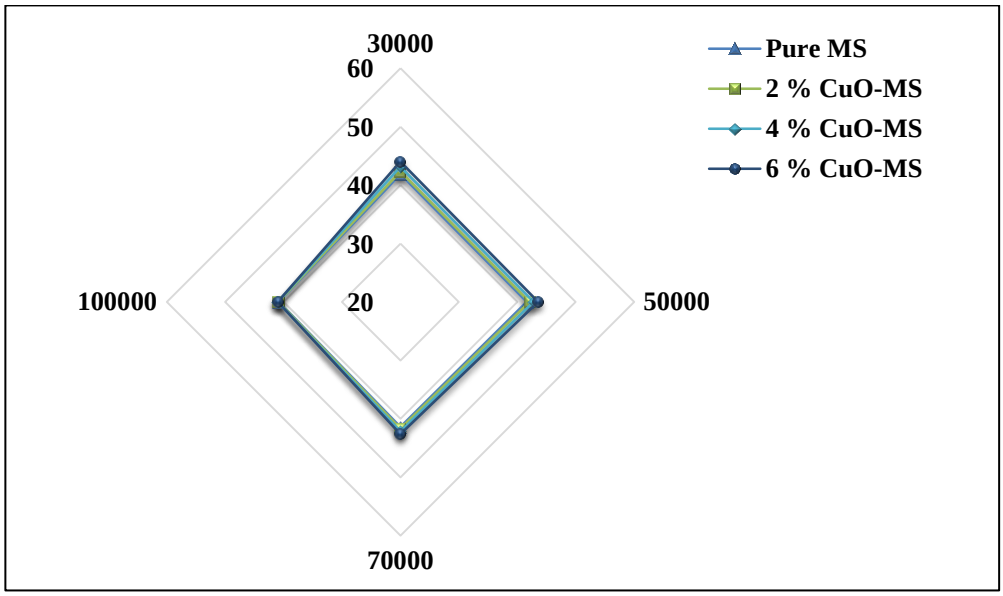

Figure 5.7(continued): Effect of nanofluids on the overall collector efficiency using molten salt (MS) base fluid.

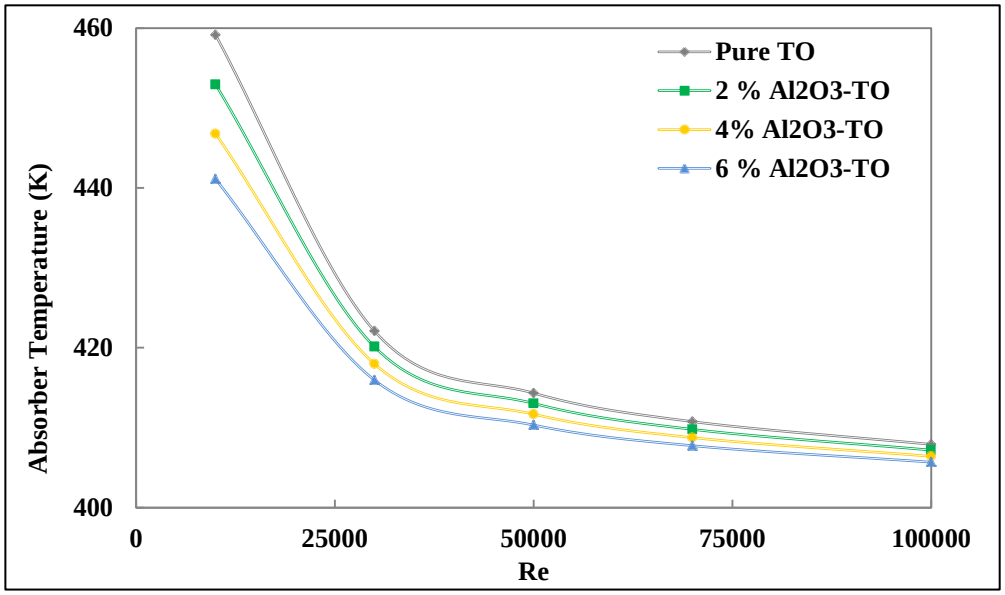

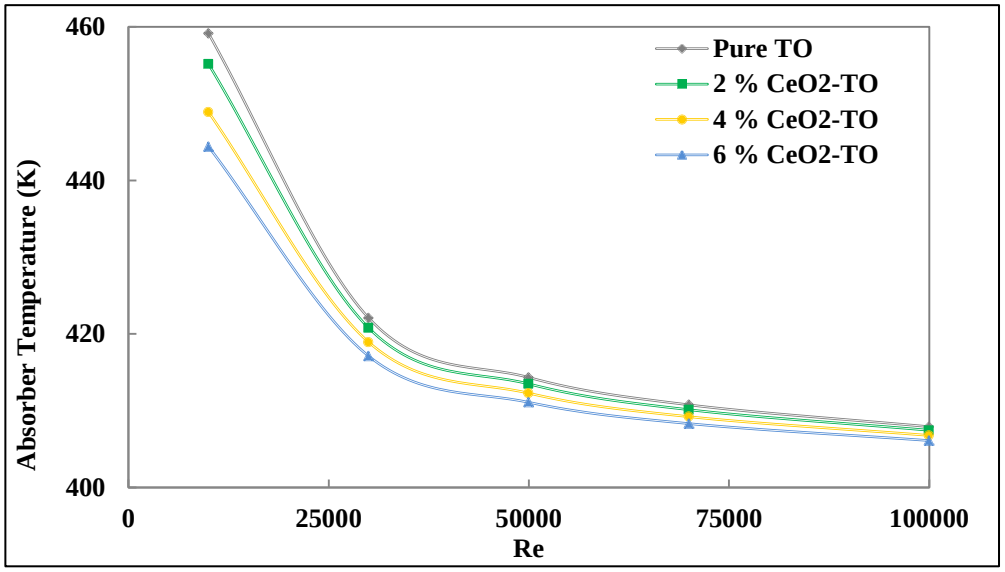

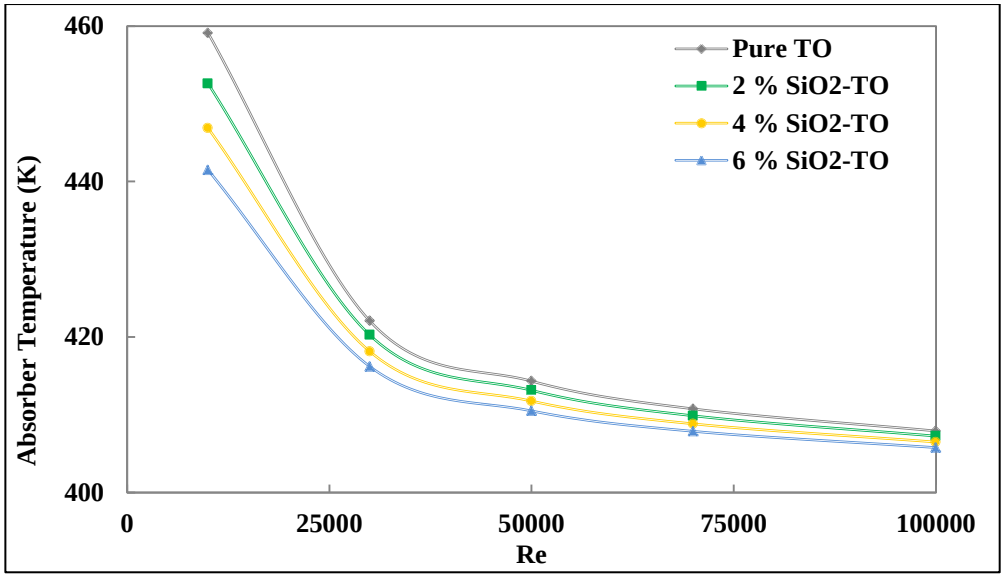

Figure 5.8: Effect of nanofluids on the inner absorber wall temperature using therminol VP-1.

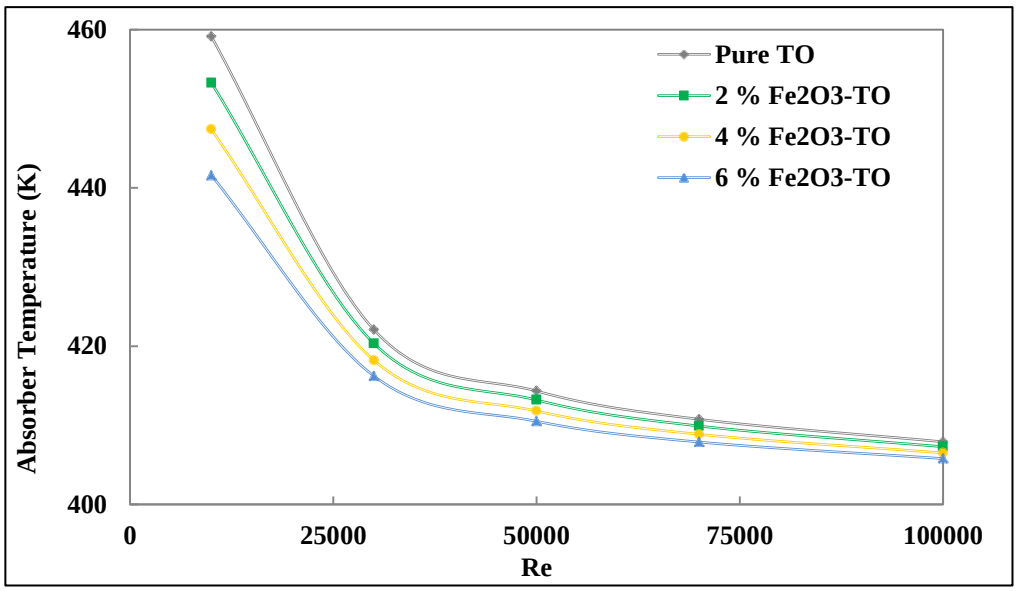

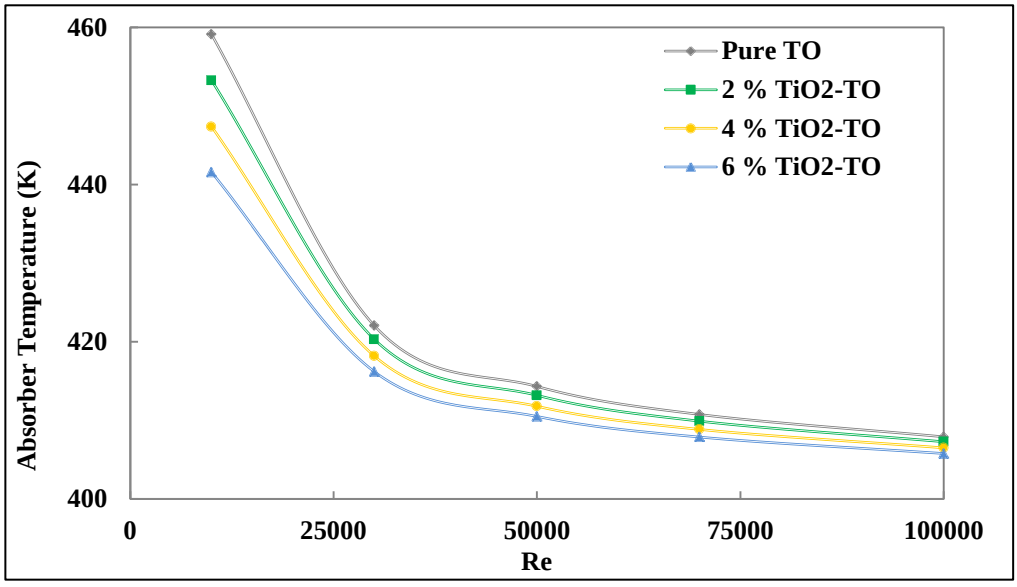

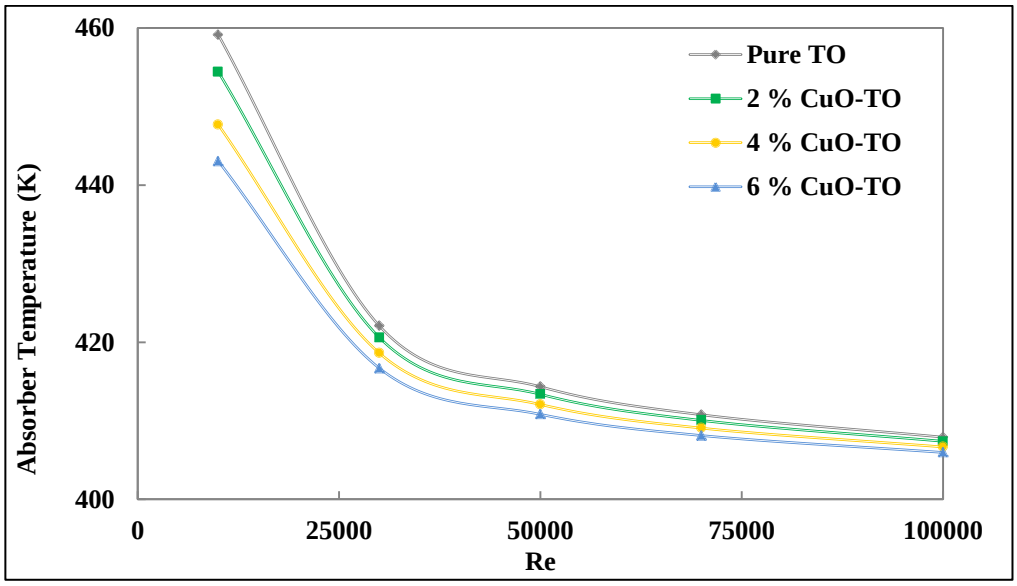

Figure 5.8(continued): Effect of nanofluids on the inner absorber wall temperature using therminol VP-1.

Table 5-7: Overall collector efficiency (%) of different nanofluids using water as a base fluid.

Nanofluid	0%	2%	4%	6%	Enhancement (%) at φ = 6%
SiO_2	35.18	36.22	36.57	36.98	5.11
TiO_2	35.18	36.08	36.28	36.53	3.83
Al_2O_3	35.18	36.08	36.27	36.51	3.78
Fe_2O_3	35.18	36.05	36.22	36.45	3.61
CuO	35.18	35.99	36.11	36.29	3.15
CeO_2	35.18	35.97	36.07	36.23	2.98

5.4.6. Thermal exergy efficiency

Another important aspect of the current work is the evaluation of effects of nanoparticles on the exergy efficiency. The exergy efficiency is an important parameter that should be taken into account since it represents the largest possible useful work extracted from the solar receiver. Figure 5.9 presents a comparison of the exergy for various nanoparticles mixed with molten salt (MS) and therminol VP-1 (TO). It is observed that the exergy efficiency increases with an increase in the VF of the nanoparticles. Much like in the previous cases, however, this increase becomes less pronounced as the Re numbers is increased. In fact, the highest gain is at the lowest Re number of 30,000, regardless of the nanoparticles and the base working fluid. This increase is due to several factors; mainly, increase in useful thermal exergy output from the solar receiver, reduction in thermal losses and enhancement of the useful heat gain.

For therminol VP-1 at the Re number of 30000, the maximum enhancement in the exergy efficiency was observed to be 9.02% for SiO_2 (with 6% VF), followed by 7.36% for Al_2O_3-TO (6% VF) and 6.24% for TiO_2-TO (6% VF). At the same conditions (6% VF and Re number of 30000) for molten salt as a base fluid, the exergy efficiency increase for various nanofluids is 10.08% for SiO_2-MS, 7.035% for TiO_2-MS and 6.96% for Al_2O_3-MS. Finally, for water as the base working fluid no marked improvements were observed as shown in Table 5-8.

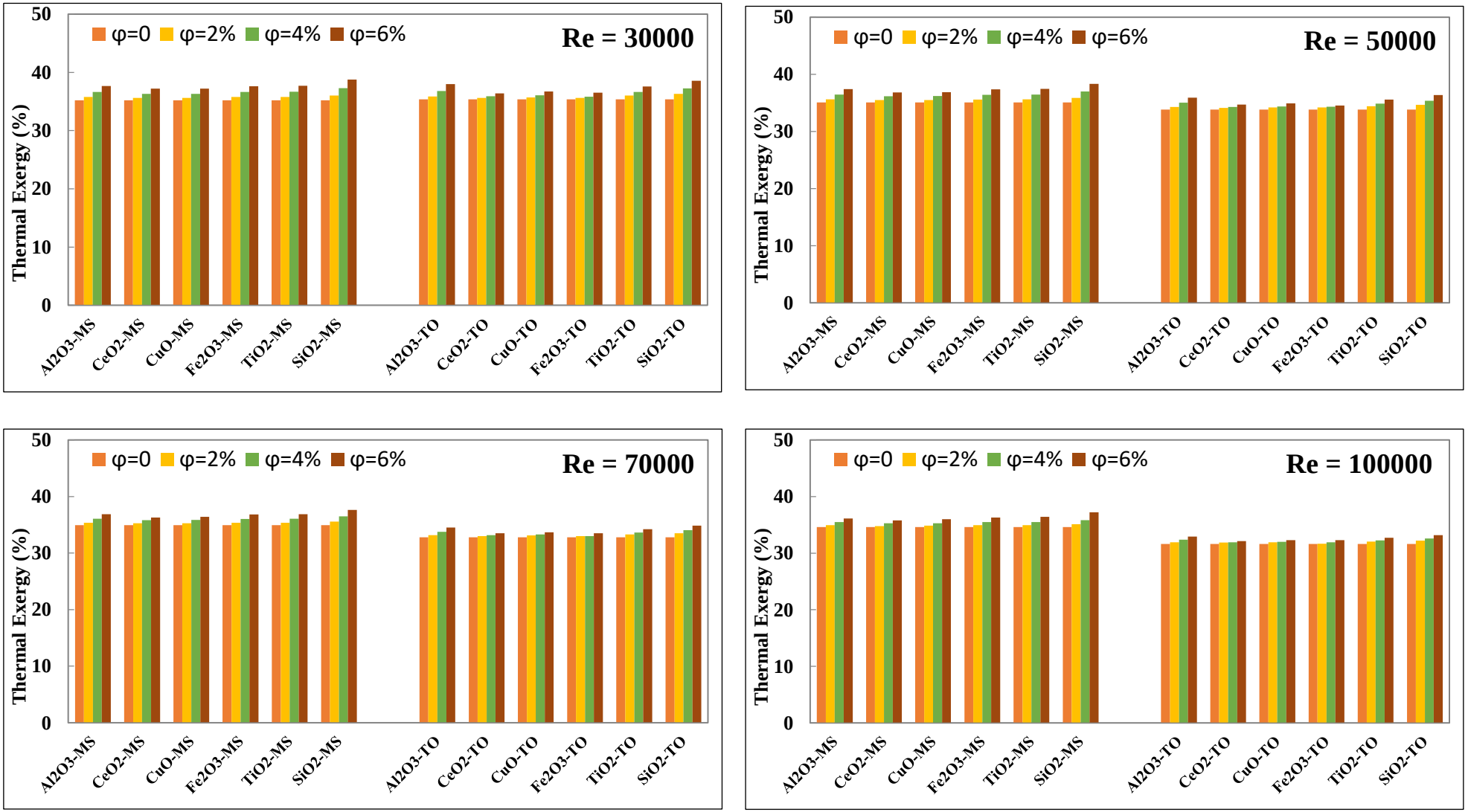

Figure 5.9: Effect of nanofluids on the exergy efficiency with molten salt (MS) and therminol (TO) base fluids at different Reynolds (Re) numbers.

Table 5-8: Thermal exergy efficiency (%) of different nanofluids using water as a base fluid.

Nanofluid	0%	2%	4%	6%	Enhancement (%) at φ = 6%
SiO_2	25.51	26.27	26.51	26.81	5.09
TiO_2	25.51	26.165	26.31	26.48	3.80
Al_2O_3	25.51	26.16	26.30	26.47	3.76
Fe_2O_3	25.51	26.14	26.27	26.42	3.56
CuO	25.51	26.10	26.18	26.31	3.13
CeO_2	25.51	26.09	26.15	26.27	2.97

5.4.7. Mean Temperature Profiles

To further study the effect of nanofluids performance the non-dimensional mean temperature (T^+) normalized by the friction temperature (T_τ) is also considered and their results are shown in Figure 5.10. These mean thermal temperature profiles are plotted at L=3.8 m (close to the absorber outlet) under uniform conditions for all nanoparticles mixed with therminol VP-1 at Re=10000. It can be seen that there is a gradual increase in the mean temperature profile inside the logarithmic region (away from the walls), accompanied by a gradual decrease in the heat conduction sub-layer close to the wall (at smaller y^+values) as the VF of nanoparticles increases. This is due to the fact that by increasing the nanoparticles VF, there is a gradual increase in the effective Pr number. An increase in the Pr number means that the near-wall sub-layer, across which heat conduction is the dominant mode of heat transfer instead of turbulence transport, is reduced in thickness.

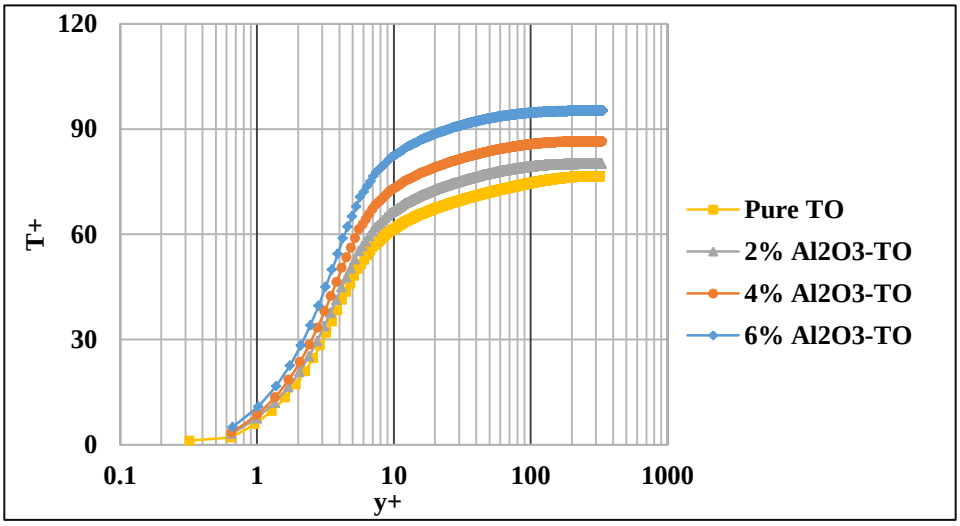

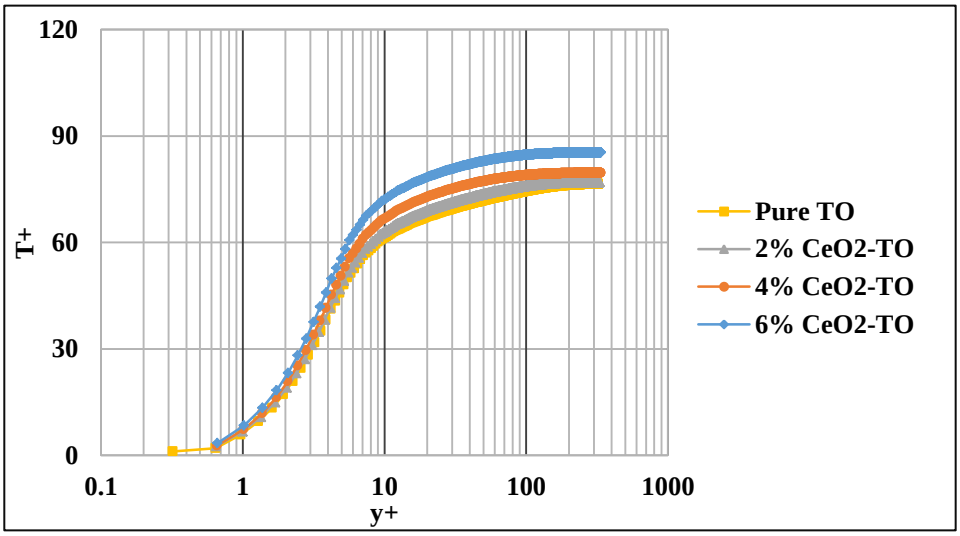

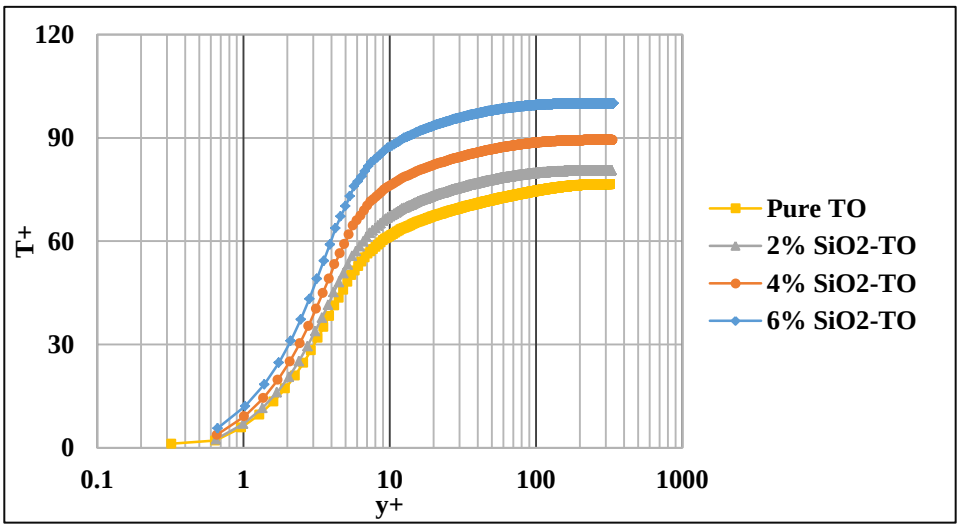

Figure 5.10: Non-dimensional temperature profiles T^+ against the non-dimensional wall distance y^+, resulting from nanofluids effect using therminol VP-1 as the base working fluid.

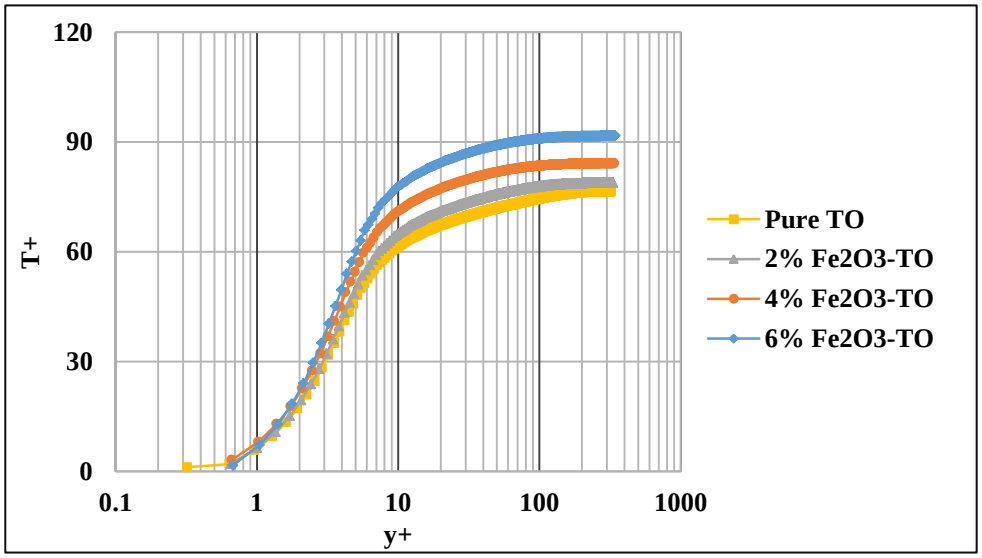

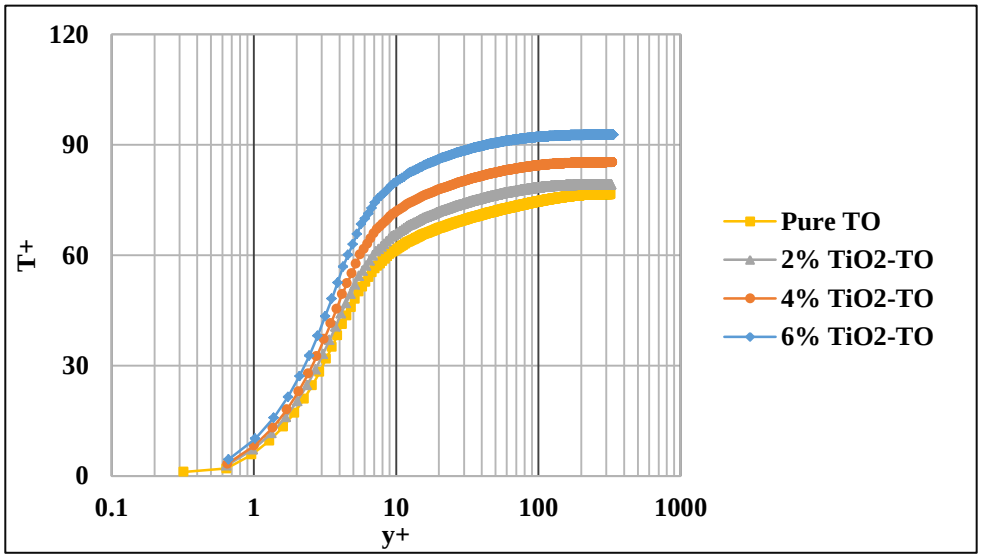

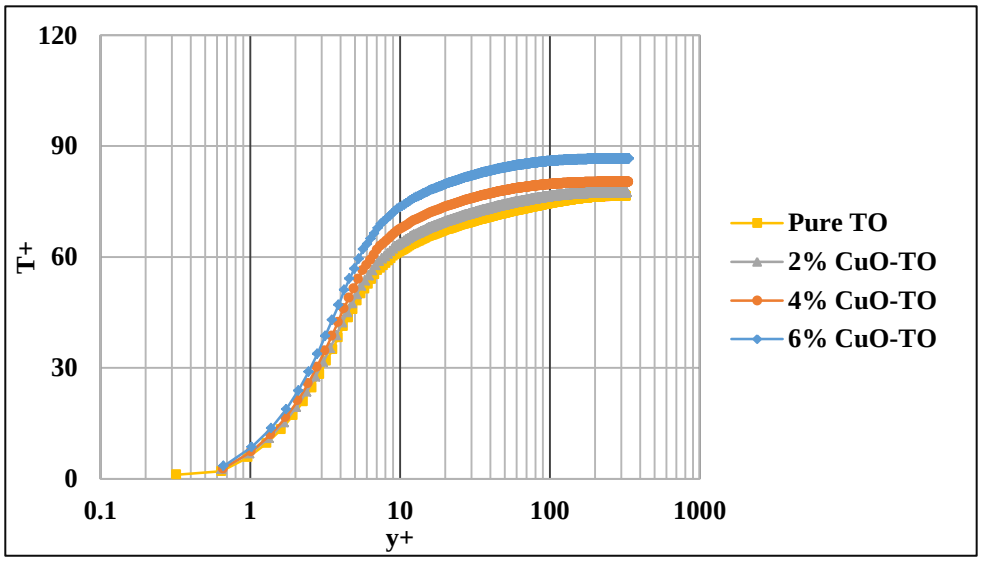

Figure 5.10(continued): Non-dimensional temperature profiles T^+ against the non-dimensional wall distance y^+, resulting from nanofluids effect using therminol VP-1 as the base fluid.

5.4.8. Comparison with previous studies

The heat transfer performance and the collector thermal efficiency of the present study are compared with existing data for a wide range of different nanofluid parameters, as illustrated in Table 5-9. It is apparent that the findings of the current study are in agreement with literature. In particular, the predictions of thermal efficiency enhancements are very close to the results of Mwesigye and Meyer (2017) for the exact same conditions (base fluid, nanoparticles and VFs i.e. TherminolVP-1 with 6% VF Al_2O_3). More specifically, Mwesigye and Meyer (2017) proved that by using 6% VF nanofluid of TherminolVP-1 with Al_2O_3 leads to 7.2% enhancement in the thermal efficiency, which is very close to the current estimates of 7.5%. Furthermore, with SiO_2 nanoparticles the increment in overall collector efficiency is 9.11%. Similarly, for the heat transfer performance, the current predictions are very close to the results of Bozorg et al. (2020), which use thermal oils with Al_2O_3 for slightly different nanoparticle VFs. It should be noted here that any differences that are observed in the present predictions compared to values found in the literature are mainly due to small differences in the Re number, inlet temperature of the base fluid or the VF of the nanofluid. Table 5-9 thus shows that the current results provided by the numerical simulations are acceptable and logical.

Table 5-9: comparison the present achievements with previous studies.

Thermal Efficiency Enhancement						
Reference	***Re***	**Tin (K)**	**Base fluid**	**NP**	**φ (%)**	**Enhancement (%)**
Mwesigye et al. (2015a)	6710	350	Syltherm800	Al_2O_3	8	7.6
Bellos et al. (2016)	-	627	Thermal oil	Al_2O_3	2	8.1
Kaloudis et al. (2016)	-	298	Syltherm800	Al_2O_3	4	10
Mwesigye and Meyer (2017)	$2x10^5$	600	TherminolVP-1	Al_2O_3	6	7.2
Bellos and Tzivanidis (2017)	-	298	Syltherm800	CuO	4	1.26
Korres et al. (2019)	698	573	Syltherm800	CuO	5	2.76
Bozorg et al. (2020)	$6x10^5$	500	Synthetic oil	Al_2O_3	3	5
Present Study	$3x10^4$	400	Therminol VP-1	SiO_2	6	9.11
Present Study	$3x10^4$	400	Therminol VP-1	Al_2O_3	6	7.5
Present Study	$3x10^4$	400	Water	SiO_2	6	5.11
Present Study	$3x10^4$	600	Molten salt	SiO_2	6	9.92
Heat Transfer Enhancement						
Zadeh et al. (2015)	-	300	Synthetic oil	Al_2O_3	5	36
Bellos et al. (2016)	-	627	Thermal oil	Al_2O_3	2	10.92
Ferraro et al. (2016)	-	300	Synthetic oil	Al_2O_3	5	1.65
Mwesigye et al. (2016)	-	400	Therminol VP-1	Cu	6	32
Korres et al. (2019)	698	298	Syltherm800	CuO	5	15.53
Bozorg et al. (2020)	$6x10^5$	500	Synthetic oil	Al_2O_3	3	7
Abu-Hamdeh and Almitani (2016)	-	298	Water	ZnO	4	14.4
Present Study	$3x10^4$	400	Therminol VP-1	SiO_2	6	15.57
Present Study	$3x10^4$	400	Therminol VP-1	Al_2O_3	4	7.32
Present Study	$3x10^4$	400	Water	SiO_2	6	32.4
Present Study	$3x10^4$	600	Molten salt	SiO_2	6	21.36

5.5. Conclusions

The use of nanoparticles in PTC applications is a useful and promising technique for thermal performance improvement. The main contribution of the present chapter is to numerically test the thermal performance and study the flow features inside a PTC by using different non-metallic nanoparticles (Al_2O_3, CeO_2, CuO, Fe_2O_3, TiO_2 and SiO_2) dispersed in three different base fluids (therminol VP-1, water, and molten salt). The simulations were performed over a range of Re numbers and three volume fractions (2, 4 and 6%). A realistic non-uniform heat flux distribution in the circumferential direction over the absorber outer surface was applied, using the MCRT technique found in the literature. Main findings of the study are summarized below:

- For water based nanofluids, the improvement in the Nu ranged from 12.72% to 32.4% with 6% VF of SiO_2 nanoparticle providing the highest improvement. Whereas for the molten salt and therminol VP-1 base nanofluids, the improvements in the Nu number was not as pronounced but the general trend was the same with SiO_2 being the most effective and CeO_2 the least.
- For molten salt base nanofluids, the enhancement in the thermal efficiency ranged from 5.1% to 9.92% with 6% VF of SiO_2 nanoparticle providing the largest enhancement and CeO_2 the least. On the other hand, for therminol VP-1 base nanofluids, the enhancement in the thermal efficiency ranged from 3.29 to 9.11% with 6% VF of SiO_2 nanoparticle providing the largest improvement and CeO_2 the least. For the water based nanofluid, no marked improvement was observed in terms of the thermal efficiency. However, SiO_2 still performed better than CeO_2.
- The improvement in the thermal exergy efficiency for the molten salt base fluids ranged from 5.2% to 10.08% with 6% VF of SiO_2 nanoparticle giving the maximum improvement and CeO_2 the minimum. On the other hand, the improvement for therminol VP-1 base nanofluids in the thermal exergy efficiency ranged from 3.18% to 9.02% with 6% VF of SiO_2 nanoparticle providing the largest improvement. Finally, for the water based nanofluids, once again the thermal exergy did not show huge gains.

Based on the performance, it is concluded that regardless of the base working fluid SiO_2 is the best candidate from all perspectives (improvement in Nu number, thermal efficiency enhancement, exergy efficiency improvement) with CeO_2 being the worst.

Chapter 6: Thermal-Hydraulic Analysis of PTCs Using Straight Conical Strip Inserts with Nanofluids

6.1. Introduction

The insertion of different types of metallic turbulators inside the solar absorber in the flow path can increase the absorption of thermal energy from the internal absorber wall. This process enhances the thermal performance of the PTC through enhancing the surface area for heat transfer. Furthermore, this technique decreases the external absorber wall temperature, resulting in lower thermal losses and higher thermal efficiencies. According to Reddy et al. (2008), using two different types of fins (longitudinal fins and porous fins) led to increase the heat transfer by 17.5% compared to a pure absorber. Ravi and Reddy (2009) numerically investigated the effect of the porous disc with different configurations (bottom half disc, full porous disc, bottom half porous disc and typical receiver). They found that the Nu number was enhanced by 64.3% by using the receiver with the top porous disc.

After placing the milt-longitudinal vortexes on the inner side of the receiver of a PTC system, Cheng et al. (2012b) found that thermal losses and wall temperature initially went down. However, when the Re number was increased, the thermal losses were reduced by 1.35%–12.1%. Thus, the augmentation in the PEC was observed to be 1.18%. Additionally, Wang et al. (2013) observed that when they used metal foam as an insert type inside the solar absorber, the Nu number, friction factor and PEC increased by 10–12 times, 400–700 times and 1.1–1.5 times, respectively, compared to a standard typical receiver. Another type of insert—perforated plate inserts—was investigated by Mwesigye et al. (2014). They observed that the Nu number, thermal enhancement factor and friction factor all improved substantially compared to an empty receiver. Mwesigye et al. (2016) modified the twisted tape type with wall-detached and examined different ratios. They observed that the heat transfer coefficient and friction factor increased from 1.05 to 2.69 and 1.6-14.5 respectively. Moreover, due to the presence of twisted tapes, the difference in temperature of the tube in the circumferential direction reduced by 68%. However, the thermal efficiency increased by 5-10 % at a twist ratio larger than 1.

Zheng et al. (2017) also modified the twisted tape by using dimpled twisted tapes. They revealed that heat transfer recorded a significant increase with using the insert type. However, the dimple side provided better heat transfer performance than protrusion side. Where the heat transfer coefficient increased by 25.53%. The wavy-tape in a PTC system

was investigated by Zhu et al. (2017) and they found that the presence of wavy-tape insert reduced the heat losses and entropy generation by 17.5-33.1% and 30.2-81.8% respectively. Bellos et al. (2017b) examined twelve fin geometries in the absorber tube and kept fin thickness as 2mm, 4mm, and 6mm and took length as 5mm, 10mm, 15mm, and 20mm. They observed that the large length and thickness provided the larger thermal and hydraulic performances. However, the length of the fins is more important than the thickness in which the enhancement index was 1.483.

Xiangtao et al. (2017) tested the effect of using pin fins arrays located only in the entrance and bottom region of the receiver tube of the PTC. They reported that the Nu number increased by 9% and thermal performance factor increased up to 12% with the optimum case of 8mm as fin diameter and Re number as 4036. After using the optimum multiple cylindrical inserts, the thermal losses reduced by 5.63% and 26.88% enhancement in the heat transfer coefficient as reported by Bellos et al. (2018b). Arshad et al., (2019) used internal toroidal rings and found that the Nu number and thermal efficiency have increased by 3.74% and 2.33 times, respectively. Thus, the usage of various types of insert types assisted in increasing the thermal performance and thermal efficiency but it needed different level of augmentation. Such as Rawani et al. (2017) found 5% increase when using serrated twisted tape inserts and 3% increase when using metal foam. Moreover, Jamal-Abad et al. (2017) found that enhancement reduced when they used porous discs. Reddy et al. (2015) and Zheng et al. (2016) also found similar results. However, Bellos and Tzivanidis (2018) and Bellos et al. (2019) reported about 1% increase when they used star flow and eccentric inserts. Liu et al. (2019a) investigated inclined conical strip inserts and they experienced a 5% enhancement in the thermal efficiency.

Yılmaz et al. (2020) introduced insert type called wire coil inserts and they found an improvement of 183% in heat transfer performance with a 0.4% increment in the thermal efficiency. Using metal foams as inserts were also investigated by Kumar and Reddy (2020) who reported a 3.71% increase in the energy efficiency and 2.32% in the exergy efficiency. However, the temperature difference reduced from 47% to 72%, compared to the plain absorber.

The typical twisted tapes were modified by Suresh et al. (2020). They attached the rings on the outer surface of the twisted tapes with taking extra step by modifying the attached rings. They found that the Nu number enhanced by 5–40%, 11–101% and 7–77% in typical twisted tape, twisted tape with attached rings and twisted tapes with modified attached rings respectively.

Recently, Xiao et al. (2021) used inclined curved-twisted baffles and revealed 0.52% and 0.22% increase in the overall efficiency and exergy efficiency, respectively. Therefore, the combination of swirl generators and nanofluids could assist in enhancing the thermal efficiency of PTC systems even it is possible to augment the heat transfer performance and reduce the thermal losses compared to the other approaches. Where, Bellos et al. (2018b) found only 0.76% enhancements in the thermal efficiency after using 6% CuO-thermal oil nanofluids. They also reported that the thermal efficiency increased by 1.1% when using internal fins. Moreover, the use of nanofluid and internal fins increased the thermal efficiency by 1.54%.

All cited previous studies investigated various types of inserts under different operating conditions and non-uniform heat flux distributions around the solar absorber on the external surface. However, optimized straight conical strip inserts have never been investigated thoroughly. Thus, in this chapter, the effects of optimized straight conical strip inserts attached to the central rod are investigated under a non-uniform heat flux profile around the absorber tube. The central rod diameter is assumed to be constant (D_r = 1.6 cm) and the height of the attached strip (H) varied from 15 mm to 30 mm with the angle of the attached strip (θ) changed from 15° to 30°. All arrangements were then examined for a range of Re numbers (10^4 to 10^5). After obtaining the optimum strip height and angle, the number of strips was increased stepwise from one to four. The results were then examined with the presence of a nanofluid using 6% of SiO_2 nanoparticles mixed in Therminol® VP-1, as this was the best candidate proposed in the previous chapter. It is important to mention that all case studies were assumed to be steady-state, incompressible and three dimensional, using Therminol® VP-1 as a heat transfer fluid with an inlet temperature of 400 K. The heat flux distribution was taken as a realistic profile by applying the MCRT model in the circumferential direction. The study evaluates and assesses the influence of the optimum case on the thermal, hydraulic and thermodynamic performances of the PTCs. Such an evaluation of PTC performance has not yet been reported in the literature.

6.2. Description of Straight Conical Strip Inserts

In the current chapter, straight conical strip inserts are attached to the central rod. The geometrical characteristics of the straight conical strip are optimized by changing different combinations of the strip height (H) and conical angle (θ), as shown in Figure 6.1. The straight conical strip attached to the central rod has a constant thickness (t) of 10 mm in the downstream direction, with the horizontal pitch distance (P) between conical strips set at 486 mm.

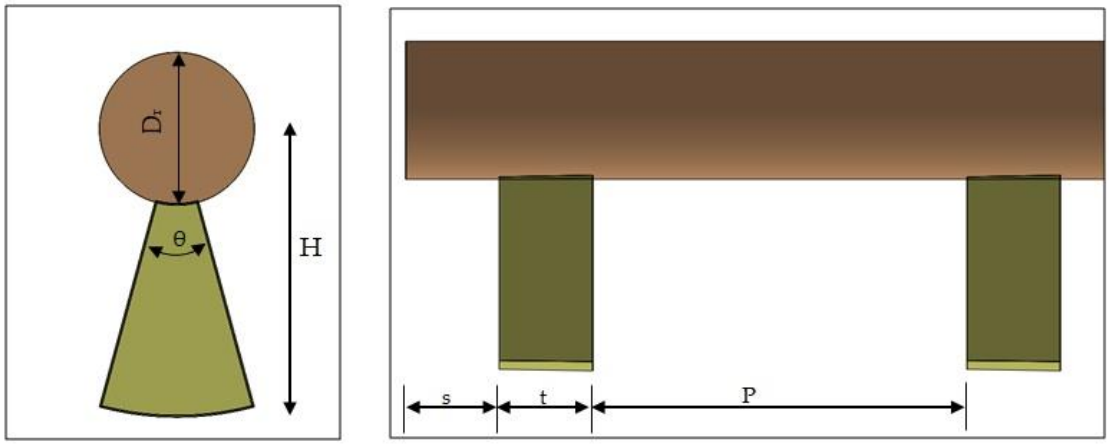

Figure 6.1: The conical strip geometry examined in the current study.

The conical angle varied, at 15°, 20°, 25° and 30°, whereas the strip height was increased from 15 mm–30 mm in increments of 5 mm. After obtaining the optimized single straight conical strip characteristics, extra cases were inspected by increasing the number of strips (N) to two, three and finally to four. All examined swirl-generator cases are presented in Figure 6.2. The first conical strip was located 10 mm (s) away from the absorber inlet, in order to allow a greater mass flow rate for the fluid entering the absorber tube.

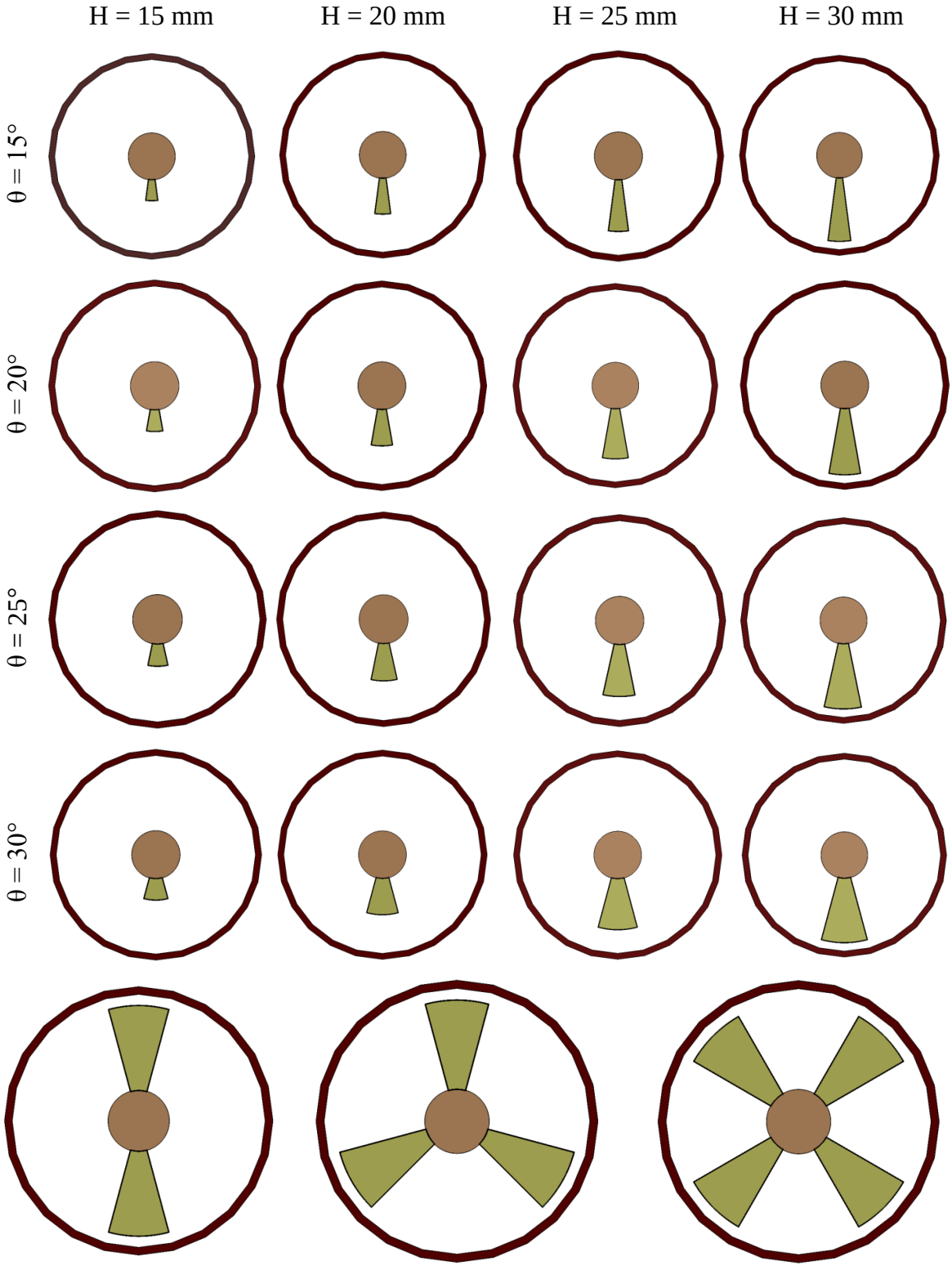

Figure 6.2: Various configurations of the examined straight conical strips in the current study.

6.3. Mesh Independence Study

The mesh independence study was performed for the geometry of a single straight conical strip with the larger geometrical parameters (H = 30 mm and θ = 30°) inside the solar receiver. Three meshes were examined for this configuration—fine mesh with 3.8 million cells, medium mesh with 3.4 million cells and coarse mesh with 2.4 million cells. All meshes were refined in near-wall regions in order to capture the flow physics for low Reynold's treatment and non-dimensional number $y^+ \approx 1$. For the absorber mesh independence study, whereas the Therminol VP-1 at 400 K inlet temperature was utilized. It is evident from Figure 6.3 that the coarse mesh failed to predict the Nu number in the fully turbulent flow region at higher Re numbers. However, the medium mesh was able to sufficiently predict the Nu numbers even in the fully turbulent flow regions over the entire range of Re numbers. No further improvement was observed with the fine mesh; thus, the medium mesh was selected for further computations. For other conical strip geometries, the mesh size was adjusted based on the conical strip parameters, i.e., height (H) and angle (θ).

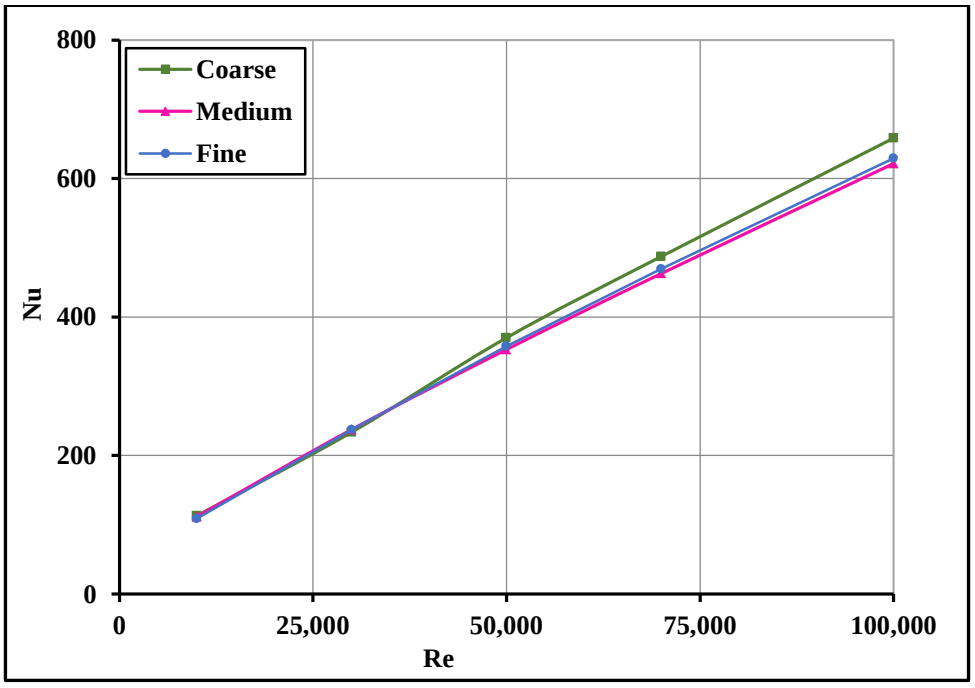

Figure 6.3: Mesh independence study for the solar receiver with a single straight conical strip insert.

6.4. Results and Discussions

6.4.1. Heat Transfer Performance

The use of swirl generators inside a PTC system decreases the temperature gradient and enhances the convective heat transfer performance. This is achieved by absorbing more energy from the inner wall of the solar receiver and from the swirl generator. Figure 6.4 shows the behaviour of the Nu number of the solar receiver as a function of the Re number for all angles and pitch heights considered in the current study. The figure also shows the effect of variation in the conical insert design, as well as the optimum case with and without nanofluid compared to the pure absorber (typical absorber). It is clearly evident from this figure that keeping the angle pitch constant and increasing the height pitch gradually (from 15 mm to 30 mm) leads to a gradual increase in the Nu number. This increase is due to two reasons: first, the increase in the contact surface area of the swirl generator with the working fluid and, second, added mixing of working fluid due to the presence of inserts.

Furthermore, increasing the angle pitch (from 15° to 30°) also enhanced the Nu number due to an increase in the contact surface area of the swirl generator. For the single conical insert configuration, the maximum Nu number was attained by the larger geometry, as shown in Figure 6.4d. These results are in line with the main findings of Mwesigye et al (2016); Bellos et al. (2017); Bellos and Tzivanidis (2018) and Liu et al. (2019a). It can be observed in Figure 6.4e that the thermal energy absorption rate increases with an increase in the number of conical inserts, and the highest heat transfer performance was achieved by the four-strip conical insert. The presence of swirl generators inside the PTC system increases the turbulence intensity of the working fluid. This leads to increased mixing with the swirl generators, as seen in the turbulent kinetic energy (TKE) distribution contours in Figure 6.5, which is beneficial for the augmentation of the heat transfer.

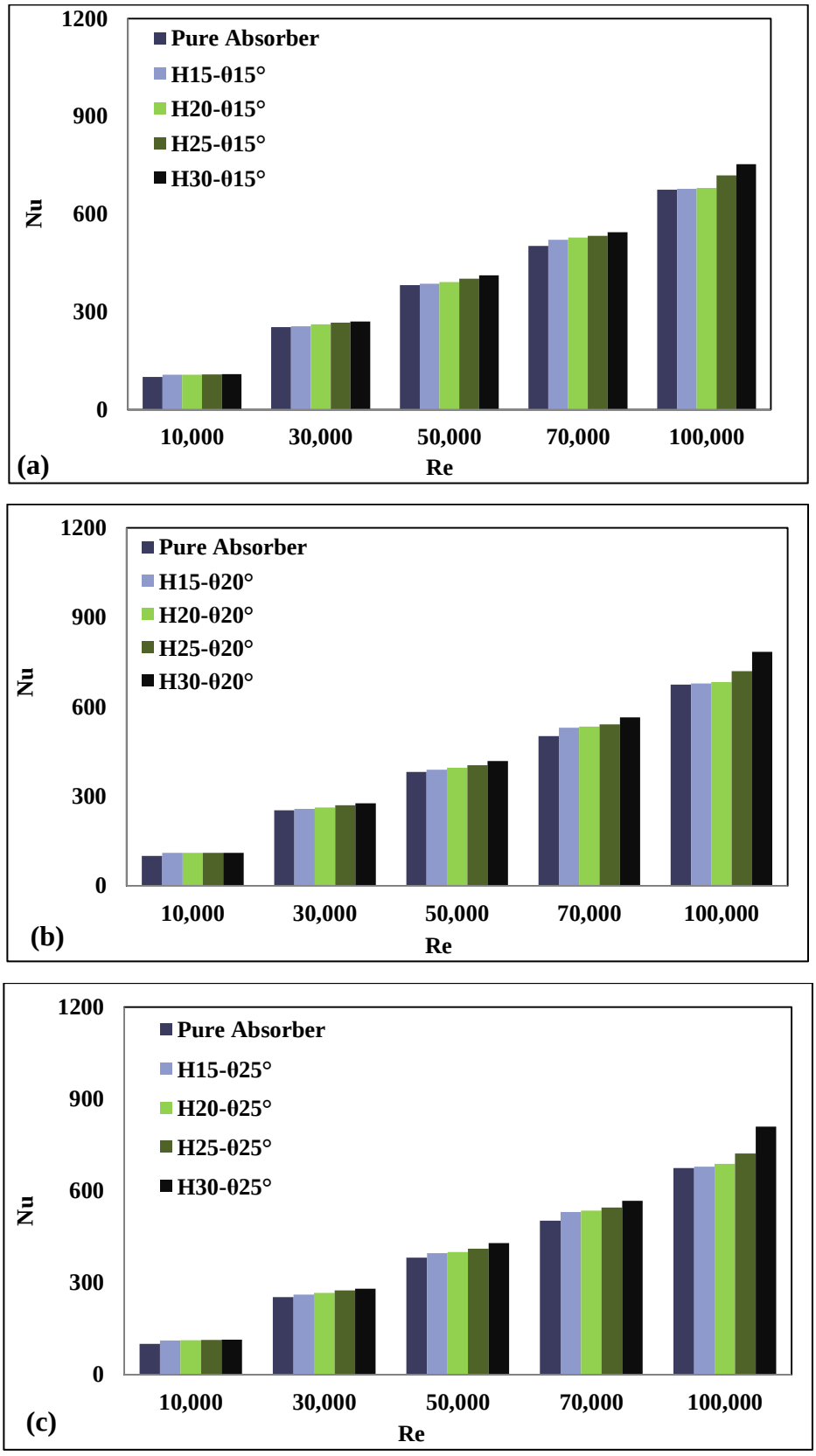

Figure 6.4: Effects of swirl generators geometries on heat transfer performance of pitch height variation with: (a) $\theta = 15^{\circ}$, (b) $\theta = 20^{\circ}$, (c) $\theta = 25^{\circ}$.

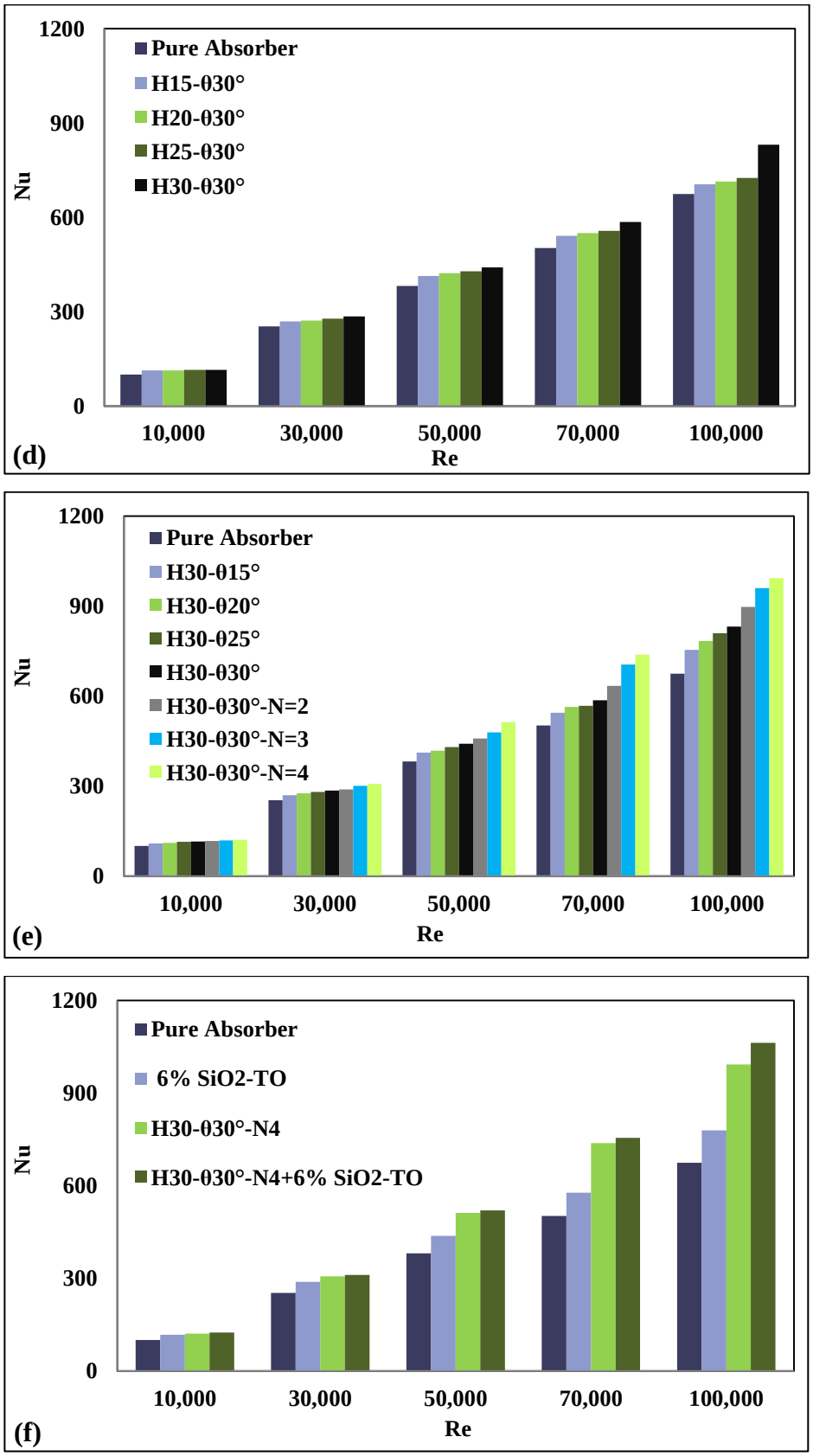

Figure 6.4(continued): Effects of swirl generators geometries on heat transfer performance. (d) Pitch height variation with $\theta = 30^{\circ}$, (e) Pitch angle (θ) and number of inserts (N) variation with fixed pitch height, (f) Optimal configuration with and without nanofluids.

The optimum conical strip case was examined further in the presence of nanofluid (SiO_2 mixed with the Therminol VP-1 (TO) using 6% volume fractions), as shown in Figure 6.4f. The introduction of nanofluid improved the thermal properties of the pure working fluid by enhancing the overall Prandtl number. This increased the thermal conductivity, increased the dynamic viscosity and reduced the specific heat capacity. It is thus obvious that the introduction of nanofluid helps in absorbing more energy from the solar receiver compared to the pure absorber configuration. It was thus concluded that combining inserts such as straight conical strips with nanofluids leads to significant augmentation in the Nu number, as also reported by Bellos and Tzivanidis (2018).

Figure 6.4 also shows that by increasing the Re number, the Nu number also increases. This was expected for several reasons; reduction in the thermal boundary layer thickness, lowering of the inside temperature of the solar receiver, and the decrease in the output working fluid temperature. The computed thermal enhancements in the Nu number of single and multiple conical cases with and without nanofluids at a Re number of 100,000 are shown in Table 6-1.

Table 6-1: Thermal enhancement in the Nu number with single and multiple conical inserts, with and without nanofluid at Re = 100,000.

Case	***Nu* Number**	**Enhancement (%)**
Pure absorber	674.83	-
H30-θ30°-N1	831.25	23.17
H30-θ30°-N2	896.55	32.85
H30-θ30°-N3	959.88	42.24
H30-θ30°-N4	992.89	47.13
6% SiO_2-TO	779.95	15.57
H30-θ30°-N4+6% SiO_2-TO	1062.78	57.4

H=30mm, θ=30°, N=1

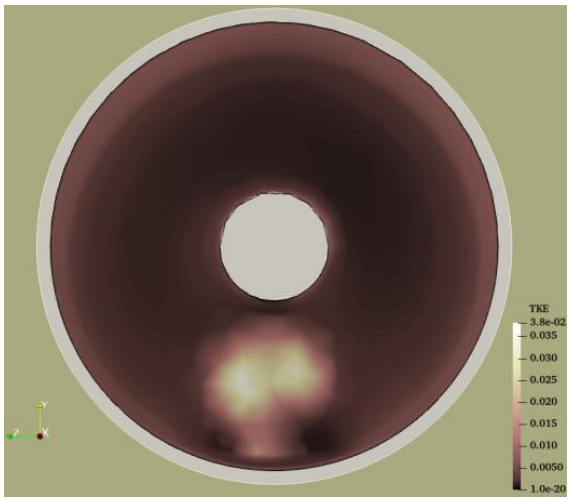

H=30mm, θ=30°, N=2

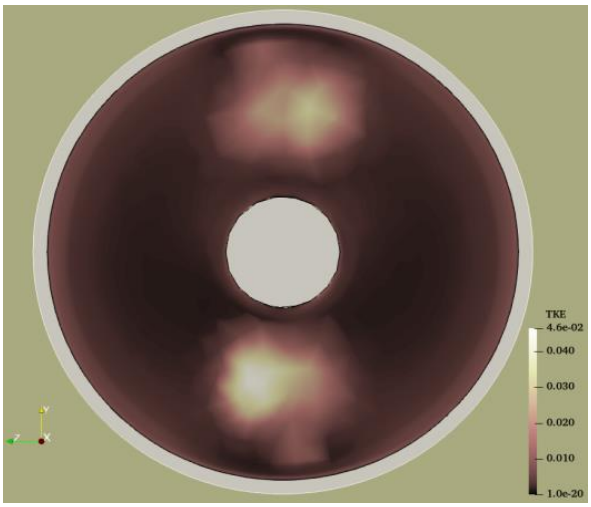

H=30mm, θ=30°, N=3

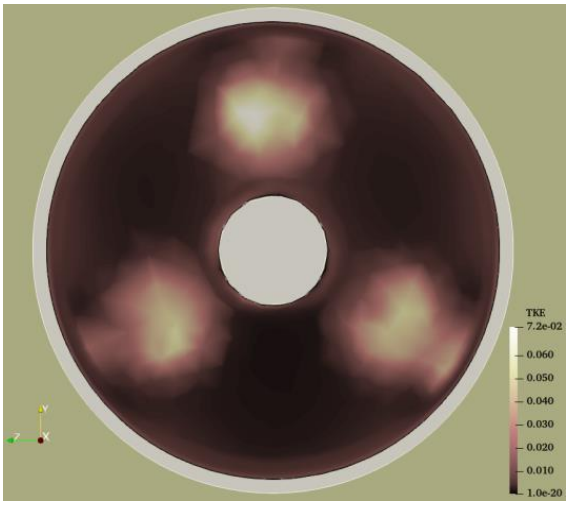

H=30mm, θ= 30°, N=4

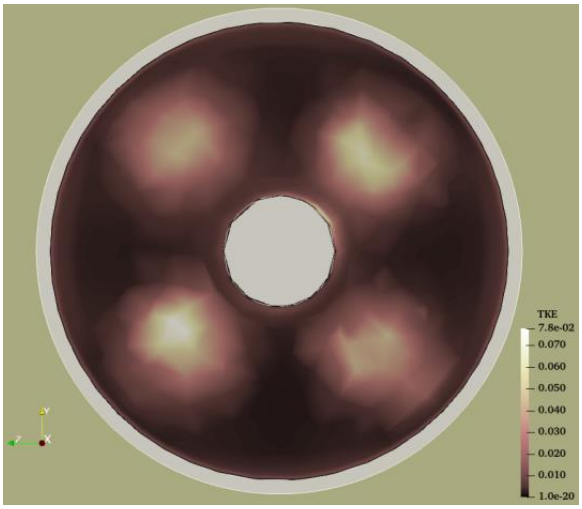

Figure 6.5: Effect of number of strip-inserts on the turbulent kinetic energy (TKE) distributions.

6.4.2. Receiver Hydraulic Characteristics

The use of swirl generators results in an added pressure drop and a higher pumping power requirement compared to the plain absorber configuration. This is not desirable, as it leads to an increase in the investment cost of the system. In fact, large swirl generators have significant effect on the working fluid pressure drop (due to the larger friction factor and blockage effects). Figure 6.6 presents the specific pressure drop (ΔP/L) change for all swirl generator configurations with and without nanofluids. It can be observed that at a constant Re number, the pressure drop increases gradually with increasing pitch height and pitch angle, reaching the maximum value for the largest single insert geometry (H30mm, θ30°), as shown in Figure 6.6e.

Similarly, a significant increase can be noted with an increase in the number of inserts. These results are in line with the findings of Mwesigye et al. (2016), Xiangtao et al. (2017) and Bellos and Tzivanidis (2018). The comparisons of thermal enhancement revealed that the pressure drop was more sensitive to the presence of the swirl generator than the Nu number. This was expected, as the insertion of swirl inserts adds to the friction and blockage.

Similar observations were made in the case of the nanofluid; an increase in the pressure drop compared to the pure working fluid configuration, due to the change in fluid characteristics such as dynamic viscosity and fluid density. Thus, the pumping requirement increases for the nanofluids. Increasing the working Re number also caused a considerable increase in the pressure drop due to the increase in the flow turbulence which requires larger pressure drop to force working fluid moving through the solar absorber tube. It is worth mentioning here that the current study combined the swirl generators with nanofluid, which resulted in an added pumping power requirement, as shown in Figure 6.6. The main aim here is heat transfer augmentation, and power requirements are not a constraint as far as this study is concerned. However, from a practical installation perspective one cannot ignore the power input requirement.

For single and multiple conical inserts with and without nanofluids, the specific pressure drop changes at a Re numbers of 100,000 are listed in Table 6-2. It can be concluded that the increase in the specific pressure drop due to the presence of the swirl generators was on average 11.78% more than that produced by the introduction of nanofluids.

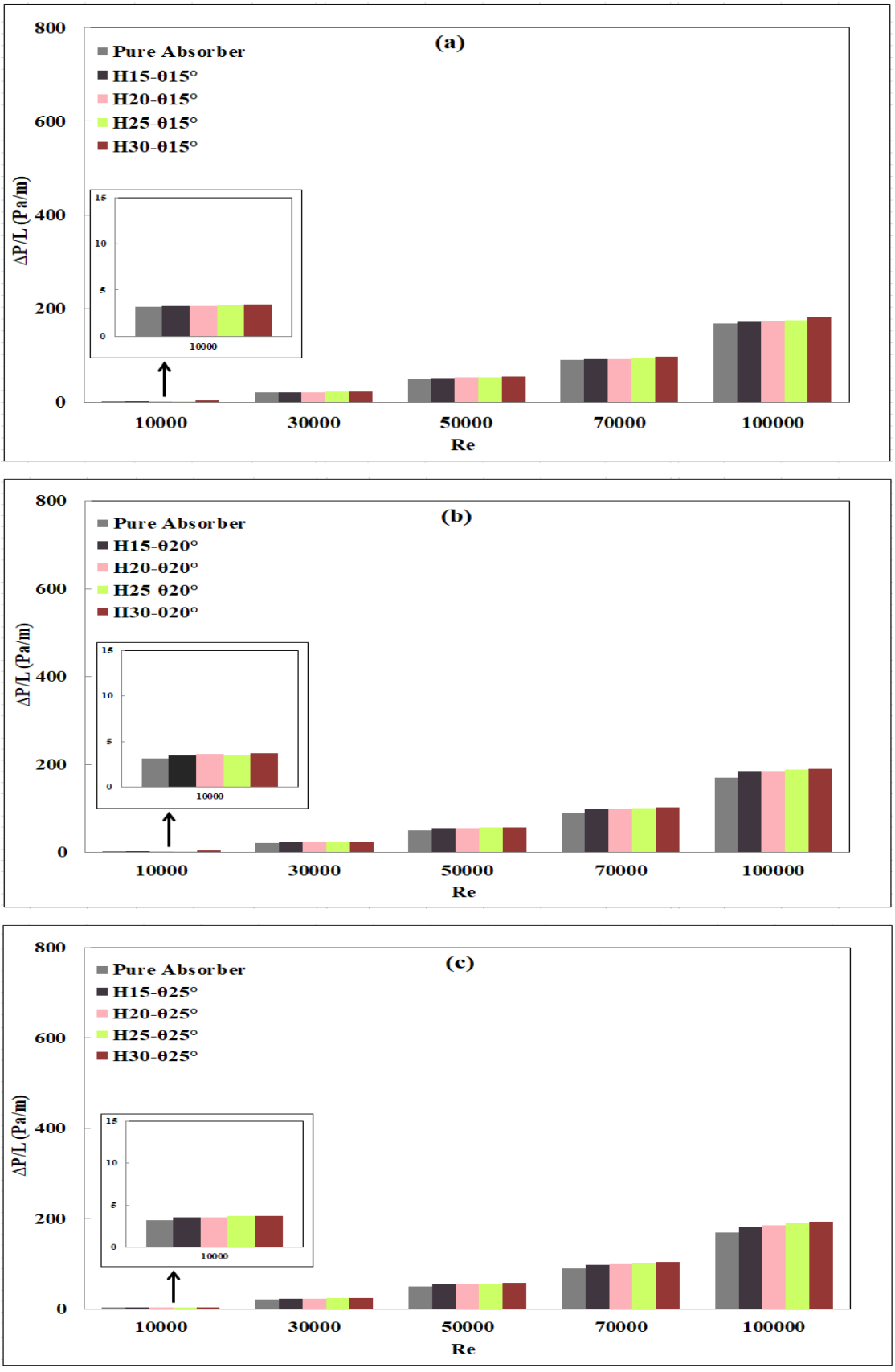

Figure 6.6: Pressure drop changes in the presence of swirl generators of pitch height variation with: (a) $\theta = 15^{\circ}$, (b) $\theta = 20^{\circ}$, (c) $\theta = 25^{\circ}$.

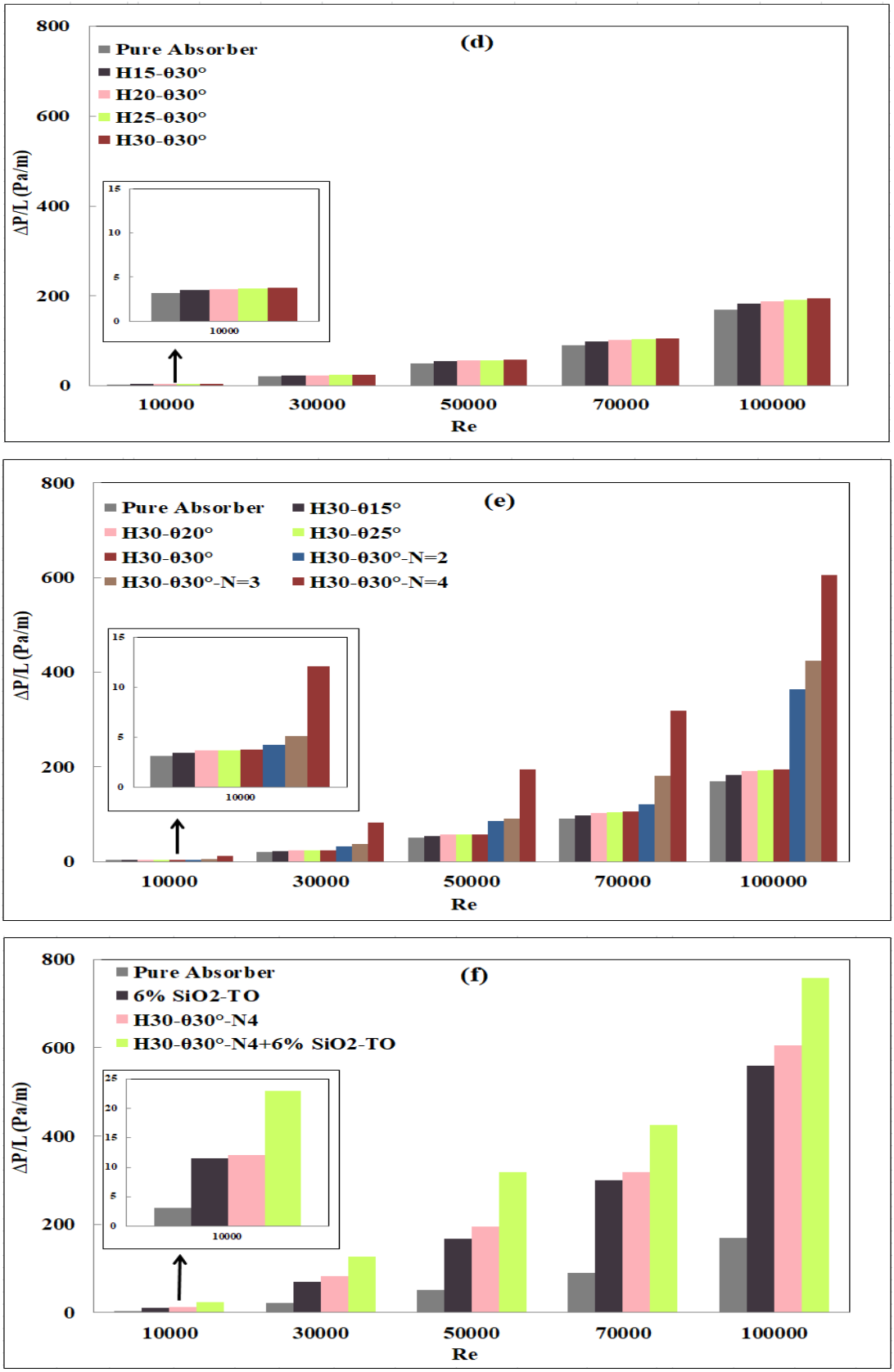

Figure 6.6(continued): Pressure drop changes in the presence of swirl generators. (d) Pitch height variation with $\theta = 30^{\circ}$, (e) Pitch angle (θ) and number of inserts (N) variation with fixed pitch height, (f) Optimal configuration with/without nanofluids.

Table 6-2: Hydraulic enhancement in the pressure drop for single and multiple conical inserts with and without nanofluid at a Re number of 100,000.

Case	ΔP/L	Enhancement (%)
Pure absorber	169.09	-
H30-θ30°-N1	218.18	29.03
H30-θ30°-N2	363.63	115.053
H30-θ30°-N3	454.54	168.81
H30-θ30°-N4	606.06	258.42
6% SiO_2-TO	560	231.18
H30-θ30°-N4+6% SiO_2-TO	757.57	348.03

6.4.3. Performance Evaluation Criterion

The performance evaluation criterion (PEC) can be used to assess the thermal and hydraulic performances of any passive or active technology that is integrated in a typical solar receiver system. This parameter is based on the relative comparison of the Nu number and friction factor of the enhancement configuration compared to the base case.

If the PEC is greater than one, it means that both the Nu number and pressure drop produced by the applied technology have been enhanced and increased. However, if the PEC is less than one, it means that the pressure drop increase is larger than the Nu number enhancement. The PEC behaviour of all insert configurations is presented in Figure 6.7. It can be observed that the levels of enhancement in the thermal and hydraulic performances fluctuate and change for all configurations, with the general trend being that the PEC increases with an increase in the pitch angle and decreases with an increase in the number of inserts. However, for the combined case of nanofluid with inserts, the gain in the Nu number is significantly larger that the increase in the pressure drop and thus the PEC for this optimal case stands at 1.423.

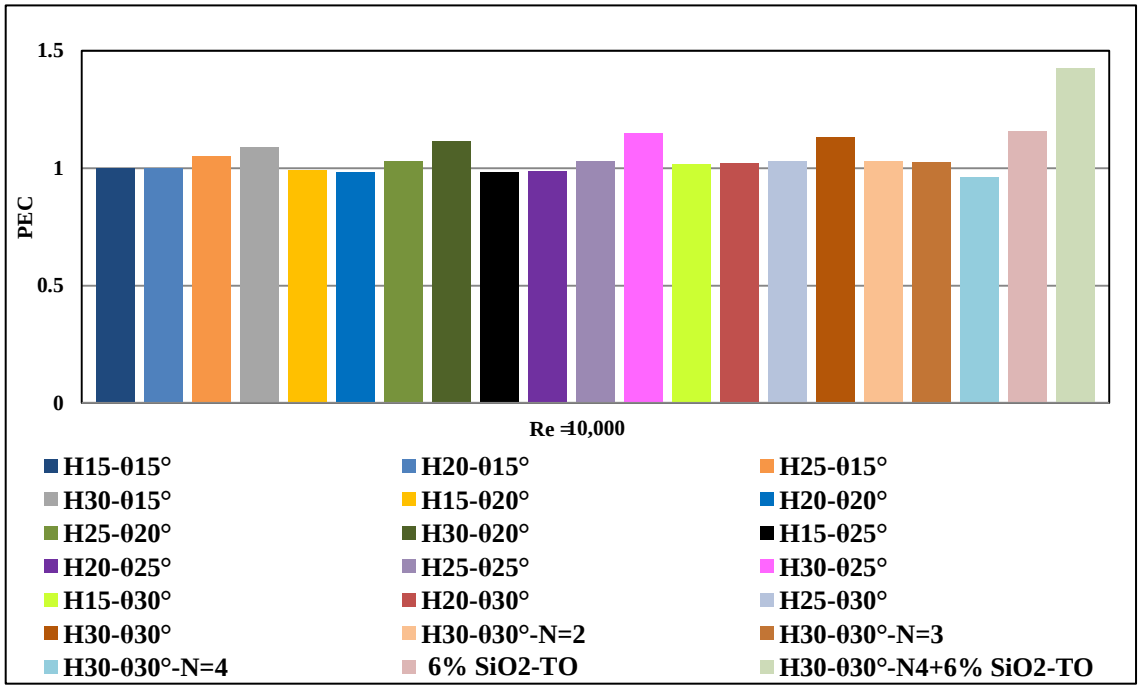

Figure 6.7: Effect of configuration changes on the performance evaluation criterion (PEC).

6.4.4. Thermal Losses

The introduction of swirl generators inside a PTC significantly reduces the thermal losses as they increase the absorption of thermal energy from the inner wall surface of the solar receiver. This results in extracting more thermal energy from the external wall of the solar receiver, thereby reducing the external wall temperature. Thus, increasing the surface area of swirl generators leads to an increase in the absorption of thermal energy, leading to a gradual reduction in the convection and radiation thermal losses over the external walls of the solar receiver. Figure 6.8 presents the thermal losses for all configurations with and without nanofluid.

It can be observed from Figure 6.8a–d that by keeping the pitch angle constant, the thermal losses can be reduced simply by increasing the pitch height. Similarly, increasing the pitch angle also reduces the thermal losses. These losses can further be reduced by increasing the number of conical strips, as show in Figure 6.8e. Similar conclusions were also drawn by a number of previous studies; Cheng et al. (2012b); Bellos and Tzivanidis (2018); Liu et al. (2019a); Arshad et al. (2019).

An additional technique examined in this study was to analyse the mixing of 6% volume fraction of SiO_2 nanoparticles in Therminol VP-1. This technique resulted in the development of a new working fluid which has better thermal properties than that of the pure working fluid, thereby reducing the thermal losses further, as shown in Figure 6.8f. Finally, the combination of swirl inserts with nanofluids leads to the most optimum case, in which the reduction of losses is about 23.7%. It is prudent to mention here that overall, the reduction in losses was found to be more sensitive to the increase in the number of inserts than to the use of the nanofluids. Another important feature that can be noted from Figure 6.8 is that the thermal losses were lower for the high Re number cases. This is due to the enhancement of turbulence and the increase in the flow path, thus the working fluid has an opportunity to collect more thermal energy than that in the case of pure absorber.

Finally, the reductions in thermal losses of single and multiple swirl generators with and without nanofluids are presented in Table 6-3, at a Re number of 10,000.

Table 6-3: Thermal loss reductions for single and multiple conical insert cases with and without nanofluid at Re = 10,000.

Case	**Specific Thermal Losses (W/m)**	**Reduction (%)**
Pure absorber	333.26	−
H30-θ30°-N1	274.29	−17.60
H30-θ30°-N2	269.21	−19.20
H30-θ30°-N3	267.206	−19.82
H30-θ30°-N4	258.88	−22.30
6% SiO_2-TO	280.85	−12.00
H30-θ30°-N4+6% SiO_2-TO	254.30	−23.70

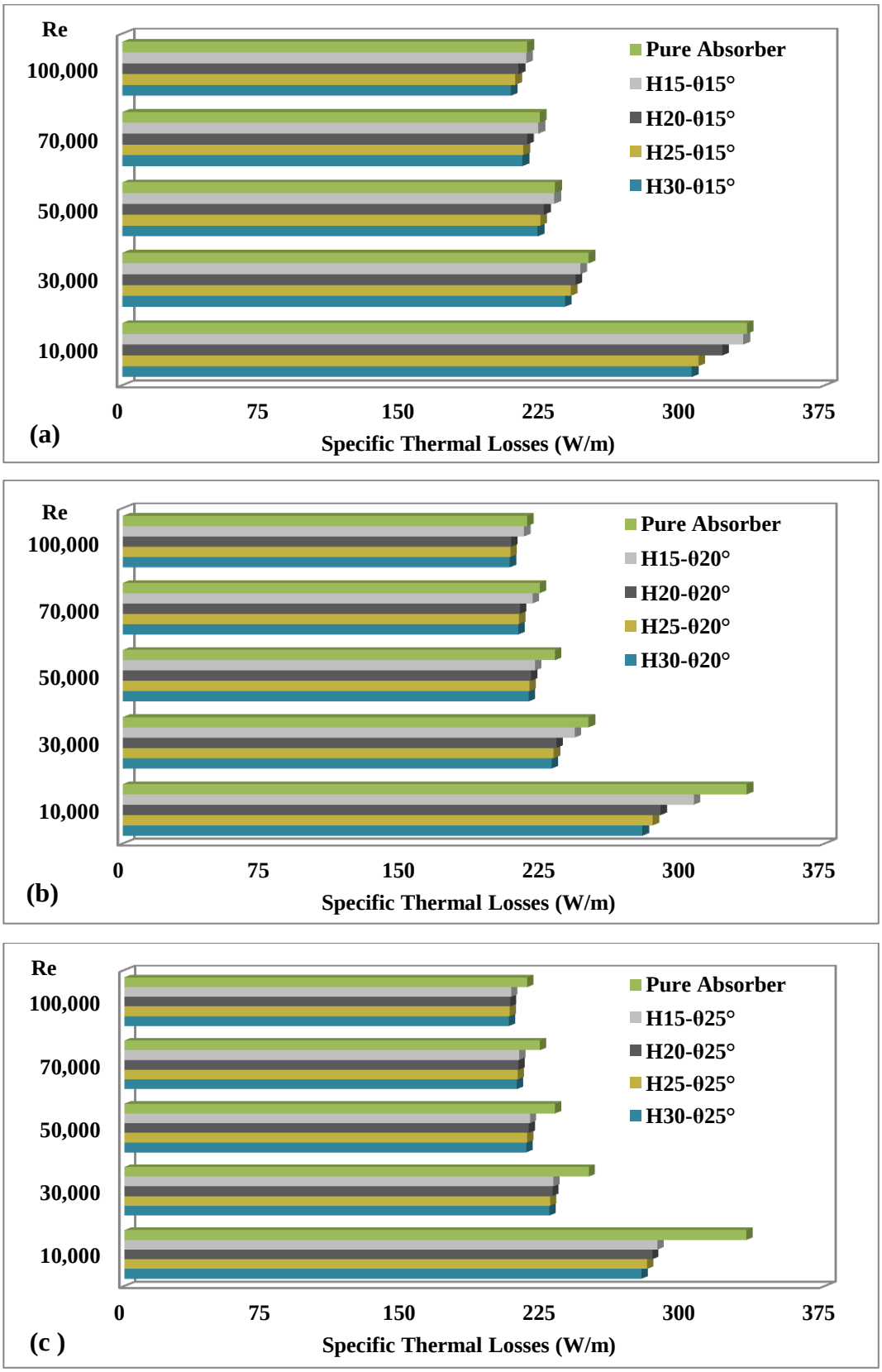

Figure 6.8: A comparison of thermal losses for all considered configurations of pitch height variation with: (a) $\theta = 15^{\circ}$, (b) $\theta = 20^{\circ}$, (c) $\theta = 25^{\circ}$.

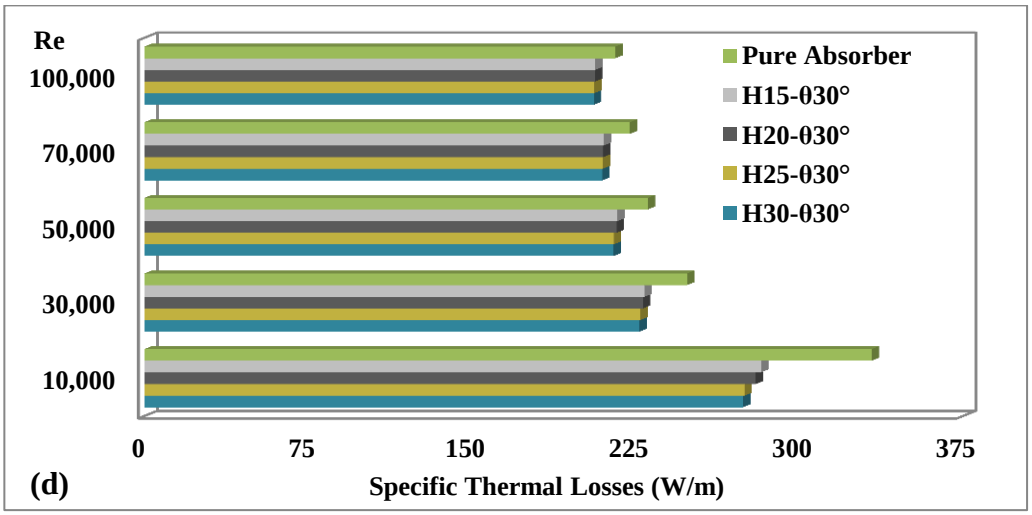

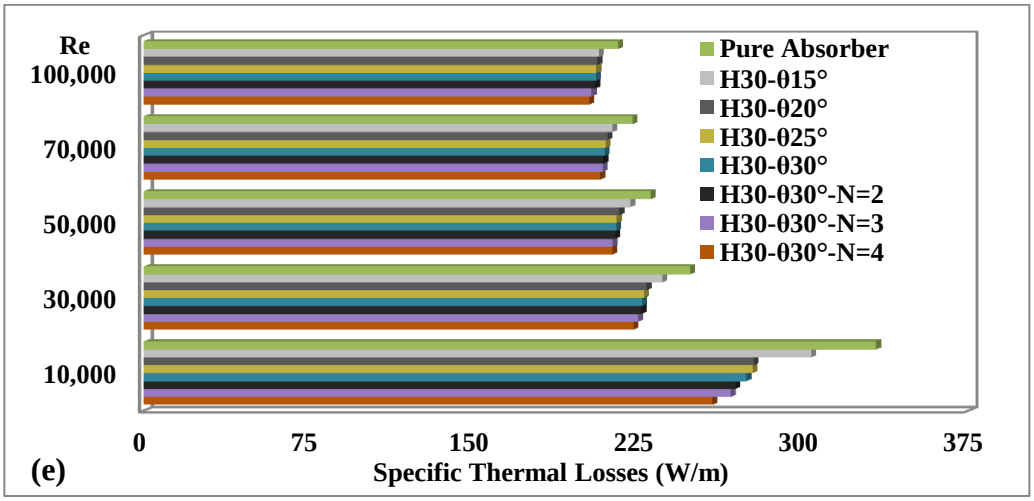

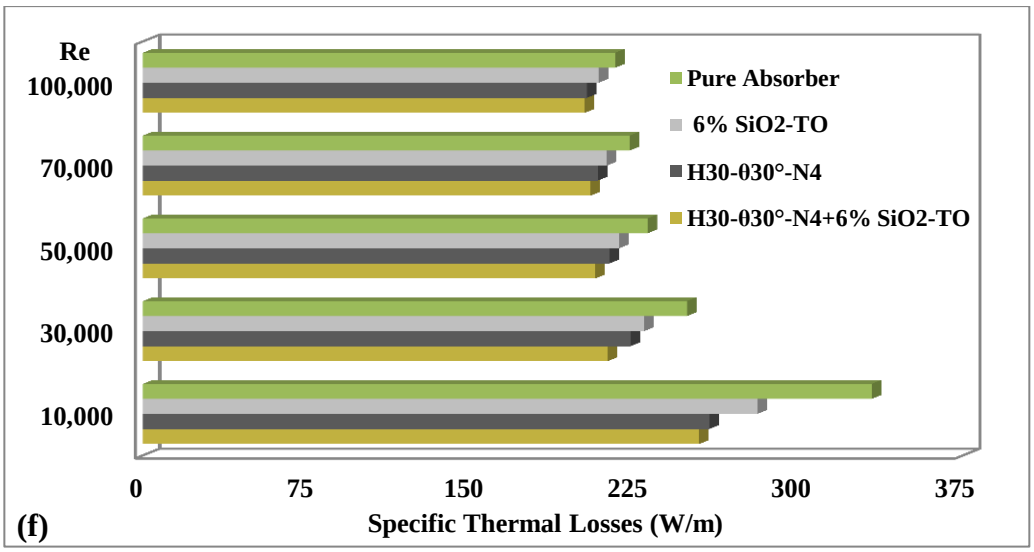

Figure 6.8(continued): Comparison of thermal losses for all considered configurations. (d) Pitch height variation with $\theta = 30^{\circ}$, (e) Pitch angle (θ) and number of inserts (N) variation with fixed pitch height, (f) Optimal configuration with and without nanofluids.

6.4.5. Overall Collector Efficiency

The overall thermal efficiency, considering the effect of pumping power required for the conical insert configuration, can be used for the evaluation of the system, as shown in Figure 6.9. It is evident from Figure 6.9a–e that the overall thermal efficiency increases with both the pitch angle and the pitch height for the single canonical insert. With the introduction of additional inserts, this efficiency further improves, as also reported by Mwesigye et al. (2014); Mwesigye et al. (2019); Bellos and Tzivanidis (2018); Liu et al. (2019a); and Arshad et al. (2019). Once again, when the two techniques were combined that is, swirl inserts with nanofluid the efficiency increase was the highest, as shown in Figure 6.9f.

The enhancement in the overall thermal efficiency is due to several factors, but it is mainly due to an increase in absorption, which leads to improved convective heat transfer behavior and reduced the convection and radiation thermal losses. This results in higher output working fluid temperatures and useful heat energy gain. Thus, one can conclude that by reducing the solar receiver wall temperature gradient, the convection and radiation thermal losses can be reduced. It can be further noted that the overall thermal efficiency was better at lower Re numbers. This is because at high Re numbers, the gain in the convection heat transfer is not enough to overcome the pressure drop and thermal losses at these high flow velocities.

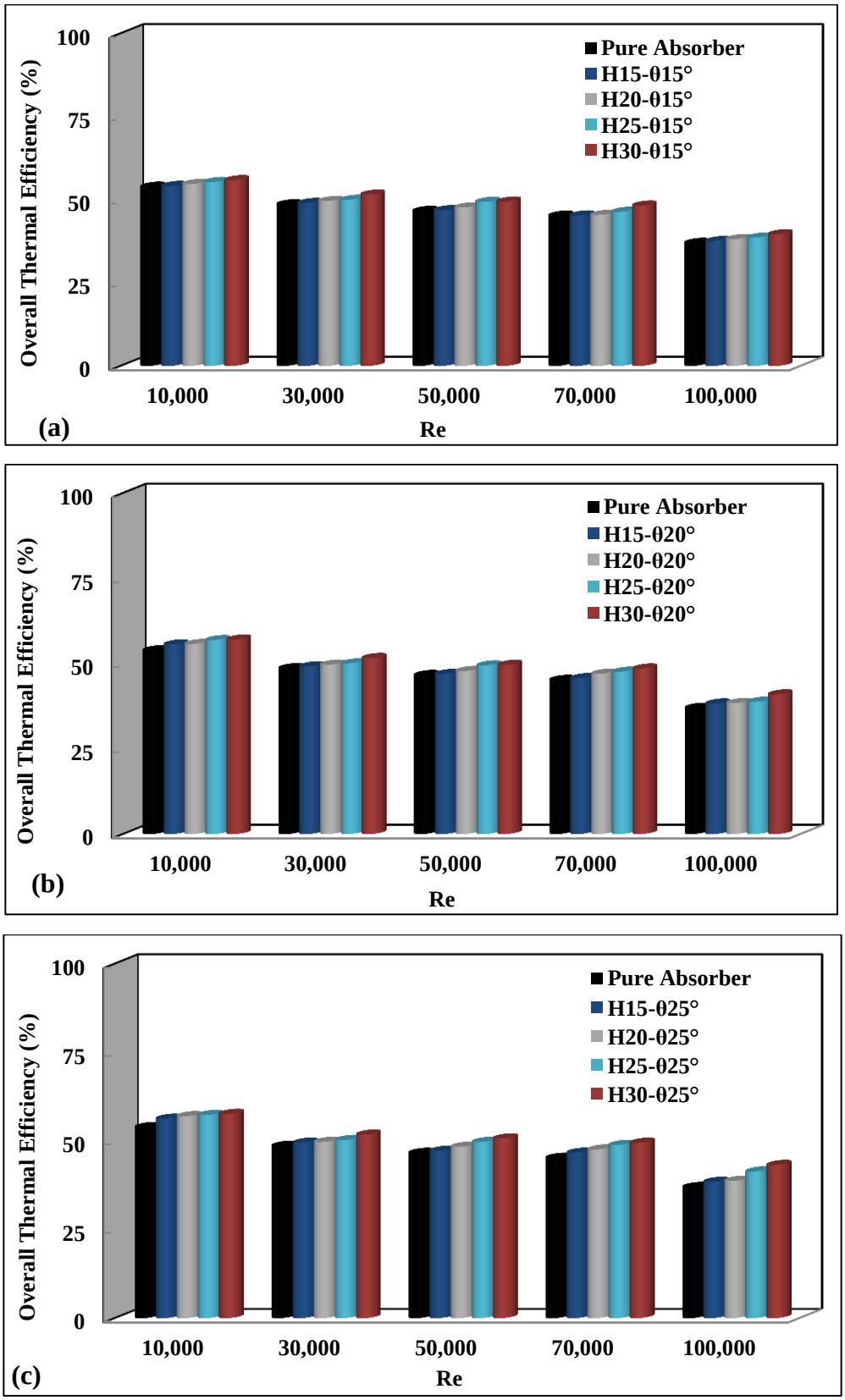

Figure 6.9: Overall thermal efficiency comparisons for all considered cases of pitch height variation: (a) $\theta = 15^{\circ}$, (b) $\theta = 20^{\circ}$, (c) $\theta = 25^{\circ}$.

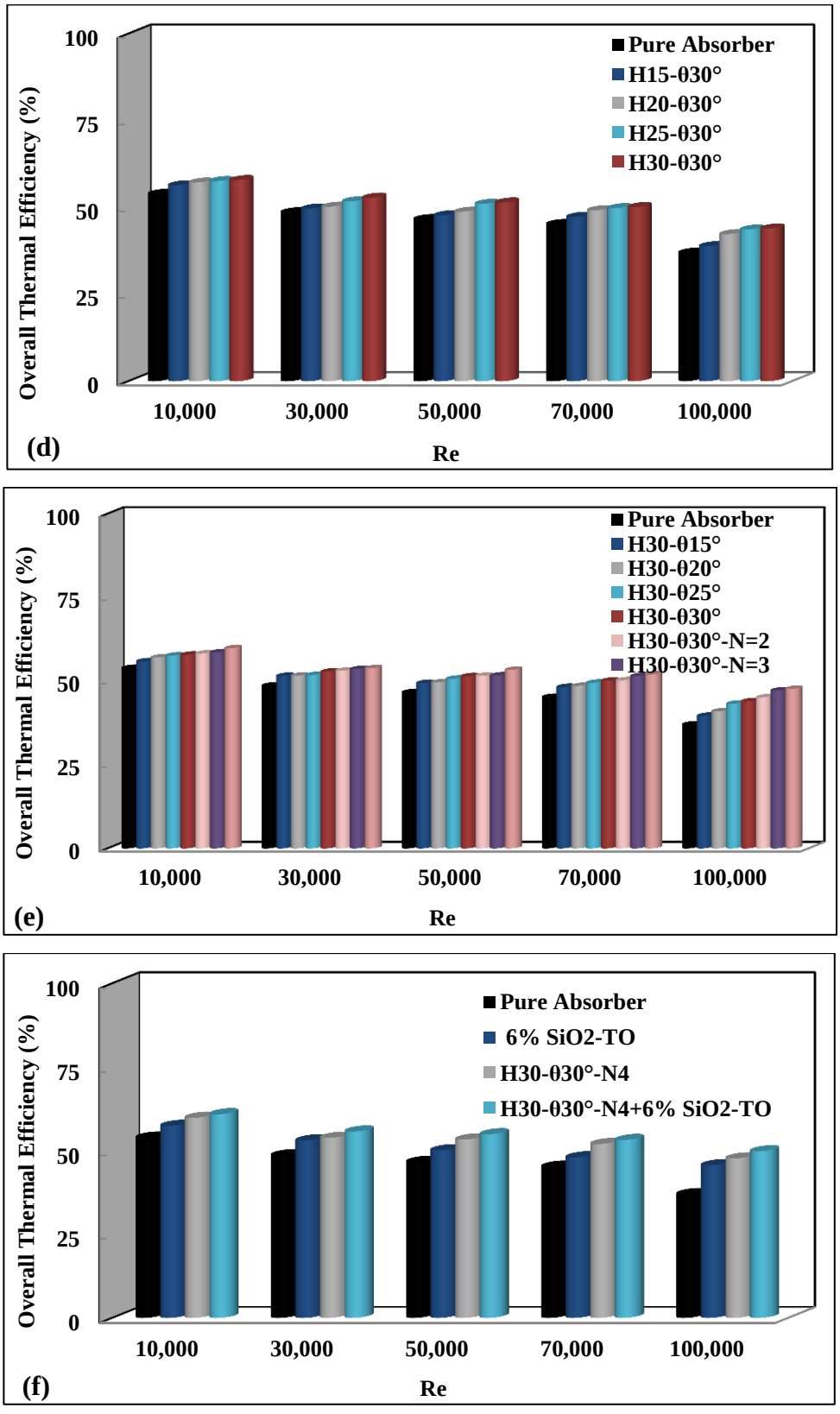

Figure 6.9(continued): Overall thermal efficiency comparisons for all considered cases: (d) pitch height variation with $\theta = 30^{\circ}$, (e) Pitch angle (θ) and number of inserts (N) variation with fixed pitch height, (f) Optimal configuration with and without nanofluids.

The main improvement in the overall thermal efficiency for single and multiple swirl generators with and without nanofluid are given in Table 6-4 for a Re number of 30,000.

Table 6-4: Overall thermal efficiency enhancement for single and multiple conical insert cases with and without nanofluid at Re = 30,000.

Case	**Overall Thermal Efficiency (%)**	**Improvement (%)**
Pure absorber	48.61	-
H30-θ30°-N1	52.81	8.637
H30-θ30°-N2	53.08	9.184
H30-θ30°-N3	53.57	10.19
H30-θ30°-N4	53.84	10.74
6% SiO_2-TO	53.05	9.11
H30-θ30°-N4+6% SiO_2-TO	55.72	14.62

6.4.6. Thermal Exergy Efficiency

To assess the actual effect of introducing swirl generators on the maximum net possible work production of the PTC system, the thermal exergy efficiency was considered for assessment. A comparison of thermal exergy efficiency for all considered cases is presented in Figure 6.10. Once again it can be observed that the trends of thermal exergy efficiency are very similar to the overall collector efficiency, i.e., it increases with an increase in the pitch angle, an increase in the pitch height, and with an increase in the number of strips, as also reported by Bellos and Tzivanidis (2018) and Bellos et al. (2018d).

Finally, it can be seen in Figure 6.10f that even though the addition of nanofluid to the insert configuration improves the exergy efficiency (in the optimal case of four inserts with nanofluid), the gain by adding only the nanofluid was not as significant as the gain in the case of inserts alone. The main improvements in the thermal exergy efficiency for single and multiple conical strips with and without nanofluids are shown in Table 6-5 at a Re number of 30,000.

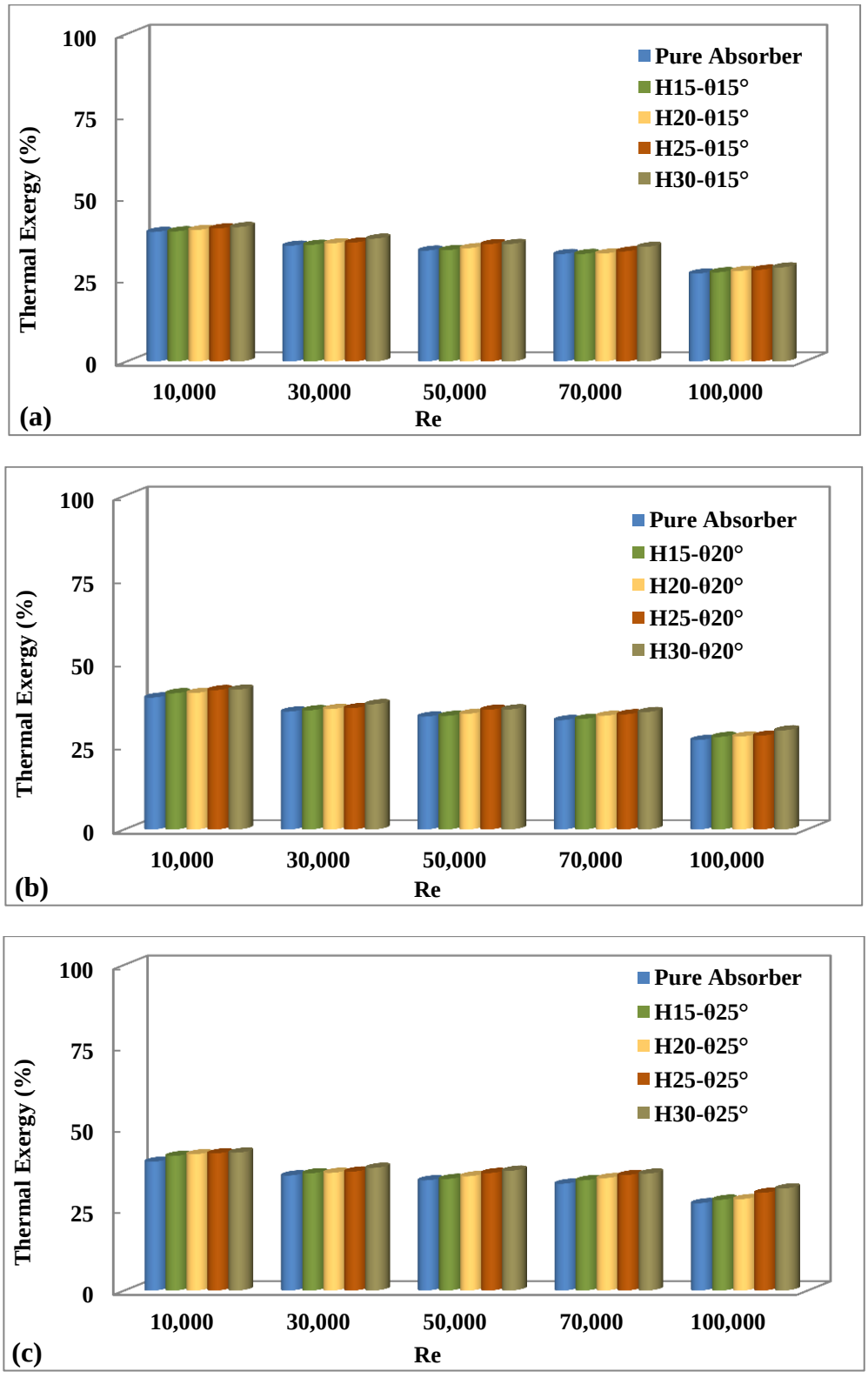

Figure 6.10: Comparison of thermal exergy efficiency for all considered cases of pitch height variation with: (a) $\theta = 15^{\circ}$, (b) $\theta = 20^{\circ}$, (c) $\theta = 25^{\circ}$.

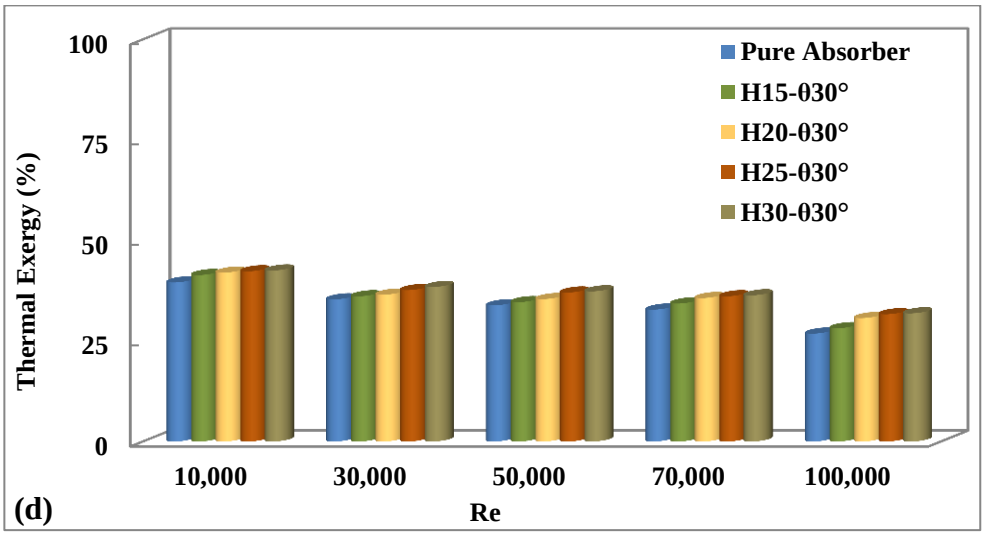

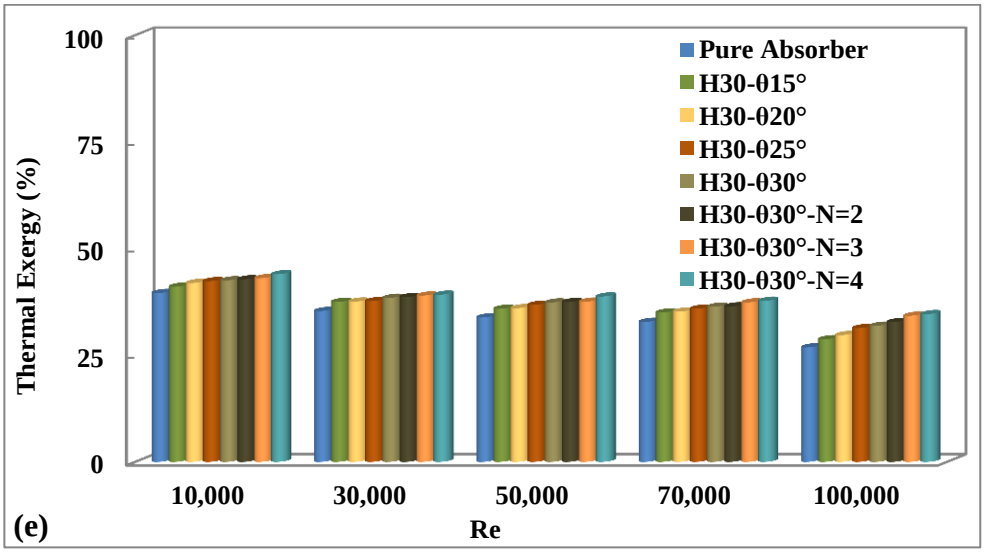

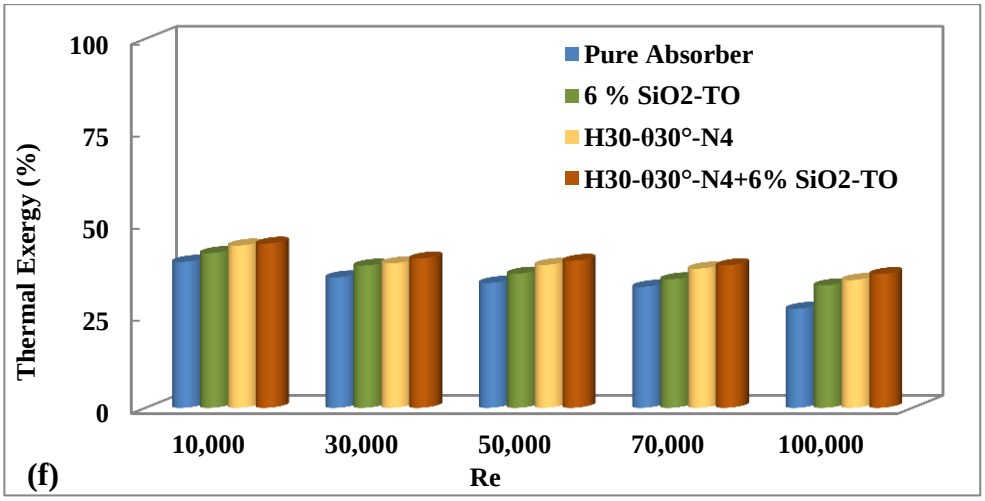

Figure 6.10(continued): Comparison of thermal exergy efficiency for all considered cases. (d) Pitch height variation with $\theta = 30^{\circ}$, (e) Pitch angle (θ) and number of inserts (N) variation with fixed pitch height, (f) Optimal configuration with and without nanofluids.

Table 6-5: Thermal exergy efficiency enhancement for single and multiple conical insert cases with and without nanofluid at Re = 30,000.

Case	Thermal Exergy Efficiency (%)	Improvement (%)
Pure absorber	35.36	-
H30-θ30°-N1	38.43	8.67
H30-θ30°-N2	38.63	9.22
H30-θ30°-N3	38.98	10.24
H30-θ30°-N4	39.18	10.79
6% SiO_2-TO	38.557	9.02
H30-θ30°-N4+6% SiO_2-TO	40.48	14.40

It should be noted here that the drop in all variables under consideration (Nu number, specific pressure drop, thermal losses, overall collector efficiency and thermal exergy efficiency) between the Re number from 10000 to 30000 and from 70000 to 100000 is larger than the change in variables in the Re number between 30000 to 50000 and from 50000 to 70000. That could be due to the fact that the flow with a smaller Re number can absorb and collect thermal energy higher than those of flow with larger Re numbers. Moreover, from 70000 to 100000, the difference in Re number (100000-70000=30000) is 30000 whereas the difference between the middle Re number (30000, 50000 and 70000) is only 10000. Therefore, it is expected to achieve higher change in all variables from Re of 70000 to 100000 compared with middle Re numbers.

6.5. Conclusions

Improving the overall efficiency of PTCs can lead to enhancements in sustainable energy extraction and the reduction of greenhouse gas emissions. This goal was accomplished using three approaches. The first approach was to investigate the optimum configuration for straight conical strip inserts, which were attached to a central rod with varying parameters of pitch height, angle pitch, and the number of strip inserts. The second approach was to introduce 6% SiO_2 nanoparticles mixed with Therminol VP-1 at an inlet temperature of 400 K. Finally, the third approach was the combination of the optimized configuration swirl generator insert with nanofluids.

The evaluation of these approaches was based on the Nu number, pressure drop, PEC, thermal losses, overall thermal efficiency and thermal exergy efficiency. The main findings of this work are summarized below:

- The use of straight conical strips enhanced the Nu number by 47.13% whereas using nanofluids alone improved the Nu number by 15.57%. However, an improvement of 57.48% was observed for the Nu number by combining the swirl inserts and nanofluids. This combination also resulted in the maximum reduction of thermal losses by 23.7%.

- The improvement in the Nu number comes at the expense of an increase in the pressure drop. Swirl generators and nanofluids alone increased the pressure drop by 258.42% and 231.18%, respectively. However, when these were combined, the pressure drop reached as high as 348.03%.

- All the examined cases showed different levels of enhancements in the overall thermal efficiency and thermal exergy efficiency. For the combined case of nanofluid with optimum swirl generator configuration, the overall thermal efficiency improved by 14.62% and the thermal exergy efficiency increased by 14.47%.

  The gain in improvement of all tested parameters was found to be more sensitive to the insert geometry and the number of inserts as opposed to the nanofluids. Thus, it can be concluded that swirl inserts are a better candidate than nanofluids for thermal performance improvement in PTC systems.

Chapter 7: Effect of various multiple strip inserts and nanofluids on the thermal-hydraulic performances of PTCs

7.1. Introduction

An effective strategy to increase the thermal performance of PTC systems is the inclusion of metallic inserts in the flow path of the heat transfer fluid inside the solar absorber as shown in the previous chapter. Depending on their design, metallic inserts can simply increase the surface area available for heat transfer, or they can also enhance the mixing and turbulence level in the heat transfer fluid. The thermal and thermodynamic performances of the PTC can be improved by containing the swirl generators inserted inside the solar receiver by collecting larger amount of thermal energy from the internal receiver wall and delivering it to the heat transfer fluid. At the same time, the external receiver wall temperature is reduced leading to decrease the radiation and convection thermal losses. Moreover, mixing the nanoparticles in heat transfer fluids results in new heat transfer fluid that has better thermal properties than those of the pure fluid which in turn helps to increase the output working fluid temperature as well as reducing the outer wall's temperature.

It was found in the previous chapter that using four straight small conical strips attached to the core rod enhanced the heat transfer by 47.13% whereas the combination of swirl generator and nanofluid (6% of SiO_2-Therminol nanofluid) increased the heat transfer by 57.48% thereby reducing the thermal losses to 22.3% and 23.7% for both cases respectively, Abed et al. (2021). Moreover, the overall collector thermal efficiency and thermal exergy efficiency were 10.74% and 10.79% for pure swirl generator cases respectively while these parameters have increased to 14.62% and 14.47% in the case of swirl generators and nanofluids. Despite these preliminary though promising investigations, a systematic assessment of the thermal performance of PTC systems operated with nanofluids and incorporating swirl generators is still missing. The objective of the work in the current chapter is to provide such an assessment. In particular, the effect of different shapes of straight strip swirl generator inserts attached to the central rod was numerically investigated under different operating conditions and non-uniform heat flux profile around the absorber tube. Four different strip arrangements are considered: 1) large conical-shape strips, 2) small conical-shape strips, 3) rectangular-shape strips, and 4) elliptical-shape strips; attached around a central rod of a diameter of Dr=1.6 cm.

Every arrangement was examined for a range of application-representative Re number values from 10^4 to 10^5. The nanofluid used was 6% of SiO_2 nanoparticles mixed in Therminol® VP-1 base fluid at an inlet temperature of 400 K, as informed by the preliminary results reported in the chapter five. All case studies are steady-state and assume incompressible three-dimensional flow where the heat flux distribution is taken as a realistic profile by applying the MCRT model in the circumferential direction.

7.2. Physical model of examined inserts

In the present chapter, various strip shapes are examined: elliptical strips, rectangular strips, small conical strips and large conical strips as shown in Figure 7.1. All strips are attached to the central rod with a right angle to study how these configurations influence the thermal and hydraulic characteristics. The geometrical characteristics of all strip shapes are clarified in Figure 7.1. All strips have a constant thickness (t) of 10 mm and constant horizontal pitch (P) between strip sets which is 486 mm. The first set of strips is positioned 10 mm downstream the tube inlet. In more details, each examined shape set has four strips that have constant height (H = 30 mm) and located in the major and minor diagonals of the absorber tube. The elliptical geometry has small diameter of 9 mm and large diameter of 60 mm whereas the rectangular geometry has width of 9.18 mm and length of 60 mm with curved ends. However, the small conical geometry has an angle 30° and 30 mm height while the large conical strip has an angle of 70° with 30 mm constant height. Each package configuration is concentrated at the center of the absorber tube. The swirl generator is designed to be a part of the whole parabolic trough collector. The strip inserts are arranged around a central rod and the whole assembly can be easily installed in a modular fashion to the inside the solar receiver. Such a configuration can also be easily taken apart for routine maintenance.

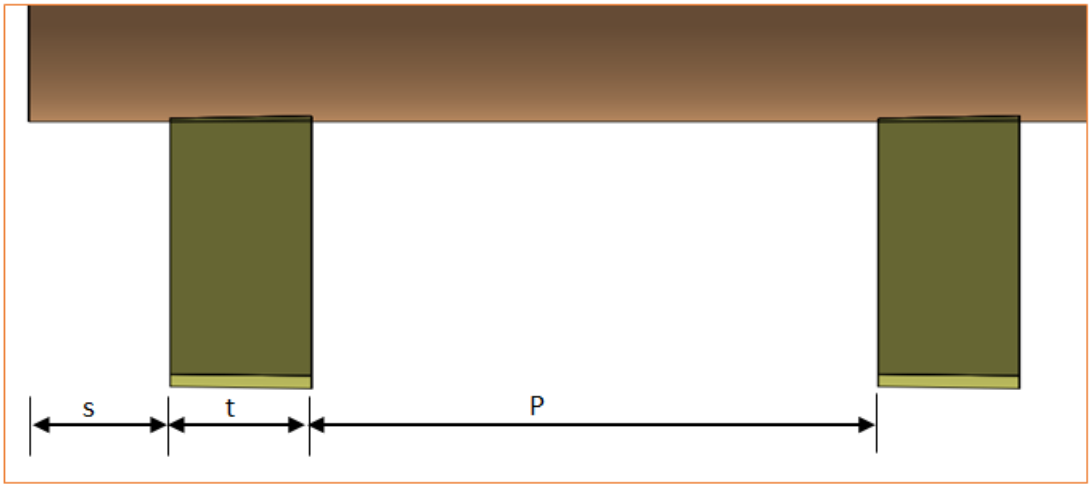

(a) Lateral view of half examined inserts

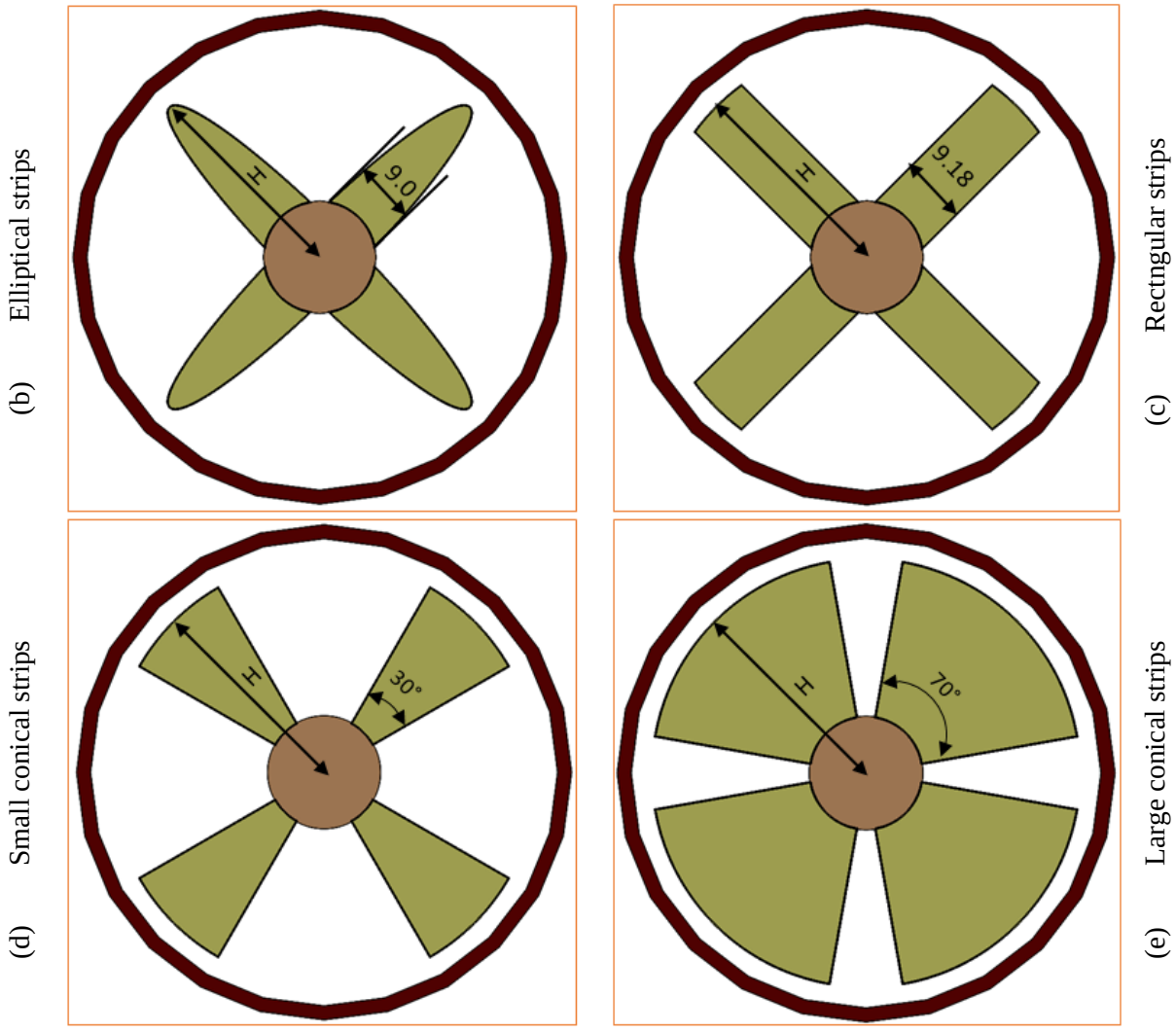

(b) Elliptical strips (c) Rectngular strips (d) Small conical strips (e) Large conical strips

Figure 7.1: The examined straight strips in the current chapter.

7.3. Results and Discussions

In this section, the numerical achievements are comprehensively illustrated and discussed with reference to various hydraulic and thermal parameters that are mostly influenced by the presence of nanofluids and swirl generator inserts in the PTC. These parameters include convection heat transfer represented by Nu number, pumping power requirements represented by the specific pressure drop, PEC, radiation and convection thermal losses, overall thermal efficiency and thermal exergy efficiency.

7.3.1. Heat Transfer Performance

Inserting swirl generators inside the solar receiver acted at absorbing energy from the internal receiver's wall and reflecting it to the heat transfer fluids thereby enhancing the convection heat transfer. The variations of average Nu numbers on the solar receiver as a function of Re number of all swirl generator cases with/without nanofluids are presented in Figure 7.2. It is clearly shown in Figure 7.2a that the thermal energy performance improves with inserting the swirl generators starting with the elliptical-shape strips and a gradual enhancement is noticed with changing the strip shape reaching the maximum thermal energy performance with the large conical strips, followed by the small conical strips then by the rectangular strips, in line with the previous findings reported by Mwesigye et al. (2016b) and Bellos et al. (2017b). The maximum heat transfer enhancement is recorded by the large conical strips due to the larger surface area of swirl generator in contact with the heat transfer fluid which reflects part of absorbed energy to the heat transfer fluid and also due to larger mixing of heat transfer fluid and higher turbulent intensity from the induced swirl, as presented in Figure 7.3. Moreover, introducing the nanofluid technology acted at enhancing the thermal properties of the heat transfer fluid resulting in larger Pr number. In other words, larger thermal conductivity is achieved with using nanofluid technology. This acted at increasing the thermal performance of the PTC system by absorbing more energy from the internal receiver walls as well as by enhancing the output working fluid temperature compared with the typical absorber tube as shown in Figure 7.2b. The third technology explored in the current study combines a 6%-concentration SiO_2-TO nanofluid with various swirl generators: elliptical-shape strips, rectangular-shape strips, small conical-shape strips and large conical-shape strips. In this case, the higher Pr number of the nanofluid and the enhanced fluid mixing due to the presence of the swirl generators combine to provide larger thermal energy enhancement compared with using only nanofluid technology or inserting only swirl generators with pure fluids.

Table 7-1 compares the enhancements in Nu number of all swirl generators and nanofluids compared with the typical solar receiver.

As can be seen, the thermal energy enhancement in the presence of nanofluid and swirl generators showed different improvement levels depending on the contact surface area of the swirl generators, where in particular the maximum enhancement in the Nu number was provided by the large conical-shape strip. On the other hand, the minimum improvement in the Nu number was recorded by the elliptical-shape strips.

Table 7-1: Thermal enhancement in the Nu number of the multiple strip-shape insert cases with nanofluid.

Case	***Nu* number**	**Enhancement (%)**
Pure absorber	674.83	-
6% SiO_2-TO	779.95	15.57
Elliptical strips + 6% SiO_2-TO	837.36	24.08
Rectangular strips + 6% SiO_2-TO	965.03	43.00
Small conical strips + 6% SiO_2-TO	1062.78	57.48
Large conical strips + 6% SiO_2-TO	1096.75	62.52

The Nu number shows gradual augmentation with increasing the Re number in all swirl generator cases with nanofluid reaching the maximum values with the maximum Re numbers as shown in Figure 7.2. This is the consequence of the reduction in the thermal boundary layer thickness with increasing the Re number, which leads to higher absorbed thermal energy compared with the smaller Re numbers due to reduction in both average wall temperature and output fluid temperature.

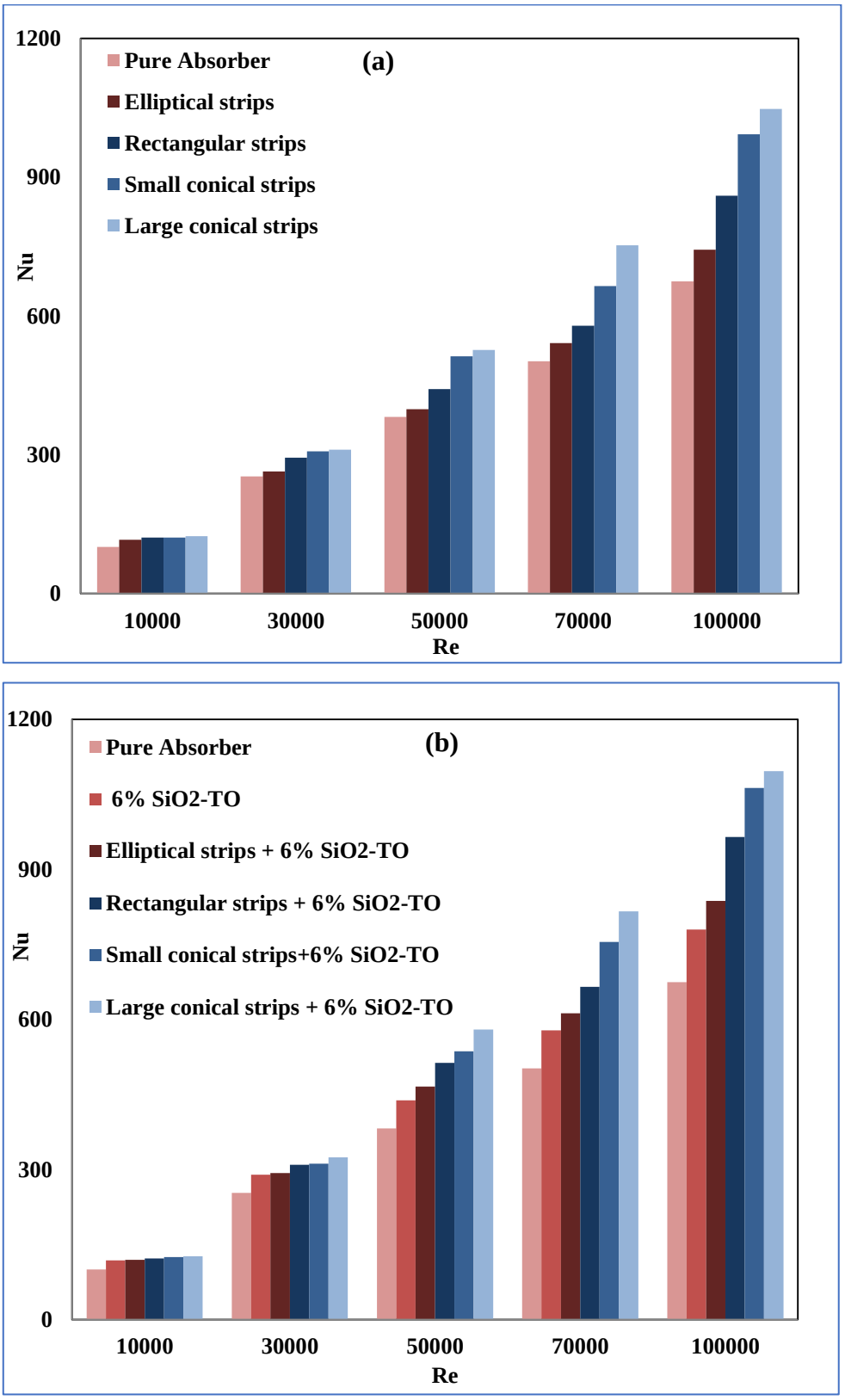

Figure 7.2: Effect of all considered cases of swirl generators and nanofluid on heat transfer performance.

Elliptical-shape strips

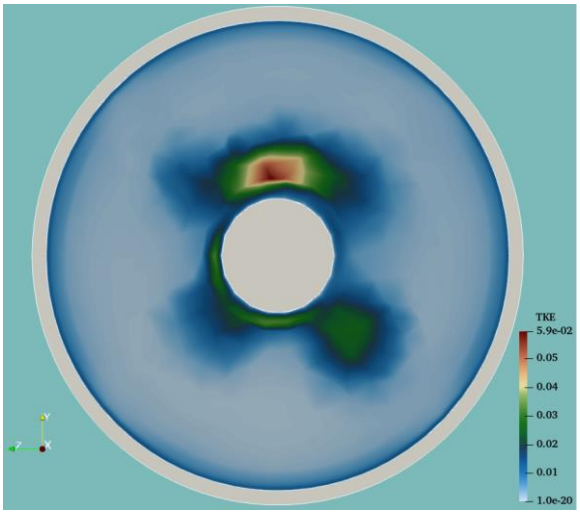

Rectangular-shape strips

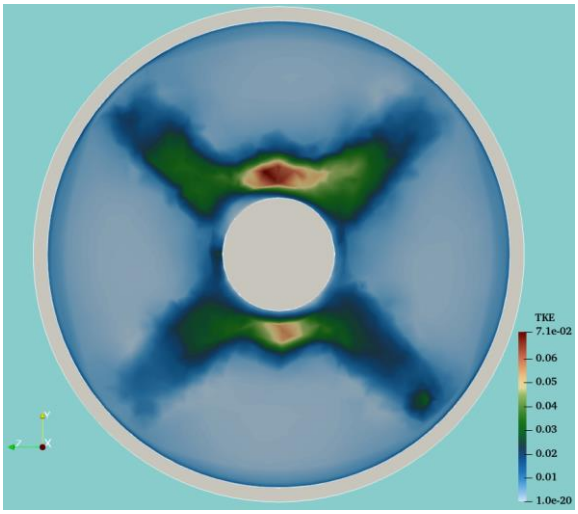

Small conical-shape strips

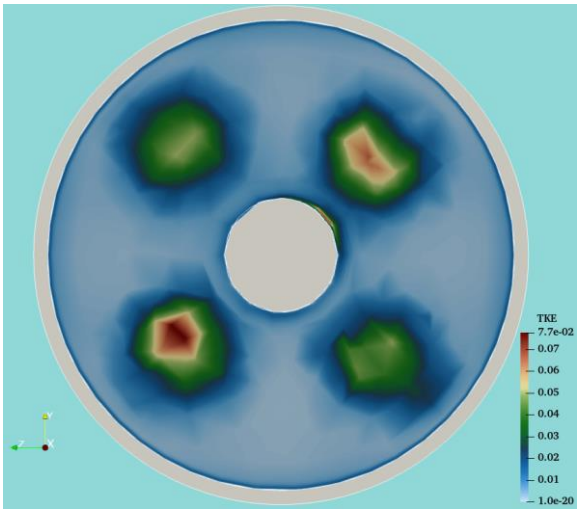

Large conical-shape strips

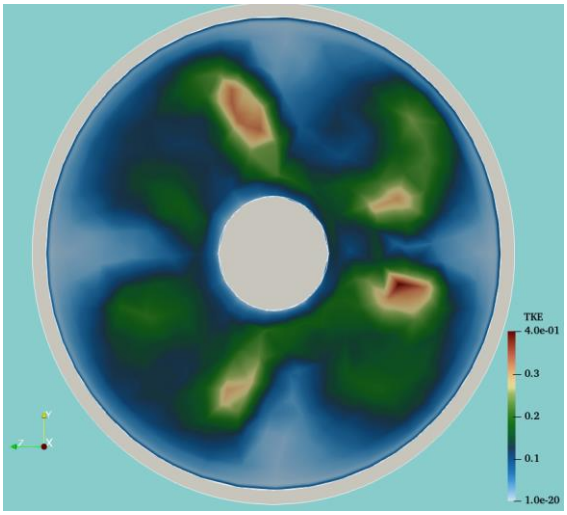

Figure 7.3: TKE distributions contours of all considered swirl generator cases at L=3.5m.

7.3.2. Receiver hydraulic characteristics

The introduction of the swirl generators inside the solar receiver improves the thermal performance, however this comes at the expense of increased pressure drop from enhanced fluid mixing and partial flow path restriction. The variations of specific pressure drop per unit channel length through the solar receiver as a function of Re number for all swirl generator cases with and without nanofluids are presented in Figure 7.4. It can be observed from this figure that there is a mild increase in the specific pressure drop when inserting the elliptical-shape strips, and a gradual increase with increasing the strip size reaching the maximum specific pressure drop with the large conical-shape strips.

This indicates that the more intense the induced swirl the larger the increase in the specific pressure drop, which is in qualitative agreement with the results previously reported by Mwesigye et al. (2016b), Xiangtao et al. (2017) and Bellos and Tzivanidis (2018).

In comparison with the base liquid, the nanofluid has higher viscosity and higher density, which also increases the specific pressure drop. It is not surprising that the combination of nanofluid and swirl generators leads to a significant increase in the specific pressure drop, as can be noted in Figure 7.4b. In turn, this leads to a significant increase in the pumping power requirements which increases the investment cost of the PTC system, reaching the maximum in the case of combining the large conical-shape strip with 6% SiO_2-TO nanofluids as compared with the plain receiver, see Table 7-2. Normally, heat transfer enhancement techniques for internal flows come with a pressure drop penalty, so that the present results are not surprising in this respect. The gain, represented by the enhancement in heat transfer, is compared with the cost, represented by the increased pressure drop, in the next section.

Table 7-2: Hydraulic increase in the pressure drop of the multiple strip-insert cases with nanofluid.

Case	**ΔP/L**	**Increase (%)**
Pure absorber	169.09	-
6% SiO_2-TO	560.00	231.18
Elliptical strips + 6% SiO_2-TO	715.15	322.94
Rectangular strips + 6% SiO_2-TO	727.27	330.11
Small conical strips + 6% SiO_2-TO	757.57	348.03
Large conical strips + 6% SiO_2-TO	1818.18	975.27

Increasing the Re number for the case means increase the fluid velocity which is clearly led to considerable enhancement in the specific pressure drop in all cases considered in the current work. This expected because of the fact that increasing the fluid velocity acted at increasing the flow impingement on the absorber tube and the swirl generator which requires larger pressure drop to overcome this issue and force the flow to cross the swirl generator's strips.

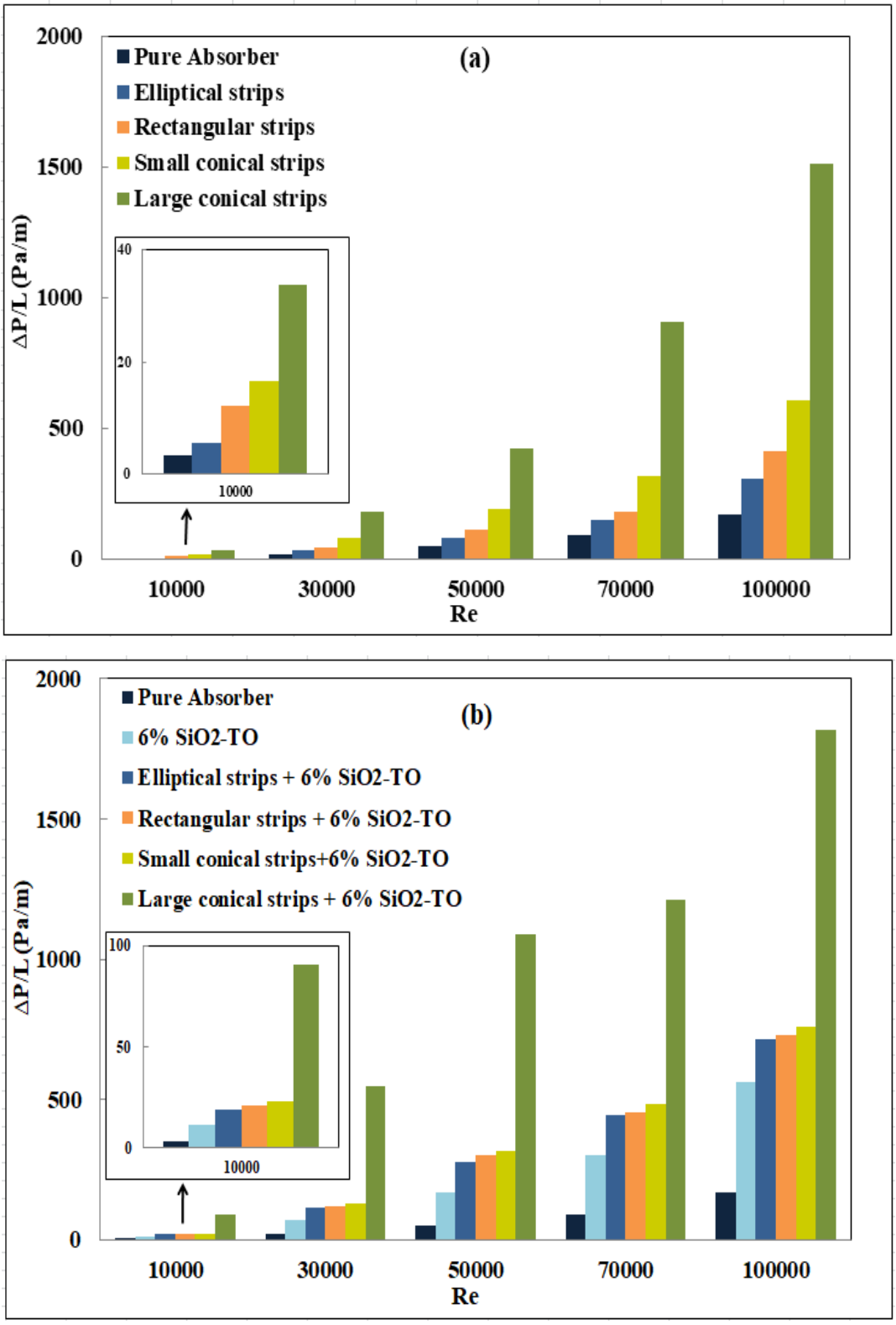

Figure 7.4: Effect of all considered cases of swirl generators and nanofluid on pressure drop characteristics.

7.3.3. Performance Evaluation Criterion

The assessment of swirl generator and nanofluid effect inside the solar receiver is carried out using the performance evaluation criterion (PEC) proposed by Ralph (1993), which compares the enhanced thermal performance (represented by the Nu number) and the increased pumping power (represented by the friction factor) with the thermal performance and pumping power of the typical solar receiver operating with the base liquid without swirl generators. For this latter baseline case, the PEC parameter equals one. Therefore, if the PEC parameter of a given design is greater than one, then the enhanced thermal performance is worth the increase in pressure drop and associated pumping power. Conversely, a PEC parameter lowers than one characterises a design where the enhanced thermal performance is not worth the increase in pressure drop and associated pumping power. The PEC parameter of all swirl generator cases with/without nanofluid at the larger Re number (Re = 10^5) is shown in Table 7-3. It can be noted that use of swirl generators with the base liquid alone is not advantageous. However, the use of the nanofluid with or without swirl generators is always advantageous with the exception of the large conical strips case. For this configuration, the combined use of nanofluid and swirl generators is always advantageous, with a remarkable increase in the PEC parameter for the rectangular and small conical strips swirl generators.

Table 7-3: PEC parameter of all considered cases of swirl generators and nanofluid.

Case	PEC
Pure absorber (no swirl generators and pure liquid)	1.00
Elliptical strips and pure liquid	0.90
Rectangular strips and pure liquid	0.94
Small conical strips and pure liquid	0.96
Large conical strips and pure liquid	0.74
No swirl generators + 6% SiO_2-TO	1.155
Elliptical strips + 6% SiO_2-TO	1.163
Rectangular strips + 6% SiO_2-TO	1.310
Small conical strips + 6% SiO_2-TO	1.423
Large conical strips + 6% SiO_2-TO	1.097

7.3.4. Thermal losses

The thermal losses in the PTC in the present case where the glass envelope is not considered take place from the external wall surface and are due to convection and radiation heat transfer. The most important parameter that affects the thermal losses of both heat transfer mechanisms is the mean wall temperature of the external surface of the solar receiver as given in the equation (2.21). As previously discussed, the use of nanofluids and swirl generators increases the energy absorbed by the heat transfer fluid from the solar receiver walls. In turns, this reduces the average wall temperature of the external surface of the solar receiver, which leads to reduced convection heat losses. This also leads to a decrease in the coating emissivity further reducing the radiation heat losses.

The specific thermal losses of the solar receiver predicted for all strip shapes with and without nanofluid are presented in Figure 7.5. It can be noticed from this figure that insertion of the swirl generators inside the solar receiver helps to gradually reduce the specific thermal losses with increasing the strip size. The most pronounced reduction was observed for the large conical-shape strips whereas the minimum reduction was recorded by the elliptical-shape strips as shown in Figure 7.5a. These results are in qualitative agreement with the findings reported by Cheng et al. (2012b), Bellos and Tzivanidis (2018), Liu et al. (2019a), and Ahmed and Natarajan (2019).

In comparison with the pure liquid, the 6% volume fraction SiO_2-TO nanofluid has better thermal properties; in particular higher thermal conductivity. This increases the energy absorbed by the working fluid from the internal receiver's wall, which in turn leads to a gradual reduction of the mean temperature of the external surface of the absorber tube, in qualitative agreement with previous findings reported by Mwesigye et al. (2015a) and Bellos et al. (2018a). Furthermore, a larger reduction in thermal losses was observed by combining the swirl generators and nanofluids for all considered cases, where in particular the maximum reduction was provided by the large conical-shape strips, followed by the small conical-shape strips, followed by the rectangular-shape strips and finally by the elliptical-shape strips, as illustrated in Table 7-4 at a Re number of 10^5.

It should be noted from Figure 7.5 that the flow with smaller Re number resulted in larger reduction in the thermal losses in all cases into consideration with and without nanofluid compared with that marked larger Re numbers. The reason behind that is the flow with smaller Re numbers has a longer path to cross the solar receiver, thus more energy is collected and absorbed and therefore more decrease in thermal losses are noted. Moreover, the flow path with presence of the swirl generator becomes even longer which in turn led to more absorbing in thermal energy and more reduction in the external wall temperature.

Table 7-4: Thermal loss reduction of the multiple strip-shapes inserts cases with nanofluid.

Case	**Specific Thermal losses (W/m)**	**Reduction (%)**
Pure absorber	333.26	-
6% SiO_2-TO	280.85	-12.00
Elliptical strips + 6% SiO_2-TO	264.02	-20.77
Rectangular strips + 6% SiO_2-TO	256.10	-23.15
Small conical strips + 6% SiO_2-TO	254.30	-23.70
Large conical strips + 6% SiO_2-TO	244.96	-26.5

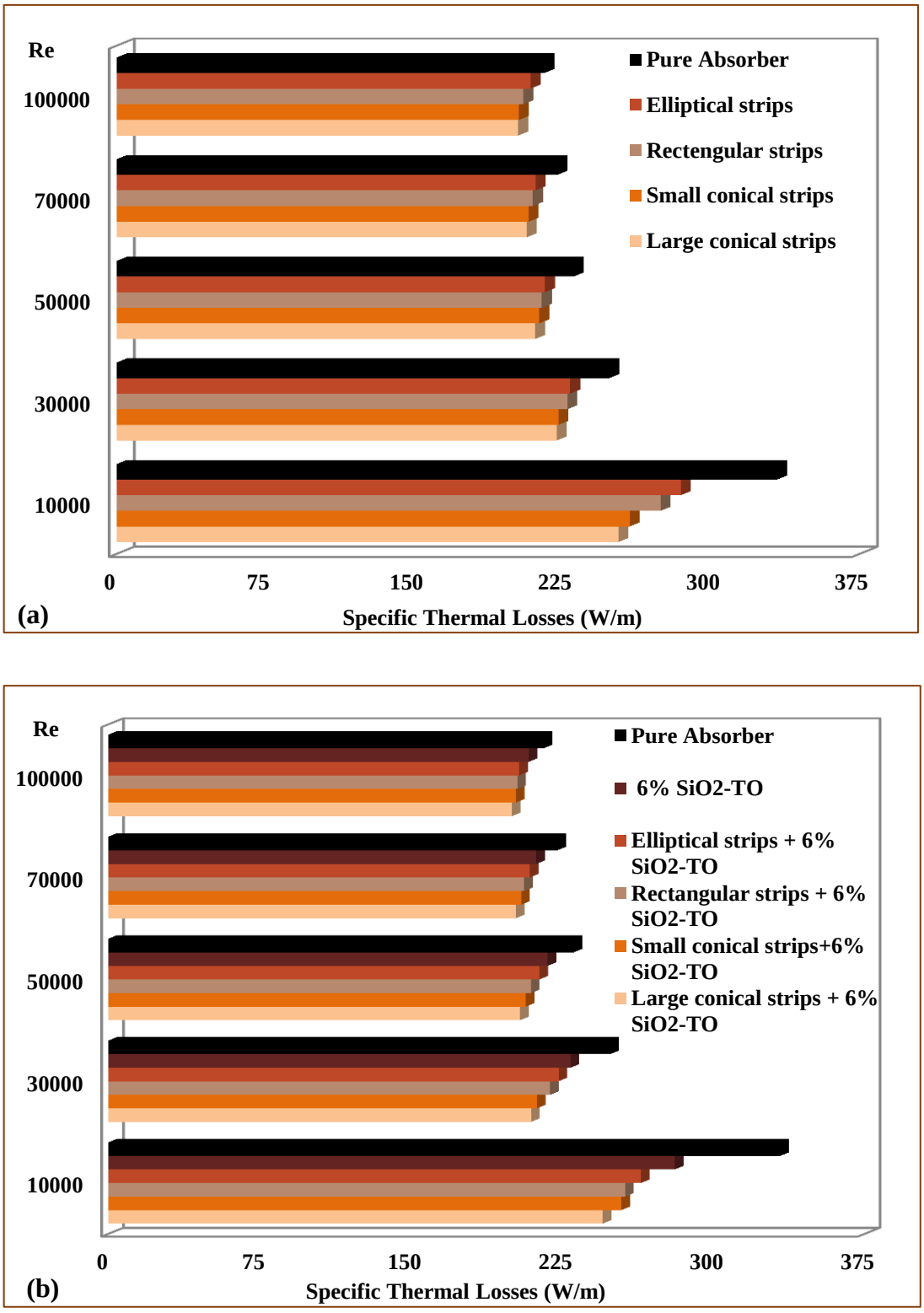

Figure 7.5: Thermal losses: swirl generators with pure liquid (a) and swirl generators with nanofluid (b).

7.3.5. Overall Collector Efficiency

The actual collector performance can be assessed by comparing the gain in the thermal energy with the corresponding increase in pumping power to calculate the overall collector efficiency based on the incident solar energy. It should be noted that the thermal efficiency can also be affected by the thermal losses as larger thermal losses results in lower thermal efficiency. This means that several parameters affect the overall collector efficiency: gain in useful thermal energy, pumping power, and thermal losses.

The presence of swirl generators has shown different levels of enhancement in the thermal energy and pressure drop and also thermal losses reduction in line with extra gain in the useful thermal energy due to increase the output fluid temperature. That acts at enhancing the overall thermal efficiency of all swirl generator cases but with different levels of enhancements as shown in Figure 7.6a. In line with the main findings of previous studies of Mwesigye et al. (2014), Mwesigye et al. (2016b), Bellos et al. (2017b), Bellos and Tzivanidis (2018), Liu et al. (2019a), Ahmed and Natarajan (2019), the maximum enhancement in the overall collector efficiency was recorded by the large conical-shape strips followed by the small conical-shape strips whereas the minimum improvement achieved was recorded for the elliptical-shape strip configuration. It should be noted here that the heat transfer enhancement of the large-shape strip was found to be the maximum with minimal thermal losses, this configuration also required a substantial increase in the pumping power demand. Thus the enhancement in the overall collector efficiency of the large conical-shape strip case did not differ much from the overall collector efficiency enhancement provided by the small conical-shape strip case. Introduction of the nanofluid leads to gradual improvement in the heat transfer and reduction of thermal losses, thereby improving the overall collector efficiency compared to the plain absorber tube configuration as shown in Figure 7.6b. The results for the combined use of swirl generators and nanofluid technologies investigated in the current work are presented in Figure 7.6b.

The improvements in the overall collector efficiency are very clear for all the cases with the maximum enhancement recorded for the large conical-shape strip with nanofluid case. This trend was found to be similar to the previous findings and thus warrants a comprehensive study of the overall collector efficiency.

It can further be noticed from Figure 7.6 that the overall collector efficiency provided at smaller Re numbers was found to be greater than that achieved at higher Re numbers for all swirl generator configurations regardless of the nanofluid. At these low Re numbers a larger reduction in the convection and radiation thermal losses were observed due to reduction in the external surface temperature in line with more gain in the useful thermal energy which is due to the higher enhancement in the output fluid temperature.

The main improvements in the overall collector efficiency of all swirl generators with 6% volume fraction of SiO_2-TO nanofluids at the Re number (30000) is presented in Table 7-5.

Table 7-5: Overall thermal efficiency enhancement of the multiple strips inserts cases with nanofluid.

Case	**Overall Thermal Efficiency (%)**	**Improvement (%)**
Pure absorber	48.61	-
6% SiO_2-TO	53.05	9.11
Elliptical strips + 6% SiO_2-TO	54.21	11.50
Rectangular strips + 6% SiO_2-TO	55.016	13.16
Small conical strips + 6% SiO_2-TO	55.72	14.62
Large conical strips + 6% SiO_2-TO	56.41	15.41

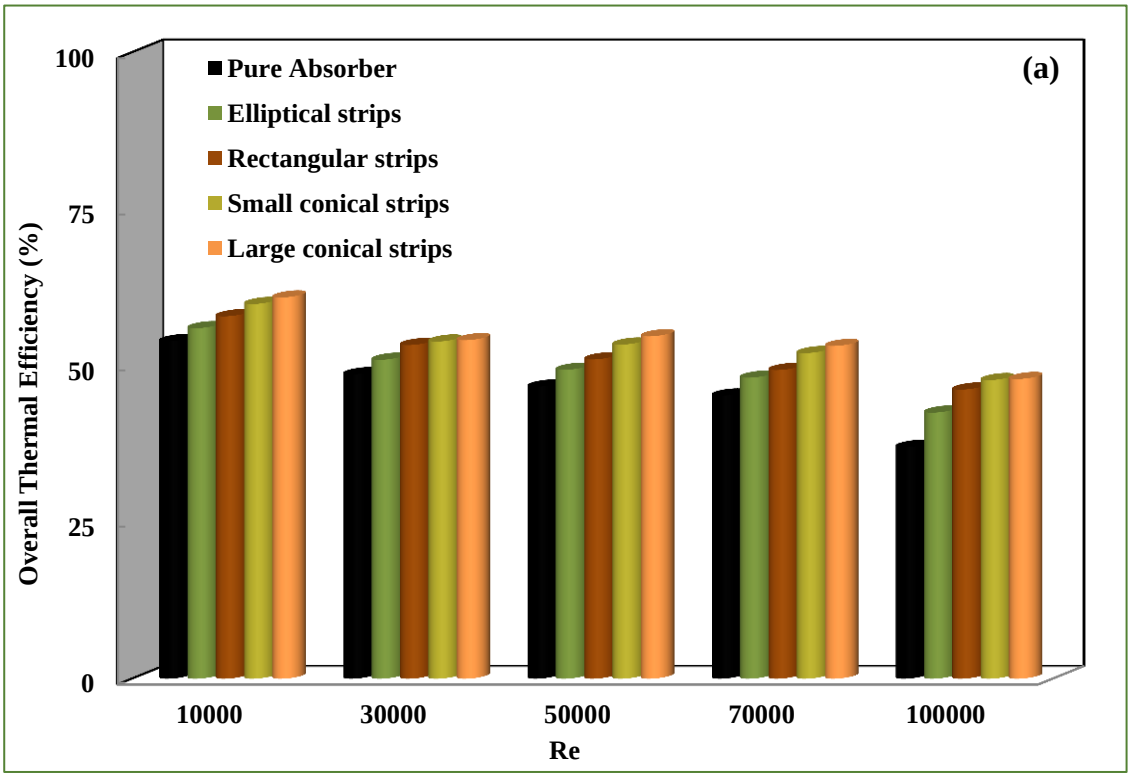

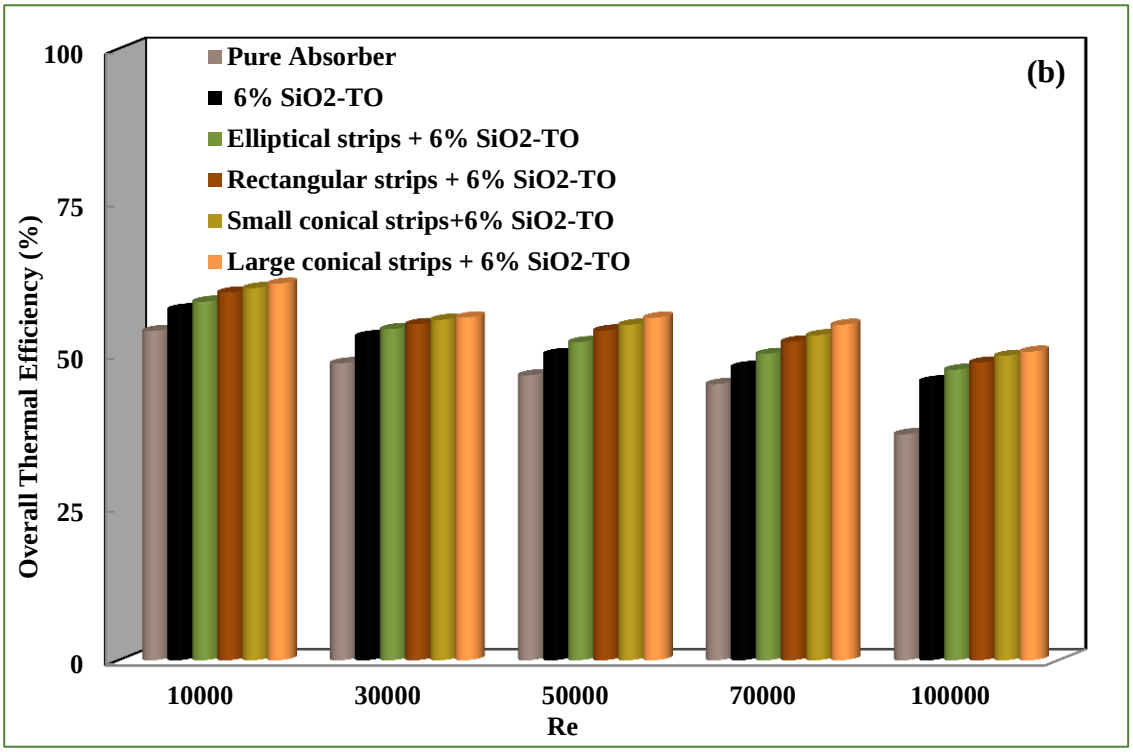

Figure 7.6: Effect of all considered cases of swirl generators and nanofluid on the overall thermal efficiency.

7.3.6. Thermal exergy efficiency

The thermal exergy efficiency is another important parameter that has been considered to evaluate the performance of inserting different swirl generators inside the solar receiver with and without nanofluid technology. The importance of this parameter is to assess the maximum net possible work production using current technologies. Figure 7.7 presents the variation of the thermal exergy efficiency over a range of Re number of 10^4-10^5 of all cases considered in the current work.

The benefit of this parameter considering the swirl generator inserts are clearly obvious from Figure 7.7a which shows that inserting the large conical-shape insert case enhances the thermal exergy efficiency more than the other swirl generator cases, whereas the minimum improvement in the thermal exergy efficiency was recorded by the elliptical-shape swirl generator case over all Re number range in which these results agreed well with the results produced by Bellos et al. (2018d) and Bellos and Tzivanidis (2018).

The trend of enhancement in the thermal exergy efficiency is similar to the overall collector efficiency trend as presented in the last section; an increase the fluid useful energy and reducing of the external surface thermal losses in line with increasing the useful exergy energy due to the presence of the swirl generators. Furthermore, adding nanoparticles to the pure liquid as working fluid further enhances the thermal exergy efficiency compared with the plain solar receiver as shown in Figure 7.7b. Notably, the combination of nanofluid and swirl generators yields a more substantial enhancement in the thermal exergy efficiency as compared with the nanofluid without swirl generators or the pure liquid with swirl generators.

Figure 7.7b shows that the maximum enhancement in the thermal exergy efficiency was achieved by the large-shape conical strips with 6% volume fractions of SiO_2-TO nanofluid followed by small conical-shape strips with nanofluid then by the rectangular-shape strip with nanofluid whereas the minimum improvements was marked by the elliptical-shape strips with nanofluids as presented in Table 7-6. The trend of thermal exergy efficiency at smaller Re numbers is the same as the performance of other parameters that have been discussed previously.

Table 7-6: Thermal exergy efficiency enhancement of the multiple strips inserts cases with nanofluid.

Case	**Thermal Exergy Efficiency (%)**	**Improvement (%)**
Pure absorber	35.36	-
6% SiO_2-TO	38.557	9.02
Elliptical strips + 6% SiO_2-TO	39.37	11.34
Rectangular strips + 6% SiO_2-TO	39.96	13.00
Small conical strips + 6% SiO_2-TO	40.48	14.47
Large conical strips + 6% SiO_2-TO	40.78	15.32

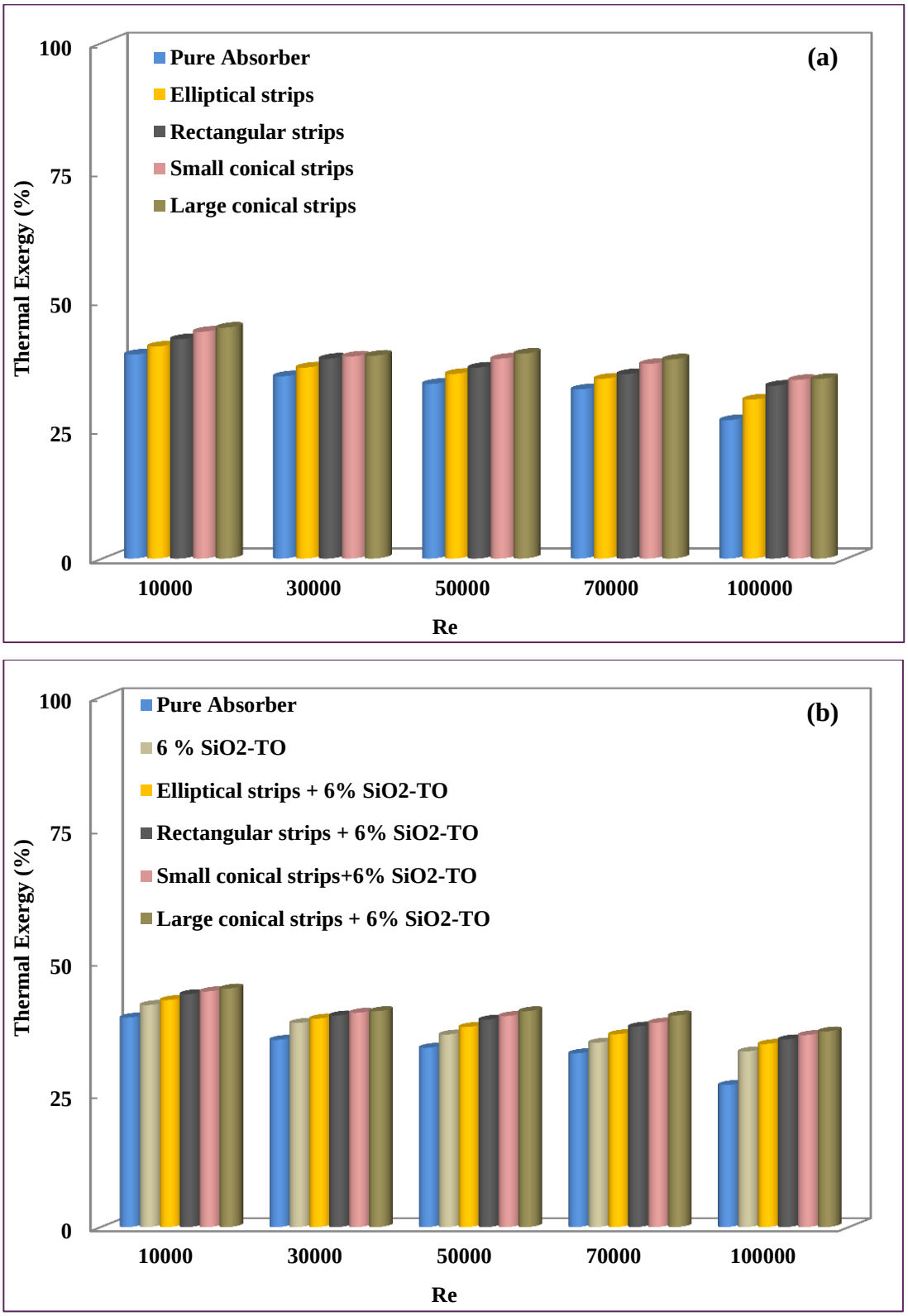

Figure 7.7: Effect of all considered cases of swirl generators and nanofluid on the thermal exergy efficiency.

7.4. Conclusions

The present chapter compares the improvements in the thermal and thermodynamic performances of the parabolic trough collector systems by introducing different techniques over a range of Re number (10^4-10^5) using the Monte Carlo ray tracing model to account for the non-uniform circumferential heat flux over the solar receiver. Different shapes of straight strips attached to a core rod inside the solar receiver; large conical-shape strips, small conical-shape strips, rectangular shape strips and elliptical shape strips with and without 6 % SiO_2-TO nanofluids were numerically investigated in this chapter with the findings as summarized below:

- For the swirl generator configurations with a pure working fluid, the maximum enhancement for all examined parameters was found to be for the larger geometry swirl generator which showed a Nu number enhancement of 10.14% to 55.23%. On the other hand, the elliptical-shape strip configuration showed the lowest enhancement. The use of nanofluid instead of a pure fluid further enhanced the Nu number increase from 24.08% to 62.52% for the large conical-shape strip configuration.

- The enhancement in the Nu number leads to a gradual reduction in the specific thermal losses which ranged from 14.57% to 24.05% for the large conical-shape strip case; this being the most effective configuration. Once again, the elliptical-shape strips configuration was found to be the least beneficial. The use of nanofluid with the large conical-shape strip configuration further reduced the losses from 20.77% to 26.50%.

- For the overall collector efficiency and the thermal exergy efficiency, a similar trend was observed where the large conical-shape strip configuration with nanofluid showed the best improvement; up to 15.41% and 15.32% respectively. Once again, the elliptical strips configuration showed the least improvement in both these parameters compared to the other shapes of the inserts.

From all the results shown above it can be deduced that the use of nanofluids with swirl generators enhance the overall thermal performance of the PTC system by increasing the Nu number, thermal exergy efficiency and overall collector efficiency. However, the use of either one of these techniques increases the base cost of the whole system both in terms of the maintenance cost and the pumping power requirement. Thus, whilst designing such a system one must compare the useful gain against the increase in cost of the PTC system.

Chapter 8: Conclusions and future work

8.1. Summary and Overall Conclusions

Enhancement in performance of PTC systems can be achieved using numerous technologies, as illustrated in this thesis. These technologies can enhance the thermal performances, or they can improve the PTC thermodynamic characteristics, which in turn leads to

- higher thermal energy production
- lower thermal losses
- higher thermal efficiency
- higher overall collector efficiency
- higher exergy efficiency

Changing the heat transfer fluid (HTF) is a viable approach to study the corresponding effect on the thermal and hydraulic performances of parabolic trough collectors (PTC). The use of nanofluid technology is another effective approach to gradually improve the PTC thermal efficiency. Both metallic and non-metallic nanoparticles can be suspended into the base fluids with different volume fractions or different weight percentage. There is no doubt that increasing the nanoparticle volume fraction would increase the heat transfer performance and reduce the thermal losses on the absorber tube, but at the same time the nanofluid stability will also be affected, leading to agglomeration and clustering of nanoparticles resulting in increased pumping power requirement to force the flow through the absorber tube. Therefore, the nanoparticle volume fraction or weight concentration should be optimized for effective thermal and hydraulic performance of the PTC system.

Another approach that can be employed to effectively enhance the thermal performance of the absorber receiver is the use of swirl generators or other flow-modifying inserts (turbulators) inside the heat collection element with different shapes and different positions. In comparison with the nanofluid approach, using turbulators is more cost-effective, and their actual implementation rather simple. Turbulators act at enhancing the thermal properties of heat transfer fluid and improving the turbulence performance inside the absorber tube which in turn lead to significantly improved thermal performance. On the other hand, the main challenge associated with this method is the potential pressure shocks due to the presence of swirl generators or turbulators, which could lead to glass envelope breakage.

The fourth possible technology which may be employed to improve the thermal performance of PTC is to combine the previous two technologies, nanofluids and flow-

modifying inserts, in the same system. For this method to be effective, clearly the nanofluid and the flow-modifying insert have to be optimized synergistically. All the previous calculations were performed over a range of Reynolds (Re) numbers of Re = 10^4 –10^5 and a realistic non-uniform heat flux distribution in the circumferential direction over the absorber outer surface was implemented using the Monte Carlo ray tracing technique. The summery of these technologies and main findings include:

- Base fluid alone: Thermal and hydraulic performances of the bare parabolic trough collectors were numerically investigated using three categorized-types of pure fluids; water was used with a temperature range of 320–500 K, Therminol® VP-1 with a temperature range of 320–600 K, and molten salt with a temperature range of 575–800 K. Results illustrated that for a temperature-range of (320–500) K, the Therminol® VP-1 performed better than water and provided larger Nu numbers, lower thermal stresses and higher thermal efficiency. However, for the common temperature-range between Therminol® VP-1 and molten salt, both preformed more or less the same with lower thermal stresses in the case of Therminol® VP-1. On the other hand, the molten salt was found to be the best choice for high operating temperatures (up to 873 K) since there was no significant reduction in the overall thermal efficiency at these high temperatures.

- Use of nano-particles: The flow features inside a PTC were studied by using different non-metallic nanoparticles (Al_2O_3, CeO_2, CuO, Fe_2O_3, TiO_2 and SiO_2) dispersed in three different base fluids (therminol VP-1, water, and molten salt). The simulations were performed over three volume fractions (2, 4 and 6%). Main findings of this approach are summarized below:

    - For water based nanofluids the improvement in the Nu number ranged from 12.72% to 32.4% with 6% volume fraction (VF) of SiO_2 nanoparticle providing the highest improvement. Whereas for the molten salt and therminol VP-1 base nanofluids, the improvements in the Nu number was not as pronounced but the general trend was the same with SiO_2 being the most effective and CeO_2 the least.
    - For molten salt base nanofluids the enhancement in the thermal efficiency ranged from 5.1% to 9.92% with 6% VF of SiO_2 nanoparticle providing the largest enhancement and CeO_2 the least. On the other hand, for therminol VP-1 base nanofluids the enhancement in the thermal efficiency ranged from 3.29 to 9.11% with 6% VF of SiO_2 nanoparticle providing the largest improvement and CeO_2 the least. For the water based nanofluid, no marked improvement was

observed in terms of the thermal efficiency. However, SiO_2 still performed better than CeO_2.

- The improvement in the thermal exergy efficiency for the molten salt base fluids ranged from 5.2% to 10.08% with 6% VF of SiO_2 nanoparticle giving the maximum improvement and CeO_2 the minimum. On the other hand, the improvement for therminol VP-1 base nanofluids in the thermal exergy efficiency ranged from 3.18% to 9.02% with 6% VF of SiO_2 nanoparticle providing the largest improvement. Finally, for the water-based nanofluids, once again the thermal exergy did not show huge gains.
- Based on the performance, it is concluded that regardless of the base working fluid SiO_2 is the best candidate from all perspectives (improvement in Nu number, thermal efficiency enhancement, exergy efficiency improvement) with CeO_2 being the worst.

➢ Single-shape insert with nanofluids: Investigating the optimum configuration for straight conical strip inserts, which were attached to a central rod with varying parameters of pitch height, angle pitch, and the number of strip inserts was also carried out. The combination of the optimized configuration swirl generator insert with nanofluids was also investigated. The main findings of this work are summarized below:

- The use of straight conical strips enhanced the Nusselt number by 47.13% whereas using nanofluids alone improved the Nusselt number by 15.57%. However, an improvement of 57.48% was observed for the Nusselt number by combining the swirl inserts and nanofluids. This combination also resulted in the maximum reduction of thermal losses by 23.7%.
- The improvement in the Nusselt number comes at the expense of an increase in the pressure drop. Swirl generators and nanofluids alone increased the pressure drop by 258.42% and 231.18%, respectively. However, when these were combined, the pressure drop reached as high as 348.03%.
- All the examined cases showed different levels of enhancements in the overall thermal efficiency and thermal exergy efficiency. For the combined case of nanofluid with optimum swirl generator configuration, the overall thermal efficiency improved by 14.62% and the thermal exergy efficiency increased by 14.47%.

- The gain in improvement of all tested parameters was found to be more sensitive to the insert geometry and the number of inserts as opposed to the nanofluids. Thus, it can be concluded that swirl inserts are a better candidate than nanofluids for thermal performance improvement in PTC systems.

➢ Multi-shape inserts with nanofluids: The introduction of different shapes of straight strips attached to a core rod inside the solar receiver with/without 6% volume fraction of SiO_2-Therminol VP-1 was also numerically investigated. The first technique was to investigate the four straight strips of different shapes attached to a core rod; large conical-shape strips, small conical-shape strips, rectangular shape strips and elliptical shape strips. The second technique was to combine the 6 % SiO_2 nanoparticles mixed with Therminol VP-1 at an inlet temperature of 400K with the effect of these strip shapes. The main achievements include:

- For the swirl generator cases with the pure working fluids, the maximum enhancement in all examined parameters was achieved by the larger geometry swirl generator case. In more details, the enhancement in the Nu number was ranged from 10.14% to 55.23% with the large conical-shape strips providing the highest enhancement while the minimum enhancement was providing by the elliptical-shape strips. These enhancements led to gradual reduction in the specific thermal losses ranged from 14.57% to 24.05% with the large conical-shape strip case being the most effective and the elliptical-shape strips case was the least. These contributions were associated to enhance the overall collector efficiency and the thermal exergy efficiency gradually in the range of 4.73% to 11.18% and 4.75% to 11.25% respectively with the large conical strips achieving the largest augmentations in both parameters (overall collector efficiency and thermal exergy efficiency) whereas the elliptical strips case providing the minimum improvement.
- For the swirl generator cases with the nanofluid technology, the largest improvement in all examined parameters was provided by the larger geometry swirl generator case with the presence of nanofluids compared with the typical solar receiver, pure swirl generator cases and pure nanofluid examined cases. In more details, the enhancement in the Nu number was ranged from 24.08% to 62.52% with the large conical-shape strips providing the highest enhancement while the smallest contribution was providing by the elliptical-shape strips. These enhancements led to gradual reduction in the specific thermal losses ranged from 20.77% to 26.50% with the large conical-shape strip case being the most effective and the elliptical-shape strips case was the least. These contributions were associated to enhance the overall collector efficiency and the thermal exergy

efficiency gradually in the range of 11.50% to 15.41% and 11.34% to 15.32% respectively with the large conical strips achieving the largest augmentations in both parameters (overall collector efficiency and thermal exergy efficiency) whereas the elliptical strips case providing the minimum improvement.

- The turbulence models used in the present work are classified as simple eddy-viscosity turbulence models. The Reynolds stress in these models is determined from the linear relationship called Boussinesq's hypothesis with the average strain rate through eddy turbulent viscosity which causes some challenges in such models such as large production rate of turbulent kinetic energy, isotropic normal stresses in the near-wall regions etc..

8.2. Some suggestions of Future work

For the PTC systems performance enhancement areas that require further investigation include:

- The optimization of the volume fraction/weight concentration of nanoparticles to fine-tune the performance of nanofluids, as well as investigations on the long-term stability of nanofluids.

- Notwithstanding their potential superior performance, hybrid nanofluids have received little attention, both experimentally and numerically, so that more studies are clearly needed to duly assess their potential. Using hybrid nanofluids instead of mono fluid (single fluid) is expected to double the thermal efficiency of the PTC, Bellos and Tzivanidis (2018a). Therefore, this is a large potential of research to examine different cases of nanofluids; metallic-metallic nanofluids, metallic-non-metallic nanofluids, and non-metallic-non-metallic nanofluids. Examining multiple base fluids with hybrid nanofluids is also needed. All such configurations are severely lacking reliable benchmark experimental data.

- Very few studies have investigated the synergy between nanofluids and flow-modifying insert, so that more studies are clearly needed to duly assess the potential of combining these two performance-enhancement technologies.

- Moreover, there are still some open questions about the thermal-physical properties of nanofluids which thus require further research. Furthermore, investigating hybrid nanofluids is still restricted to investigations.

- Studies related to the testing of the combined effect of flow-modifying devices are much needed and should be the focus of further research.

- The use of hybrid nanofluids with swirl generators offers good potential since different inserts could be investigated with numerous types of hybrid nanofluids.

- The turbulence models used in the present work are limited to simple eddy-viscosity turbulence models. The Reynolds stress in these models is determined from the linear relationship called Boussinesq's hypothesis with the average strain rate through eddy turbulent viscosity which causes large errors in these models such as an excessive production rate of turbulent kinetic energy, isotropic normal stresses in the near-wall regions etc.. On the contrary, the Second Moment Closure (full Re stress transport equations) can be examined with different types of swirl generators in which the effects of swirl is represented exactly in the production terms of the full Re stress tensor.

References

Abed, N., Afgan, I., Cioncolini, A., Iacovides, H., & Nasser, A. "Assessment and Evaluation of the Thermal Performance of Various Working Fluids in Parabolic trough Collectors of Solar Thermal Power Plants under Non-Uniform Heat Flux Distribution Conditions". Energies. 13, 15 (2020a): 3776.

Abed, N., Afgan, I., Cioncolini, A., Iacovides, H., Nasser, A., & Mekhail, T. Thermal performance evaluation of various nanofluids with non-uniform heating for parabolic trough collectors. Case Studies in Thermal Engineering. (2020b): 22, 100769.

Abed, N., Afgan, I., Nasser, A., Iacovides, H., Cioncolini, A. & Meakhail, T. "Numerical Investigations of parabolic trough collectors using different nanofluids." Proceedings of 5th International Conference on Energy Engineering, 24-26 December, 2019, Aswan-Egypt.

Abed, N. & Afgan, I. Enhancement Techniques of Parabolic Trough Collectors: A Review of Past and Recent Technologies. Adv. Civ. Eng. Tech. (2019), 33, 313–318.

Abed, N. & Afgan, I., "An extensive review of various technologies for enhancing the thermal and optical performances of parabolic trough collectors". International Journal of Energy Research. (2020). 44, 5117-5164.

Abed, N., Afgan, I., Cioncolini, A., Iacovides, H., Ilyas K. & Nasser, A. Thermal-hydraulic and thermodynamics analysis for parabolic trough collectors using straight conical strip inserts and nanofluids. Nanomaterials. (2021): 11, 853. https://doi.org/10.3390/nano 11040853.

Abid, Muhammad, Tahir A. H. Ratlamwala, and Ugur Atikol. "Solar Assisted Multi-Generation System Using Nanofluids: a Comparative Analysis." International Journal of Hydrogen Energy. 42.33 (2017): 21429-21442.

Abubakr, M., Amein, H., Akoush, B. M., El-Bakry, M. M., & Hassan, M. A.. "An intuitive framework for optimizing energetic and exergetic performances of parabolic trough solar collectors operating with nanofluids". Renewable Energy. (2020), 157, 130-149.

Abu-Hamdeh, N.H, and K.H Almitani. "Solar Liquid Desiccant Regeneration and Nanofluids in Evaporative Cooling for Greenhouse Food Production in Saudi Arabia." Solar Energy. 134 (2016): 202-210.

Agagna, Belkacem, Arezki Smaili, Quentin Falcoz, and Omar Behar. "Experimental and Numerical Study of Parabolic Trough Solar Collector of Microsol-R Tests Platform." Experimental Thermal and Fluid Science. 98 (2018): 251-266.

Aguilar, Rafael, Loreto Valenzuela, Antonio L. Avila-Marin, and Pedro L. Garcia-Ybarra. "Simplified Heat Transfer Model for Parabolic Trough Solar Collectors Using Supercritical Co2." Energy Conversion and Management. 196 (2019): 807-820.

Alashkar, Adnan, and Gadalla, Mohamed. "Performance Analysis of an Integrated Solar-Based Power Generation Plant Using Nanofluids." International Journal of Energy Research. 42.9 (2018): 2875-2900.

Alashkar, Adnan, and Gadalla, Mohamed. "Thermo-economic Analysis of an Integrated Solar Power Generation System Using Nanofluids." Applied Energy. 191 (2017): 469-491.

Allouhi, A, Amine M. Benzakour, R Saidur, T Kousksou, and A Jamil. "Energy and Exergy Analyses of a Parabolic Trough Collector Operated with Nanofluids for Medium and High Temperature Applications." Energy Conversion and Management. 155 (2018): 201-217.

Amina, Benabderrahmane, Aminallah Miloud, Laouedj Samir, Benazza Abdelylah, and J P. Solano. "Heat Transfer Enhancement in a Parabolic Trough Solar Receiver Using Longitudinal Fins and Nanofluids." Journal of Thermal Science. 25.5 (2016): 410-417.

Arshad, Ahmed K, and E Natarajan. "Thermal Performance Enhancement in a Parabolic Trough Receiver Tube with Internal Toroidal Rings: a Numerical Investigation." Applied Thermal Engineering. 162 (2019): 114224.

Arslan, F.M.; Günerhan H. "Investigation of Energetic and Exergetic Performances of Parabolic Trough Collector with Using Different Heat Transfer Fluids". In E3S Web of Conferences; EDP Sciences: Les Ulis, France, 2019; Volume 111.

Bakos, George C. "Design and Construction of a Two-Axis Sun Tracking System for Parabolic Trough Collector (ptc) Efficiency Improvement." Renewable Energy. 31.15 (2006): 2411-2421.

Barron, B.R.;Barron, R.F. "Design for Thermal Stresses". John Wiley & Sons: Hoboken, NJ, USA, (2013).

Basbous N, Taqi M, and Belouaggadia N. "Numerical study of a study of a parabolic trough collector using a nanofluid". Asian J Curr Eng Math. (2015): 3:40–4.

Basbous, Nabil, Mohamed Taqi, and Moulay A. Janan. "Thermal Performances Analysis of a Parabolic Trough Solar Collector Using Different Nanofluids." (2016): 322-326.

Batchelor, G K. "The Effect of Brownian Motion on the Bulk Stress in a Suspension of Spherical Particles." Journal of Fluid Mechanics. 83.1 (1977): 97-117.

Bellos, E, C Tzivanidis, and D Tsimpoukis. "Thermal Enhancement of Parabolic Trough Collector with Internally Finned Absorbers." Solar Energy. 157 (2017b): 514-531.

Bellos, E, C Tzivanidis, K.A Antonopoulos, and G Gkinis. "Thermal Enhancement of Solar Parabolic Trough Collectors by Using Nanofluids and Converging-Diverging Absorber Tube." Renewable Energy. 94 (2016): 213-222.

Bellos, E., and Tzivanidis, C. "Alternative Designs of Parabolic Trough Solar Collectors." Progress in Energy and Combustion Science. 71 (2019): 81-117.

Bellos, E., Tzivanidis, C., and Zafar Said. "A Systematic Parametric Thermal Analysis of Nanofluid-Based Parabolic Trough Solar Collectors." Sustainable Energy Technologies and Assessments. 39 (2020): 100714.

Bellos, E.; Daniil, I.; Tzivanidis, C. "A cylindrical insert for parabolic trough solar collector". Int. J. Numer. Meth. Heat Fluid Flow. (2019), 29, 1846–1876.

Bellos, E.; Korres, D; Tzivanidis, C.; Antonopoulos, K.A. "Design, Simulation and Optimization of a Compound Parabolic Collector". Sustain. Energy Technol. Assess. (2016), 16, 53–63.

Bellos, Evangelos, and Tzivanidis, Christos. "Investigation of a Star Flow Insert in a Parabolic Trough Solar Collector." Applied Energy. 224 (2018): 86-102.

Bellos, Evangelos, and Tzivanidis, Christos. "Parametric Investigation of Nanofluids Utilization in Parabolic Trough Collectors." Thermal Science and Engineering Progress. 2 (2017): 71-79.

Bellos, Evangelos, Christos Tzivanidis, and Dimitrios Tsimpoukis. "Thermal, Hydraulic and Exergetic Evaluation of a Parabolic Trough Collector Operating with Thermal Oil and Molten Salt Based Nanofluids." Energy Conversion and Management. 156 (2018a): 388-402.

Bellos, Evangelos, Christos Tzivanidis, and Dimitrios Tsimpoukis. "Enhancing the Performance of Parabolic Trough Collectors Using Nanofluids and Turbulators." Renewable and Sustainable Energy Reviews. 91 (2018b): 358-375.

Bellos, Evangelos, Christos Tzivanidis, and Dimitrios Tsimpoukis. "Optimum Number of Internal Fins in Parabolic Trough Collectors." Applied Thermal Engineering. 137 (2018c): 669-677.

Bellos, Evangelos, Christos Tzivanidis, and Kimon A. Antonopoulos. "A Detailed Working Fluid Investigation for Solar Parabolic Trough Collectors." Applied Thermal Engineering. 114 (2017a): 374-386.

Bellos, Evangelos, Christos Tzivanidis, Ilias Daniil, and Kimon A. Antonopoulos. "The Impact of Internal Longitudinal Fins in Parabolic Trough Collectors Operating with Gases." Energy Conversion and Management. 135 (2017c): 35-54.

Bellos, Evangelos, Ilias Daniil, and Christos Tzivanidis. "Multiple Cylindrical Inserts for Parabolic Trough Solar Collector." Applied Thermal Engineering. 143 (2018d): 80-89.

Benoit, H.; Spreafico, L.; Gauthier, D.; Flamant, G. "Review of Heat Transfer Fluids in Tube-Receivers Used in Concentrating Solar Thermal Systems: Properties and Heat Transfer Coefficients". (2016). Renew. Sustain. Energy Rev., 55, 298–315.

Bhowmik, N.C, and S.C Mullick. "Calculation of Tubular Absorber Heat Loss Factor." Solar Energy. 35.3 (1985): 219-225.

Biencinto, Mario, Rocío Bayón, Esther Rojas, and Lourdes González. "Simulation and Assessment of Operation Strategies for Solar Thermal Power Plants with a Thermocline Storage Tank." Solar Energy. 103 (2014): 456-472.

Bigoni, Riccardo, Stefan Kötzsch, Sabrina Sorlini, and Thomas Egli. "Solar Water Disinfection by a Parabolic Trough Concentrator (ptc): Flow-Cytometric Analysis of Bacterial Inactivation." Journal of Cleaner Production. 67 (2014): 62-71.

Bilal, F.R, U.C Arunachala, and H.M Sandeep. "Experimental Validation of Energy Parameters in Parabolic Trough Collector with Plain Absorber and Analysis of Heat Transfer Enhancement Techniques." Journal of Physics: Conference Series. 953.1 (2018).

Blanco M.J., and Miller S. Introduction to Concentrating Solar Thermal (CST) Technologies. Advances in Concentrating Solar Thermal Research and Technology. Elsevier Inc, (2017).

Bozorg, Mehdi V, Doranehgard M. Hossein, Kun Hong, and Qingang Xiong. "Cfd Study of Heat Transfer and Fluid Flow in a Parabolic Trough Solar Receiver with Internal Annular Porous Structure and Synthetic Oil-Al2o3 Nanofluid." Renewable Energy. 145 (2020): 2598-2614.

Bretado, de R. M. S, Carlos I. Rivera-Solorio, and Alejandro J. García-Cuéllar. "Thermal Performance of a Parabolic Trough Linear Collector Using Al2O3/H2O Nanofluids." Renewable Energy. 122 (2018): 665-673.

Brinkman, H C. "The Viscosity of Concentrated Suspensions and Solutions." The Journal of Chemical Physics. 20.4 (1952): 571.

Bruggeman, D A. G. "Berechnung Verschiedener Physikalischer Konstanten Von Heterogenen Substanzen. I. Dielektrizitätskonstanten Und Leitfähigkeiten Der Mischkörper Aus Isotropen Substanzen." Annalen Der Physik. 416.7 (1935): 636-664.

Buongiorno, J. "Convective Transport in Nanofluids." Transactions- American Society of Mechanical Engineers Journal of Heat Transfer. 128.3 (2006): 240-250.

Burkholder, Frank, and Charles F. Kutscher. Heat Loss Testing of Schott's 2008 Ptr70 Parabolic Trough Receiver. Golden, CO: National Renewable Energy Laboratory, 2009.

Çengel, Y.A.; Cimbala, J.M. “Fluid Mechanics: Fundamentals and Applications“. (2006); Singapore: McGraw-Hill Education.

Chang, C, C Xu, Z.Y Wu, X Li, Q.Q Zhang, and Z.F Wang. "Heat Transfer Enhancement and Performance of Solar Thermal Absorber Tubes with Circumferentially Non-Uniform Heat Flux." Energy Procedia. 69 (2015): 320-327.

Chang, Chun, Adriano Sciacovelli, Zhiyong Wu, Xin Li, Yongliang Li, Mingzhi Zhao, Jie Deng, Zhifeng Wang, and Yulong Ding. "Enhanced Heat Transfer in a Parabolic Trough Solar Receiver by Inserting Rods and Using Molten Salt As Heat Transfer Fluid." Applied Energy. 220 (2018): 337-350.

Chaudhari, K.S., Walke, P.V., Wankhede, U.S., Shelke, R.S., “An experimental investigation of a nanofluid (Al2O3+H2O) based parabolic trough solar collectors”. Br. J. Appl. Sci. Technol. 9 (6), (2015), 551-557.

Chen, Haisheng, Yulong Ding, Yurong He, and Chunqing Tan. "Rheological Behaviour of Ethylene Glycol Based Titania Nanofluids." Chemical Physics Letters. 444 (2007): 333-337.

Cheng, Z.D, Y.L He, and F.Q Cui. "Numerical Study of Heat Transfer Enhancement by Unilateral Longitudinal Vortex Generators Inside Parabolic Trough Solar Receivers." International Journal of Heat and Mass Transfer. 55 (2012b): 5631-5641.

Cheng, Z.D, Y.L He, F.Q Cui, R.J Xu, and Y.B Tao. "Numerical Simulation of a Parabolic Trough Solar Collector with Nonuniform Solar Flux Conditions by Coupling Fvm and Mcrt Method." Solar Energy. 86.6 (2012a): 1770-1784.

Cheng, Z.-D, Y.-L He, K Wang, B.-C Du, and F.Q Cui. "A Detailed Parameter Study on the Comprehensive Characteristics and Performance of a Parabolic Trough Solar Collector System." Applied Thermal Engineering. 63.1 (2014): 278-289.

Coccia, G, Nicola G. Di, L Colla, L Fedele, and M Scattolini. "Adoption of Nanofluids in Low-Enthalpy Parabolic Trough Solar Collectors: Numerical Simulation of the Yearly Yield." Energy Conversion and Management. 118 (2016): 306-319.

Davidson, Lars. "An introduction to turbulence models". (2018).

Craft, T.J., A.V. Gerasimov, B.E. Launder, and C.M.E. Robinson. ‘A Computational Study of the Near-Field Generation and Decay of Wingtip Vortices’. International Journal of Heat and Fluid Flow 27, no. 4 (August 2006): 684–95. https://doi.org/10.1016/j.ijheatfluidflow.2006.02.024.

Davidson, P A. "Turbulence: An Introduction for Scientists and Engineers". (2015). Oxford: Oxford University Press.

Dudley, V.E., Kolb, G.J, Sloan, M. & Keamey, D. “Test Results: SEGS LS-2 Solar Collector. SAND94-1884”, (1994), p. 1–12.

Duffie, John A, and William A. Beckman. Solar Engineering of Thermal Processes. Hoboken: Wiley, 2013.

Ebrahimi-Moghadam, Amir, Behnam Mohseni-Gharyehsafa, and Mahmood Farzaneh-Gord. "Using Artificial Neural Network and Quadratic Algorithm for Minimizing Entropy Generation of Al2o3-Eg/w Nanofluid Flow Inside Parabolic Trough Solar Collector." Renewable Energy. 129 (2018): 473-485.

Einstein, A. "Eine Neue Bestimmung Der Moleküldimensionen." Annalen Der Physik. 324.2 (1906): 289-306.

Einstein, A. “Eine Neue Bestimung Der Molekuldimensionen”. Annalen Der Physik, 34, (1911): 591–592.

Fadar, El, A, A Mimet, A Azzabakh, M Pérez-García, and J Castaing. "Study of a New Solar Adsorption Refrigerator Powered by a Parabolic Trough Collector." Applied Thermal Engineering. 29 (2009): 1267-1270.

Ferraro, V, J Settino, M A. Cucumo, and D Kaliakatsos. “Parabolic Trough System Operating with Nanofluids: Comparison with the Conventional Working Fluids and Influence on the System Performance”. (2016).

Forristall, Russell E. “Heat Transfer Analysis and Modeling of a Parabolic Trough Solar Receiver Implemented in Engineering Equation Solver”. Golden, Colo: National Renewable Energy Laboratory, (2003). Internet resource.

Fuqiang, Wang, Cheng Ziming, Tan Jianyu, Yuan Yuan, Shuai Yong, and Liu Linhua. "Progress in Concentrated Solar Power Technology with Parabolic Trough Collector System: a Comprehensive Review." Renewable & Sustainable Energy Reviews. 79 (2017): 1314-1328.

García, Sergio, Heriberto Sánchez–Mora, Marco A. Polo–Labarrios, and Ricardo I. Cázares–Ramírez. "Modeling and Simulation to Determine the Thermal Efficiency of a Parabolic Solar Trough Collector System." Case Studies in Thermal Engineering. 16 (2019): 100523.

Geete, A, S Kothari, R Sahu, P Likhar, A Saini, and A Singh. "Experimental Analysis on Fabricated Parabolic Solar Collector with Various Flowing Fluids and Pipe Materials." International Journal of Renewable Energy Research. 6.4 (2016): 1454-1463.

Ghadirijafarbeigloo, Sh, A.H Zamzamian, and M Yaghoubi. "3-d Numerical Simulation of Heat Transfer and Turbulent Flow in a Receiver Tube of Solar Parabolic Trough Concentrator with Louvered Twisted-Tape Inserts." Energy Procedia. 49 (2014): 373-380.

Ghasemi S, and Ranjbar A. Akbar. "Numerical Thermal Study on Effect of Porous Rings on Performance of Solar Parabolic Trough Collector." Applied Thermal Engineering. 118 (2017): 807-816.

Ghasemi, Seyed E, and Ranjbar, Ali A.. "Thermal Performance Analysis of Solar Parabolic Trough Collector Using Nanofluid As Working Fluid: a Cfd Modelling Study." Journal of Molecular Liquids. 222 (2016): 159-166.

Gnielinski, V.. “New Equations for Heat and Mass Transfer in Turbulent Pipe and Channel Flow.” International Chemical Engineering 16 (1976), pp. 359–368.

Gong, Guangjie, Xinyan Huang, Jun Wang, and Menglong Hao. "An Optimized Model and Test of the China’s First High Temperature Parabolic Trough Solar Receiver." Solar Energy. 84.12 (2010): 2230-2245.

Good, P, G Zanganeh, G Ambrosetti, M C. Barbato, A Pedretti, and A Steinfeld. "Towards a Commercial Parabolic Trough Csp System Using Air As Heat Transfer Fluid." Energy Procedia. 49 (2014): 381-385.

Grena, R. "Optical Simulation of a Parabolic Solar Trough Collector." International Journal of Sustainable Energy. 29.1 (2009): 19-36.

Hachicha, A.A., I. Rodríguez, R. Capdevila, and A. Oliva. "Heat Transfer Analysis and Numerical Simulation of a Parabolic Trough Solar Collector". Applied Energy. 111(2013): 581-592.

Hamilton, R L, and Crosser, O K.. "Thermal Conductivity of Heterogeneous Two-Component Systems." Industrial & Engineering Chemistry Fundamentals. 1.3 (1962): 187-191.

Hanjalic, K. and Launder, B. E.. "Modelling Turbulence in Engineering and the Environment, Second-Moment Routes to Closure". (2011). Cambridge University Press, Cambridge, UK.

Happel, John. "Viscosity of Suspensions of Uniform Spheres." Journal of Applied Physics. 28.11 (1957): 1288-1292.

He, Ya-Ling, Jie Xiao, Ze-Dong Cheng, and Yu-Bing Tao. "A Mcrt and Fvm Coupled Simulation Method for Energy Conversion Process in Parabolic Trough Solar Collector." Renewable Energy. 36.3 (2011): 976-985.

Hewett, Russell, R Gee, and E K. May. Solar Process Heat Technology in Action: The Process Hot Water System at the California Correctional Institution at Tehachapi. Golden, CO: National Renewable Energy Laboratory, (1991).

Heyhat, M.M, M Valizade, Sh Abdolahzade, and M Maerefat. "Thermal Efficiency Enhancement of Direct Absorption Parabolic Trough Solar Collector (daptsc) by Using Nanofluid and Metal Foam." Energy. 192 (2020): 116662.

Hoseinzadeh, Hamed, Alibakhsh Kasaeian, and Shafii M. Behshad. "Geometric Optimization of Parabolic Trough Solar Collector Based on the Local Concentration Ratio Using the Monte Carlo Method." Energy Conversion and Management. 175 (2018): 278-287.

Huang, Z, G.L Yu, Z.Y Li, and W.Q Tao. "Numerical Study on Heat Transfer Enhancement in a Receiver Tube of Parabolic Trough Solar Collector with Dimples, Protrusions and Helical Fins." Energy Procedia. 69 (2015): 1306-1316.

Incropera, Frank P, and David P. DeWitt. "Fundamentals of Heat and Mass Transfer." (2006).

Islam, M.K.; Hasanuzzaman, M.; Rahim, N.A. "Modelling and Analysis of the Effect of Different Parameters on a Parabolic-Trough Concentrating Solar System". RSC Adv. (2015), 5, 36540–36546.

Jafar, K.S, and Sivaraman, B. "Thermal Performance of Solar Parabolic Trough Collector Using Nanofluids and the Absorber with Nail Twisted Tapes Inserts." International Energy Journal. 14.4 (2014): 189-198.

Jaramillo, O.A, Mónica Borunda, K.M Velazquez-Lucho, and M Robles. "Parabolic Trough Solar Collector for Low Enthalpy Processes: an Analysis of the Efficiency Enhancement by Using Twisted Tape Inserts." Renewable Energy. 93 (2016): 125-141.

Jeter, Sheldon M. "Calculation of the Concentrated Flux Density Distribution in Parabolic Trough Collectors by a Semifinite Formulation." Solar Energy. 37.5 (1986): 335-345.

Jeter, Sheldon M. “Optical and thermal effects in linear solar concentrating collectors”. Georgia Institute of Technology, (1979). http://hdl.handle.net/1853/32784.

Kaloudis, E, E Papanicolaou, and V Belessiotis. "Numerical Simulations of a Parabolic Trough Solar Collector with Nanofluid Using a Two-Phase Model." Renewable Energy. 97 (2016): 218-229.

Kasaeian, A, R Daneshazarian, R Rezaei, F Pourfayaz, and G Kasaeian. "Experimental Investigation on the Thermal Behavior of Nanofluid Direct Absorption in a Trough Collector." Journal of Cleaner Production. 158 (2017): 276-284.

Kasaiean, Alibakhsh, Mohammad Sameti, Reza Daneshazarian, Zahra Noori, Armen Adamian, and Tingzhen Ming. "Heat Transfer Network for a Parabolic Trough Collector As a Heat Collecting Element Using Nanofluid." Renewable Energy. 123 (2018): 439-449.

Kasperski, Jacek, and Nemś, Magdalena. "Investigation of Thermo-Hydraulic Performance of Concentrated Solar Air-Heater with Internal Multiple-Fin Array." Applied Thermal Engineering. 58 (2013): 411-419.

Khakrah, H, A Shamloo, and S.K Hannani. "Determination of Parabolic Trough Solar Collector Efficiency Using Nanofluid: a Comprehensive Numerical Study." Journal of Solar Energy Engineering, Transactions of the Asme. 139.5 (2017).

Khakrah, Hamidreza, Amir Shamloo, and Hannani S. Kazemzadeh. "Exergy Analysis of Parabolic Trough Solar Collectors Using Al2o3/synthetic Oil Nanofluid." Solar Energy. 173 (2018): 1236-1247.

Khanafer, K, and K Vafai. "A Critical Synthesis of Thermophysical Characteristics of Nanofluids." International Journal of Heat and Mass Transfer. 54 (2011): 4410-4428.

Khandelwal, Deepak K, Ravi K. K, and Subhash C. Kaushik. "Heat Transfer Analysis of Receiver for Large Aperture Parabolic Trough Solar Collector." International Journal of Energy Research. 43.9 (2019): 4295-4311.

Kizilkan, Onder, Ahmet Kabul, and Ibrahim Dincer. "Development and Performance Assessment of a Parabolic Trough Solar Collector-Based Integrated System for an Ice-Cream Factory." Energy. 100 (2016): 167-176.

Korres, Dimitrios, Evangelos Bellos, and Christos Tzivanidis. "Investigation of a Nanofluid-Based Compound Parabolic Trough Solar Collector Under Laminar Flow Conditions." Applied Thermal Engineering. 149 (2019): 366-376.

Kreith F and Goswami DY. Handbook of Energy Efficiency and Renewable Energy. Taylor & Francis; 2007.

Kumar and Kumar. “Thermal performance of solar parabolic trough collector at variable flow rates: An experimental investigation”. International Journal of Ambient Energy, (2016), DOI: 10.1080/01430750.2016.1269673.

Kumar, B.N.; Reddy, K.S. “Numerical investigations on metal foam inserted solar parabolic trough DSG absorber tube for mitigating thermal gradients and enhancing heat transfer“. Appl. Therm. Eng. (2020), 178, 115511.

Kumar, K, and Reddy, K.S. "Thermal Analysis of Solar Parabolic Trough with Porous Disc Receiver." Applied Energy. 86.9 (2009): 1804-1812.

Kumaresan, G, R Sridhar, and R Velraj. "Performance Studies of a Solar Parabolic Trough Collector with a Thermal Energy Storage System." Energy: Technologies, Resources, Reserves, Demands, Impact, Conservation, Management, Policy. 47.1 (2012): 395-402.

Kurşun, Burak. "Thermal Performance Assessment of Internal Longitudinal Fins with Sinusoidal Lateral Surfaces in Parabolic Trough Receiver Tubes." Renewable Energy. 140 (2019): 816-827.

Larson, Dennis L. "Operational Evaluation of the Grid-Connected Coolidge Solar Thermal Electric Power Plant." Solar Energy. 38.1 (1987): 11-24.

Launder, B.E. & Sharma, B.I.. “Application of the energy-dissipation model of turbulence to the calculation of flow near a spinning disc“. (1974), Letters in Heat and Mass Transfer, 1(2), pp.131–137.

Lei, Dongqiang, Qiang Li, Zhifeng Wang, Jian Li, and Jianbin Li. "An Experimental Study of Thermal Characterization of Parabolic Trough Receivers." Energy Conversion and Management. 69 (2013): 107-115.

Liu, P, N Zheng, Z Liu, and W Liu. "Thermal-hydraulic Performance and Entropy Generation Analysis of a Parabolic Trough Receiver with Conical Strip Inserts." Energy Conversion and Management. 179 (2019a): 30-45.

Liu, Peng, Jinyi Lv, Feng Shan, Zhichun Liu, and Wei Liu. "Effects of Rib Arrangements on the Performance of a Parabolic Trough Receiver with Ribbed Absorber Tube." Applied Thermal Engineering. 156 (2019b): 1-13.

Lu, Jianfeng, Jing Ding, Jianping Yang, and Xiaoxi Yang. "Nonuniform Heat Transfer Model and Performance of Parabolic Trough Solar Receiver." Energy. 59 (2013): 666-675.

Maiga, S E, S J. Palm, C T. Nguyen, G Roy, and N Galanis. "Heat Transfer Enhancement by Using Nanofluids in Forced Convection Flows." The International Journal of Heat and Fluid Flow. 26.4 (2005): 530-546.

Malekan, Mohammad, Ali Khosravi, and Sanna Syri. "Heat Transfer Modeling of a Parabolic Trough Solar Collector with Working Fluid of Fe3o4 and Cuo/therminol 66 Nanofluids Under Magnetic Field." Applied Thermal Engineering. 163 (2019): 114435.

Mathieu, Jean, and Julian Scott. "An introduction to turbulent flow". (2000). Cambridge: Cambridge University Press.

Maxwell, J. C. “A treatise on electricity and magnetism (2nd ed.)”. Oxford: Clarendon. (1881).

Menter, F.R. “Two-equation eddy-viscosity turbulence models for engineering applications”. AIAA journal, 32(8). (1994). pp.1598–1605.

Michaelides, Efstathios. Nanofluidics: Thermodynamic and Transport Properties. Cham : Springer, 2016.

Mooney, M. "The Viscosity of a Concentrated Suspension of Spherical Particles." Journal of Colloid Science. 6.2 (1951): 162-170.

Mouaky, Ammar, Merrouni A. Alami, Nour E. Laadel, and El G. Bennouna. "Simulation and Experimental Validation of a Parabolic Trough Plant for Solar Thermal Applications Under the Semi-Arid Climate Conditions." Solar Energy. 194 (2019): 969-985.

Moukalled, F., L. Mangani, and M. Darwish. "The Finite Volume Method in Computational Fluid Dynamics: An Advanced Introduction with OpenFOAM® and Matlab". (2016). Cham: Springer.

Muñoz-Anton, J.; Biencinto, M.; Zarza, E.; Díez, L.E. "Theoretical Basis and Experimental Facility for Parabolic Trough Collectors at High Temperature Using Gas as Heat Transfer Fluid". Appl. Energy (2014), 135, 373–381.

Mwesigye, A, J.P Meyer, and T Bello-Ochende. "Heat Transfer and Thermodynamic Performance of a Parabolic Trough Receiver with Centrally Placed Perforated Plate Inserts." Applied Energy. 136 (2014): 989-1003.

Mwesigye, A, Z Huan, and J.P Meyer. "Thermal Performance of a Receiver Tube for a High Concentration Ratio Parabolic Trough System and Potential for Improved Performance with Syltherm800-

Cuo Nanofluid." Asme International Mechanical Engineering Congress and Exposition, Proceedings (imece). (2015b).

Mwesigye, Aggrey, and Meyer, Josua P.. "Optimal Thermal and Thermodynamic Performance of a Solar Parabolic Trough Receiver with Different Nanofluids and at Different Concentration Ratios." Applied Energy. 193 (2017): 393-413.

Mwesigye, Aggrey, İbrahim H. Yılmaz, and Josua P. Meyer. "Numerical Analysis of the Thermal and Thermodynamic Performance of a Parabolic Trough Solar Collector Using SWCNTS-Therminol®vp-1 Nanofluid." Renewable Energy. 119 (2018): 844-862.

Mwesigye, Aggrey, Tunde Bello-Ochende, and Josua P. Meyer. "Heat Transfer and Entropy Generation in a Parabolic Trough Receiver with Wall-Detached Twisted Tape Inserts." International Journal of Thermal Sciences. 99 (2016b): 238-257.

Mwesigye, Aggrey, Zhongjie Huan, and Josua P. Meyer. "Thermal Performance and Entropy Generation Analysis of a High Concentration Ratio Parabolic Trough Solar Collector with Cu-Therminol®vp-1 Nanofluid." Energy Conversion and Management. 120 (2016a): 449-465.

Mwesigye, Aggrey, Zhongjie Huan, and Josua P. Meyer. "Thermal Performance and Entropy Generation Analysis of a High Concentration Ratio Parabolic collectors: A comprehensive review Trough Solar Collector with Cu-Therminol®vp-1 Nanofluid." Energy Conversion and Management. 120 (2016): 449-465.

Mwesigye, Aggrey, Zhongjie Huan, and Josua P. Meyer. "Thermodynamic Optimisation of the Performance of a Parabolic Trough Receiver Using Synthetic Oil-Al2O3 Nanofluid." Applied Energy. 156 (2015a): 398-412.

Nahhas, Tamar, Xavier Py, Sophie Grégoire, Christian Cristofari, Minh D. Pham, Catherine Bessada, and Régis Olives. “Materials and thermal storage systems by sensible heat for thermodynamic electro-solar plants”. Thèse de doctorat : Energétique et Génie des Procédés : Perpignan : 2017.

Nan, C W, Z Shi, and Y Lin. "A Simple Model for Thermal Conductivity of Carbon Nanotube-Based Composites." Chemical Physics Letters. 375 (2003): 666-669.

Natividade, Pablo S. G, Moraes M. G. de, Elson Avallone, Filho E. P. Bandarra, Rogério V. Gelamo, and Júlio C. S. I. Gonçalves. "Experimental Analysis Applied to an Evacuated Tube Solar Collector Equipped with Parabolic Concentrator Using Multilayer Graphene-Based Nanofluids." Renewable Energy. 138 (2019): 152-160.

Nelson AT, Rittman DR, White JT, Dunwoody JT, Kato M, McClellan KJ. "An evaluation of the thermophysical properties of stoichiometric CeO2 in comparison to UO2 and PuO2". J Am Ceram Soc. (2014); 97(11):3652-3659.

Nguyen, C.T, F Desgranges, G Roy, N Galanis, T Maré, S Boucher, and Mintsa H. Angue. "Temperature and Particle-Size Dependent Viscosity Data for Water-Based Nanofluids - Hysteresis Phenomenon." International Journal of Heat and Fluid Flow. 28.6 (2007): 1492-1506.

Noman, Muhammad, Ahmad Wasim, Muzaffar Ali, Mirza Jahanzaib, Salman Hussain, Hafiz M. K. Ali, and Hafiz M. Ali. "An Investigation of a Solar Cooker with Parabolic Trough Concentrator." Case Studies in Thermal Engineering. 14 (2019): 100436.

Norouzi, Amir M, Majid Siavashi, and Oskouei M. H. Khaliji. "Efficiency Enhancement of the Parabolic Trough Solar Collector Using the Rotating Absorber Tube and Nanoparticles." Renewable Energy. 145 (2020): 569-584.

Odeh, S.D, G.L Morrison, and M Behnia. "Modelling of Parabolic Trough Direct Steam Generation Solar Collectors." Solar Energy. 62.6 (1998): 395-406.

O'Hanley, Harry, Jacopo Buongiorno, Thomas McKrell, and Lin-wen Hu. "Measurement and Model Validation of Nanofluid Specific Heat Capacity with Differential Scanning Calorimetry." Advances in Mechanical Engineering. 4 (2012): 181079.

Okafor, I.F, J Dirker, and J.P Meyer. "Influence of Non-Uniform Heat Flux Distributions on the Secondary Flow, Convective Heat Transfer and Friction Factors for a Parabolic Trough Solar Collector Type Absorber Tube." Renewable Energy. 108 (2017): 287-302.

Okonkwo, Eric C, Muhammad Abid, and Tahir A. H. Ratlamwala. "Effects of Synthetic Oil Nanofluids and Absorber Geometries on the Exergetic Performance of the Parabolic Trough Collector." International Journal of Energy Research. 42.11 (2018b): 3559-3574.

OpenCFD. "OpenFOAM 3.0.1 Programmer's Guide". 2015..

Osorio, Julian D, and Rivera-Alvarez, Alejandro. "Performance Analysis of Parabolic Trough Collectors with Double Glass Envelope." Renewable Energy. 130 (2019): 1092-1107.

Ouagued, and Khellaf, A. "Simulation of the Temperature and Heat Gain by Solar Parabolic Trough Collector in Algeria". International Journal of Mathematical, Computational, Physical, Electrical and Computer Engineering Vol:6, No:7, (2012), 746-752.

Ouagued, Malika, Abdallah Khellaf, and Larbi Loukarfi. "Estimation of the Temperature, Heat Gain and Heat Loss by Solar Parabolic Trough Collector Under Algerian Climate Using Different Thermal Oils." Energy Conversion and Management. 75 (2013): 191-201.

Pacheco, J.E.; Ralph, M.E.; Chavez, J.M.; Dunkin, S.R.; Rush, E.E.; Ghanbari, C.M.; Matthews, M.W. "Results of Molten Salt Panel and Component Experiments for Solar Central Receivers: Cold Fill, Freeze/Thaw, Thermal Cycling and Shock, and Instrumentation Tests". Sandia National Labs.: Albuquerque, NM, USA, (1995).

Pak, Bock C, and Cho, Young I. "Hydrodynamic and Heat Transfer Study of Dispersed Fluids with Submicron Metallic Oxide Particles." Experimental Heat Transfer. 11.2 (1998): 151-170.

Paul, T.C, J.A Khan, A.K.M.M Morshed, and E.B Fox. "Enhanced Thermophysical Properties of Neils As Heat Transfer Fluids for Solar Thermal Applications." Applied Thermal Engineering. 110 (2017): 1-9.

Paul, Titan C, A.K.M.M Morshed, Elise B. Fox, and Jamil A. Khan. "Thermal Performance of Al2o3 Nanoparticle Enhanced Ionic Liquids (neils) for Concentrated Solar Power (csp) Applications." International Journal of Heat and Mass Transfer. 85 (2015): 585-594.

Peng, Hao, Wenhua Guo, and Meilin Li. "Thermal-hydraulic and Thermodynamic Performances of Liquid Metal Based Nanofluid in Parabolic Trough Solar Receiver Tube." Energy. (2019).

Petela, R. "Exergy of Undiluted Thermal Radiation." Solar Energy Phoenix Arizona Then New York. 74.6 (2003): 469-488.

Petrova, R. "Finite Volume Method – Powerful Means of Engineering Design". (2012). Edited by Radostina Petrova. Janeza Trdine 9, 51000 Rijeka, Croatia.

Petukhov, B.S. "Heat Transfer and Friction in Turbulent Pipe Flow with Variable Physical Properties." (1970).

Philibert C, Frankl P. International Energy Agency. Technology roadmap: concentrating solar power. Paris (France): IEA/OECD; (2010).

Pope, Stephen B. "Turbulent flows". (2019). Cambridge: Cambridge University Press.

Price, Hank, Eckhard Lu¨pfert, David Kearney, Eduardo Zarza, Gilbert Cohen, Randy Gee, and Rod Mahoney. "Advances in Parabolic Trough Solar Power Technology." Journal of Solar Energy Engineering. 124.2 (2002): 109-125.

Qiu, Yu, Ming-Jia Li, Ya-Ling He, and Wen-Quan Tao. "Thermal Performance Analysis of a Parabolic Trough Solar Collector Using Supercritical Co2 As Heat Transfer Fluid Under Non-Uniform Solar Flux." Applied Thermal Engineering. 115 (2017): 1255-1265.

Raja, Narayanan S, and Vijay, S.. "Desalination of Water Using Parabolic Trough Collector." Materials Today: Proceedings. (2019).

Ralph, L.W. Principles of Enhanced Heat Transfer; John Wiley and Sons, Inc.: Hoboken, NJ, USA, 1993.

Rawani, A., Sharma, S.P. and Singh, K.D.P. "Enhancement in performance of parabolic trough collector with serrated twisted-tape inserts", International Journal of Thermodynamics. (2017), Vol. 20. No. 2, pp. 111-119.

Ray, S, A.K Tripathy, S.S Sahoo, and H Bindra. "Performance Analysis of Receiver of Parabolic Trough Solar Collector: Effect of Selective Coating, Vacuum and Semitransparent Glass Cover." International Journal of Energy Research. 42.13 (2018): 4235-4249.

Razmmand, Farhad, Ramin Mehdipour, and Sayed M. Mousavi. "A Numerical Investigation on the Effect of Nanofluids on Heat Transfer of the Solar Parabolic Trough Collectors." Applied Thermal Engineering. 152 (2019): 624-633.

Reddy, K. S. and Satyanarayana, G. V. "Numerical Study of Porous Finned Receiver for Solar Parabolic Trough Concentrator." Engineering Applications of Computational Fluid Mechanics. 2.2 (2008): 172-184.

Reddy, K. S., K. Ravi Kumar, and G. V. Satyanarayana. "Numerical Investigation of Energy-Efficient Receiver for Solar Parabolic Trough Concentrator". Heat Transfer Engineering. (2008). 29, no. 11: 961-972.

Reddy, K.S, Kumar K. Ravi, and C.S Ajay. "Experimental Investigation of Porous Disc Enhanced Receiver for Solar Parabolic Trough Collector." Renewable Energy. 77 (2015): 308-319.

Rehan, Mirza A, Muzaffar Ali, Nadeem A. Sheikh, M S. Khalil, Ghulam Q. Chaudhary, Tanzeel . Rashid, and M Shehryar. "Experimental Performance Analysis of Low Concentration Ratio Solar Parabolic Trough Collectors with Nanofluids in Winter Conditions." Renewable Energy. 118 (2018): 742-751.

Roesle, Matthew, Volkan Coskun, and Aldo Steinfeld. "Numerical Analysis of Heat Loss From a Parabolic Trough Absorber Tube With Active Vacuum System". Journal of Solar Energy Engineering. (2011). 133, no. 3.

Şahin, Hacı M, Eşref Baysal, Ali R. Dal, and Necmettin Şahin. "Investigation of Heat Transfer Enhancement in a New Type Heat Exchanger Using Solar Parabolic Trough Systems." International Journal of Hydrogen Energy. 40.44 (2015): 15254-15266.

Sanchez, David, and Rosengarten, Gary. "Improving the Concentration Ratio of Parabolic Troughs Using a Second-Stage Flat Mirror." Applied Energy. 159 (2015): 620-632.

Scarborough, J.B. "Numerical Mathematical Analysis". (1958). 4th edn, Johns Hopkins University Press, Baltimore, MD.

Schiestel, Roland. "Modeling and Simulation of Turbulent Flows". (2010). https://nbn-resolving.org/urn:nbn:de:101:1-201412222763.

Selvakumar, P, P Somasundaram, and P Thangavel. "Performance Study on Evacuated Tube Solar Collector Using Therminol D-12 As Heat Transfer Fluid Coupled with Parabolic Trough." Energy Conversion and Management. 85 (2014): 505-510.

Sivaram, P.M, N Nallusamy, and M Suresh. "Experimental and Numerical Investigation on Solar Parabolic Trough Collector Integrated with Thermal Energy Storage Unit." International Journal of Energy Research. 40.11 (2016): 1564-1575.

Sokhansefat, T, A.B Kasaeian, and F Kowsary. "Heat Transfer Enhancement in Parabolic Trough Collector Tube Using Al2o3synthetic Oil Nanofluid." Renewable and Sustainable Energy Reviews. 33 (2014): 636-644.

Song, Xingwang, Guobo Dong, Fangyuan Gao, Xungang Diao, Liqing Zheng, and Fuyun Zhou. "A Numerical Study of Parabolic Trough Receiver with Nonuniform Heat Flux and Helical Screw-Tape Inserts." Energy. 77 (2014): 771-782.

Soo, Too Y. C, and R Benito. "Enhancing Heat Transfer in Air Tubular Absorbers for Concentrated Solar Thermal Applications." Applied Thermal Engineering. 50.1 (2013): 1076-1083.

Subramani, J, P.K Nagarajan, Somchai Wongwises, S.A El-Agouz, and Ravishankar Sathyamurthy. "Experimental Study on the Thermal Performance and Heat Transfer Characteristics of Solar Parabolic Trough Collector Using Al_2o_3 Nanofluids." Environmental Progress & Sustainable Energy. 37.3 (2018a): 1149-1159.

Subramani, J., Nagarajan, P.K., Mahian, O., Sathyamurthy, R.,. Efficiency and heat transfer improvements in a parabolic trough solar collector using TiO2 nanofluids under turbulent flow regime. Renew. Energy 119 (2018b), 19-31.

Sundar, L S, and Sharma, K.V. "Turbulent Heat Transfer and Friction Factor of Al2o3 Nanofluid in Circular Tube with Twisted Tape Inserts." International Journal of Heat and Mass Transfer. 53 (2010): 1409-1416.

Suresh, Isravel R, S Saravanan, V Vijayan, and M Raja. "Thermal Augmentation in Parabolic Trough Collector Solar Water Heater Using Rings Attached Twisted Tapes." Materials Today: Proceedings. 21 (2020): 127-129.

Swinbank WC. Long-wave radiation from clear skies. Q J R Meteorol Soc(1963);89:339–48.

Tabatabaian, Mehrzad. "Cfd Module: Turbulent Flow Modeling". (2015). Dulles, Virginia: Mercury Learning and Information, David Pallai.

Tahtah, Reda, Ali Bouchoucha, Cherifa Abid, Mahfoud Kadja, and Fouzia Benkafada. “Experimental Study of Heat Transfer in Parabolic Trough Solar Receiver: Using Two Different Heat Transfer Fluids”. (2017).

Tajik, Jamal-Abad M, S Saedodin, and M Aminy. "Experimental Investigation on the Effect of Partially Metal Foam Inside the Absorber of Parabolic Trough Solar Collector." International Journal of Engineering, Transactions B: Applications. 30.2 (2017): 1286-1292.

Tao, Y.B, and Y.L He. "Numerical Study on Coupled Fluid Flow and Heat Transfer Process in Parabolic Trough Solar Collector Tube." Solar Energy. 84.10 (2010): 1863.

Tennekes, Hendrik, and John L. Lumley. "A first course in turbulence". (1994). Cambridge: The MIT Press.

Thomas, A, and Guven, Halil M. "Effect of Optical Errors on Flux Distribution Around the Absorber Tube of a Parabolic Trough Concentrator." Energy Conversion and Management. 35.7 (1994): 575-582.

Toghyani, Somayeh, Ehsan Baniasadi, and Ebrahim Afshari. "Thermodynamic Analysis and Optimization of an Integrated Rankine Power Cycle and Nano-Fluid Based Parabolic Trough Solar Collector." Energy Conversion and Management. 121 (2016): 93-104.

Tripathy, A.K, S Ray, S.S Sahoo, and S Chakrabarty. "Structural Analysis of Absorber Tube Used in Parabolic Trough Solar Collector and Effect of Materials on Its Bending: a Computational Study." Solar Energy. 163 (2018): 471-485.

Tseng, W J, and Lin, K C.. "Rheology and Colloidal Structure of Aqueous Tio2 Nanoparticle Suspensions." Materials Science and Engineering a. 355 (2003): 186-192.

Tseng, Wenjea J, and Chen, Chun-Nan. "Effect of Polymeric Dispersant on Rheological Behavior of Nickel-Terpineol Suspensions." Materials Science & Engineering a. 347.1 (2003): 145-153.

Turkyilmazoglu, Mustafa. "Condensation of Laminar Film Over Curved Vertical Walls Using Single and Two-Phase Nanofluid Models." European Journal of Mechanics / B Fluids. 65 (2017): 184-191.

Valizade, M, M.M Heyhat, and M Maerefat. "Experimental Study of the Thermal Behavior of Direct Absorption Parabolic Trough Collector by Applying Copper Metal Foam As Volumetric Solar Absorption." Renewable Energy. (2020): 261-269.

Van Leer, B.. “Towards the ultimate conservative difference scheme. II. Monotonicity and conservation combined in a second-order scheme“. (1974) Journal of Computational Physics, 14(4), 361–370.

Vutukuru, R.; Pegallapati, A.S.; Maddali, R. "Suitability of Various Heat Transfer Fluids for High Temperature Solar Thermal Systems". Appl. Therm. Eng. (2019), 159, 1–9.

Waghole, Dnyaneshwar R, R.M Warkhedkar, V.S kulkarni, and R.K Shrivastva. "Experimental Investigations on Heat Transfer and Friction Factor of Silver Nanofliud in Absorber/receiver of Parabolic Trough Collector with Twisted Tape Inserts." Energy Procedia. 45 (2014): 558-567.

Wang, P, D.Y Liu, and C Xu. "Numerical Study of Heat Transfer Enhancement in the Receiver Tube of Direct Steam Generation with Parabolic Trough by Inserting Metal Foams." Applied Energy. 102 (2013): 449-460.

Wang, Ruilin, Wanjun Qu, Hui Hong, Jie Sun, and Hongguang Jin. "Experimental Performance of 300 Kwth Prototype of Parabolic Trough Collector with Rotatable Axis and Irreversibility Analysis." Energy. 161 (2018): 595-609.

Wang, X, X Xu, and S U. S. Choi. "Thermal Conductivity of Nanoparticle-Fluid Mixture." Journal of Thermophysics and Heat Transfer. 13.4 (1999): 474-480

Wang, Yanjuan, Jinliang Xu, Qibin Liu, Yuanyuan Chen, and Huan Liu. "Performance Analysis of a Parabolic Trough Solar Collector Using Al2O3/synthetic Oil Nanofluid." Applied Thermal Engineering. 107 (2016): 469-478.

Wang, Yanjuan, Qibin Liu, Jing Lei, and Hongguang Jin. "A Three-Dimensional Simulation of a Parabolic Trough Solar Collector System Using Molten Salt As Heat Transfer Fluid." Applied Thermal Engineering. 70.1 (2014a): 462-476.

Wirz, Men, Jules Petit, Andreas Haselbacher, and Aldo Steinfeld. "Potential Improvements in the Optical and Thermal Efficiencies of Parabolic Trough Concentrators." Solar Energy. 107 (2014): 398-414.

Wu, Yu-Ting, Shan-Wei Liu, Ya-Xuan Xiong, Chong-Fang Ma, and Yu-Long Ding. "Experimental Study on the Heat Transfer Characteristics of a Low Melting Point Salt in a Parabolic Trough Solar Collector System." Applied Thermal Engineering. 89 (2015): 748-754.

Wu, Zhiyong, Shidong Li, Guofeng Yuan, Dongqiang Lei, and Zhifeng Wang. "Three-dimensional Numerical Study of Heat Transfer Characteristics of Parabolic Trough Receiver." Applied Energy. 113 (2014): 902-911.

Xiangtao, Gong, Fuqiang Wang, Haiyan Wang, Jianyu Tan, Qingzhi Lai, and Huaizhi Han. "Heat Transfer Enhancement Analysis of Tube Receiver for Parabolic Trough Solar Collector with Pin Fin Arrays Inserting." Solar Energy. 144 (2017): 185-202.

Xiao, H.; Liu, P.; Liu, Z.; Liu, W. Performance analyses in parabolic trough collectors by inserting novel inclined curved-twisted baffles. Renew Energy (2021), 165, 14–27.

Xiao, X, P Zhang, D D. Shao, and M Li. "Experimental and Numerical Heat Transfer Analysis of a V-Cavity Absorber for Linear Parabolic Trough Solar Collector." Energy Conversion and Management. 86 (2014): 49-59.

Xu, Li, Feihu Sun, Linrui Ma, Xiaolei Li, Dongqiang Lei, Guofeng Yuan, Huibin Zhu, Qiangqiang Zhang, Ershu Xu, and Zhifeng Wang. "Analysis of Optical and Thermal Factors' Effects on the Transient Performance of Parabolic Trough Solar Collectors." Solar Energy. 179 (2019): 195-209.

Xu, Li, Zhifeng Wang, Guofeng Yuan, Xing Li, and Yi Ruan. "A New Dynamic Test Method for Thermal Performance of All-Glass Evacuated Solar Air Collectors." Solar Energy. 86.5 (2012): 1222-1231.

Xuan, Yimin, and Wilfried Roetzel. "Conceptions for Heat Transfer Correlation of Nanofluids." International Journal of Heat and Mass Transfer. 43.19 (2000): 3701-3707.

Yaghoubi, M, F Ahmadi, and M Bandehee. "Analysis of Heat Losses of Absorber Tubes of Parabolic Through Collector of Shiraz (iran) Solar Power Plant." Journal of Clean Energy Technologies. (2013): 33-37.

Yang B, Zhao J, Xu T, Zhu Q. "Calculation of the concentrated flux density distribution in parabolic trough solar concentrators by Monte Carlo ray-trace method". (2010). Symposium on photonics and optoelectronics. IEEE; 2010. p.1–4.

Yazdanpanahi, Javad, Faramarz Sarhaddi, and Adeli M. Mahdavi. "Experimental Investigation of Exergy Efficiency of a Solar Photovoltaic Thermal (pvt) Water Collector Based on Exergy Losses." Solar Energy. 118 (2015): 197-208.

Yilmaz, I.H.; Mwesigye, A.; Goksu, T.T. "Enhancing the overall thermal performance of a large aperture parabolic trough solar collector using wire coil inserts. Sustain". Energy Technol. Assess. (2020), 39, 10066.

Yu, W, and Choi, S.U.S. "The Role of Interfacial Layers in the Enhanced Thermal Conductivity of Nanofluids: a Renovated Hamilton-crosser Model." Journal of Nanoparticle Research. 6.4 (2004): 355-361.

Zadeh, Mohammad,P, T Sokhansefat, A B. Kasaeian, F Kowsary, and A Akbarzadeh. "Hybrid Optimization Algorithm for Thermal Analysis in a Solar Parabolic Trough Collector Based on Nanofluid." Energy. 82 (2015): 857-864.

Zhang, Liang, Zitao Yu, Liwu Fan, Wujun Wang, Huan Chen, Yacai Hu, Jianren Fan, Mingjiang Ni, and Kefa Cen. "An Experimental Investigation of the Heat Losses of a U-Type Solar Heat Pipe Receiver of a Parabolic Trough Collector-Based Natural Circulation Steam Generation System." Renewable Energy. 57 (2013): 262-268.

Zhao, D, E Xu, Q Yu, and D Lei. "The Simulation Model of Flux Density Distribution on an Absorber Tube." Energy Procedia. 69 (2015): 250-258.

Zheng, Lu, Yonghui Xie, and Di Zhang. "Numerical Investigation on Heat Transfer Performance and Flow Characteristics in Circular Tubes with Dimpled Twisted Tapes Using Al2o3-Water Nanofluid." International Journal of Heat and Mass Transfer. 111 (2017): 962-981.

Zheng, Z., Xu, Y. and He, Y.-L. (2016), “Thermal analysis of a solar parabolic trough receiver tube with porous insert optimized by coupling genetic algorithm and CFD”, Science China Technological Sciences, Vol. 59 No. 10, pp. 1475-1485.

Zhu, Xiaowei, Lei Zhu, and Jingquan Zhao. "Wavy-tape Insert Designed for Managing Highly Concentrated Solar Energy on Absorber Tube of Parabolic Trough Receiver." Energy. 141 (2017): 1146-1155.

Appendix A: Finite Volume Method

The computational domain in the FVM is divided into small cells called control volumes and the integration of the principal conservation equations is performed over each control volume. The schematic of two neighboring cells is presented in Figure which is taken as an example. As can be seen that each cell is surrounded by a set of discrete faces.

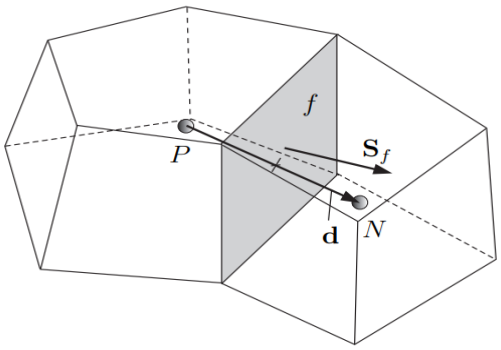

Figure A1: The configuration of two neighbouring cells in FVM with cell centres of N and P, OpenFOAM, (2015).

The conservation transport equation for a scalar parameter ϕ (e.g. temperature, velocity components, etc..) can be formulated as:

$$\underbrace{\frac{\partial \rho\phi}{\partial t}}_{transient\ term} + \underbrace{\frac{\partial}{\partial x_j}\left(U_j \rho\phi\right)}_{convective\ term} = \underbrace{\frac{\partial}{\partial x_j}\left(\Gamma \frac{\partial \phi}{\partial x_j}\right)}_{diffusion\ term} + \underbrace{S_\phi}_{source\ term}. \tag{A-1}$$

The term $\frac{\partial \rho\phi}{\partial t}$ is the time-change rate of the scalar quantity at a generic location in space whereas the terms $\frac{\partial}{\partial x_j}\left(U_j \rho\phi\right)$ and $\frac{\partial}{\partial x_j}\left(\Gamma \frac{\partial \phi}{\partial x_j}\right)$ represent the convection and diffusion terms of the scalar quantity respectively. Whereas, the last term S_ϕ represents the source term that could act at destroying or generating the scalar quantity ϕ which may represent the pressure force in the momentum equation and heat generation per unit volume in the energy equation. The above equation in the steady-state condition is obtained by removing the rate of time-change term as follows:

$$\frac{\partial}{\partial x_j}\left(U_j \rho\phi\right) = \frac{\partial}{\partial x_j}\left(\Gamma \frac{\partial \phi}{\partial x_j}\right) + S_\phi. \tag{A-2}$$

As stated previously that the FVM is integrated over each element of the whole domain (volume ΔV), therefore the proceeding formula can be given as:

$$\int_{\Delta V} \frac{\partial}{\partial x_j}(U_j \rho\phi) dV = \int_{\Delta V} \frac{\partial}{\partial x_j}\left(\Gamma \frac{\partial \phi}{\partial x_j}\right) dV + \int_{\Delta V} S_\phi \, dV. \quad \text{(A-3)}$$

Then, both convection and diffusion terms are re-written using the divergence theorem in order to replace the volume integral by the surface integral to yield:

$$\int_{S_i} \rho\phi(\underline{U}.\underline{n}) dA = \int_{S_i} \Gamma(\nabla\phi.\underline{n}) dA + \int_{V_i} S_\phi \; dV. \quad \text{(A-4)}$$

Here S_i represents the surface area of the cell i and dA is the infinitesimally small area on the given surface whereas $\underline{n}$ represents the unit vector located in the normal direction to the infinity small area.

The source term in the transport equation is obtained by assuming the average value of S_ϕ over the volume V_i is similar to that computed at the cell i centroid expressed as:

$$\int_{V_i} S_\phi \; dV \approx S_\phi V_i. \quad \text{(A-5)}$$

A.1 Convective Term

In the convection term, the mathematical term represents the scalar ϕ transport by the medium bulk motion at the $i-th$ cell face. The convection term can be transferred to a summation of mass flow rate of the scalar quantity ϕ_f over the faces that enclose the cell i which in turn yield to:

$$\int_{S_i} \rho\phi(\underline{U}.\underline{n}) dA = \sum_{f=1}^{N_{f,i}} \rho_f (\underline{U}.\underline{n})_f A_f \phi_f = \sum_{f=1}^{N_{f,i}} \dot{m_f} \; \phi_f. \quad \text{(A-6)}$$

Here, the $N_{f,i}$ represents the total number of cell faces, the subscript f represents the cell faces, A_f represents the area of the face f and $\dot{m_f}$ represents the face mass flow rate. The value of ϕ is computed only at the cell nodes, thus the value of ϕ_f has to be interpolated. Some of the treatment methods of the interpolation proposed in the literate are explained in more details below:

- **Upwind-difference Scheme**

The main idea of this method is that the value of the variable ϕ_f at the interface is equal to the down-stream cell value or up-stream cell value depending on the mass flow rate $\dot{m_f}$ of the interface f as yield to:

$$\phi_f = \begin{cases} \phi_P & if\ \dot{m_f} \geq 0 \\ \phi_N & if\ \dot{m_f} < 0 \end{cases} \quad \text{(A-7)}$$

The upwind-scheme provides a physically realistic solution since there are no negative coefficients arising in the equation which makes this scheme stable and bounded. However, this scheme is only first order accurate and it smooths the variable gradients in a case of applying this scheme in high-gradient regions. The accuracy order is highly important since it may provide information about how the numerical errors are rapidly reduced as the mesh is refined. Therefore, applying a high order scheme is usually preferable.

- **The Central-Differencing (CD) Scheme**

The convection term in the Central-Differencing (CD) scheme is obtained through using two nodes straddling faces as:

$$\phi_f = f_x\phi_P + (1 - f_x)\phi_N. \quad \text{(A-8)}$$

Here $f_x \equiv \frac{\overline{fN}}{\overline{PN}}$, where $\overline{fN}$ and $\overline{PN}$ represent the distances between surface f and the center of cell N and the distance between the centers of cell P and N respectively. This scheme is derived by the Taylor series expansion which involves the derivative of the second order whereas the higher derivatives are neglected, i.e. it is second order accurate. This interpolation for the uniform grid is achieved by a simple linear interpolation as follows:

$$\phi_f = \frac{1}{2}(\phi_P + \phi_N). \quad \text{(A-9)}$$

This assumption is based on the idea that the interface is mid-way between two cells and thus the ϕ_f is computed based on the average values of cells. However, the above formulation may yield an unacceptable discretization as it is highly unstable. Some other alternative methods have been proposed in the literature to provide a better prescription such as:

- **Hybrid difference scheme**

The convection term can also be calculated using the Hybrid difference scheme as:

$$\phi_f = (1-\gamma)\left(\phi_f\right)_{UD} + \gamma\left(\phi_f\right)_{CD}. \quad \text{(A-10)}$$

Where γ defines whether upwind differencing (UD), central differencing (CD) or a blended approach will be utilized. Blending the upwind differencing scheme and the central differencing scheme prevents the unphysical solution that may be generated by a pure central differencing scheme and, at the same time, to yield more accurate results than those obtained by the upwind scheme, Scarborough (1958). However, the only disadvantage of this scheme is the accuracy in terms of Taylor series truncation error is still first order.

- **Van Leer limiter**

As explained previously, the upwind scheme is the most stable scheme and bounded by default but suffers from the low order of accuracy. High order schemes can provide unrealistic results especially when they are applied for solving turbulent quantities. To overcome these challenges, Total Variation Diminishing (TVD) schemes are proposed and designed to provide oscillation-free solutions at high order of accuracy. Among various TVD schemes, the Van Leer limiter is used in the present study which is given as:

$$\phi_f = \phi_P + 0.5\Upsilon(\phi_E - \phi_P). \quad \text{(A-11)}$$

Here, Υ represents the flux limiter function which is a function of the ratio of upwind-side gradient to down-side gradient r which are defined as:

$$\Upsilon = \frac{r + |r|}{1 + r}, \quad \text{(A-12)}$$

where

$$r = \frac{\phi_P - \phi_W}{\phi_E - \phi_P}. \quad \text{(A-13)}$$

The subscripts W and E refer to the cells in the west and east directions respectively. The flux limiter function is second-order accurate scheme.

A.2 Diffusive Term

For the diffusive flux the Gauss's theorem is used to convert the volume integral to surface integral as

$$\int_V \frac{\partial}{\partial x_j}\left(\Gamma \frac{\partial \phi}{\partial x_j}\right) dV = \int_{S_i} \Gamma(\nabla\phi.\underline{n})dA = \sum_{f=1}^{N_{f,o}} \Gamma_f A_f.(\nabla\phi)_{f.} \tag{A-14}$$

The gradient $(\nabla\phi)_f$ at the cell faces is computed using the central difference scheme, thus the diffusive term results in a second order approximation as

$$A_f.(\nabla\phi)_f = |A_f| \frac{\phi_N - \phi_P}{|\overline{PN}|}. \tag{A-15}$$

Here the parameter $|\overline{PN}|$ represents the distance vector between the cell center P and cell center N.

A.3 Pressure-Velocity Coupling

The pressure gradient in the flow equation (momentum) represents the main source term in most of the engineering flows. If the scalar variables such as pressure, temperature, etc. are stored at the same locations of velocity components, then the resulting pressure field would act as a uniform (zero) momentum source in the discretized equation which is physically unacceptable. In such grid arrangements (which are called collocated grids), the pressure gradient in the discretized momentum equation does not contain the pressure at the central cell. This weak linkage produces the behaviour of chequerboard oscillations in the pressure field. Among the different algorithms that have been proposed to overcome this issue, the PISO algorithm follows a different strategy in which the velocity components are defined at the cell faces whereas the scalar variables, including pressure, are stored at the nodes. This grid arrangement is defined as staggered grid approach. However, the chequerboarding can be prohibited even in the collocated grid by introducing the Rhie-Chow interpolation, Moukalled et al. (2016), which is used in OpenFOAM.

Appendix B: Numerical Investigations of parabolic trough collectors using different nanofluids

Abstract— this part presents three dimensional numerical simulations of parabolic trough collectors (PTC) based on two low-Reynolds eddy viscosity turbulence models, namely; Launder and Sharma k-epsilon and k-omega SST models. For the simulations, water was used as the Heat Transfer Fluid (HTF) with four different nanoparticles; Al_2O_3, TiO_2, CuO and Cu. Different volume fractions (φ) of the nanoparticles were investigated for various Reynolds (Re) numbers with uniform heat flux. Results showed that the overall performance of the system is more sensitive to changes in the thermal properties of nanofluid than the thermal properties of the HTF. At a volume fraction of 6% and a Re number of 70,000, the Nusselt number (Nu) enhancement of nanofluids TiO_2-water, Al_2O_3-water, CuO-water and Cu-water were found to be 21.5%, 20.2%, 18.11% and 15.7% respectively while the performance evaluation criteria (PEC) were 1.214, 1.2, 1.18 and 1.155 respectively.

B.1 Introduction

To tackle the climate change and global warming, the world needs to reduce its dependency on fossil fuels. In recent years, clean renewable and sustainable sources of energy such as solar, wind, tidal etc. have thus become widely popular. In particular, solar thermal energy has emerged as a major contender in the quest to reduce CO_2 emissions especially for regions with hot tropical climate. The light or solar energy/heat from the sun can be harnessed to produce electricity via Photovoltaic Devices (PV) or Concentrating Solar Power (CSP) plants. The CSP plants operate on Direct Normal Irradiance (DNI), which is defined as the amount of received solar energy per unit area on the surface held normal to the rays of the sun. Depending upon the methodology to capture the suns energy, the CSP technology can be categorized into several technologies, four of the most common ones being; parabolic trough collectors (PTC: which is our focus), linear Fresnel reflectors, parabolic dishes and solar towers.

The PTC system consists mainly of three important sub-systems; the solar field systems, the storage system and the power block system. The solar field sub-system can be categorized as a type of a large heat exchanger with the main components being the solar collector and the reflector surface. The reflector surface is generally made up of a series of mirrors that directs the solar energy to the solar collector. The solar collector then converts the absorbed incident solar radiation into thermal energy which is carried through the

collector via the Heat Transfer Fluid. Within the solar collector, an absorber tube is generally made from a metal which is coated with black colour to achieve larger solar absorbance and to reduce the thermal emittance. The absorber tube is encased within a glass envelope which is itself covered with an anti-reflective coating to reduce the heat losses by convection.

B.2 Thermal performance of PTCs

The absorber tube (it is referred also to heat collection element (HCE)) is one of the most important elements in a PTC system. A high efficiency of the absorber tube means higher thermal efficiency, lower plant costs and a lower temperature gradient of absorber tube; all of these lead to a better plant reliability. Because of these advantages, four main technologies of heat transfer enhancement have been considered particularly within the absorber tube. The thermal performance of a PTC can be improved by either changing the heat transfer fluid or by adding nanoparticles (metallic or non-metallic) to it thus enhancing its thermal properties. The possible third technology is to insert swirl generators inside the HCE to enhance the heat augmentation. The fourth technique is to use inserts within the HCE using nanofluids.

B.3 Thermal performance by adding nanoparticles

One of the most useful techniques used to improve the thermal performance in PTCs is to add metallic or non-metallic nanoparticles inside the base working fluid which in turn leads to creation of the medium called nanofluid. The main function of nanofluid in solar fields is to capture the solar energy in such a way that it is more effective than the base fluid leading to improvement in the thermal performance of the absorber. Increasing the φ of the nanoparticles not only enhances the convection heat transfer but also decreases the thermal stresses on the absorber tube. However, an increase in the nanoparticle density may lead to their agglomeration in certain areas thus raising the pressure required to pump the fluid. Thus, one needs to optimize the φ ratio of nanoparticles for heat transfer enhancement.

There are two entirely different approaches to modelling the nanofluids; either as a single-phase or a two-phase model. Both these approaches have successfully been used in the past with the two-phase approach being costly but more accurate.

Furthermore, accurate numerical predictions depend heavily on the selection of the thermos-physical properties of the nanoparticles. Various theoretical forms of their thermos-physical properties are available in the literature along with some correlations as presented in [1].

B.4 Literature review of nanofluids in PTCs

Reference [2] used Al_2O_3 in Ionic Liquids with various values of φ (0.9, 0.18 and 0.36) reported enhancement of thermal conductivity by 11% and heat capacity by 49% for φ=0.9. Using both single and two phase modelling approaches by [3] reported a 36% increase in the heat transfer coefficient with Al_2O_3 immersed in synthetic oil at φ of 5 %. Reference [4] examined the effect of mixed nanoparticles of $CuO–Al_2O_3$ in water with different ratios of φ. The optimum values of PH, sonication time, and mass concentration were 7.5-8.5, 100-120 min and 1.25 which lead to the maximum level of repulsive and dispersion forces between the nanoparticles. In 2017, [5] used the same nanoparticles but with two different base fluids (Water and water-EG (ethylene glycol)) with φ of 0.05, 0.1 and 0.2%. According to their findings the thermal efficiency was higher for pure water since the mixture of water-EG had much higher boiling and freezing temperatures. Another issue highlighted by [6] is that the absorber deformation decreased substantially from 2.11 mm to 0.54 mm when φ was increased from 0 to 0.05% for Al_2O_3-synthetic oil. Reference [7] used another type of nanofluids (Cu- Therminol®VP-1) and reported heat transfer enhancements of 8%, 18% and 32% at φ of 2%, 4% and 6% respectively. Recently, [8] used metallic and non-metallic nanoparticles in Syltherm 800-base fluid with φ of (3 and 5%). The authors reported the relative gain in thermal energy were 1.46, 1.25 and 1.4 for Al_2O_3, CuO and TiO2 respectively. However, the maximum exergy efficiency obtained was about 9.05% by using 3% of CuO. Reference [9] used another type of non-metallic nanoparticle, NiO immersed in biphenyl and diphenyl oxide. This resulted increasing the heat transfer coefficient by 50% and thermal conductivity by 96%. In the present work, the metallic and non-metallic nanoparticles (Alumina (Al_2O_3), Copper oxide (CuO), Titanium Oxide (TiO2) and Copper (Cu)) are immersed in water with different φ and Re numbers under uniform heat flux in the circumferential direction.

B.5 Solar Receiver

In this section we present the CFD results of a solar absorber of 2m length and 60mm diameter, as shown in “Fig. 1a”. Open source solver, OpenFOAM, was used to study flow characteristics and heat transfer utilizing two low-Reynolds turbulence models; Launder and Sharma k-ε and Shear Stress transport k-ω models. For the simulations, the heat flux

(q) was fixed at 50000 "W/m^2". The base fluid and nanofluid were incompressible and the effect of gravity was neglected. Three different meshes were tested for the mesh independence study; Coarse (0.5 million cells), Medium (1.3 million cells) and Fine (2.1 million cells). For all grids the near wall non-dimensional distance was kept at a $Y^+$of 1 to resolve the viscous sublayer. A comparison of the Nu number with the Re number is shown in "Fig 1b" for all the three meshes. From the "Fig. 1b" it can be observed that the medium grid is sufficient for the present study as further mesh refinement had almost no effect on the Nu number profile.

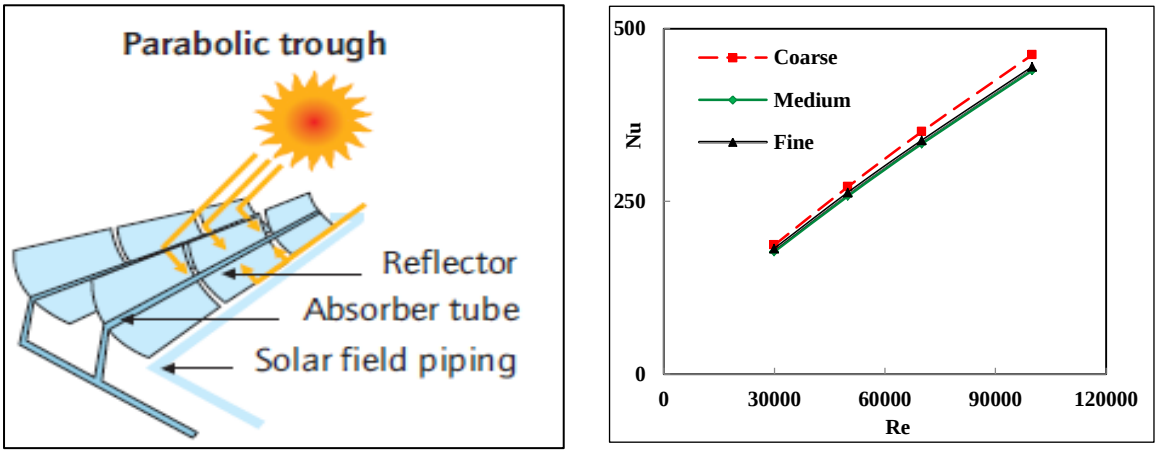

(a) (b)

Fig. 1. (a) Schematic of the parabolic trough receiver and (b) Mesh independence study for three different grids.

Boundary conditions

The boundary conditions (BC's) used in the present study are listed in Table 1; FV and ZG mean fived value and zero gradient respectively

Table 1: boundary conditions applied in the present work.

BC's	U (m/s)	P (Pa)	T (K)	K (m^2/s^2)	ε (m^2/s^3)	ω (1/s)
inlet	FV	ZG	FV	FV	FV	FV
wall	0	ZG	q=c	0	0	FV
outlet	ZG	Zero	ZG	ZG	ZG	ZG

Thermo-physical properties of nanofluid

In the present study, a single-phase modelling method is used to model the nanofluid which is based on the physics of mixture of two different materials; a base fluid of water at T=320.15K mixed sequentially with four different nanoparticles (Al_2O_3, CuO, TiO_2 and Cu). Their properties (density, ρ (kg/m^3), thermal conductivity, k (W/m.K), specific heat capacity, C_p (J/kg.K) and dynamic viscosity, μ ($N.s/m^2$)) at the ambient temperature are listed in "Table 2". Three different Re numbers were considered for the present study (30,000, 50,000 and 70,000) and three values of φ (2%, 4% and 6%).

Table 2: Thermal properties of water and various tested nanoparticles, [10].

Property	water	Al_2O_3	CuO	TiO_2	Cu
ρ (kg/m^3)	988.9	3970	6320	4250	8933
k (W/m.K)	0.6398	40	77	8.95	401
C_p (J/kg.K)	4180.4	765	532	686	385
μ ($N.s/m^2$)	0.00058	-	-	-	-

The single-phase approach is reasonably accurate when φ of the nanoparticles is smaller than 10% and the diameter of nanoparticles is less than 100 nm, [7]. In this approach, the nanofluid density (ρ_{nf}) is calculated depending on the classical form of heterogeneous mixture. Whereas, the specific heat capacity (C_{nf}) was determined depending on the thermal equilibrium between the solid particles and surrounding base fluid. However, several models were used for determining the nanofluid viscosity and thermal conductivity and the most appropriate models are used in the present work.

$$\rho_{nf} = \rho_p \varphi + \rho_b (1 - \varphi) \quad \text{(B.1)}$$

$$C_{p,nf} = \frac{1}{\rho_{nf}} \left[\rho_p C_{p,p} \varphi + C_{p,b} \rho_b (1 - \varphi) \right] \quad \text{(B.2)}$$

$$\mu_{nf} = \mu_b (1 + 7.3\varphi + 123\varphi^2) \quad \text{(B.3)}$$

$$k_{nf} = k_p(3\varphi - 1) + [3(1-\varphi) - 1]k_b + \sqrt{\Delta}$$

$$\Delta = (3\varphi - 1)^2 {k_p}^2 + [3(1-\varphi) - 1]^2 {k_b}^2 + 2[2 + 9\varphi(1-\varphi)]k_p k_b \quad \text{(B.4)}$$

Where the subscript (nf) represents nanofluids, (p) refers to the nanoparticle and (b) the base fluid. The properties of nanofluids resulting from these equations are presented in "Fig. 2" which shows the Prandtl number ($Pr = \mu_{nf}.Cp_{nf}/k_{nf}$) for each of the nanofluid. The highest value of Pr number was observed for (TiO2).

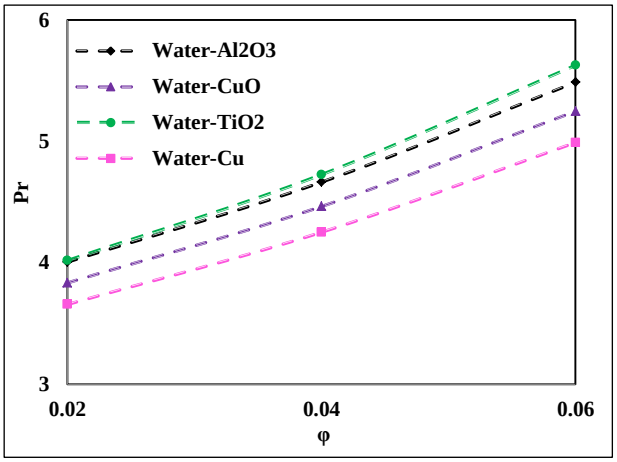

Fig. 2. The Pr number behaviour of nanofluids under consideration at T=320.15 K.

B.6 Model validation

Results are compared to the DNS data of [11] at a bulk Re of 5500 and Pr number of 1. The non-dimensional stream-wise velocity ($U^+ = U/U_\tau$) of pure water and the dimensionless mean temperature ($T^+ = (\langle T_w \rangle - T)/T_\tau$) profiles are shown in "Fig. 3" where the friction velocity is defined as ($U_\tau = \sqrt{\tau/\rho}$), where ($\tau$) is the wall shear stress (Pa) and the friction temperature is defined as ($T_\tau = q//\rho C_p U_\tau$). It was observed that both tested RANS model predictions were decent compared to the DNS of [11].

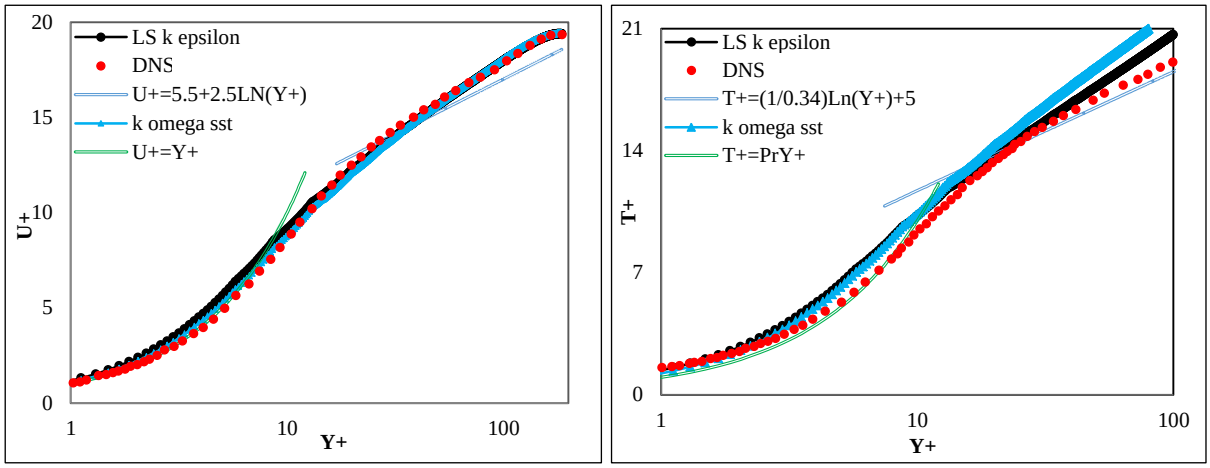

(a) (b)

Fig. 3: Comparison between the dimensionless parameters with the DNS data of [11] (a) Mean velocity profile (b) Mean temperature profile.

The model predictions were also validated against the experimental correlation of [12] for Nu number and friction factor and with the experimental correlation of [13] for only Nu number. These correlations for the fully developed turbulent flow are respectively given by:

$$Nu = \frac{\left(\frac{f}{8}\right) Re\ Pr}{1.07 + 12.7\left(\frac{f}{8}\right)^{0.5}\left(Pr^{\frac{2}{3}} - 1\right)} \quad for \begin{Bmatrix} 0.5 \le Pr \le 2000 \\ 10^4 < Re < 5 \times 10^6 \end{Bmatrix} \qquad (B.5)$$

$$f = (0.75\ ln\ Re^{-1.64})^{-2}. \quad for\ \{3000 < Re < 5 \times 10^6\} \qquad (B.6)$$

$$Nu = \frac{\left(\frac{f}{8}\right)(Re - 1000)\ Pr}{1 + 12.7\left(\frac{f}{8}\right)^{0.5}\left(Pr^{\frac{2}{3}} - 1\right)}. \quad for \begin{Bmatrix} 0.5 \le Pr \le 2000 \\ 3 \times 10^3 < Re < 5 \times 10^6 \end{Bmatrix} \qquad (B.7)$$

It can be noticed from "Fig. 4" that the present CFD predictions by the SST k-ω model are better than those of LS k-ε model as it agrees well with the experimental correlations showing an error of only 6.1% for the Nusselt number and 7.5% for the friction factor.

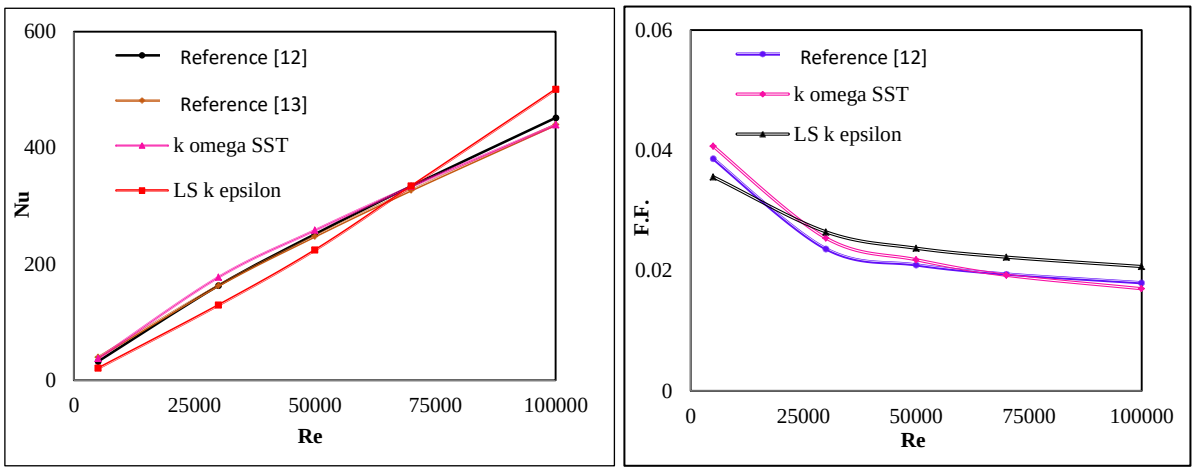

(a) (b)

Fig. 4. Comparisons of current results with experimental correlations of [12] and [13] (a) Average Nu number (b) Friction factor

B.7 Discussion of Results

The mean velocity profiles at Re=30,000 at the location of 1.75m for all types of nanofluids are presented in "Fig. 5". It can be observed that by increasing the φ of a particle, the velocity profiles become more uniform with a noticeable increase in regions away from the wall. However, at φ=2%, the increase in velocity is larger for water-Al_2O_3 and water-TiO2 than the other two nanofluids which becomes more prominent at higher ratios of φ. On the other hand an opposite trend is observed for the temperature away from the walls, where for increasing the φ, the temperature in the middle of the channel decreases. Again this decrease is more prominent for higher φ as shown in "Fig. 6".

The average Nu number in the parabolic trough receiver is given by ($Nu = hD/k$) and the heat transfer coefficient by $h = q/(T_w - T_b)$ where D is the receiver diameter, k the thermal conductivity, T_w the average wall temperature and T_b the average bulk temperature calculated as$(T_{inlet} + T_{out})/2$. The average Nu number profiles of the base fluid and nanofluids for all values of φ is illustrated in "Fig. 7". It can be observed that the Nu number increases as the φ is raised. The positive slope in "Fig. 7" represents the behaviour of the (Pr) number, as presented in "Fig. 2". A similar trend is observed for increasing Re number which is due to the reduction in the thickness of the viscous sublayer.

At a φ of 6% and Re=70000, the Nu number enhancement of nanofluids water-TiO_2, water-Al_2O_3, water-CuO and water-Cu are found to be 21.5, 20.2, 18.11 and 15.7% respectively.

The pressure drop (ΔP) and Darcy friction factor (f) in the parabolic trough receiver are respectively given by $\Delta P = f\left(\frac{L}{D}\right)(\frac{\rho U_{ave}^2}{2})$ and$f = (8\tau_w)/(\rho U_{ave}^2)$. The pressure drop in the solar receiver occurs due to the frictional force acting on the heat transfer fluid as it flows. The two factors directly affecting this frictional force are the flow velocity and the viscosity. According to the aforementioned equations, the frictional shear force and the pressure drop within the pipe are directly proportional. Therefore, the higher the shear force, the larger the pressure drop across the receiver section. This is confirmed by "Fig. 8" which presents the pressure drop of the base fluid and nanofluids for all the tested configurations. Here it can be noted that the pressure drop increases with both Re number and the φ of the nanoparticles.

A comparison of (PEC) of all considered nanofluids is shown in "Fig. 9" which presents data at a Re number of 70,000 and φ=6%. This parameter can be calculated by ($PEC = (\frac{Nu}{Nu_o})/(\frac{f}{f_o})^{1/3}$), where Nu_o is the Nu number and f_o the friction factor of the pure working fluid. Here a PEC value of more than 1, indicates an enhancement in the flow performance. Larger magnitudes of the PEC (>1) indicate larger thermal performance of nanofluids under the same power pumping requirements. Considering this parameter, the largest value was recorded with TiO2-water for all the tested values of φ. At a φ of 6% and Re = 70000, the PEC of nanofluids water-TiO_2, water-Al_2O_3, water-CuO and water-Cu were found to be 1.214, 1.2, 1.18 and 1.155 respectively.

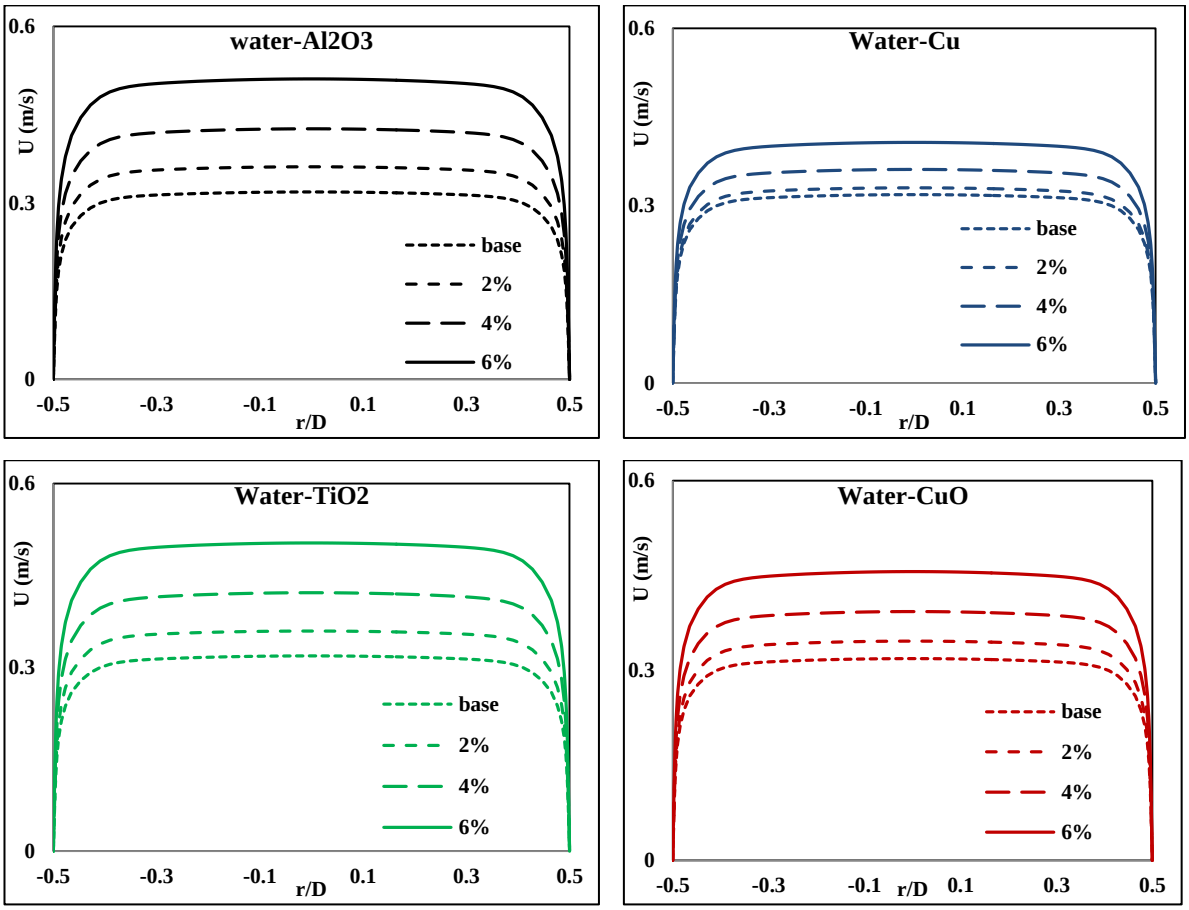

Fig. 5. Effect of particle loading on the mean velocity profiles at L=1.75m and Re=30,000.

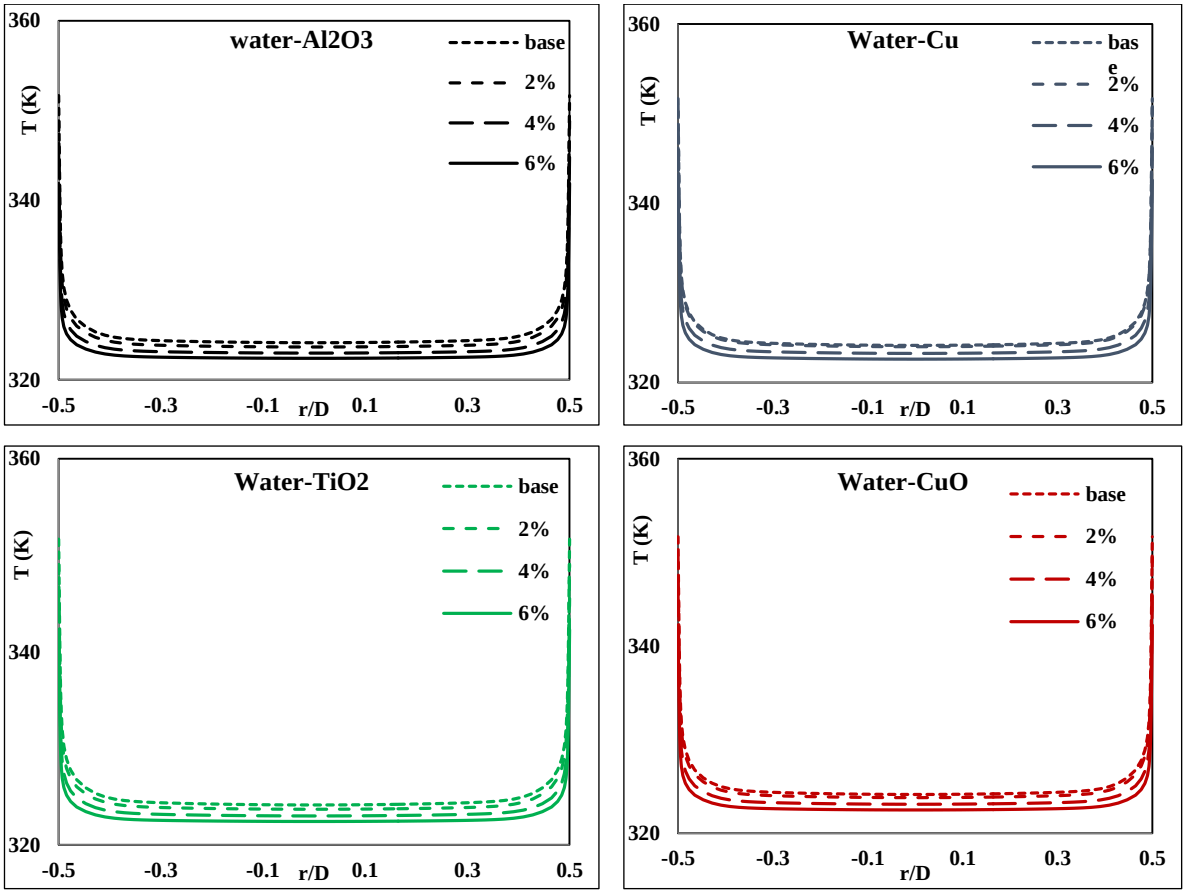

Fig. 6. Effect of particle loading on the mean temperature profiles at L=1.75m and Re=30,000.

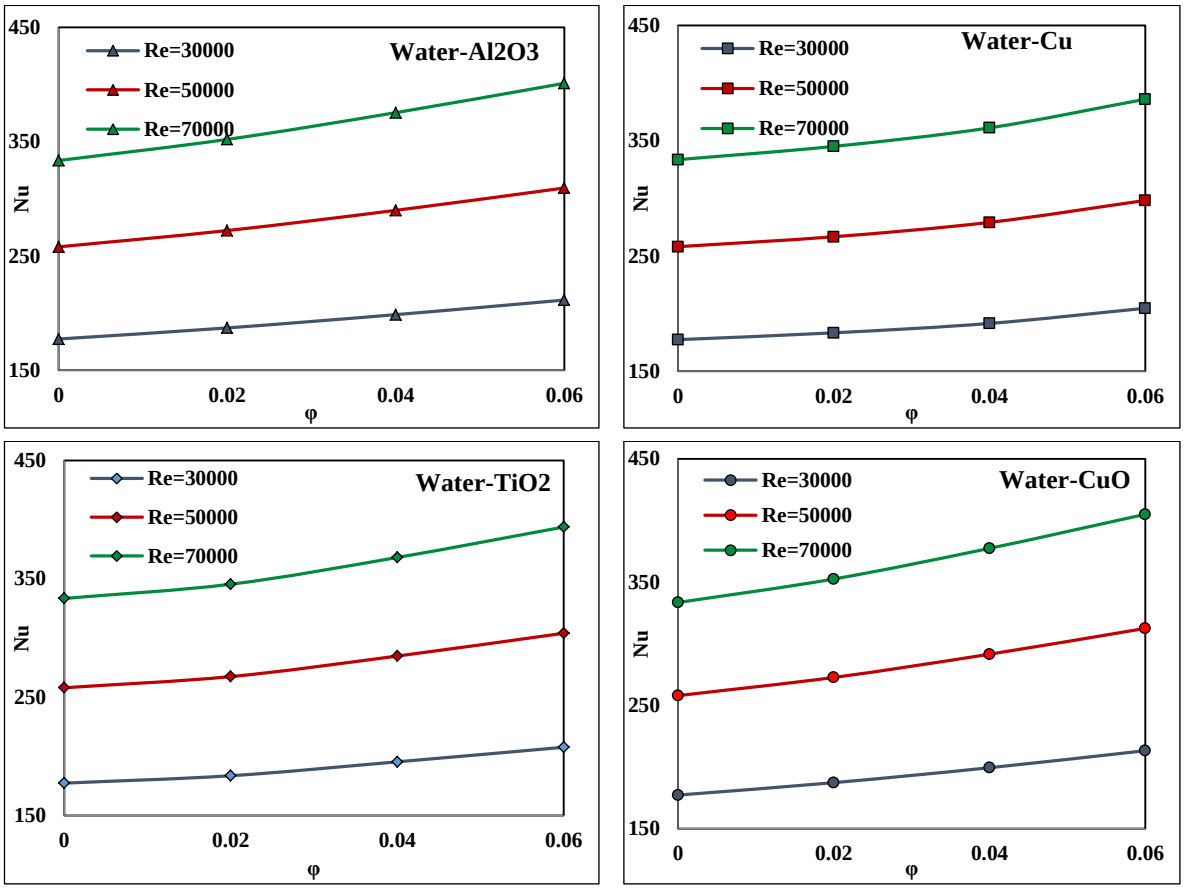

Fig. 7. Effect of particle loading on the Nu number for various Re numbers.

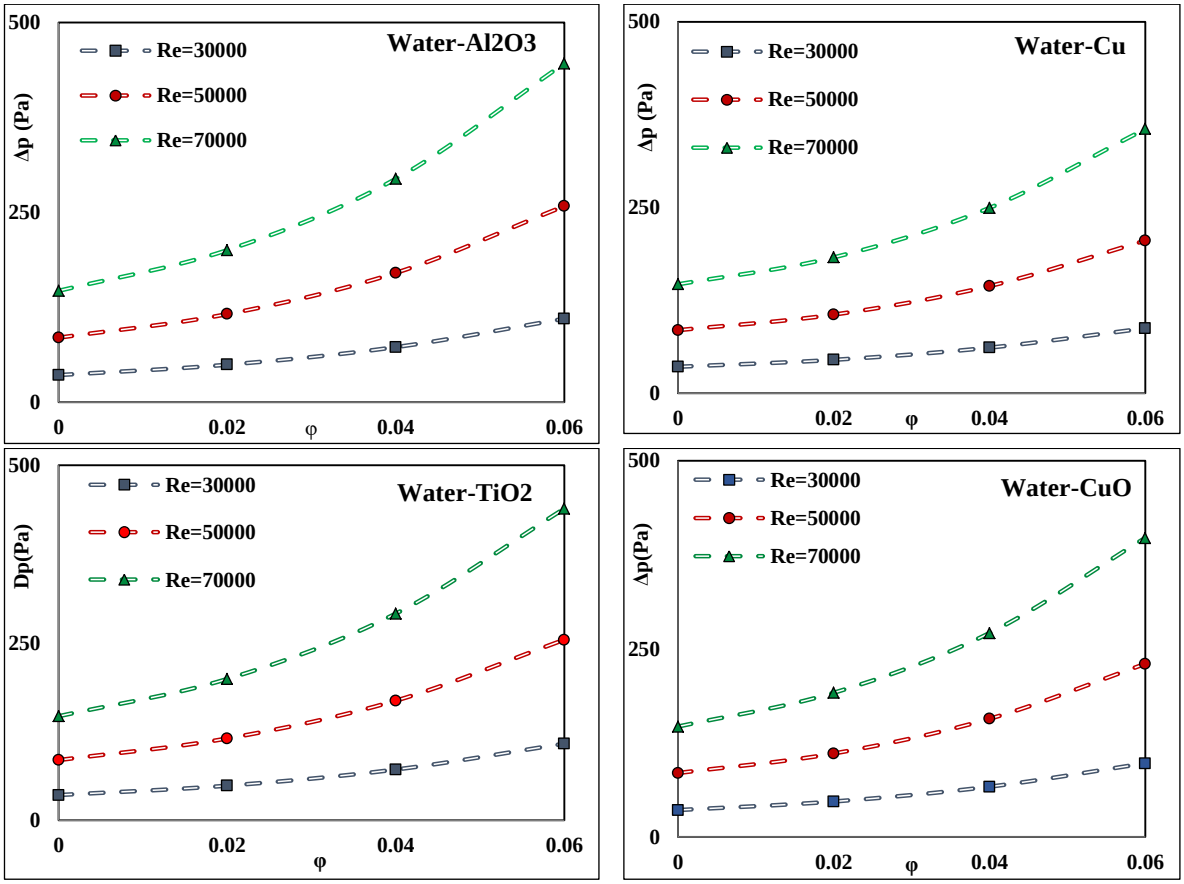

Fig. 8. Effect of particle loading on the pressure drop (Pa) for various Re numbers.

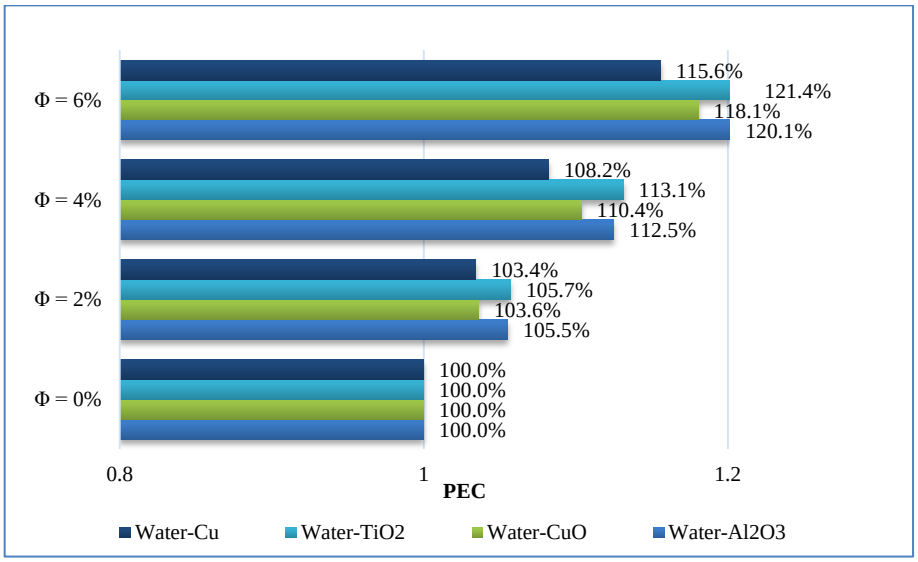

Fig. 9. The (PEC) of various nanofluids at Re= 70000 with different values of φ.

B.8 Conclusion

Based on the literature, it can be concluded that the utilization of nanoparticles in base fluids for improving thermal properties is still an emerging field. The knowledge gap in literature is still considerable in terms of testing different types of nanoparticles with different volume fractions for conjugate heat transfer problems. Furthermore, there are still some open questions about the thermal-physical properties of nanofluids which thus require further research. The current work tries to address this gap by studying the behavior of various nanofluids.

This paper presents results for the behavior of various nanoparticles mixed with water. Four different nanoparticles namely Al_2O_3, TiO_2, CuO and Cu were numerically tested in a uniformly heated receiver tube with different volume fractions at various Re numbers (30,000, 50000 and 70,000). Based on the results it can be concluded that water-TiO2 is the best candidate for the nanofluids mixture as it has the highest Nu number profile and the lowest pressure drop compared to the other tested nanoparticles. At a volume fraction of 6% and Re = 70000, the Nu number enhancements of the nanofluids water-TiO_2, water-Al_2O_3, water-CuO and water-Cu were found to be 21.5, 20.2, 18.11 and 15.7% with the (PEC) of 1.214, 1.2, 1.18 and 1.155, respectively.

B.9 References

[1] K. Khanafer, and K. Vafal, “A critical synthesis of thermophysical characteristics of nanofluids”. International Journal of Heat and Mass Transfer, 2011, 54, pp. 4410-4428.

[2] T. C. Paul, A. Morshed, E. B. Fox, and J. A. Khan, “Thermal performance of Al2O3 Nanoparticle Enhanced Ionic Liquids (NEILs) for Concentrated Solar Power (CSP) applications”. International Journal of Heat and Mass Transfer, 2015, 85, pp. 585-594.

[3] P. Zadeh, T. Sokhansefat, A.B. Kasaeian, F. Kowsary, and A. Akbarzadeh, “Hybrid optimization algorithm for thermal analysis in a solar PTC based on nanofluid”. Energy, 2015, 82, pp. 857-864.

[4] A. Menbari, A. A. Alemrajabi, and Y. Ghayeb, “Investigation on the stability, viscosity and extinction coefficient of CuO-Al2O3/Water binary mixture nanofluid”. Experimental Thermal and Fluid Science, 2016, 74, pp. 122-129.

[5] A. Menbari, A. A. Alemrajabi, and A. Rezaei, “Experimental investigation of thermal performance for direct absorption solar PTC (DASPTC) based on binary nanofluids”. Experimental Thermal and Fluid Science, 2017, 80, pp. 218-227.

[6] Y. Wang, J. Xu, Q. Liu, Y. Chen, and H. Liu, “Performance analysis of a parabolic trough solar collector using Al2O3/synthetic oil nanofluid”. Applied Thermal Engineering, 2016, 107, pp. 469-478.

[7] A. Mwesigye, Z. Huan, and J.P. Meyer, “Thermal performance and entropy generation analysis of a high concentration ratio parabolic trough solar collector with Cu-Therminol®VP-1 nanofluid”. Energy Conversion and Management, 2016, 120, pp. 449-465.

[8] A. Allouhi, M. Benzakour, R. Saidur, T. Kousksou, and A. Jamil, “Energy and exergy analyses of a parabolic trough collector operated with nanofluids for medium and high temperature applications”. Energy Conversion and Management, 2018.

[9] T. Aguilar, N. Javier, S. Antonio, I. Elisa, J. Juan, M. Paloma, G. Roberto, C. P. José, A. Rodrigo, and F. Concha, “Investigation of Enhanced Thermal Properties in NiO-Based Nanofluids for Concentrating Solar Power Applications: A Molecular Dynamics and Experimental Analysis”. *Applied* Energy, 2018, 211, pp. 677-688.

[10] M. Turkyilmazoglu, “Condensation of laminar film over curved vertical walls using single and two-phase nanofluid models”. European Journal of Mechanics -B/Fluids, 2017, 65, pp.194-191.

[11] L. Redjem, M. Ould-Rouiss, and G. Lauriat, “Direct numerical simulation of turbulent heat transfer in pipe flows: Effect of Prandtl number”. International Journal of Heat and Fluid Flow, 2007, pp. 847-861.

[12] B. Petukhov, “Heat Transfer and Friction in Turbulent Pipe Flow with Variable Physical Properties”. Advance in heat transfer, 1970, V6, pp. 503-564.

[13] V. Gnielinski, “New Equations for Heat and Mass Transfer in Turbulent Pipe and Channel Flow”. International Chemical Engineering, 1976, pp. 359–368.